Uniaxial compression of a highly crushable granular material - a 3D DEM study

Marta Stasiak

Communauté
UNIVERSITÉ Grenoble Alpes

THÈSE

Pour obtenir le grade de

DOCTEUR DE LA COMMUNAUTE UNIVERSITE GRENOBLE ALPES

Spécialité : **2MGE Matériaux, Mécanique, Génie civil, Électrochimie**
Arrêté ministériel : 25 mai 2016

Présentée par

Marta STASIAK

Thèse dirigée par **Gaël COMBE,** Professeur des Universités**,** Grenoble-INP
codirigée par **Vincent RICHEFEU,** Maître de Conférences, UGA
et **Pascal VILLARD,** Professeur des Universités, UGA

préparée au sein du **Laboratoire Sols, Solides, Structures et Risques**
dans **l'École Doctorale I-MPE2 – Ingénierie – Matériaux, Mécanique, Environnement, Énergétique, Procédés, Production**

Uniaxial compression of a highly crushable granular material – a 3D DEM study

Compression uniaxiale d'un matériau granulaire fragile très compressible – une étude par éléments discrets 3D

Thèse soutenue publiquement le **12 juillet 2019** devant le jury composé de :

Monsieur Farhang RADJAÏ
Directeur de Recherche, Université de Montpellier, Rapporteur, Président

Monsieur Itai EINAV
Professeur, University of Sydney, Australia, Rapporteur

Monsieur Jean-Claude DUPLA
Directeur de Recherche, École des Ponts ParisTech, Examinateur

Monsieur Jad ZGHONDI
Cadre scientifique des EPIC, Andra, Examinateur

Monsieur Allbens ATMAN
Professeur, CEFET-MG, Brasil, Invité

Monsieur Gaël COMBE
Professeur des Universités**,** Grenoble-INP, Directeur de thèse

Monsieur Vincent RICHEFEU
Maitre de Conférences, UGA, Co-directeur

Monsieur Pascal VILLARD
Professeur des Universités, UGA, Co-directeur

Abstract

The french national radioactive waste management agency (**FR** Andra) suggested a new way to design a tunnel lining, especially, beneficial in the case of very deep tunnels. To avoid very thick tunnel segments, they propose to integrate a layer of granular material on the extrados of the thinner lining. This approach takes the advantages of the compressible capacity of the crushable particles and the load transfer in the granular material. A tunnel segment with such design is called a Mono-block Compressible Arch-segment VMC (Andra's & CMC's pending patent) and is an innovative new type of tunnel linings.

This PhD dissertation is dedicated to the creation of a numerical model capable of reproducing the mechanical behaviour of this compressible granular layer using 3D Discrete Element Method (DEM). The granular packing is made of the brittle hollow coarse-size cylindrical particles, called *shells*. Each shell is a 2 cm long tube with a diameter of 2 cm. Its small thickness makes the cylindrical shell mainly made of void surrounded by a thin layer of clay. In the model, a breakable cluster (shell) is generated using sphero-polyhedral elongated clumps. These clumps, called *sectors*, are glued together using two adhesive contact force laws. If the combination of the normal and tangential contact forces exceeds a suitable failure criterion, a de-clustering of the shell (breakage) occurs. The DEM tool Rockable developed for this research can operate on such crushable particles. The mechanical properties of the shell model, composed of 12 to 24 sectors, are adjusted in the case of a uniaxial (vertical) radial compression of shells. The preceding grain-scale experiments on the true shells made of baked clay serve as a reference. We determine the true range of the failure tensile load and its statistical Weibull distribution. The user-specified parameters is then successfully validated in the case of radial compression of a horizontally constrained shell.

Firstly, the macroscopic study of shell assemblies focuses on the experimental characterisation of the samples with a control of the initial state variables like a number density and a spatial arrangement of shells (shells orientations). 3D reconstruction from X-ray tomographies of the original coated shells samples extracted from the extrados of a tunnel segment help us to characterise the anisotropy of the shells orientation. This is a piece of valuable information to the generation the numerical samples of shells with relevant initial features. Secondly, a series of DEM oedometric tests on $\langle 1\,000 : 2\,000 \rangle$ shells is simulated. A parametric study successfully leads to the understanding of each internal state variable role. A well-chosen set of initial variables with properly adapted DEM parameters give the relevant predictive simulations for a final comparison with the experimental oedometer tests. Thanks to a discrete insight into the micromechanics, the evolutions of the breakage level, the orientation anisotropy and the local stresses exerted on the shells (and/or the fragments) are quantified during the compression. Shell breakage results in a high compressibility of the material. Therefore, the mechanical response is seen as a consequence of the breakage evolution. Finally, an analytical model is suggested in order to predict the stress-void ratio relationship knowing the initial state of the sample and the tensile strength of the constituents: the shells.

Keywords: Crushable granular material, Tunnel lining, Sphero-polyhedral clumps, Bonded Particles, Analytical prediction model, Oedometeric compression.

Résumé

L'Agence nationale pour la gestion des déchets radioactifs (l'Andra) en France propose un nouveau type de voussoirs de tunnel pour les ouvrages très profonds. Pour éviter des segments de tunnel trop épais, ils proposent d'intégrer une couche de matériau granulaire sur l'extrados d'un voussoir moins épais. Cette approche prétend utiliser la grande compressilibité de la couche granulaire constituée de particules broyables et les transfert de charge interne au matériau granulaire pour réduire l'épaisseur du voussoir tout en gardant des performances mécaniques importantes. Un segment de tunnel avec une telle conception est appelé un VMC monobloc compressible (brevet en instance de l'Andra & CMC). Il s'agit d'un nouveau type de revêtement de tunnel particulièrement innovant.

Cette thèse est consacrée à la création d'un modèle numérique capable de reproduire le comportement mécanique d'une couche granulaire très compressible à l'aide de la méthode aux éléments discrets (DEM) en 3D. Le milieu granulaire est constitué de particules d'argile cylindriques creuses appelées textitcoques. Chaque coque est un tube de 2 cm de long avec un diamètre de 2 cm. La faible épaisseur de la coque cylindrique la rend essentiellement constituée de vide entourée d'une fine couche d'argile. Dans le modèle, un cluster sécable (la coque) est généré à l'aide de clumps sphéro-polyédriques allongées . Ces clumps, appelés *secteurs*, sont associés entre eux en utilisant deux lois de contact adhésives. Si la combinaison des forces de contact normales et tangentielles satisfait un critère de charge spécifique, la coque se casse au niveau de l'interface entre les deux secteurs. L'outil DEM Rockable mis au point pour cette recherche peut fonctionner sur ces particules fragiles. Les propriétés mécaniques des coques, composé de 12 à 24 secteurs, sont ajustées à l'aide d'essais de compression radiale uniaxiale (verticale). Les expériences à l'échelle du grain sur les coques en argile cuite ont servi de référence. Nous avons déterminé la plage réelle de rupture et sa distribution statistique (Weibull). Les paramètres numériques et mécaniques ainsi obtenus ont été validés avec succès dans le cas de la compression radiale d'une coque contrainte latéralement.

Dans un premier temps, l'étude des assemblages de coques porte sur la caractérisation expérimentale des échantillons avec un controle sur les variables d'état initiales telles que la densité et l'orientations des coques. La reconstruction 3D à partir de tomographies à rayons X d'échantillons de coques carottés dans l'extrados d'un voussoir nous a permis de caractériser l'anisotropie de l'orientation des particules. Il s'agit là d'une information précieuse pour la génération d'échantillons numériques ayant les caractéristiques initiales pertinentes. Deuxièmement, des simulations DEM de compressions œdométriques sur des échantillons de 2 000 coques sont réalisées. Une étude paramétrique permet de mettre en évidence le rôle des variables d'état initiales. Un ensemble bien choisi de variables initiales et des paramètres DEM correctement adaptés permettent d'obtenir des simulations prédictives pertinentes pour une comparaison avec les expériences de laboratoire. Une analyse micro-mécanique de l'effet de la proportion des grains cassés sur les contraintes locales exercées sur les coques (et les fragments) est effectuée. Il est observé que la rupture des coques entraîné une compressibilité élevée du matériau. Par conséquent, la réponse mécanique en déformation est considérée comme une conséquence directe de l'évolution de la rupture des particules. Pour finir, un modèle analytique de prédiction de la relation contrainte-déformation est proposé dans le cas de la compression œdométrique. Ce modèle prédictif tient compte des variables internes du milieu granulaire comme la résistance mécanique en compression des coques.

Keywords : Matériaux granulaire compressible, Voussoirs, Sphèro-polyhèdre, Compression œdométrique, Modèle de prédiction analytique, Particules collées.

Acknowledgements

This manuscript is a story of a granular material, both literally and metaphorically. I am the grain in the assembly, I collide with other grains to change my direction, I am supported by other grains and I can break easily if my coordination number is low. This is why I would like to thank other grains:

- special gratitude to **Gaël Combe, Vincent Richefeu** and **Pascal Villard** for guidance, patience, time, confidence, freedom and support,
- **Jad Zghondi** and **Gilles Armand** (Andra) for cooperation and opportunities,
- **Radja El Andaloussi, Jean-Claude Dupla** and **Jean Canou** (Laboratory Navier) for showing me the experimental world at the macroscopic scale,
- **Itai Einav** and **Farhang Radjaï** for the work and time invested in your reviews as well as inspiring remarks. Thanks to the remaining jury members **Allbens Atman, Jean-Claude Dupla** and **Jad Zghondi** for the discussion and comments,
- **Edward Ando** and **Olga Stamati** (Laboratory 3SR) for help with discovering X-ray tomography,
- **Cino Viggiani and Emmanouil Vairaktaris** for showing me who supportive "strangers" are
- **Stasiak Helena, Agata, Teofil** and **Kasia Mucha** for who and how you are/were,
- **Eduard Puig Montealla, Mathias Tolomeo, Fabio Gracia, Ilaria Soriano, Kaveh Oghalei Thibault Forestier, Liliana Gramegna, Gaël Combe, Maria Delli Carpini, Floriana Anselmucci** for making me feel like home. I am grateful to meet, in 3SR laboratory, so many fiends who made my day: **Albert Argilaga, Jeanne Doreau, Thanos Papazoglou, Dorjan Dauti, Mohamad Yehya, Olumide Okubadejo, Maddi Etxegarai, Antalya Ho Shui Ling, Ivan Deiros, Aina Foz, Cyrille-B Couture, Chiara Balbinot, Maria Celeste Balsone, Ritesh Gupta, Ankit Gupta, Angela Casarella and so many others**,
- **Kasandra i Bartek Szczepanik, Ania i Rafał Fizia, Ania i Darek Słaby, Ania i Marcin Kulosa, Tomek Iwanek, Błażej Wojaczek, Aleksandra Weber, Monika Adamiecka, Magda Stecura, Dorota Słabosz, Alekasndra Rogozik** and **Aleksandra Husak** to whom it was always pleasure to come back.

My neighbourhood list, thank you!

Contents

Introduction

Contents

Dear Reader,

We are honoured to present you our work. Before you encounter a purely scientific content, we offer you a fast mind warm-up.

We wish you a pleasant lecture!

Presented hereinafter, PhD dissertation originates from an innovative technological concept for the deep tunnel lining, but essentially it is dedicated to the granular matter. The connotation to the engineering application is explained in the section **1.1**. Herein, we have introduced the French National Agency of Radioactive Waste Management (Andra) and briefly commented on their main objectives. However, a more elaborated explanation was dedicated to the concept and the construction of Compressible Arch Segments (VMC). A granular material, that is object of our work, is then introduced together with a brief description of previous findings concerning the material. Further, we summarised the benefits which brings the combination of the compressible layer and a classic concrete segment. Finally, we presented the missing components of Andra's background research, that actually motivate our work.

Section **1.2** is a brief description of the thesis further structure in view of the following review of the manuscript. A short abstract of each chapter is given side to side with some keywords. The section has been designed for the convince of the reader.

List of symbols and abbreviations

Symbol / Abbreviation	**Explanation**
VMC	Compressible monobloc arch-segment (Voussoir Monobloc Compressible)
Shell	Tube-shaped grain
σ_H	Maximal horizontal stress (MPa)
σ_h	Minimal horizontal stress (MPa)
σ_V	Maximal vertical stress (MPa)
ν	Poisson's ratio
E	Young's modulus

1.1 Motivation – Nuclear waste management

Agence nationale pour la gestion des déchets radioactifs is a national french agency being in charge of the study on the possibility of disposal for radioactive wastes in deep clay-stone formation (Andra, 2005). Preparation of such a facility, called *Cigéo*[1], must be preceded by decades of study and preparation involving: data acquisition, repository design, evolution of behaviour of the repository and long-term safety analyses. To this end, the Underground Research Laboratory (URL) has been constructed in Northeastern France and is territorially shared between two departments: Meuse and Haute-Marne (MHM). Thus, the repository is buried 420 m and 550 m deep in Callovo-Oxfordian (COx) clayey layer, resting in between limestone formations (**Figure 1.1**).

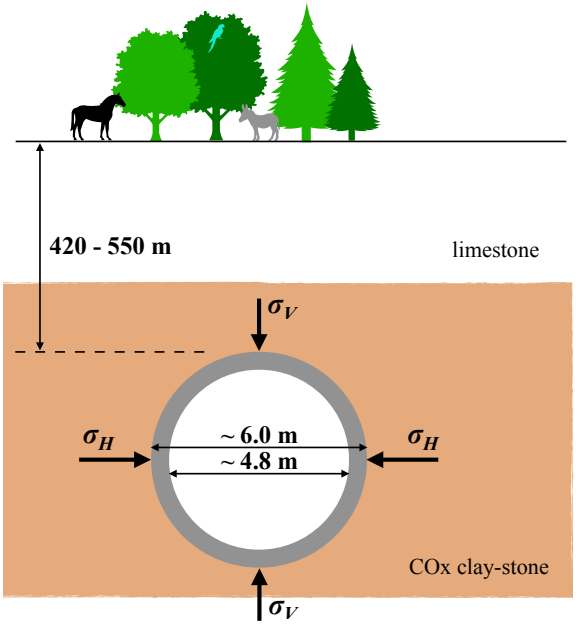

Figure 1.1 : Sketch of GVA2 UL drift presenting location of deep tunnel of Meuse and Haute-Marne Underground Research Laboratory (MHM URL).

The research work of Andra has been divided into two phases. First one focused on the characterisation of COx clay-stone properties (Andra, 2005; Delay et al., 2014) Among many experimental observations, we draw special attention toward a couple of aspects. A high-stress level at the level of URL has been measured by Wileveau et al. (2007). In-situ tests allowed to determine an anisotropy in the stress state with:

- maximal vertical stress $\sigma_V = 12.7$ MPa,
- maximal horizontal stress $\sigma_H = 16.0$ MPa,
- minimal horizontal stress $\sigma_h = 12.4$ MPa,

Thus, an anisotropy of host rock convergence is inevitable but can be reduced if the tunnel is aligned with the direction of σ_H (Armand et al., 2013; Guayacán-Carrillo, 2016). This gives a sense of segment bearing capacity needed to resist the convergence of the host rock.

Second, an ongoing research program is mainly dedicated to technological improvements, and our work, presented hereinafter, originates from this part.

Figure 1.2 : Compressible arch-segment (VMC) is an element of tunnel lining constructed as an union of classic concrete segment and coated granular layer – according to joined US Patent (pending) of Andra and CMC.

Andra faced the challenge of modern underground constructions and came up with an innovative way to design the arch-segments (Andra & CMC[2] pending US patent). *Voussoir Monobloc Compressible* (VMC), which translates to monoblock compressible arch-segment, is a pre-casted

[1] Centre industriel de stockage géologique
[2] Constructions Mécaniques Consultants – a consulting company.
[3] The concept is explained in the video of Andra available online (Andra, 2016).

element of tunnel lining (Andra, 2016; Zghondi et al., 2018)[3]. **Figure 1.2** shows the construction of VMC. 13 cm thick granular layer (with coating) is integrated onto the concrete tunnel linings, such that its compressible behaviour and load transfer capability are activated close to the tunnel's extrados. As is seen, the granular layer is composed of tube-shaped grains, that are manufactured from excavated COx clay-stone by means of the mechanical and thermic treatments. Hence, the grains are classified as ceramic material and one can expect their brittle response to any mechanical loading.

Following (Guayacán-Carrillo, 2016), the elastic properties of COx clay-stone are characterised by Young's modulus $E = 4$ GPa and Poisson's ratio $\nu = 0.29$. Due to the treatment, the elastic properties of the material can be modified[4], but one can already understand that the material is not capable to experience high deformation itself. Thus, high compressibility of layer must originate from the high intra-grain porosity, *i.e.*, the internal void (**Figure 1.3**). Thanks to this peculiar "porous" geometry of grain, we refer to each grain as *shell*.

Figure 1.3 : A *shell* is a tube-shaped particles with large internal void manufactured from COx clay-stone by mens of the mechanical and thermic treatments.

This type of particles can be recognised as *Raschig-rings*[5] used in the field of chemical engineering for distillation and other processes thanks to its large surface. In this context, there exist solutions of other type[6] in the nuclear waste management which involve the Raschig-rings, for example, Pyrex glass rings tested by Jacobson et al. (1998). Despite the different application, there were studies taking into count the strength of Raschig particles, for example, Salem and Akbari Sene (2012) showed the variability of strength for zeolite-based Rashig-rings using the statistical distribution of Weibull (1951). Similarly, VMC emphasises mainly the mechanical behaviour of shells

Let us discuss the motives and benefits of VMC solutions. A priori, we ought to mention that in MHM URL the gallery with the lining of VMC has been already constructed and ongoing in-situ monitoring supports all the conceptual claims (Bosgiraud et al., 2017). Onwards, we will refer to different scales as follows: the tunnel as the *mega scale*, an assembly of shells as the *macro scale*, and single shell as the *micro scale*.

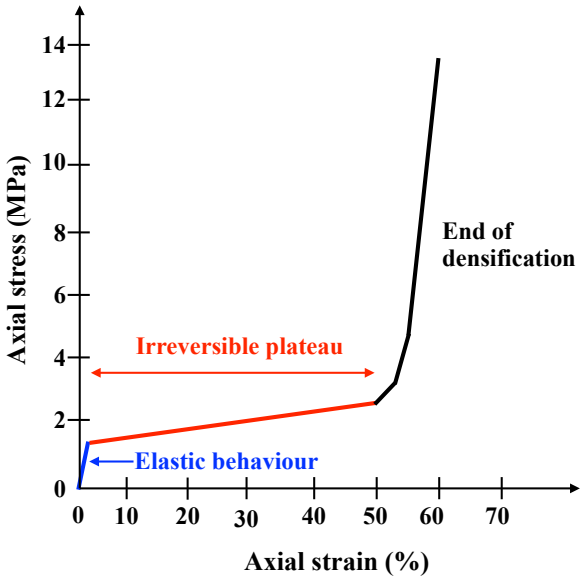

Figure 1.4 : Typical mechanical response of compressible layer (coated shells) obtained from uniaxial compression.

Figure 1.4 shows a typical compressible response of layer obtained from the macro scale experiment (Elandalousi et al., 2018; Ly and Robinet, 2017; Ly, 2018). The compressible layer is an agglomerate – shells have been mixed with the cement mortar to enhance its performance during the segment installation. The strength of cemented links, in between the shells, are relatively weak comparing to the stresses applied on the

[4] For example, the typical values of E for brick are higher $10 - 50$ GPa
[5] There exist a variety of shapes and materials choices in the application for chemical engineering.
[6] Methods directly involved in the prevention of molecular diffusion.

compressible layer (σ_h, σ_V). It is interesting that the behaviour of industrially created layer bears significant resemblance to some natural geological formation like highly porous limestone with weak cemented bonds (Papazoglou, 2018).

Figure 1.5 : Photo of sample before (right) and after (left) uniaxial compression. Test performed by *Euro-Géomat-Consulting EGC* (Orléans) on sample with diameter of 30 cm and height of 13.5 cm (Ly, 2018).

One can distinguish three phases in the mechanical response: elastic behaviour, highly compressible plastic zone and final rapid densification. The plastic plateau rules the high compressibility of the layer. Looking at the sample after uniaxial compression (**Figure 1.5**), one can understand that the high compressibility is activated throughout shells breakage which releases a high amount of the internal voids (discussed in more details in chapter 6). Furthermore, in the concept of brittle fracture, adequate to shell breakage, a change in the free energy is required for crack propagation. A basic and most common thermodynamic framework proposed by Griffith (1921) was based on the conversion of the potential energy (caused by the load) into surface energy needed to break apart the atomic bonds. Essentially, this phenomenon leads to the reduction of the stresses experienced by the compressible layer such that plateau is observed in the **Figure 1.4**.

Then, the compressible layer between concrete lining and surrounding rock spreads stresses by means of load transfer mechanisms as shown in the **Figure 1.6** (Chevalier et al., 2012). When the stress applied by the rock becomes locally very high, the granular material adapts by the breakage combined with the large contact force rearrangements. The forces distributed on the extrados of the concrete segment are reduced as long as the granular layer preserves the compressible properties. This has been confirmed experimentally (Bosgiraud et al., 2017; Zghondi et al., 2018). A retrievability requirement of the waste (over 100 – 150 years) leads to an extra design constraint. For instance, the irreversible behaviour of the compressible material should permit to cap the transferred stresses, due to COx convergence, to the concrete part of the lining. The challenge lies in providing the compressible material will effectively stay in the "irreversible plateau" zone during the requested life time of the structure (Andra, 2005).

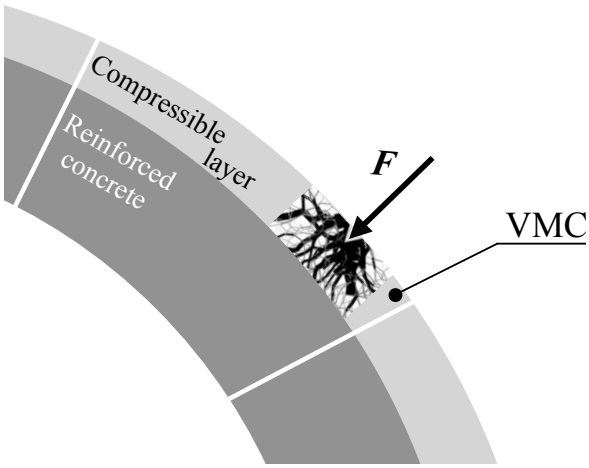

Figure 1.6 : Heterogenous distribution of forces characteristic for the granular materials is expected in the compressible layer.

Summary

The advantages of compressible layer:

- The compressible layer is characterised by good chemical properties – it is chemically inert and has non-caloric load.
- The cement coating of shells allows to adjust the initial elastic behaviour needed to install the lining segments.
- The granular skeleton of the layer transfers the load and reduces the stresses applied on the concrete part.

The advantages of VMC:

- The excavated host rock COx is recycled while manufacturing the shells.
- The compressible layer is also equivalent to classic mortar backfill of pre-casted tunnel lining. With VMC one gains the control over the backfill, such that the homogenous thickness and density are obtained and (radially) uniform mechanical response is guaranteed.
- The technological process limits the usage of the concrete. Firstly, thanks to the reduced load applied on the concrete the thickness of pre-casted concrete can be reduced. Secondly, the lack of injected backfill mortar contributes to this reduction too.
- The compressible behaviour of layer encourages the log-time time safety of the concrete, and thereby, the structure.

The remaining challenges that define our study:

- the understanding of the mechanical behaviour,
- the investigation of the breakage phenomena,
- the generation of the numerical model able to predict long-term behaviour,
- the optimisation of the parameters of the granular material.

1.2 Guide for The Reader

Chapter 2

Keywords: Literature review, Grain crushing, DEM, Fragment replacement, Particle bonding, Breakage Criterion, Shape discretisation, Complex shapes.

This chapter is a bibliographic review introducing the research domains to which we aspired to contribute. Studying the literature, one can easily understand the importance of grain breakage on the behaviour and the properties of the granular materials. Thus, at first, the state of art is dedicated to a discrete numerical modelling with grain crushing. We placed a strong emphasis on Discrete Element Method (DEM). Although we have acknowledged some combined methods, we mainly focused on the DEM as an independent modelling method. The chapter elaborates on two modelling approaches: a Fragment Replacement Method and a Bonded Particles Method. Secondly, we looked into the existing alternatives to the spherical shapes. The more complex ways to form a grain, including features like a concavity or an angularity, are also considered.

Chapter 3

Keywords: Grain scale, Experimental tests, True tensile force, Force scattering, DEM tool Rockable, Cluster model, Cohesive links, Sphero-polyhedron, Model verification.

This part is dedicated to a grain-scale study of tube-shaped grains (shells). The work contains both experimental and numerical study that resulted in a generation of a reliable model of grain breakage. We described the experimental campaigns of two simple tests conducted on a single shell: (*i*) a uniaxial radial compression and (*ii*) a biaxial radial compression with the horizontal strain contains. Moreover, the numerical reflexions of those tests were performed thanks to the Discrete Element Method (DEM). Therefore, we partially dedicate our attention to the basic concepts of the method. The DEM software Rockable is introduced including its advantages and its limitations. Herein, we contemplate the influence of the numerical parameters and explain some of the final choices.
In **Appendix A.1** one can find all the cluster shapes used in the modelings compared together in a transparent way. **Appendix A.2** is dedicated to the additional finite element modelling of the shell in the context of the strength determination. The knowledge of internal stress state supports the choice of the numerical parameters in DEM.

Chapter 4

Keywords: Experimental estimation, X-ray CT, Grain orientation, Numerical deposit, Rigid boundary effect, Preferential orientation.

This part is the introduction of the macro scale both experimentally and numerically. Experimental characterisation of the true material has been performed in the first place. One can find here the measurements of a density range, an estimation of the shell-shell friction angle or the mortar strength assessment. The sample acquired from true VMC segment has been scanned using the X-ray computer tomography (CT). We discussed a solution to detect grains in the 3D image adapted to the tubes. Therefore, a statistical distribution of the shell orientation could be compared with the numerical samples. The protocol to deposit an assembly under the gradational downfall has been enhanced with the additional schemes such that either a random or a preferential orientation could be obtained. The DEM models were constructed using a rigid boundary, the effect of the constraints has been evaluated thanks to the anisotropy of shells orientation. **Appendix B** is dedicated to a more detail description of the initial state of the sample. A table contains a set of the parameters that describes the assembly of shells like the density, void ratio and coordination number.

Chapter 5

Keywords: Macro scale, DEM modelling, Oedometer tests, Parametric study, Final model, Experimental comparison, Unloading-Reloading cycles.

This chapter continues the numerical study of the shell assembly. The mechanical response to a medium-pressure oedometric compression has been obtained thanks to discrete modelling. The extensive parametric study was conducted in order to understand the parameters roles and to classify their importance. The study shows how the force parameters, the initial state and the shell thickness affect the mechanics. The answer is clearly manifested by the changes in the compression curves. The final comparison between the macroscopic experiments[7] and the final representative modelling have been done including the primary investigations of both micro- and macro-mechanics as well as their co-dependance.
Appendix C includes a tabular summary of all the significant user-specified parameters for all the discussed modelings.

Chapter 6

Keywords: Analysis, Breakage level, Sieve analysis, Grain size distributions, Orientation anisotropy, Local stress, Void reduction, High porosity, Analytical model.

Firstly, a detailed analysis of the shell breakage is shown addressing the consequences of breakage on the response to the oedometric load. A distinction between a primary and the secondary crushing is made, because of the internal porosity of those peculiar grains. Thus we discussed the evolution of primary breakage and the modifications of grain size distributions. Furthermore, the statistical analysis concerns both the growth of the orientation anisotropy and the local stress exerted on a shell or a fragment. An interesting modification of the consolidation curve can be found if the accessibility of the internal voids of the tube-shaped shells is acknowledged. The chapter finishes with the construction of analytical constitutive models predicting the classic and the modified consolidation curves with respect to either the axial strain or stress.

Chapter 7

Keywords: Summary, Conclusions, Perspectives.

The objectives of this brief chapter is a comprehensive closure of our study. Classically, we summarise the work and conclude the most important findings of the study. Finally, some prospects to continue and/or complete this research work are proposed.

For reader comfort, a prior to each chapter we also recall the actual table of content, introduce the sections in a proem and pre-define the symbols and abbreviations used afterward.

[7] External data.

Modelling grain crushing: a state of the art

Contents

Introduction

Section **2** is a literature overview of the matters we found most important to build our study. Initially, we desire to introduce grain crushing as a factor of great importance to overall understanding granular material behaviour, but we also wish to point out the attention given to breakage in the research studies dedicated to the industrial applications, mainly in civil engineering.

Section **2.1** briefly shows the compressible behaviour is influenced by grains crushing. The uniaxial "oedometric" compression is a fundamental test investigating the compressibility of material. The experimental study performed on, probably the most standard granular material, sand but also some examples of the artificial porous materials are mentioned.

This experimental observations must have led to enhancement of numerical methods that initially did not take into account grins breakage. The overview is dedicated mainly to discrete element modelling method such as Discrete Element Method or Contact Dynamics – section **2.2**. However, in sections **2.2.1** and **2.2.2**, we acknowledged an existence of method combinations which mix the discrete and the continuum approaches. Section **2.2.3** elaborate on the DEM modelling including particle breakage. Two categories were distinguished: a Fragment Replacement Method and a Bonded Particle Method. We discussed the basic concepts as well as the pros and cons of both. Further, we went into details by looking at the failure criteria and the shape discretisation used by various researchers. This section references the studies made on circular/spherical shapes.

Section **2.3** is dedicated to a treatment of the complex shapes and higher degree of contact complexity. It is divided into two parts:

- Section **2.3.1** presents rigid clumps of disc/spheres with semi-complex and highly complex shapes. The breakage was not acknowledged in the mentioned studies but the influence of grain non-convexity was discussed.
- Section **2.3.2** elaborates on the angular shapes – polygons (2D) and polyhedra (3D). A considerable attention was paid to the shpere-cylinders which are simple examples of shapes used in our work presented afterwards.

List of symbols and abbreviations

Symbol / Abbreviation	Explanation
Section **2.1**	
σ'_v	Vertical effective stress (MPa)
e	Void ratio
p	Mean pressure (Pa)
p_a	Reference pressure (MPa)
S_{1D}	Slope of line (Hardin, 1987)
Section **2.2**	
BPM	Bonded Particle Method
BVP	Boundary Volume Problem
CD	Contact Dynamics
DEM	Discrete Element Method
NHL	Numerical Homogenisation Law
FDEM	Combined Finite-Discrete Element Method
FEM	Finite Element Method
FEM×DEM	Double scale approach: FEM at large scale and DEM at the small scale
FRM	Fragment Replacement Method
SBFEM	Scaled Boundary Finite Element Method
XFEM	Extended Finite Element Method
α	Power (parameter in power law)
σ_{crit}	Failure tensile stress at mass canter of disc (Pa)
σ_{fM}	Critical tensile stress for the largest grain (Pa)
σ_{pb}	Strength of parallel bond (MPa)
$\sigma_{crit\,1\,\mathrm{mm}}$	Critical tensile stress for grain with $R = 1$ mm (Pa)
σ_{max}	Maximum principal stress (Pa)
σ_{min}	Minimum principal stress (Pa)
σ_t	Maximum tensile inter-disc stress (Pa)
$\sigma_{1,2,3}$	Average principle stresses in 3D (Pa)
b	Power in the hardening law – material constant
b_n	Normal contact force limit of simple point bond (N)
b_s	Shear contact force limit of simple point bond (N)
D	Diameter of disc (m)
D_M	Size of the biggest particle (m)
F_{max}, P_1	Maximum principal contact force (N)
F_{min}	Minimum principal contact force (N)
F_{crit}	Critical force causing tensile failure (N)
$F^{\star}_{crit}$	Critical shear force (N)
f_W	Variability parameter
f_D	Parameter acknowledging contacts isotropy
f_{CN}	Parameter acknowledging curvature of the loading path
k, K	Pre-factor of power law concerning force and stress, respectively
K_{pb}	Stiffness of parallel bond (GPa/mm)
L	Thickness of disc (m)

Continued on next page...

Symbol / Abbreviation	Explanation
N	Normal force force (N)
m	Weibull modulus
R	Radius of disc (m)
R_{min}, R_{max}	Minimum, maximum radii of sphere sub-particle (m)
R	Radius of disc (m)
S	Shear force (N)
W_0	The critical energy density (J/m^3)
W_i^{max}	The critical energy causing de-clustering (J)
q	The octahedral shear stress (Pa)
q_{crit}	Critical octahedral shear stress (Pa)
q_0	Scaled octahedral shear stress (Pa)
V_i	Volume of cluster (m^3)
Section **2.3.1**	
α	Concavity parameter for clump
ΔR	Difference between prescribe an inscribe circle radius (m)
ϕ', ϕ	Vector's radial inclination in neighbour and contact frames, respectively
θ', θ	Vector's inclination with respect to vertical axis in neighbour and contact frames, respectively
$\vec{l}$	Branch vector (m)
$\vec{n}', \vec{n}$	Normal unit vector of neighbour and contact frames, respectively
R_1	Radius of circle prescribe on the complex shape (m)
R_2	Radius of circle inscribe in the complex shape (m)
$\vec{t}', \vec{t}$	Tangential unit vector of neighbour and contact frames, respectively
Section **2.3.2**	
BCM	Bonded Cell Model
λ	Irregularity parameter
C_s	Tensile cohesion of bond (Pa)
C_t	Shear strength of bond (Pa)
d_0	Typical cell size (m)
l	Distance between the centroids of two cells (m)
l_{min}	Minimum limit of distance between two cell's centroids (m)
r	Radial coordinate of vertex in the half-plane ring (m)
r_{min}, r_{max}	Minimum, maximum radii of half-plane ring (m)

If a symbol or an abbreviations is not distinguished in the current section, please search in the previous sections.

Granular material

"A granular material is composed of discrete solids which are in contact most of the time." It is one of the most basic definition given by Duran (2000). The author has also pointed out that *"the granular materials occupy a prominent place in our culture. The worldwide annual production of grains and aggregates of various kinds is gigantic, reaching approximately ten billion metric tons. [...] The construction industry (housing, hydraulic concrete needs, public works projects, and so on) consumes aggregates at the rate of seven tons per capita per year"*. No wonder, so many research projects were, are and will be dedicated to understanding of the mechanical behaviour of such materials.

A number of studies shown that grain fragmentation plays an important role in various industrial processes like grinding – clinker grinding in cement industry (Esnault and Roux, 2013) or wheat grinding (Blanc et al., 2017) – powder compaction (Nguyen et al., 2015) or civil engineering works and structures – pile installation and cyclic solicitation (Colliat-Dangus, 1986; Doreau-Malioche, 2018; Yang et al., 2010), railway ballast degradation (Zhang et al., 2017), dams maintenance (Alonso et al., 2005), and so forth.

By now, the microscopic properties and macroscopic behaviour are well known to be interdependent. Grain breakage leads to the significant changes of density volume, strength, hydraulic conductivity, *etc.* On one side, the appearance and amount of grains breakage within granular packing has a grain scale origins, like particle shape and particle strength. On the other side, there exist significant connection to the macroscopic characteristic: initial grain size distribution, initial void ratio, effective stress, stress path, presence of water (Hardin, 1985; Fukumoto, 1992; Lade et al., 1996).

2.1 Contribution of grain crushing to the compressible behaviour

"For the type of deformation that primarily produces volume change, such as one-dimensional strain or isotropic compression, particle breakage adds to the reduction in volume" (Hardin, 1985). This is adequately illustrated by **Figure 2.1** coming from the work of Bauer et al. (2017). As is seen, on the example of classic consolidation curve for isotopic compression (semi logarithmic $e : p$ space), the strain range, *i.e.* void ratio, for crushable material is significantly enlarged with respect to the assembly of non-crushable particles.

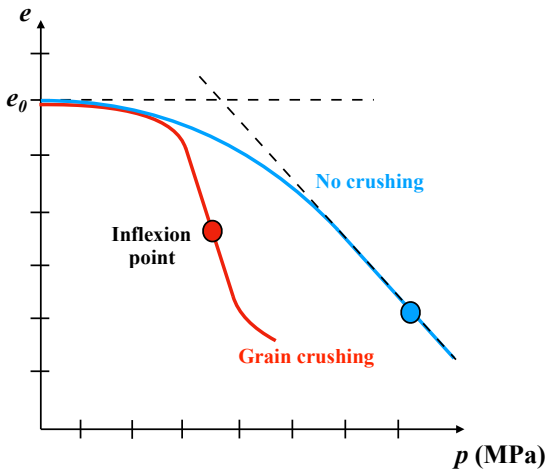

Figure 2.1 : Influence of grains breakage on the compressible behaviour of granular material. Typical compression curves.

As discussed in section **1.1**, the compressible behaviour of VMC is of the highest priority. It was suggested that the plastic plateau observed in the **Figure 1.4** is a consequence of particles crushing. Also, many research studies support this claim.

Early on, Hardin (1987) connects the shape of compression curve in case of 1-D compression with the phases of significant and minor insignificant breakage. **Figure 2.2a** recalls the stress-strain relationship in a modified space $1/e : (\sigma'_v/p_a)^p$, using inverse of void ratio e and normalised effective stress σ'_v/p_a risen to power p. This approach linearised the compression curve when the breakage was insignificant (*ab* segment). Particle crushing was suggested to be significant along curve bend *bcd* with decreasing slope

$$S_{1Dmax} > S_{1D} > S_{1Dmin}. \tag{2.1}$$

The trend got linearised once again (*de* segment) approaching a linear asymptote when the material was being crushed to silt size. As seen in **Fig-**

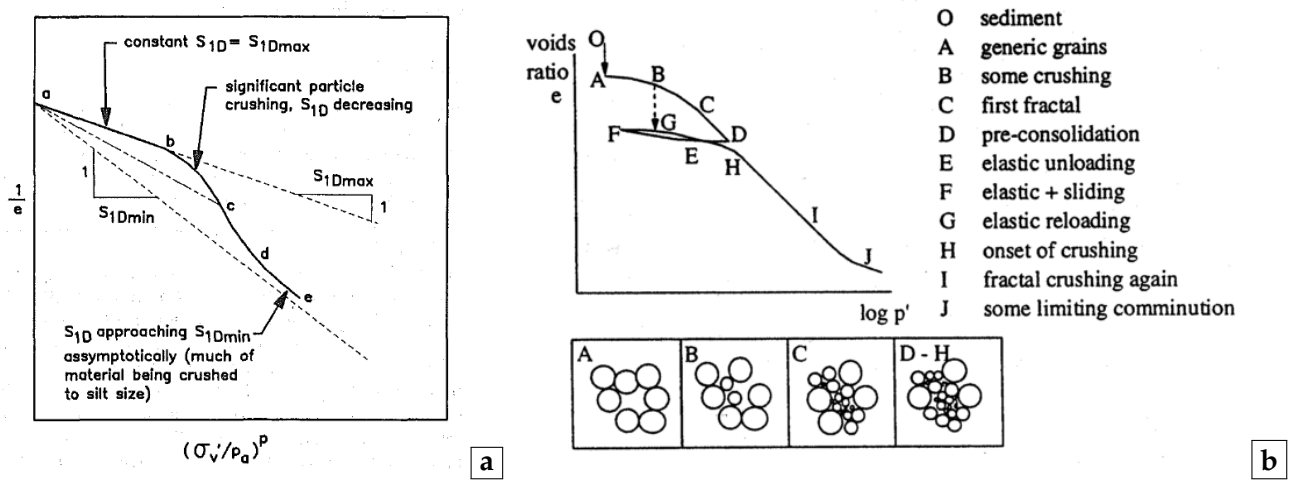

Figure 2.2 : Scheme of oedometric compression explaining influence / importance of grain breakage on the compressible behaviour: **a** – Hardin (1987) and **b** – Bolton and McDowell (1997).

ure 2.2b, Bolton and McDowell (1997) confirmed that correlation within framework of clastic mechanics based on the concept of fractal fragmentation (Turcotte, 1986). The onset of breakage is related to the point of curvature and is referred to as the yielding point (C). The yield stress is characteristic for each material and depends on density, particle strength, and so forth. Furthermore, it is followed by isotropic hardening (HI) that is related to the evolution of the particle sizes and the modification of the contact network.

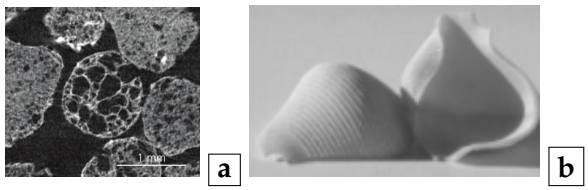

Figure 2.3 : Highly porous artificial material used in an oedometer test: **a** – Guida et al. (2018) and **b**– Di Emidio et al. (2009).

The majority of studies confirming this yielding phenomenon has been conducted on the classical cohesion-less geo-materials, such as sand. Yet nowadays, more often the artificial and highly porous grains are chosen as an object of study. For example, Casini et al. (2013); Guida et al. (2018) studied the compressible behaviour of light-expanded clay aggregate (**Figure 2.3a**), while Di Emidio et al. (2009) performed uniaxial compression on the assembly of "sea-shell" pasta (**Figure 2.3b**). Those study not only presented equivalent evolution of macroscopic behaviour, but also clearly showed that the breakage is, even more, a key factor ruling the compressible response.

Summarising, the characterisation of grain crushing is a fundamental step to understand the mechanics of granular materials. Therefore, if the study aims to build representative numerical model of compressible granular layer, taking into account particle crushing is absolutely necessary. To this end, in the following section we will focus on different approaches to model breakage.

2.2 Strategies for modelling crushing with DEM

2.2.1 Double scale approach

As already discussed, there exists a wide industrial need to predict the behaviour of granular materials, including the granular soils. The progress of technology and computer science constantly enables a development of new numerical methods and an enhancement of already existing once. Since the behaviour of granular matter is highly connected to phenomena of breakage of the constituents, the numerical models must accommodate it in their algorithms.

Within the domain of geomechanics and civil engineering, Finite Element Method (FEM) is clas-

sically used for engineering structures (*e.g.*, tunnels and foundations) and continuum media (like clays), whereas Discrete Element Method (DEM) is widely applied for granular materials such as sand. DEM has been initiated by Cundall and Strack (1979). It has received considerably wide attention across the disciplines. It is simply due to its theoretical simplicity and clear physical meaning.

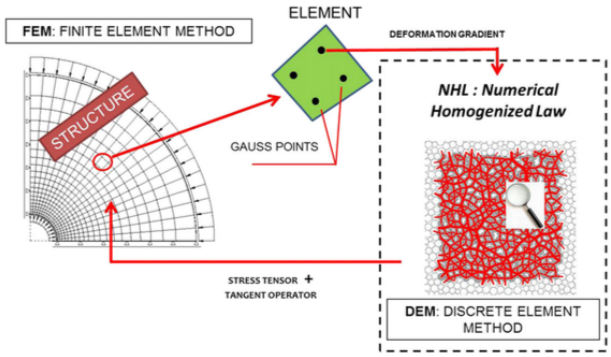

Figure 2.4 : The scheme of double scale approach FEM×DEM (Desrues et al., 2019).

Quite recently researchers tried to combine those two into double scale approach FEM×DEM. This method is working both for the engineering modelling, like the deformation of rock formation around the tunnel (Desrues et al., 2019), and the macro-scale modelling such as a biaxial test (Nguyen et al., 2014). **Figure 2.4** presents a general scheme of this double-scale coupling method as presented by Desrues et al. (2019). At the larger scale, the resolution of boundary volume problem (BVP) of a finite continuum is accomplished through finite element modelling. A numerical homogenisation law (NHL) is simulated with DEM and serves as an extremely rich constitutive law, *i.e.*, expresses the stress as a function of the displacement gradient, at each Gauss point of mesh. Therefore, DEM computations are performed for each integration point so that the main effects of granular materials are adequately captured. Within this method, the particle breakage can be included in the discrete modelling. Since, DEM is a self-sufficient modelling method, various approaches to reflect particle crushing has already been developed.

2.2.2 Combined and enriched approaches

There exist combinations of those two methods (FEM and DEM) also in the inverse configuration. Such methods are limited to solve the macroscopic system of grain. For example, Ma et al. (2016) used the combined finite-discrete element method (FDEM) in which the fragmentation, contact detection, interaction between separate bodies are treated with DEM, while the internal stress state and deformation for each grain are found from FEM (**Figure 2.5**). Similar system was employed by Luo et al. (2017), yet using a Scaled Boundary Finite Element Method. This method handles the breakage within the SBFEM framework instead of DEM. Another study (Druckrey and Alshibli, 2016) has been using an extended finite element method (XFEM) which is less mesh dependent in predicting crack path. In general, the combination of two methods has higher computation cost due to detail finite computations of each grain. Also a hybrid computational framework was presented by Zhu and Zhao (2019) combining the peridynamics and Contact Dynamics (CD) engine. The peridynamics, a continuum-based mesh free method, is used to analyse breakage, while the non-smooth intergranular contacts are managed by the CD method.

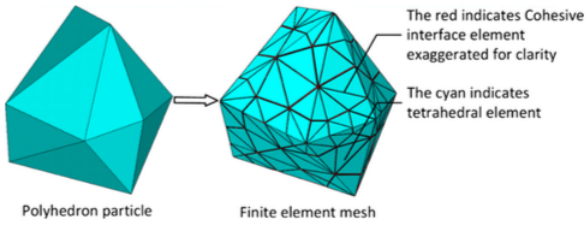

Figure 2.5 : Grain meshing in the combined approach FDEM used by Ma et al. (2016).

2.2.3 Purely discrete modelling

Let us focus on modelling of particle breakage within the discrete element modelling itself[1]. The existing numerical strategies capable of modelling particle breakage can be simply categorised in two groups (**Figure 2.6**):

[1]We refer to the studies using DEM and CD (contact dynamics).

- Bonded Particle Method (BPM) in which the particle is generated as a cluster of smaller particles connected together by means of bonds (force-law).
- Fragment Replacement Method (FRM) operates on undivided particles that are replaced by smaller ones when the breakage occurs – that is when a given limit criterion is satisfied.

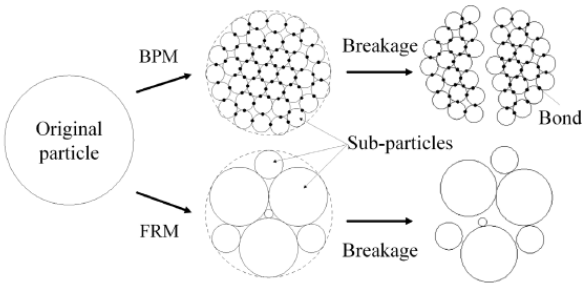

Figure 2.6 : Two main approaches in modelling grain breakage: Bonded Particles Method and Fragment Replacement Method (Zhou et al., 2019).

Further, this literature review delves into more detail concepts of discrete element modelling. Essentially, a basic knowledge of discrete element method is required from the reader. If at a given point one is missing the concept of contact recognition or basic force laws, we recommend to familiarise oneself with a brief section **3.1** in **Chapter 3**.

2.2.3.1 Fragment Replacement Method (FRM)

When dealing with FRM two challenges arise. Both the particle breakage criterion and the fragment replacement mode need to be properly selected. The first one aims to capture the load level and the configuration that trigger the replacement, and therefore, it is related to the particle strength and the loading type. The second one targets the realistic evolution of grain size distribution throughout the adjustment of the size and the number of the replacement particles, packed in the initial surface (2D) or volume (3D).

Åström and Herrmann (1998) investigated the fragmentation of elastic discs with a two-dimensional model. The authors distinguished the following requirements of the fracture mode: (*i*) a low number of fragments per breakage event (to preserve the possibility of breakage), (*ii*) a replacement resulting in the decrease of the local pressure and (*iii*) a realistic fragment replacement mode. Note that discs were always replaced by smaller discs featuring the fractal fragmentation. Two different approaches were suggested, both respecting the mass conservation. In first, they simply replaced a disc in two equal-size fragments, while in second approach 12 fragments of three different sizes were packed within the area of master-grain and the missing mass was balanced by adding discs in neighbouring voids. Also, two various breakage criteria have been probed, essentially showing that limiting threshold of pressure leads to an unstable process. Presumably, due to lack of some phenomena such as size hardening. Thus, it was suggested to apply the threshold of the maximum compressible force.

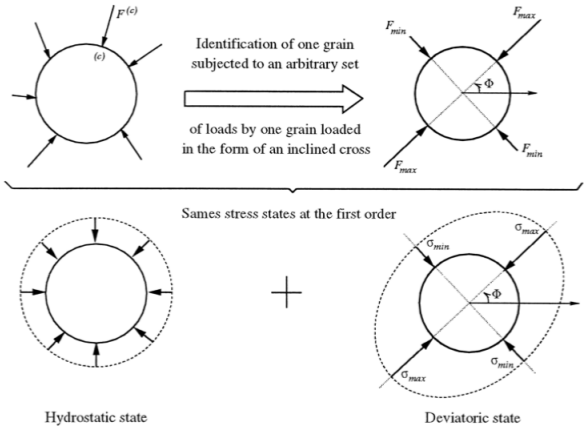

Figure 2.7 : Breakage criterion used by Tsoungui et al. (1999). The set of forces is converted to biaxial compression (top) and an equivalent stress state which can be decomposed into an isotropic and the deviatoric part (bottom).

Tsoungui et al. (1999) proposed to calculate the principal stresses for each disc (2D) taking into account the true state of particle contacts. Instead of working with the set of contact forces, the grain was compressed in the form of a cross by F_{max} and F_{min}, analogously to biaxial loading, as shown in the **Figure 2.7**. Tsoungui et al. (1999) specified that stress state at the centre of a disk is a function of both forces, because the occurrence of σ_{min}, equivalent to appearance of F_{min}, reduces

Author	Shape
Tsoungui et al. (1999)	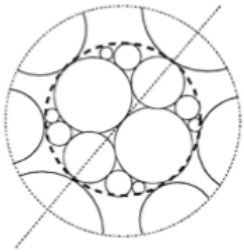
Lobo-Guerrero and Vallejo (2005)	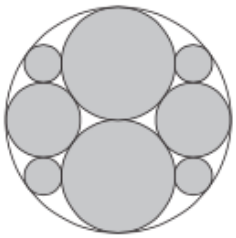
Ben-Nun and Einav (2010)	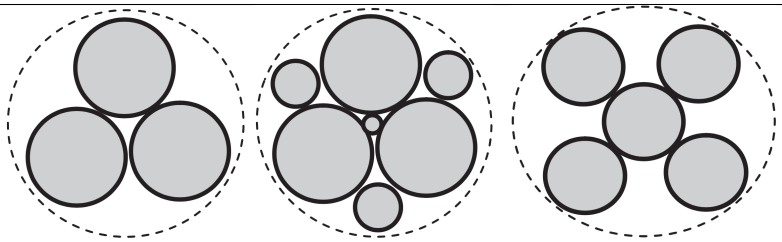
McDowell and De Bono (2013)	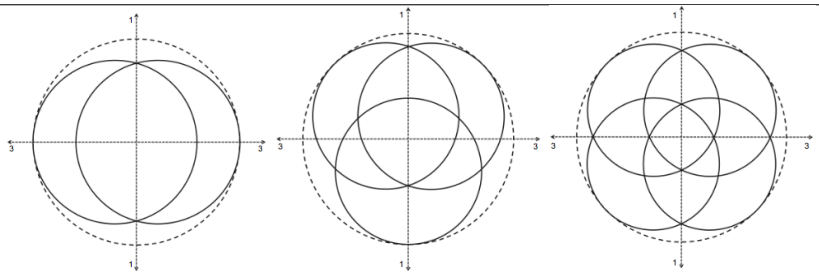
de Bono and Mcdowell (2016a)	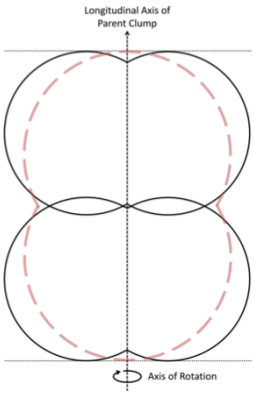

Table 2.1 : FRM – The shapes of clusters proposed by various researchers.

the deviatoric state. McDowell and Bolton (1998); Nakata et al. (2001b) also stated that the average number of contacts per particle should be taken into account since its large amount leads to more isotropic stress state inside the grain. Then, this approach indirectly included the strength hardening due to the coordination number. If the tensile stresses σ_t, seen as a function of F_{max} and F_{min}, exceeded the critical stress σ_{crit}, the particleAs commonly known, the ultimate streng was replaced by set of smaller constituents shown in **Table 2.1**. As is seen, each disc was replaced into 12 subparticles in 4 different sizes. Following Åström and Herrmann (1998), more discs were placed in the "pockets" of the assembly to preserve the original mass of grain. A minimum size was imposed on the fragments in order to reduce the computation time and to prevent material inaccuracies.

As commonly known, the ultimate force is particle size dependent and a power law

$$F_{crit} = k(R/R_u)^{\alpha} \tag{2.2}$$

was used to reflect particles hardening due to size (Vallet and Charmet, 1995; McDowell and Amon, 2000; Nakata et al., 2001a), where R is the particle radius, normalised by unit radius R_u. Note that those parameters include the variability (α) and the material nature (k). Furthermore, it was assumed that the stress limit can be found from uniaxial compression of the disc ($F_{min} = 0$ N). In fact, this approach was used by many researchers both in the experimental determination of true tensile strength and in the modelling for adjustment of tensile failure (Mellor and Hawkes, 1971; McDowell and Bolton, 1998; McDowell and Harireche, 2002; Cheng et al., 2003; Bolton et al., 2008; Laufer, 2015; Cantor García, 2017). Following the framework build for Brazilian compression, Tsoungui et al. (1999) obtained critical stress:

$$\sigma_{crit} = \frac{2}{\pi}\frac{F_{crit}}{D} = \frac{K}{\pi}\left(R/R_u\right)^{\alpha-1}. \tag{2.3}$$

Finally, the model has provided realistic grain size distributions, but a state of reduced breakage was reached, most probably due to the comminution limit.

Lobo-Guerrero and Vallejo (2005) performed DEM simulation of 2D granular material using PFC^{2D} code[2]. The breakage is considered only for discs with 3 or fewer contacts. Constituents compressed by a larger set of forces are considered to be in a fairly hydrostatic stress state, and thereby, have a high probability of survival. This approach imitates the influence of the contact number.

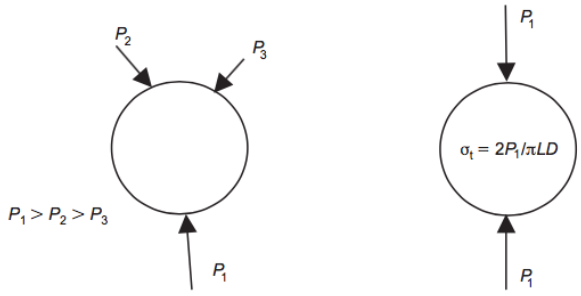

Figure 2.8 : The set of three (or less) contact forces P_i is always converted to simple uniaxial compression (Brazilian compression). Grains with a larger number of neighbours are considered unbreakable (Lobo-Guerrero and Vallejo, 2005).

Although in some cases it might mismatch the true breakage, it surely acknowledges the contact network and minimises the discrepancy resulting from a complete absence of hardening effect. When the disc can break, the load is simplified and grain is always treated as diametrically compressed, despite the number and the arrangement of the contact forces P_i. Thus, the tensile stress at the centre of grain is found using the classical theoretical approach, where the tensile stress

$$\sigma_t = \frac{2}{\pi}\frac{P_1}{LD}, \tag{2.4}$$

with $L = 1$ m and D being dimensions of disc (**Figure 2.8**). To include the hardening effect due to grain size, the ultimate tensile stress is a function of grain radius R:

$$\sigma_{crit} = \sigma_0(R/R_0)^{-1}, \tag{2.5}$$

where σ_0 is the critical stress of 1 mm grain, and R_0 is a reference grain size, here taken as 1 mm.

Table 2.1 shows the replacement packing with

[2] Itasca Consulting Group Inc.

8 circular particles in 3 different sizes. This mode actually violated the mass conservation due to 3 % of mass loss. Although the simulations of the sheared assembly were reported to develop a fractal distribution, the authors did not probe the method in other cases and those simplifications should be treated with a dose of caution.

More comprehensive studies have emerged quite recently considering many possible factors that may trigger the fragment replacement.

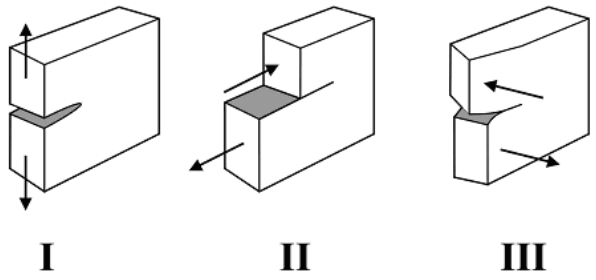

Figure 2.9 : Three modes of fracture: *I* – the tensile opening, *II* – in-plane shear and *III* – out of plane shear.

While working in two-dimensions, Ben-Nun and Einav (2010) focused on a couple of fracture modes: *I* and *II* (**Figure 2.9**). What concerns the breakage criterion in mode *I*, the concept used by Tsoungui et al. (1999) has been re-defined (**Figure 2.7**). Note that authors operated on forces, whereas the studies presented hereinbefore used stresses. Then, the failure criterion for the biaxial compression of grain took a form:

$$2S - N \leq F_{crit}, \tag{2.6}$$

where S is a shear force, N is a normal force and both were determined from the major and minor principal forces (F_{max}, F_{min} in **Figure 2.7**). The critical force was set to:

$$F_{crit} = D\sigma_{fM} f_W. \tag{2.7}$$

The scaling of critical force is based on the reference tensile stress σ_{fM} for the biggest particle size D_M. Then, the force is adjusted using true dimension of particle D and the parameter including the variability of strength f_W. The variability of strength is represented by widely accepted for granular materials statistical distribution of Weibull (1951) also used by McDowell and Amon (2000); McDowell (2001); Laufer (2015); Cantor García (2017).

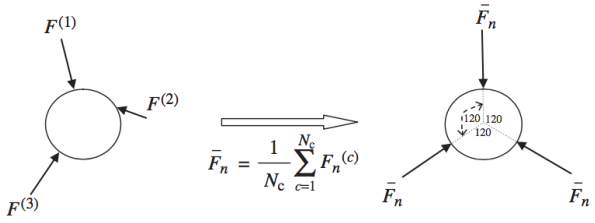

Figure 2.10 : The set of forces was replaced with three equal forces $\overline{F_n}$ isotropically arranged. Such configuration triggers the shear splitting (Sukumaran et al., 2006; Ben-Nun and Einav, 2010).

Figure 2.10 shows the treatment of the mode *II* fracture. As is illustrated, the random arrangement of contact network has been replaced with an equal distributed configuration of three contact forces. The disc was then compressed by force triplets with an identical magnitude set to the true average of normal contact forces $\overline{F}_n$. The critical force F_{crit} has been slightly adjusted to shear throughout its multiplication by two additional factors:

$$F^{\star}_{crit} = F_{crit} f_D f_{CN}. \tag{2.8}$$

First one (f_D) stands for the influence of the number of contacts on the isotropic state, while the latter include the curvature of the loading path. The mode *II* breakage occurred only if

$$F^{\star}_{crit} \leq \overline{F}_n. \tag{2.9}$$

It is interesting to notice that, in contrast to previously described methods, this mode *II* fracture criterion can develop a failure under the isotropic loading.

Looking at the replacement criterion, three different patterns were probed as shown in the **Table 2.1**. Authors have proposed a two-step method to fulfil two conditions: mass conservation and decrease of the local pressure. Initially, sub-particles are described by sizes such that no overlap of discs occurs within the circumference of the original grain. No contact force acted between the particles but there existed a mass loss (**Table 2.1**). In following time steps the spheres have been incrementally enlarged until the mass loss was balanced to zero. Thus, to support this

strategy two different timescales were considered: local and global. Finally, extensive analysis has shown that the fractal grain size distribution tends asymptotically to an ultimate power-law distribution. The influence of the discretisation scheme was detected only due to change of the power-law coefficient. Finally, the choice of fracture mode and the initial state has been found non-influential for the fractal dimension.

Another approach is a foundation of PFC^{3D} software[3]. This tool has been used, for example, by McDowell and De Bono (2013); de Bono and Mcdowell (2016b, 2018). The breakage criterion considers the octahedral shear stress q calculated using the average principle stresses:

$$q = 1/3[(\sigma_1 - \sigma_2)^2 + (\sigma_2 - \sigma_3)^2] + (\sigma_1 - \sigma_3)^2]^{1/2}. \tag{2.10}$$

The octahedral shear stress also provided a convenient way of taking into account multiple contacts and their distribution. For example, de Bono and Mcdowell (2016a) showed the change of q for different set of contact forces with $q = 0$ for an isotopic state. The authors deduced that for diametrical compression q is related to the tensile strength $\sigma_t = F_{max}/D^2$ through a pre-factor 0.9. Essentially, this tensile failure determines the failure for sphere subjected to multiple contacts such that

$$q_{crit} = 0.9F_{max}/D^2. \tag{2.11}$$

Owing to the reduction of size D, the strength hardening takes a general form as:

$$q_0 \propto D^b, \tag{2.12}$$

where b is a material constant. To this end, McDowell and De Bono (2013) employed the Weibull distribution. More precisely, the authors used its width by employing Weibull modulus m:

$$q_0 \propto D^{-3/m}. \tag{2.13}$$

Variation of m showed independence of results from m, but simultaneously the importance of average particle strength was highlighted. Two alternative hardening methods were tested: (*i*) a scaling based on Griffith's law[4]

$$q_0 \propto D^{-1/2}, \tag{2.14}$$

and (*ii*) the surface-initiated flaws

$$q_0 \propto D^{-2/m}. \tag{2.15}$$

The importance of implementing adequate hardening law has been marked both on the compression curve and in the grain size distribution. Study of de Bono and Mcdowell (2016a) not only showed the further investigation of breakage criterion used by McDowell and De Bono (2013) but also juxtaposed the octahedral stress method with others. The realistic compression curve and grain size distribution were obtained for two of tested breakage criterions: octahedral stress and major-contact-force stress. In contrast, following the mean pressure p or the major principal stress σ_1 were not recommended.

Classically, a self-similar replacement was introduced using a set of 2, 3 or 4 identical smaller spheres (McDowell and De Bono, 2013). Ensuring the mass conservation the overlaps in the replacement configuration were approved, causing the contact forces between sub-particles. **Table 2.1** shows the discretisation schemes as the two-dimensional projections, but one must remember that the modelling operated on the 3D objects. The authors commented that the normal compression lines and the grading curves did not exhibit many differences. In other words, the size of the spheres was of secondary importance.

Those examples illustrated the variety, the progress and the enhancements of available approaches. However, in other research works one can find with different methods with their adjustments and argumentation behind choices mode (Esnault and Roux, 2013; Ciantia et al., 2015; Tapias et al., 2015). An important matter, not yet commented, concerns the particle shape. The concavity and the angularity are known to be important features of granular material. We briefly mention the example of CD modelling of Cantor and Estrada (2015), who presented modellings of not

[3] A commercial software of Itasca Consulting Group Inc.

[4] With an additional assumption that the size of fractures inside the grains is always proportional to the grain size D.

only discs but also the polygons as presented in the **Figure 2.11**. The matter of shape will be addressed further, in section **2.3**.

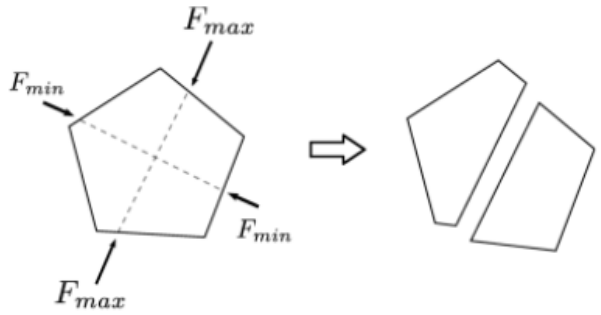

Figure 2.11 : Polygonal shapes used by Cantor and Estrada (2015), where the largest force lead to splitting of grain along the direction of F_{max}.

Fragment replacement method (FRM) has a reputation for simple and easy to implement numerically. It also offers better computational efficiency. On the other side, it requires a reliable framework, especially considering breakage criterion. Granular materials with high intrinsic complexity require many assumptions occasionally leading to some oversimplifications or purely arbitrary choices.

2.2.3.2 Bonded Particle Method (BPM)

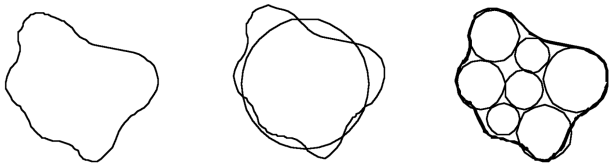

Figure 2.12 : "(left) *Profile of sand particle.* (middle) *Circular DEM element superimposed over a sand particle.* (right) *Assemblage of DEM particles joined together in a semi-rigid configuration, called a cluster, which more closely resembles the geometry of an actual particle."* (Jensen et al., 2001)

In discrete modelling, a technique of particles bonding has proven itself very comprehensive, since it can be used to model intra- and inter-granular cohesion. Thus, not only breakage of grains can be achieved but it works also for other geo-materials, like the cemented sands (de Bono and McDowell, 2014)[5], the rocks (Potyondy and Cundall, 2004) or the composites (Bažant et al., 1990).

By nature, the constituents of granular materials present a variety of random, complex shapes. Let us assume that **Figure 2.12** (left) represents a sand grain in two-dimensions. FRM operating on the circular shapes significantly oversimplifies the true shape as is visible in the **Figure 2.12** (middle). Thanks to the symmetric geometry, the discs or spheres are the most simple and easy to handle shapes. For example, two spheres in contact can have only one contact point, which simplifies the analysis of contact forces. Then, by combining a number of discs one can still benefit from the simplicity provided by the spherical sub-particles. Simultaneously, the complex geometry of the real particle can be easily reflected as demonstrated in the **Figure 2.12** (right).

A discrete element modelling scheme to combine a set of sub-particles with each other such that they form a larger grain can be called *clustering* (recall **Figure 2.6**). By default, these sub-particles are rigid and unbreakable elements. To constitute a cluster, the sub-particles are joined together throughout *bonds* that might either break under loading or stay intact. Once the cluster remains intact, the movement of its constituents has to be consistent with each other, both in translation and rotation, to imitate the motion of a rigid body. However, bodies within the cluster can behave in two ways. Truly rigid behaviour does not allow any relative movement between sub-particles. Such a structure can be called a *clump*. Then, the term *cluster* will refer only to a semi-rigid structure, that follows the same global motion but the inter-cluster contacts can be either deepened or opened. Whereas the clump is widely appreciated in the modelling of complex shapes that cannot break, modelling breakage requires the semi-rigid clusters. Despite the number of sub-particles constructing the clump, it can have either three degrees of freedom in 2D or six in 3D. Therefore, some steps of the numerical algorithm can be omitted in the case of the clump: the contact detection, the computation

[5]This study combines the modelling methods. FRM used for breakage while BPM is used for inter-particle bonding.

of the relative displacement between sub-particles and the computation of intra-clump forces. Then, the computation gains on time efficiency with respect to semi-rigid clusters. In the latter case, the internal forces, necessary to split the packing, can develop. Hence, it is compulsory for each sub-particle to maintain its degrees of freedom independently from others and full computations need to be conducted. A fundamental assumption of DEM is the proportionality of the contact forces to the relative movement of two bodies[6]. One must understand that the rupture of bond requires a realistic force limitation. To this end, similarly as in FRM, the breakage criterion is specified. Recall that in FRM the breakage recognition was based on the critical load (stress or force) applied on the grain. Whereas FRM models the failure of grain, BPM represents the failure of the material (atomic) bonds. Hence, the failure criterion must be related to the material strength at more discrete intra-grain scale. Usually, some numerical parameters emerge from the concept, which are not the straightforward experimental measurements/estimation, as σ_t was for FRM. The replacement model is not needed in BPM, but the choice of sub-particles size/sizes and number have to be made prior to the simulations. This discretisation degree is of great importance since it actually determines the limit of the numerical comminution. The optimum size needs to be selected consciously. Too large size pares the validity of the model, but applying a tiny size makes the computation highly time-consuming and is not storage friendly. Furthermore, constructing a cluster with only one size of sub-particles introduces an unrealistic intra-porosity, thus one might consider employing more sizes or even a well graded sub-particles size distribution to build a grain. Regarding those consequences, the procedure to build one grain needs optimisation.

First of all, the contact laws need to be modified to include a possibility of the tensile failure and an enhancement to classic repulsive DEM contact need to be implemented. For example, to acknowledge also the tensile forces in the grain, the model of Thornton and Yin (1991) considered an appearance of the auto-adhesive forces between the discs. Authors based the bond rapture on the energy criterion verified in the contacts between the sub-particles. Breakage occurs when the total energy of the bond reached the critical value. The bond was not seen as an infinitesimal point, such that its total energy was computed over a contact area. The theoretical framework behind the concept is too wide to present it herein, but we wish to highlight that the failure criteria were defined such that breakage can appear either due to peel or slide mechanism (Thornton and Yin, 1991). This approach was used in the 2D simulation of Thornton et al. (1996), in which the authors considered only one particle at the time. Thus it was possible to use a large (1 000) number of discs bonded together into one cluster (**Table 2.2**).

Jensen et al. (2001) based the rapture criterion on the plastic work dissipating the energy during frictional sliding. Using an energy density is appealing because the critical energy density[7] W_0 is a size-independent, material constant. With W_0 being an user-specified input the critical energy

$$W_i^{max} = W_0 V_i \tag{2.16}$$

causing de-bonding can be computed for any cluster with volume V_i. A contribution to the total plastic work of cluster i appeared at each contact point of the cluster. For both the intra-cluster and the inter-cluster interactions, the plastic work was computed from the tangential contact force and an increment of relative displacement. Then, their sum W_i broke the cluster if

$$W_i \geq W_i^{max}. \tag{2.17}$$

Although the criterion was limited to the sliding work, it was sufficient for the investigations of the effects of particle damage on structure-media interfaces. This highlights that the model can be simplified or restricted to a specific research need. Jensen et al. (2001) have conducted simulations of ring shear test using various shape and sizes of clusters as shown in the **Table 2.2**. Only several

[6] Referring to an overlap between them.

[7] $W_0 = 10^7 \mathrm{J/m^3}$ was found by Jensen et al. (2001).

Author	Shape
Thornton et al. (1996)	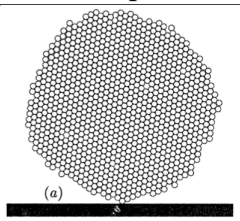
Jensen et al. (2001)	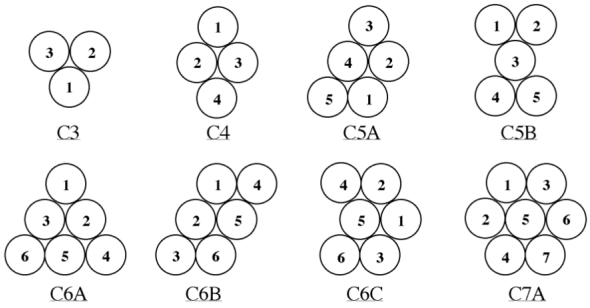
McDowell and Harireche (2002)	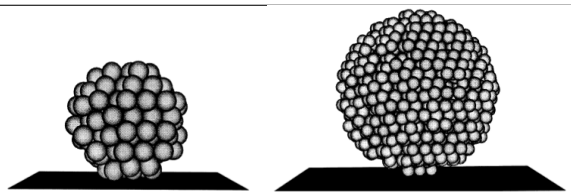
Cheng et al. (2003)	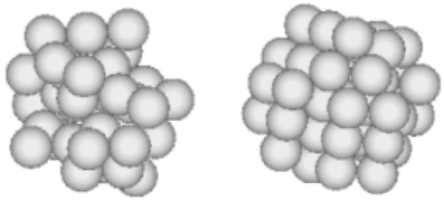
Cil and Alshibli (2012)	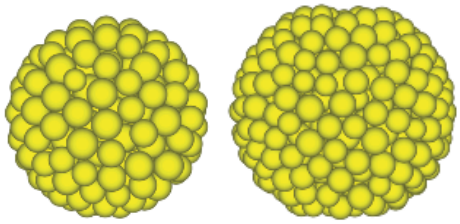
Laufer (2015)	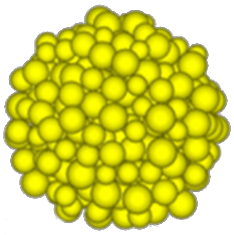
Ueda et al. (2013)	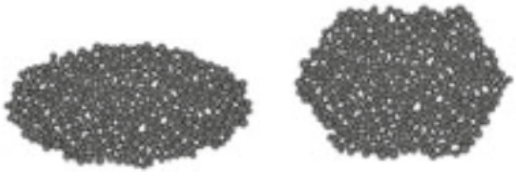

Table 2.2 : BPM – The shapes of clusters proposed by various researchers.

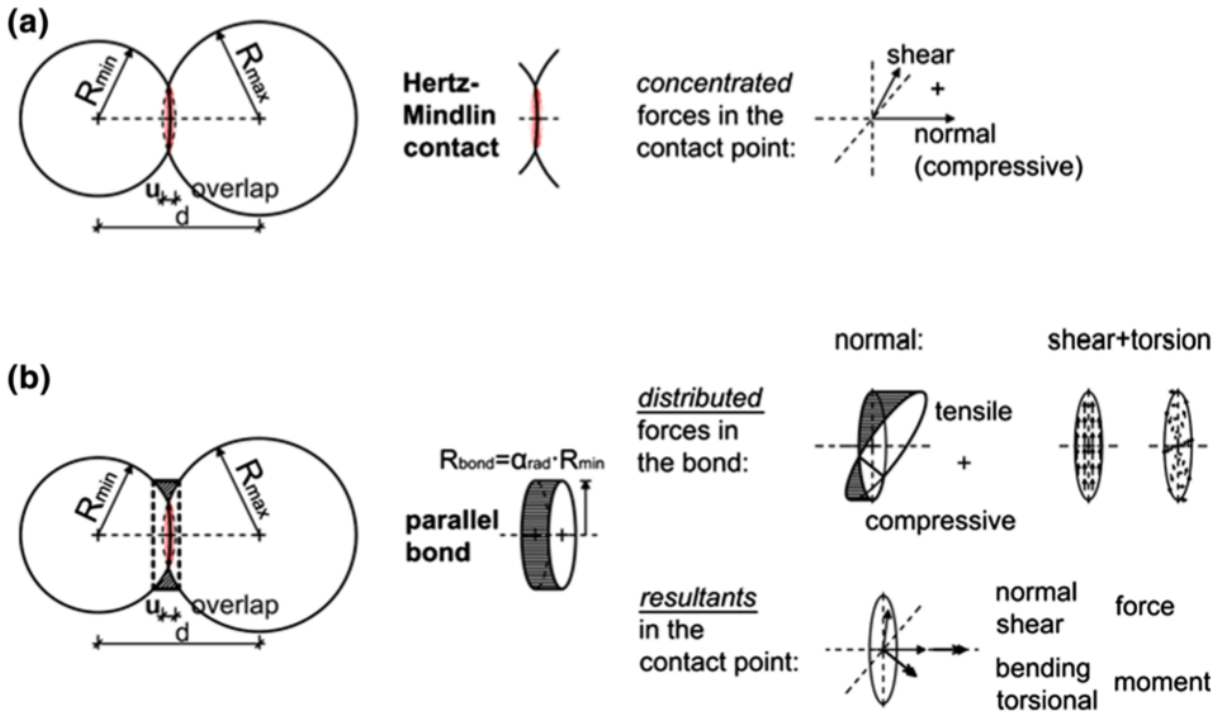

Figure 2.13 : The concept of parallel bonds is employed in the commercial code PFC^{3D} (Laufer, 2015).

sub-particles were used to construct the cluster. However, different cluster geometries introduced an interesting variability of the shape including stronger non-convexity and non-symmetry. In the macro scale, an assembly of 500 clusters was simulated.

Many DEM studies were conducted using the commercial code PFC^{3D} developed by Itasca Consulting Group Inc. The constitutive representation in the intra-cluster contact includes a stiffness model, a bonding model and a slip model. In the literature, two clustering concept was reported:

- a simple contact bond, used by McDowell and Harireche (2002); Cheng et al. (2003); Bolton et al. (2008),
- a "parallel bond" – the option selected by Wang and Yan (2011); Cil and Alshibli (2012); Laufer (2015).

Figure 2.13 demonstrates the later one, for which the sub-particles interact throughout two types of contacts simultaneously, which explains the term "parallel". First one is a frictional cohesion-less contact ruled by the Hertz-Mindlin model as shown in the **Figure 2.13 (a)**. Hertzian force law is an elastic non-linear relationship expressing the magnitude of the compression as a function of the overlap between sub-particles u. Thanks to Mindlin model the code approximates the tangential contact forces using the actual compression in the normal direction of contact. One must understand, that the tensile contact forces are not active. Typically, the sliding occurs according to *Coulomb's* law of friction.

"Bond" (bonded contact) refers to the second type of contact representing the material cementation. In **Figure 2.13 (b)**, the parallel bond is presented as a finite-sized circular cross-section of a beam, and therefore, the problem is dedicated to solving the beam with a user-specified bearing capacity. This approach needs specifying two additional contact parameters: the stiffness K_{pb} and the strength σ_{pb} of this beam-bond. Such bond can be submitted not only to the normal and the tangential forces but also to the bending and the torsional moments. As explained by Laufer (2015), *"The load-deformation-relationships for tension and compression, bending, shear and torsion are linear. The load-bearing capacity is calculated as the elastic bearing capacity of a cylindrical beam."* Essentially, a

sum vector of all the forces carried by the bond and the frictional contact provides the resultant contact force and the moment.

The simple contact bond is a more direct approach, yet the method is equivalent to the parallel bond. Using classic force laws (linear or Herzian elasticity), the force network is established with *Coulomb's* law ruling the sliding point in the tangential contact direction. Additionally, the contact bond with infinitesimal size represents the material internal cohesion. Two forces are user-specified limits working separately in the normal b_n and tangential b_s directions. The breakage of bond occurs when one of these limits is exceeded in either tension or shear. In contrast to the parallel bond, the point of glue cannot sustain any bending or torsion, but it also includes tension. Therefore, unrealistic rolling can be prevented only if the sub-particle has more than one bond.

The majority of the mentioned studies concerned the modelling of the sand particles with fairly spherical clusters. Let us consider the level of shape discretisation selected by those authors (**Table 2.2**):

- McDowell and Harireche (2002) used a hexagonal close packing to represent a sand particle, and essentially two different sizes were compressed vertically. The grains in the size 0.5 mm were represented by 135 spheres and the clusters of 1 mm were build from 1 477 sub-particles. The point bonds between the sub-particles have uniform strength $b_n = b_s = 0.72$ N. Although those discrete values seem very low, the microscopic stress for the tensile failure followed the Weibull distribution in the approximate range $\langle 20 \text{ MPa} : 250 \text{ MPa} \rangle$[8]. Note that the macroscopic behaviour of the assembly was not investigated, thus the high degree of discretisation could have been introduced.

- Cheng et al. (2003) presented 20 different clusters with a typical size 1 mm. The number of sub-particles was varied between 36 and 50. Consequently, the number of bonds per cluster was found between 88 and 177, respectively. The material strength parameters, set to $b_n = b_s = 4$ N, led to the tensile stress in the range $\langle 40 \text{ MPa} : 160 \text{ MPa} \rangle$[8]. Interestingly, the numerical parameters b_n, b_s were ~ 5.56 times larger than for McDowell and Harireche (2002), but the ranges of tensile stresses coincided. Perhaps the difference in b_n, b_s originates from the size of sub-particles. Despite the fact that contact is treated as the point bond, physically larger spheres correspond to a higher amount of atomic bonds. Thus, the discretisation degree influences the *numerical strength* parameters. Note that this is a hypothetical remark based on a comparison between only two research studies.
  Finally, the authors were able to perform the macro-scale simulations on the assembly of 398 clusters.

- Wang and Yan (2011) also worked on the clusters with a diameter of 1 mm. One grain was an assemblage of uniform spheres with radius 0.2 mm, which gives $\langle 60 : 70 \rangle$ elementary balls per cluster. The typical specimen was composed of 1 000 grains, that is 2.5 more that Cheng et al. (2003). This study operated on parallel bonds, but there exists a lack of knowledge about their strength.

- Cil and Alshibli (2012) used the clusters in a tight dimension range $\langle 0.6 \text{ mm} : 0.8 \text{ mm} \rangle$. The sub-spheres size varied such that the minimum radius R_{min} was either 0.035 mm or 0.045 mm and the maximum radius was found from the ratio $R_{max}/R_{min} = 1.2$. The concept of parallel bands was employed with the strength $\sigma_{pb} = 475$ MPa and the normal stiffness $K_{pb} = 70$ GPa/mm. The macro-scale simulation of uniaxial compression was conducted on the assembly of 239 clusters.

- In the discrete modelling of Laufer (2015) three cluster sizes were considered with

[8] Our estimation of the range form the results of McDowell and Harireche (2002) or Cheng et al. (2003).

some details given as follows in the **Table 2.3**. If the parallel bond strength was $\sigma_{pb} = 465$ MPa, the tensile stresses ranged from 10 MPa to 25 MPa. A further variation of σ_{pb} resulted in the proportional modification of tensile stress range. The authors used highly stiff bonds with $K_{pb} = 475$ GPa/mm. The number of particles used in the simulation of the odometer test was restricted to only 128.

Size (mm)	No. sub-particles	No. bonds
2	48	84
3	155	341
4	365	881

Table 2.3 : Discretisation of sand grains proposed by Laufer (2015) with various sizes of elementary spheres such that $R_{min} = 0.2$ mm and $R_{max}/R_{min} = 1.5$.

A final remark concerns the variability of particle strength. For example, Laufer (2015) showed in case of vertical compression, that even if all the bonds were identically strong there existed a variability of cluster strength σ_t. The anisotropic contact network inside the cluster exhibited a variation of σ_t when the grain was simply rotated. However, the experimental-like Weibullian statistical distribution of σ_t was achieved, if either some percentage of bonds were degraded or a normal distribution of contact strength was applied in the bonds.

To conclude, let us predict the number of elementary spheres needed to generate one shell. Keeping the same detail level as McDowell and Harireche (2002), we estimated that $\sim$ 660 000 sub-particles per shell would be necessary for our study. For the macroscopic scale modellings the discretisation level was reduced, but still, the size of the assembly was quite restricted. In such a case, our estimation decreased to the range $\langle 2\,600 : 31\,300 \rangle$ spheres per shell. Note that the shell has around 550 times larger volume than a typical sand grain. To balance the number of sub-particles in computation, we would be able to use 1 shell following Cheng et al. (2003), 3 shells following Wang and Yan (2011) or 9 shells following Laufer (2015). On one side, those are very rough estimations and perhaps the assumptions could be less strict for larger grains. On the other side, the backed clay does not have a highly porous structure itself, thus keeping a high detail level seems true. Nevertheless, it exposes a need for enhancements in this matter.

2.3 Representation of more complex shapes

In this section we will present the exiting solutions to handle the grains with more complex shapes in the conditions with and without breakage. Initially, taking into consideration the complex shapes led to the development of the conceptual background with higher theoretical complexity. Nevertheless, more complex tools are not any less appropriate for the simple forms. Some of those modelling enhancements can resolve the problem of numerous sub-particles and constitute a perspective and a starting point for future developments.

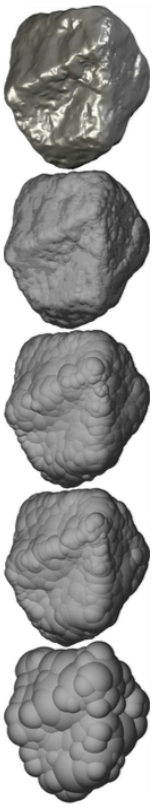

Figure 2.14 : Grain of true railway ballast (top) and its DEM representations using 5 500, 800, 400 and 100 spheres – top to bottom, respectively (Ferellec and McDowell, 2008).

2.3.1 Clump of spheres

Originally, Cundall and Strack (1979) worked on two colliding circular bodies. Despite the fact that the angularity and the concavity of the constituents influence the mechanical behaviour of assembly, simplification of shape to disc in 2D or sphere in 3D has been often accepted, both experimentally (Calvetti et al., 1997) and numerically (McDowell and De Bono, 2013). Even if this might be sufficient for the "full" grains, one can easily understand that a highly porous material such as the tube-shaped shells (introduced in section **1.1**) requires an accurate shape representation.

Clustering can introduce a low level of geometrical imperfection. In BPM, the representation of a perfect sphere still leads to a "surface roughness". This is a slight step towards the true shape, especially compared with a perfect sphere used in FRM. Generating shapes based on a simple symmetrical contour, like the sphere, is easier to implement. For example, Laufer (2015) isotopically compressed the assembly of elementary balls into cubic packing to remove afterwards the subparticles that are not fully enclosed inside a perfectly spherical domain. Then, the clusters were sphere alike. Similar cases seem to be true for many other studies as shown in the **Table 2.2**. Ueda et al. (2013) increased the complexity of a cluster form, but still operated on the basic shapes: an ellipse and a hexagon. Jensen et al. (2001) was able to distinguish the differences between less and more convex shapes, but the authors used relatively simple shapes made of only several subparticles. Thus, it would be easy to place the grains manually. The limitation of semi-rigid cluster originates from equal or tending to zero initial overlaps. The rigid-clusters are complementary in this matter because the realistic internal forces are irrelevant to the user. More advanced shape optimisation procedures have been proposed in the literature, *e.g.*, Ferellec and McDowell (2008); Matsushima et al. (2003). Thanks to the many random, highly realistic forms can be created, such as a railway ballast presented in the **Figure 2.14**. As is seen, the level of accuracy directly depends on the number and the size of the sub-spheres.

[9]This study work contributed also to CEGEO et al. (2012).

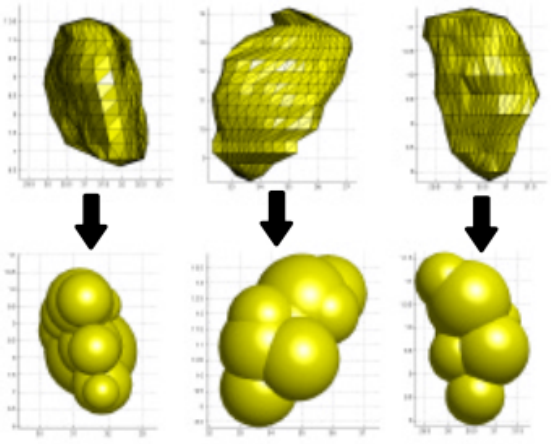

Figure 2.15 : 3D clump with complex shape presented in x, y and z view (Matsushima et al., 2003).

A smaller number of constituents can reproduce complex shapes most satisfactory if adequately placed. As mentioned, those algorithms allow the unphysical overlaps between the spheres, clearly visible in the **Figure 2.15**. Thus, losing the benefit of knowing the inter-cluster force chains brings the breakage model back the fragment replacement method, like in de Bono and Mcdowell (2016a).

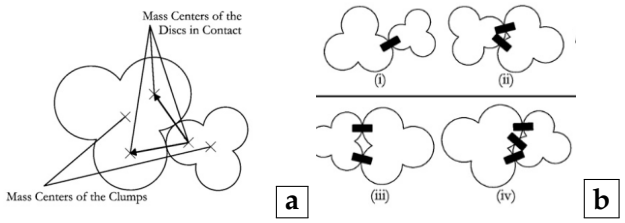

Figure 2.16 : a – 2D clump as a rigid assemblage of three spheres used by Szarf et al. (2011). **b** – Different geometries of contact are possible. Both the tangent contacts and the interlocking contacts can be distinguished.

Still, the discrete modelling using unbreakable clumps, with a various shape complexity, led to a better understanding of mechanical behaviour. For example, Szarf et al. (2011)[9] performed 2D simulations on the clumps composed of 3 overlapping discs as shown in the **Figure 2.16a**. Such a structure allows to easily control concavity of the shape with a straightforward parameter $\alpha = \Delta R/R_1$, where R_1, R_2 are the radii of prescribing

and inscribe circles and ΔR is their difference. The higher is α the less convex is the shape. The authors investigated the influence of grains geometry on the mechanical behaviour of assembly under biaxial compression. Comparing non-convex grains with simple discs, higher internal friction angle and larger volumetric strains were reached. Naturally, the concavity can increase the level of contact complexity. **Figure 2.16b** shows that a simple single disc-to-disc contact (i) can appear, but most often one must deal with multiple contacts between two clumps (ii-iv). Multiple contacts are more possible to appear for higher concavity when the interlocking of particles must be stronger.

Work of Azéma et al. (2013b) considered an equivalent clump, yet in three dimensions (**Figure 2.17a**). The additional third dimension enlarged the amount of possible complex contacts as seen in the **Figure 2.17b**. Authors distinguished two coordination numbers: the average number of neighbours and the average number of interactions. Stronger non-convexity increased the number of interactions, although the number of neighbouring clumps was of the same order (the interlocking effect). This time the influence of concavity was investigated also in case of sheared assemblies but due to the macroscopic triaxial compaction. The observations stayed in a good agreement with the work of Szarf et al. (2011).

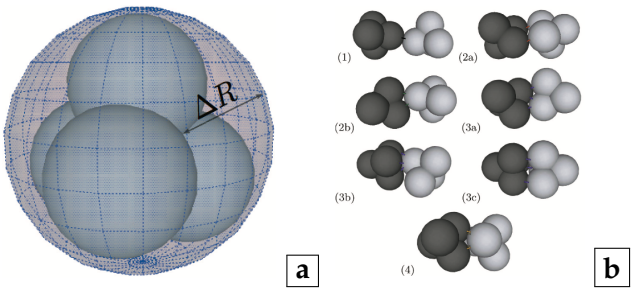

Figure 2.17 : **a** – 3D geometry of clump used in the modellings of triaxial compression on the non-convex granular materials. **b** – Possible type of contact appearing between two neighbouring clumps, starting from simple single contact evolving to complex multiple contacts (Azéma et al., 2013b).

The assembly of 3D clumps subjected to uniaxial compression has been simulated, for example, by de Bono and Mcdowell (2016a). Their simple clump was composed of only 2 spheres as shown in the **Figure 2.18a**. For this case, we have obtained $\alpha \approx 0.42$ which indicates a significant degree of concavity according to the literature (Szarf et al., 2011; Azéma et al., 2013b). Work of de Bono and Mcdowell (2016a) did not elaborate in details on the degree of concavity or its variation mainly because the authors stated that in the uniaxial compression the particle shape played a secondary role in the mechanical behaviour. **Figure 2.18b** shows that the interlocking is significant only to the initial state such that the initial packing fraction is higher. Still, the isotopic hardening was actually ruled by the particle size hardening law, and after the yielding point (the onset of fractal breakage) the curves merged as shown in the **Figure 2.18b**. Though a benefit of concavity was observed. The more realistic value of the lateral earth pressure at rest was found for the interlocking clumps.

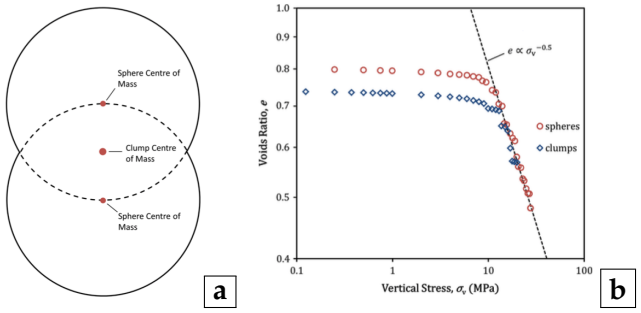

Figure 2.18 : Study of de Bono and Mcdowell (2016a): **a** – a cross-section presenting the geometry of clump made of 2 spheres and **b** – the compression curve for two convex and concave shapes resulting from DE simulations with grain breakage modelled by FRM.

Also, Ueda et al. (2013) stated:
"Despite the difference in crushing type due to particle shape, all samples converged under grain crushing to a critical state characterised by a unique void ratio, grain size distribution and aspect ratio, with a similar distribution of a number of contact points."
Ueda et al. (2013) tested various shapes: spherical, elongated and angular (**Table 2.2**). It was shown that the shape influences the initial packing, and therefore, the mechanical behaviour in over-consolidated state, but an equivalent critical state was reached. Interesting observations were done at the microscale: the round-shaped par-

ticles presented mainly cleavage destruction, the elongated particles tended to develop a bending fracture and an edge abrasion was frequently observed for the angular particles.

Finally, we would like to emphasise again that the complex geometry must lead to the higher complexity of the contact network analysis. Thus, more sophisticated frameworks are needed. To this end, we refer once more to the work of Azéma et al. (2013b) who transparently separated the concept of neighbours from the contact points. **Figure 2.19** shows two clumps in contact. A branch vector $\vec{l}$ joins the mass centres of two clumps that follows the normal direction $\vec{n}'$ in orthogonal inter-centre frame $(\vec{n}', \vec{t}')$, *i.e*, the neighbours frame. The interactions force $\vec{f}$ is described in the contact frame $(\vec{n}, \vec{t})$. As is seen in **Figure 2.19**, those two orthogonal system are not aligned, and therefore, their spatial orientation in 3D coordinate system will be described by different pairs of angles (θ, ϕ) and (θ', ϕ'). This concept enables the authors with a comprehensive and detailed analysis of the fabric and the force anisotropy.

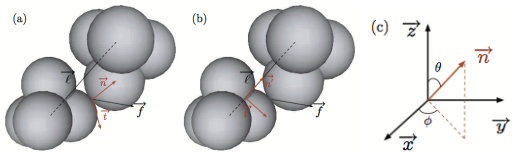

Figure 2.19 : According to Azéma et al. (2013b) the local geometry is described by two frames: a contact frame $(\vec{n}, \vec{t})$ and the neighbours frame $(\vec{n}', \vec{t}')$ in which a branch vector $\vec{l}$ is defined. The contact frame is related to 3D global coordinate system throughout two angles (θ, ϕ).

2.3.2 Polygonal and polygonal-like shapes

The irregularity and the angularity of particle shape are expected to influence to the mechanical behaviour and finally to the critical state. The irregularity modifies the extreme void ratios e_{max} and e_{min}. Well-rounded particles give sharper yielding transition than angular particles because the small strain zone exhibits higher stiffness. Furthermore, the angular assemblies also present higher compressibility in the uniaxial compression, *e.g.*, Cho and Dodds (2006).

[10] (Azéma et al., 2012; Azéma et al., 2013a)

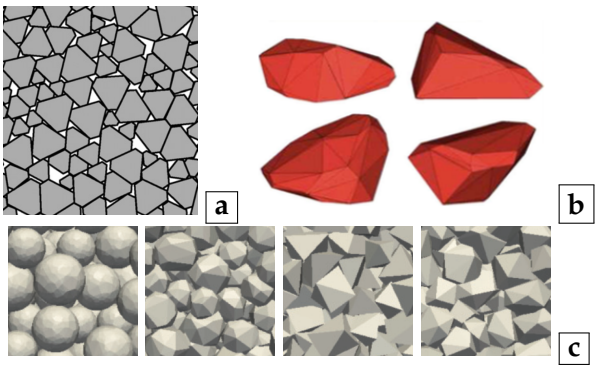

Figure 2.20 : Examples of polygonal shapes used by: **a** – Szarf et al. (2011), **b** – Azéma et al. (2009) and **c** – Azéma et al. (2013a).

Numerically, the polygonal shapes are an alternative to the discs and the spheres for a few decades. Classically, the development started in two-dimensional space (Issa and Nelson, 1992; Szarf et al., 2011), but with a time the simulations were extended to 3D as presented in the **Figure 2.20**. Most often in the literature the polygons or the polyhedra were convex. Still, Szarf et al. (2011) showed that the non-convexity and the angularity do have a similar impact on the mechanical response to the biaxial compression. Authors of Azéma et al. (2009)[10] very often in their research operated on the 3D polygonal shapes (**Figures 2.20b** and **2.20c**). Those were important enhancements in the modelling allowing a direct comparison with the packings composed of the circular particles. Thus, not only the investigations of the origins and consequences were possible, but also the analysis framework was developed for issues such as the anisotropy of contact networks, the force transmission, *ect.*

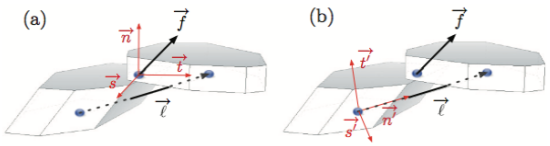

Figure 2.21 : The geometry of contact for polygonal shapes used by Azéma et al. (2009) is equivalent to the one presented by the clumps, shown in the **Figure 2.19** (Azéma et al., 2013b).

One must understand, that for the polygonal shapes the recognition and the geometry of contacts are even more complex than for the clumps of spheres. The miss-alignment of the contact and the neighbourhood frames already showed in **Figure 2.19**, is totally valid and applicable in the case of polygonal shapes as presented in the **Figure 2.21**. Yet the force transmission is more complicated than for two spheres. **Figure 2.16a** clearly showed that despite the multi-contacts, the points of interaction lies between the mass centres of two sub-particles, which simplifies the contact frame. Furthermore, the contact is considered a one point transmitting the force. In contrast, most probably it will not be the case for the polygons or the polyhedra. Sketch **2.22** presented by Cantor García (2017) exposes the variety of contact types. The shape of a polyhedron is described by the points, the edges and the faces. Those elements can interact in random combinations such that finite-size contacts are created. The author replaced the continues (edge-to-edge, face-to-edge) or the surface (face-to-face) contacts with multiple point contacts: two or three, respectively (white bullets). This simplification brings the approach to the case of the clump configuration.

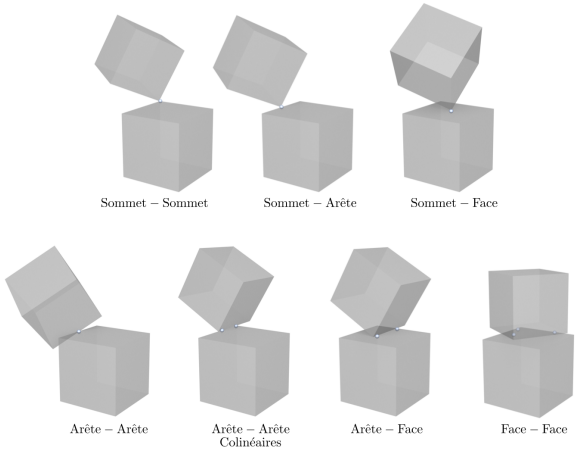

Figure 2.22 : Possible types of contact once two polyhedra collide (Cantor García, 2017). Read: *sommet* as vertex, *arête as* edge, *face* as surface and *colinéaires* as collinear.

One can object to the reliability of those models for the study of one-dimensional compression since they did not include grain breakage. Nowadays, this gap is being filled and the models of non-spherical crushable particles have also been constructed. Those solutions can be included in the group of bonded particles methods but within different numerical frameworks. For example, Bonded Cell Model (Nguyen et al., 2015; Cantor García, 2017) was applied within the contact dynamics (CD) simulations, whereas Nader et al. (2017) used a classic DEM approach. Note that both two- and three-dimensional angular shapes were used in the combined methods mentioned in section **2.2.2**.

Let us consider the BCM in which a cell is the sub-particle connected to other sub-particles by edge-to-edge contact such that the grain is perfectly filled with matter. The lack of intra-cluster pores can be either a benefit or a drawback. Surely one can avoid introducing the unrealistic intra-granular porosity. However, the full structure is a disadvantage while dealing with more porous granular materials.

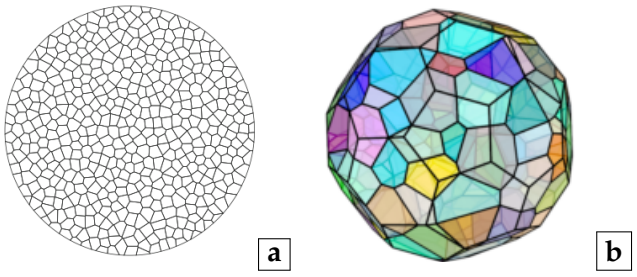

Figure 2.23 : Bonded cell model (BCM): **a** – 2D example of Nguyen et al. (2015) with $\lambda = 0.8$, and **b** – 3D shape of Cantor García (2017) with $\lambda = 0.5$.

In BCM one must decide upon the number of the cell a priori. The discretisation of the particle into cells is based on Voronoi tessellation. A number of rigid cells are distributed randomly over the surface or the volume of grain, such that the distance l between their canters fulfils the following requirement:

$$l \geq l_{min} = \lambda d_0, \tag{2.18}$$

where d_0 is the typical size of the cell. Additionally, this method allowed the user to specify a desired degree of irregularity throughout the parameter λ. Cantor García (2017) provides more details on the algorithm used to fulfil the requirements of a centroidal Voronoi tessellation. Since randomly distributed points do not necessarily char-

acterise the centroids of the sub-particle, an iterative method adjusts the positions with λ being a tolerance of the convergence criterion. If $\lambda = 0$, a highly irregular shape is created. Then, the variety of post-breakage shapes is admirable. We can observe semi-disordered structure in **Figure 2.23a** and quite regular mesh in **Figure 2.23b**.

As the name of the method implies, there exist the inter-cell bonds with a user-specified cohesion. Only edge-to-edge in 2D or face-to-face in 3D contacts (converted to points as shown in the **Figure 2.22**) were consider within the grain. Between two cells the limits of normal and tangential contact forces appeared, such that those thresholds were calculated from the contact length (or the surface) and two material parameters: an internal tensile cohesion C_s and a shear strength C_t. When either of the two threshold forces was reached for each of the three points, the bonds broke and a flag of contact was switched to frictional type.

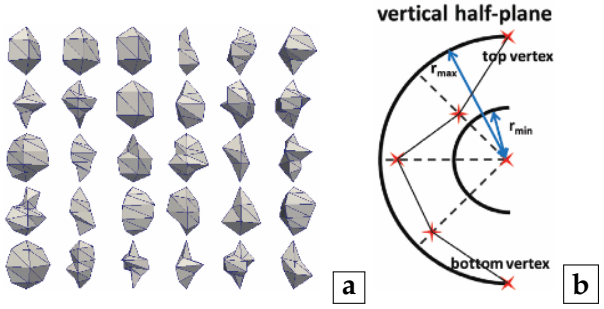

Figure 2.24 : a – Examples of breakable polyhedra generated by Nader et al. (2017). **b** – The scheme explaining how the authors created random polyhedra.

Figure 2.24a shows more angular and elongated shapes generated by Nader et al. (2017). The authors used a different technique to construct the grains. First, the global shape was generated distributing the vertices of grain in the vertical half-planes, *i.e*, half of the vertical cross-section (**Figure 2.24b**). A number of half-planes were predefined by the user, then each half-plane was considered separately. The vertices (red cross) were distributed with random radial distance r within an imposed half ring contour ($r_{min} < r < r_{max}$). The discretisation of shape is a simple meshing of the polyhedron into the elementary tetrahedra, which are then joined together using a Mohr-Coulomb law allowing the normal and tangential cohesion.

Nader et al. (2017) performed oedometric compression on 855 grains such that each was subdivided into 8-12 tetrahedra (**Figure 2.25a**). Typical size of polyhedra was 4cm, thus in the ultimate grain size distribution only the coarse fractions can be reached.
Cantor García (2017) presented two modellings on the assembly of:

- 1 000 grains made of 10 bonded cells
- 2 500 grains made of 30 bonded cells (**Figure 2.25b**)

Comparing to the grains generated as an assemblage of bonded spheres (section 2.2.3), the number of sub-particles per cluster was reduced at least by a factor of 2. Reducing the number of sub-particles is computationally-efficient, but this gained efficiency is usually used to include more grains in the modelling. A sufficiently large number of particles is essential to the reliability of results. Especially, when using the rigid boundary conditions (**Figure 2.25**) which are well known to lead to an undesired boundary effect.

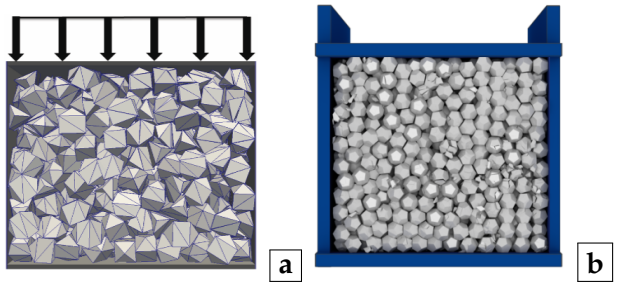

Figure 2.25 : Assemblies of angular breakable polyhedra before 1D compression: **a** – by Nader et al. (2017) and **b** – by Cantor García (2017).

An interesting alternative to creating a particle is a concept called sphero-polyhedron, presented hereinafter. The easiest possible 3D shape made with this technique is a sphere-cylinder (Abreu et al., 2003; Langston et al., 2004). For the sake of simplicity, we are going to use it in the explanation, even if sphere-cylinder does not suit the shape of classic granular geomaterials.

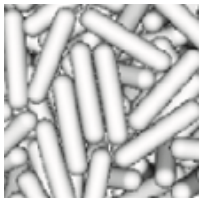

Figure 2.26 : A 3D sphere-cylinder used in simulations of Abreu et al. (2003).

In 3D sphere-cylinder resemblances a longitudinal pill as shown in **Figure** 2.26. Its structure can be presented as the clump made of sub-elements with two different geometries: a sphere and a cylinder. In a two-dimensional sketch from **Figure** 2.27 (a) shows that at each end of cylinder two spheres with the same radius are placed. Due to this sub-division one can distinguish three types of contacts:

- cylinder-to-cylinder – **Figure** 2.27 (b),
- cylinder-to-sphere – **Figure** 2.27 (c),
- sphere-to-sphere – **Figure** 2.27 (c).

The advantage of this rounded geometry is that an analytical method can be used to detect the contacts. The simplification of complex shape to basic symmetric shapes helps to determine the overlaps. Sphere-sphere overlap is a straightforward calculation based on the location of two mass centres. Considering the cylinder, its full axis is the reference instead of the mass centre. For cylinder-sphere overlap, simply the smallest distance between the mass centre and the axis needs to be determined. Similarly, the overlap between two cylinders is approached as shown in the **Figure** 2.27 (b). One can understand, that since cylinders are not perfectly symmetric the orientation of the axis must be constantly updated.

Interestingly, the technique can be extended to more complex 3D shapes. Let us focus on a simple polyhedron shown in **Figure** 2.22. The idea consists in replacing the edges of the polyhedron with the cylinders (**Figure** 2.27 (b)), that are rigidly connected to the spheres, that is to the 3D corners. Then, a vertex-to-vertex contact becomes the sphere-to-sphere interaction, the cylinder-to-cylinder is equivalent to edge-to-edge contact, *ect.* Finally, the concept also requires that the faces gain a thickness equal to the radius of the spheres and cylinders. Onwards, such a structure is called a *sphero-polyhedron*.

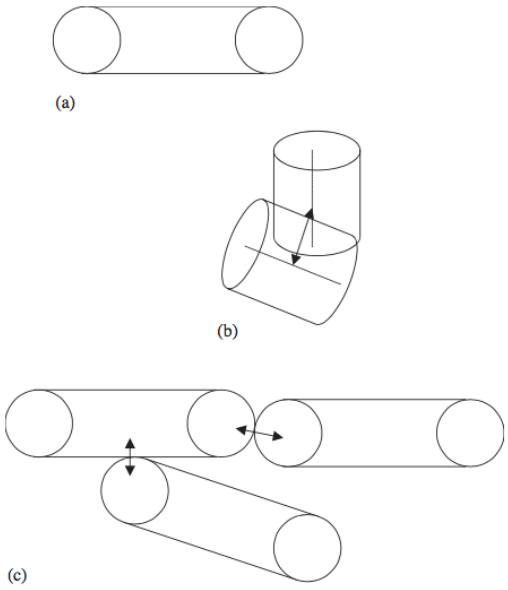

Figure 2.27 : (a) – a 2D representation of sphere-cylinder, (b) – a cylinder-to-cylinder overlap, and (c) – other types of contacts (Langston et al., 2004).

Modelling grain crushing with DEM

Contents

Introduction

The objective of the work is to create micro-scale model capable of reflecting the mechanical behaviour of a shell by means of Discrete Element Method (DEM). Therefore, section **3.1** briefly presents the classic concept of DEM. It will give the reader a sense of the principles such as the definitions of the contacts (overlap) and show some basic force laws (linear elasticity, Coulomb's friction). The choice of numerical algorithms and related to them parameters will be commented herein.

The model was required to realistically reproduce shell breakage, otherwise highly compressible behaviour cannot be obtained numerically. To this end, we have decided upon the modelling approach using clustering of particles (the bonded particle method). Section **3.2** explains how the model of shell with a complex tube geometry is generated. It discusses the cohesive interactions for which standard force laws have been modified such that parameters correlated with a grain strength were included. Also, details of a failure criterion can be found in this section.

Any numerical model requires some input parameters. Therefore, a tensile strength of the shell has been studied in the experimental campaign using uniaxial radial compression on a single grain. Section **3.3.1** will present the results of the experiments on two shells sizes *d18* and *d20*. Both the raw data and the statistical analysis compared with *Weibull's* distribution are included. Finally, an insight into the strength scattering will be discussed.

The experimental response needs to be reproduced numerically by the proposed model. Section **3.3.2** presents how, aiming for a reference response, the numerical parameters can be adjusted, or in other words, how the model calibration was conducted. The influence of the contact stiffness and the tensile strength parameter are explained. Next, the sector size is varied throughout different shape discretisation number of axial and radial directions such that a final choice was established. The changes were connected with the modification of numerical parameters. Finally, the influence of the shell shear strength is estimated numerically.

Acknowledging the simplicity of uniaxial radial compression loading condition, we will present another verification of the model in section **3.4**. It is both numerical and experimental attempt to increase the complexity of loading conditions. A biaxial radial compression – vertical load and a constrained horizontally is perhaps only slightly more advanced but it is experimentally straightforward method that enhanced our level of confidence.

Finally, the most important numerical and experimental observations will be wrapped up into a brief summary in section **3.5**.

List of symbols

Symbol	Explanation
Section 3.1	
ΔT	Time step (s)
Δf_t	Increment of tangential force (N)
$\Delta \delta_t$	Increment of relative tangential displacement (N)
δ_n	Overlap in contact (m)
μ	Coulomb's friction coefficient
$\vec{\omega}_i$	Angular velocity (rad/s)
a_i, a_j	Radii of shapers i and j (m)
$\vec{f}_c$	Vector force acting in the contact c (N)
$\vec{f}_i$	Vector of total force acting on the grain i (N)
f_n	Length of normal force vector (N)
f_t	Length of tangential force vector (N)
$\vec{g}$	Gravity vector (m/s^2)
I_i	Moment of inertia (kg m^2)
k_n	Normal contact stiffness in the frictional contact (N/m)
k_t	Tangential contact stiffness in the frictional contact (N/m)
m_i	Mass of particle i (kg)
m_{ij}	Reduced mass (kg)
$\vec{n}$	Unit vector in normal direction of interaction
$\vec{r}_i, \vec{r}_j$	Position vector of body i and j (m)
$\vec{t}$	Unit vector in tangential direction of contact
T_c	Critical time (s)
$\vec{\Gamma}_i$	Total torque (N m/rad)
Section 3.2	
φ	Yield function
f_I	Length of normal force vector for the cohesive (N)
$f_I^\star$	Normal yield threshold in pure tension (N)
f_{II}	Length of tangential force vector for the cohesive (N)
$f_{II}^\star$	Tangential yield threshold in pure share (N)
I_{mn}	Breakable interface between sectors m and n
k_I	Normal contact stiffness in the cohesive contact – link (N/m)
k_{II}	Tangential contact stiffness in the cohesive contact – link (N/m)
$N^\star$	Total number of sectors
$N_{axial}^\star$	Number of sectors in the axial direction of tubes
$N_{circ}^\star$	Number of sectors in the ring cross-section (circumferentially)
q	Shape parameter of the yield surface
Section 3.3	
URC	Uniaxial Radial Compression of single shell
Δd	Uniaxial reduction of shell diameter (mm)
σ_I	Tensile stress causing mode I fracture (MPa)
σ_t	Critical stress for non-symmetric grains (MPa)
d	Diameter of ring in the shell cross-section – typical grain size (mm)

Continued on next page...

Symbol	Explanation
d_0	Initial diameter of ring in the shell cross-section (mm)
F	Diametrical load applied to the shell (N)
F_I	Ultimate applied force in the uniaxial radial compression (N)
$K(\bar{r})$	Stress concentration factor
h	Height of shell in the axial direction of tube (mm)
$\bar{r}$	Retaliative radius of the ring
r_{in}	Internal radius of the ring
r_{out}	External radius of the ring
t	Thickness of ring in the shell cross-section (mm)
Section **3.3.1**	
α	Power describing the law of force scattering
$d18, d20$	Fabricated sizes of shells distinguished by a target diameter $d \sim 18$ mm and d$\sim$ 20 mm
E_0	Microscopic void ratio analysing only shell
k	Pre-factor of power law of force scattering
m	*Weibull's* modulus / shape parameter of Weibull distribution
MP1, MP2	Population of shells with various manufacturing protocols
P_0	Microscopic porosity analysing only shell
P_f	Probability of failure
P_s	Probability of survival
V_v^i	Volume of internal void of tube (mm^3)
V_s^i	Volume of the solid of tube per shell (mm^3)
V_{tot}^i	Total shell volume measured within the external contour of the tube (mm^3)
x_0	Scale parameter of Weibull distribution
Section **3.3.2**	
F_I	Diametrically applied load in the numerical uniaxial radial compression
$F_{I\,true}$	Mean experimental value of vertical compression
Section **3.4**	
BRC	Biaxial Radial Compression constrained horizontally
F_V	Vertical force compressing a shell in BRC modelling
$F_{V\,true}$	Experimental vertical force compressing a shell in BRC

If a symbol or an abbreviations is not distinguished in the current section, please search in the previous sections.

3.1 Main principles of DEM

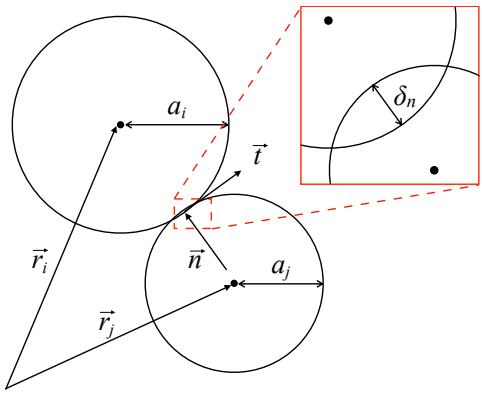

Figure 3.1 : Definition of contact throughout a normal overlap δ_n. 2D projection.

By nature, the majority of granular materials are inhomogeneous microstructures consisting of non-spherical particles. Discrete Element Method (DEM) is a particle-scale numerical method commonly used to reflect the behaviour of granular materials (Cundall and Strack, 1979; Radjaï and Dubois, 2011). In many discrete element modelings, the complex constituents are idealised to circular shapes: discs (2D) or spheres (3D), *e.g.*, Luding (1997); de Bono and Mcdowell (2018). Let us assume that our constituents are spherical, rigid and frictional objects, for the sake of simplicity. In classic DEM, a *contact* c_{ij} between spheres i and j is recognised as the overlap δ of two bodies (**Figure 3.1**).

The contact can be characterised using two unit vectors $\vec{n}$ and $\vec{t}$ which mark its normal and tangential directions, respectively. Then, the overlap in the normal direction δ_n is determined from geometrical relationship:

$$\delta_n = (\vec{r}_i - \vec{r}_j) \cdot \vec{n} - (a_i + a_j), \tag{3.1}$$

where: a_i, a_j are the radii of spheres $\vec{r}_i$ and $\vec{r}_j$ are the position vectors of particles and 0.1cm

$$\vec{n} = \vec{n}_{ij} = \frac{(\vec{r}_i - \vec{r}_j)}{|\vec{r}_i - \vec{r}_j|}.$$

If $\delta_n < 0$ the contact force $\vec{f}_c$ can be determined using various force laws. $\vec{f}_c$ can be decomposed into normal and tangential parts: $\vec{f}_c = f_n\vec{n} + f_t\vec{t}$. The normal component can be ruled by a linear elastic law (**Figure 3.2a**):

$$f_n = -k_n\,\delta_n, \tag{3.2}$$

where k_n is the normal stiffness of the interaction. On the contrary, when $\delta_n > 0$, the particles are separated and no force is acting in the interaction point, $f_n = 0$ (**Figure 3.2a**). Above force law represents contact as a liner spring model in which the interaction is a harmonic oscillator (mass+spring). Then, the contact duration between two colliding bodies i and j is typically:

$$T_c = \pi\sqrt{\frac{m_{ij}}{k_n}}, \tag{3.3}$$

where m_{ij} is a reduced mass[1]. The numerical stability requires the integration time to be smaller than the interaction duration. The division of the critical time t_c into $N_{\Delta T}$ steps provides a secure time increment ΔT (equation 3.4), if N is sufficiently large. For example, $N_{\Delta T} = 40$ was used by Luding (1997).

$$\Delta T = \frac{T_c}{N_{\Delta T}} \tag{3.4}$$

As is seen in the **Figure 3.2b**, the tangential force f_t partially follows similar linear relationship:

$$f_t = -k_t\,\delta_t, \tag{3.5}$$

where k_t is a tangential stiffness. Yet f_t is limited between $\pm\mu f_n$. **Figure 3.2c** demonstrates the coefficient of friction μ using the *Coulomb* yield criterion. In practice, within the numerical scheme the tangential force f_t results from an accumulation of the increments:

$$f_t^{(t)} = f_t^{(t-1)} + \Delta f_t, \text{where} \quad \Delta f_t = -k_t \Delta\delta_t \tag{3.6}$$

with $\Delta\delta_t$ being the increment of relative tangential displacement in the interaction within a time increment δ_t. $(t-1)$ and (t) stand for previous and current time step, respectively. The tangential force f_t falls down to zero if the contact is lost

[1] $m_{ij} = m_i m_j/(m_i + m_j)$

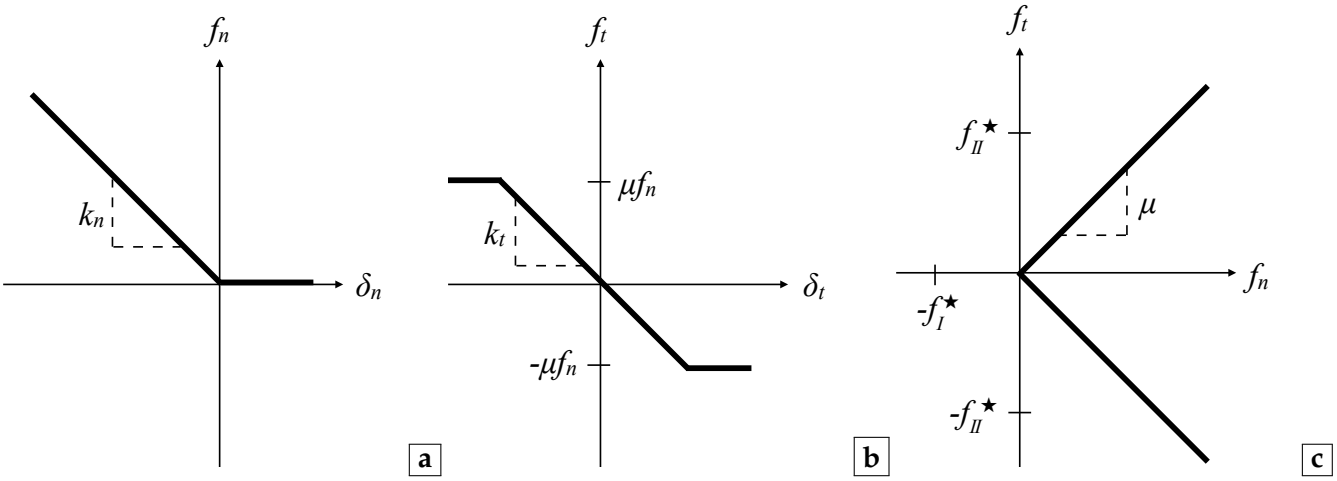

Figure 3.2 : Force laws for the cohesion-less frictional contacts: **a** –in the normal direction, **b** – in the tangential direction, and **c** – *Coulomb's* yielding criterion.

($\delta_n > 0$).

The constituents most often interact with more than one neighbouring particle. Then, the resultant load $\vec{f}_i$, is a sum of all the interaction forces acting on the sphere i. The resultant torque $\vec{\Gamma}_i$ obeys the same logic but implies the calculation of an arm vector from the position of the particle to the contact point (the middle of the gap). Essentially, $\vec{f}_i$ and $\vec{\Gamma}_i$ are used to solve Newton's equations of motion for the translation (equation 3.7) and for the rotation (equation 3.8):

$$m_i \frac{\mathrm{d}^2}{\mathrm{d}t^2}\vec{r}_i = \vec{f}_i + m_i\vec{g} \tag{3.7}$$

$$I_i \frac{\mathrm{d}}{\mathrm{d}t}\vec{\omega}_i = \vec{\Gamma}_i\,, \tag{3.8}$$

with the gravity $\vec{g}$, the moment of inertia I_i, the angular velocity $\vec{\omega}_i$ and the total torque $\vec{\Gamma}_i$. Then, the problem is reduced to the integration of differential equations (3.7) and (3.8).

In this work, the numerical study has been conducted with a parallelised tool named Rockable, developed by Richefeu (2016). Among many possible schemes to integrate Newton's equation of motion, the velocity Verlet algorithm has been implemented in Rockable (Allen and Tildesley, 1989).

In DEM, energy dissipation is always a matter of concern (Atman et al., 2009). The energy dissipation can be managed through various mechanisms. A *Coulomb* friction is one of the possible mechanisms. Additionally, we used two other dissipation models: (*i*) the viscous damping that acts in addition to normal elastic forces (Luding et al., 1994), and (*ii*) the numerical damping that affects the resultant forces of the rigid bodies, like in Cundall and Strack (1979). Both damping strategies are, in the context of quasi-static loadings, only used to increase dissipation efficiency. Particle breakage releases a lot of energy, which must be dampened for the sake of numerical stability.

3.2 Description of a breakage model adapted to hollow grains with DEM

For our application, Rockable has two main specificities:

- it operates on *sphero-polyhedral* shapes,
- and it manages *breakable interfaces*.

Therefore, it is most sufficient to model the complex shapes and to reflect the breakage. Herein, the concepts of both *sphero-polyhedral* shapes and *breakable interfaces* are explained.

Numerical representation of shape

As discussed in section 2.2, two main technic to model the breakage are possible. Between them,

the *cluster model* (Bonded Particles Method) has been selected for this work. If the shell is considered as a semi-rigid cluster, the shape and size of the constituents need to be adapted. As commented in the section 2.2.3, the spheres as constituents would require its tiny size, *e.g.* $d_0 = 0.2$ mm or less, and still would lead to an unrealistic for ceramics intra-porosity. Furthermore, the small diameter of spheres results in an extremely large number of sub-particles which usually harms the computational efficiency. But in case of the big grains like shells[2], the simulations of the large assembly would be impossible to perform if keeping the sub-particles size at 0.2 mm. Therefore, we have considered a polygonal-like shape enabling us to use a large size without introducing the material porosity.

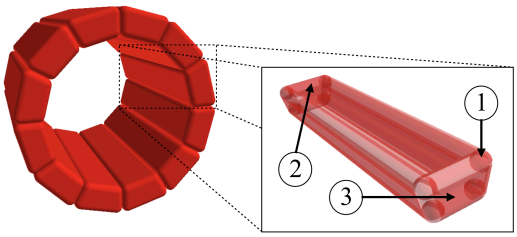

Figure 3.3 : A tube-shaped shell modelled as a cluster of 12 rigid *sphero-polyhedra* elements called *sectors*. The sector is itself composed of sub-elements (spheres ①, tubes ④ and thick planes ③) with no relative movement.

Ignoring the geometrical imperfection, the most adequate simplification of shell shape is a tube (recall **Figure** 1.3). Let $N^\star$ be a number of identical constituents per cluster. Then, subdivision of the tube can be distinguished by its radial and axial direction, denoted as $N^\star_{circ}$ and $N^\star_{axial}$, such that $N^\star = N^\star_{circ} N^\star_{axial}$. **Figure** 3.3 presents an example of numerical shell using $N^\star_{axial} = 1$ and $N^\star_{circ} = 12$. The manner of breakage is adequate to the experimental breakage in uniaxial radial compression of the shell. This non-spherical 3D constituents are onwards called *sectors*. As presents the inset of **Figure** 3.3, the sector is a clump (a rigid cluster) composed of sub-elements of 3 types, with no relative movement:
① spheres as corners,
② tubes as edges,
③ thick planes as faces.
Although, the overall sector shape reminds polyhedron, it has a rounded contour due to the sub-elements. Hence, its name *sphero-polyhedron*.

[2] Around 500 times larger than a sand grain.

Types of collisions

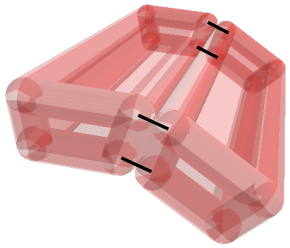

Figure 3.4 : Two adjacent sectors are glued with 4 cohesive links (black lines) only throughout the sphere-sphere contacts.

One must notice that the construction of the sector as a rigid clump of sub-elements has consequence in contact recognition, equivalently to sphere-cylinder discussed in section 2.3.2 (recall **Figure** 2.27). Naturally, it is possible to have the simplest type of interaction when two corner spheres collide, as was shown in the **Figure** 3.4. This type was imposed within the cluster but rarely appeared within the model of assembly between two shells. Since, different sub-elements of clumps can come into contact with each other, there exist more complex types of interaction like sphere-tube, sphere-face and so forth. Those types were observed in the packing, and therefore more details will be given once the assembly is discussed. At this point, only nomenclature has to be clarified, and onwards there is a strict distinction:

- *Link* – an interaction **within the cluster**, for which the tensile cohesion and the shear resistance act to prevent the separation (**Figure** 3.4).
- *Contact* – a non-linked point of force transmission **between two sectors** interacting throughout sub-elements (sphere-tube, sphere-face and so forth). Due to sector structure they can occur in an extremely

small distance. The force laws given in section 3.1.

- *Neighbours* – two clusters having **one or more contacts** between each other.

Modelling breakage – the links

To model the breakage, the clusters behave non-rigidly[3], such that a relative movement between sectors can occur. Within the cluster, the sectors are bonded only through the adjacent spheres (**Figure 3.4**) – only four sphere-to-sphere links are active. These links act elastically in the two directions related to the opening of the common plane (joined faces) as in fracture modes *I* and *II* (recall **Figure 2.9**). The elastic relations are formally written in a tensorial form:

$$\begin{pmatrix} f_I \\ f_{II} \end{pmatrix} = - \begin{pmatrix} k_I & 0 \\ 0 & k_{II} \end{pmatrix} \cdot \begin{pmatrix} \delta_I \\ \delta_{II} \end{pmatrix} \qquad (3.9)$$

In a pure mode-*I* loading (tensile loading), the elastic force normal to the plane cannot exceed a tensile threshold force $f_I^\star$ (**Figure 3.5a**). For a pure mode-*II* loading (shear loading), a tangential elastic force withstands, if it is in the range of $\pm f_{II}^\star$ (**Figure 3.5b**).

$f_I^\star$ and $f_I^\star$ are the yield forces reflecting the material strength and are required only in case of *cohesive* links. When modes *I* and *II* are activated at once, a cohesive interaction holds as long as a yield function φ remains negative:

$$\varphi = \frac{f_I}{-f_I^\star} + \left(\frac{|f_{II}|}{f_{II}^\star} \right)^q - 1, \qquad (3.10)$$

where q is a numerical parameter that controls the shape of the function, as suggested by Delenne (2002). The yield function φ in the $f_I : f_{II}$ plane is shown in the **Figure 3.5c** for a given value of q. In this model, the mechanical behaviour of a cluster is elastic and brittle, but the mechanical parameters (the stiffnesses and the threshold forces) and the fracture pattern are related to the initial slicing of the cluster (**Figure 3.3**).

Due to specificity of ROCKABLE, if the cohesive link between the sector m and sector n is imposed, a *breakable interface* I_{mn} is created. All the following links between those sectors are assigned to the same interface I_{mn}, *e.g.*, 4 links belongs to 1 interface in the case shown in the **Figure 3.4**. As soon as $\varphi \geq 0$ for one of the bonds belonging to the interface I_{mn}, the rest of bonded interactions are broken simultaneously. This compels the rupture to be brittle whatever the link mechanical parameters are.

We recall the reader that shell-to-shell contacts are ruled by the normal and the tangential laws described in section 3.1 if the cemented joints are not included in the model.

[3] One must remain cautious and do not be mistaken by rigid sectors (clumps) that are constructing the cluster.

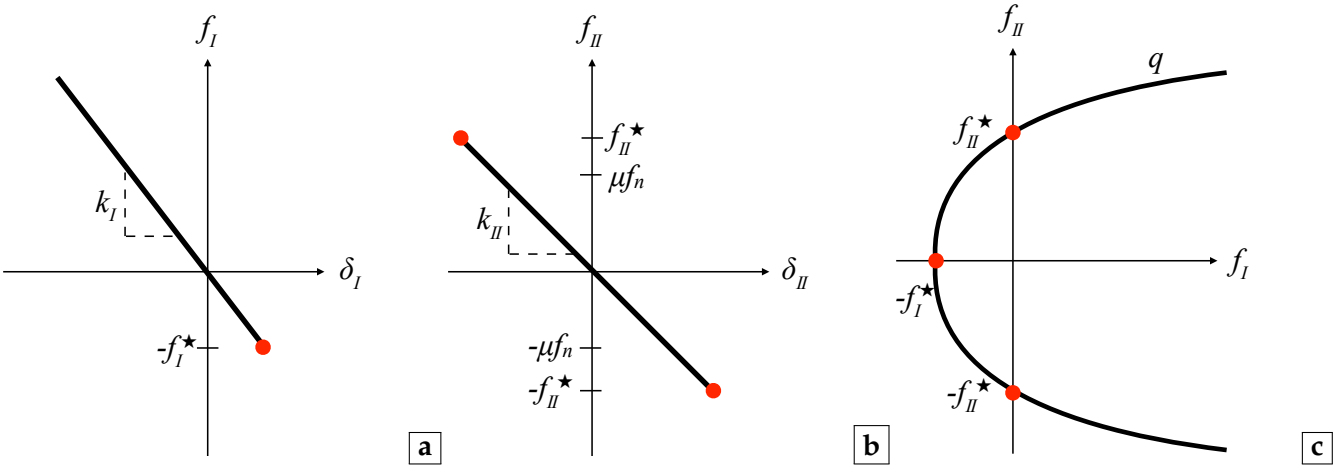

Figure 3.5 : Force laws for cohesive interactions: **a** – in the normal direction (mode-*I*), **b** – in the tangential direction (mode-*II*), and **c** – failure criterion as defined in the equation (3.10).

3.3 Calibration of the model on a single crushable shell

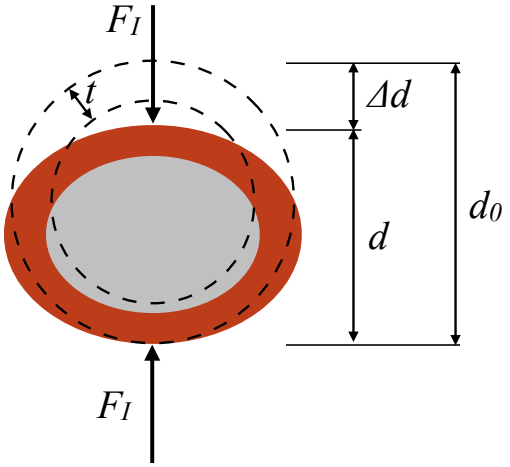

Figure 3.6 : An Uniaxial Radial Compression of the shell. This scheme is also valid for the Brazilian test. Dash lines show the contour of initial ring with diameter d_0. Remaining notation: Δd – a reduction of diameter, and F_I – the ultimate force causing a tensile failure.

The *Brazilian test* is a simple testing method that allows indirect measurement of tensile strength. It simply consists in a diametrical compression of a thin cylindrical specimen (along the axial direction) till its failure. The rupture force F_I can be then related to the tensile strength. The Brazilian test has received considerable attention not only experimentally, but also theoretically. For example, Hondros (1959) has provided a complex, yet useful, formula for the determination of an internal stress state. It has also enabled a calculation of the tensile stresses at failure, hereinafter, denoted as σ_I, because it provokes mode I fracture. Knowing that in the Brazilian test the tensile stress arises at the centre of the disc, *i.e.*, the cross-section of the cylinder, the tensile stress is simplified to:

$$\sigma_I = 2F_I/(\pi d_0 h), \tag{3.11}$$

where F_I is the critical load applied on the specimen with a diameter d_0 and a length h in the axial direction (similarly to **Figure** 3.6).

To avoid the biaxial stress filed in the Brazilian test, the equivalent test on the annuli (or the ring) specimens was developed early on (called the *ring test*) but did not receive the appeal as wide as the Brazilian test. In the ring, the tensile stress at failure can be assumed as:

$$\sigma_I = 2F_I K(\bar{r})/(\pi d_0 h). \tag{3.12}$$

One can notice that this relationship is obtained by a multiplication of the formula (3.11) by, $K(\bar{r})$, a the stress concentration factor[4]. In such a case, the failure occurs at the point of maximum tensile stress is located as shown in the **Figure** 3.7. Following Hobbs (1964), Hudson (1969) confirmed that $K(\bar{r})$ is a function of the internal void size. If the ring is described by the external r_{out} and the internal r_{in} radii, then the size of intrinsic void can be expressed as a relative radius $\bar{r} = r_{in}/r_{out}$ (**Figure** 3.8).

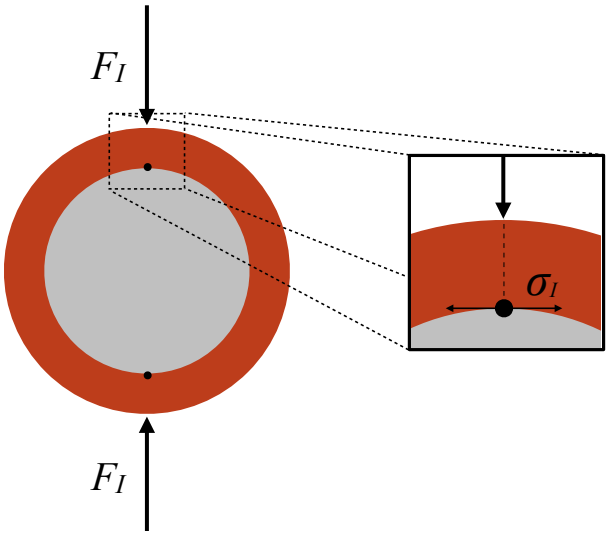

Figure 3.7 : A diametrically compressed shell fails in tension at the point of maximum tensile stress σ_I for the mode I fracture (the opening of crack), that is in the axis of loading at the inner edge of ring – black point.

By nature, each particle has irregular shape, which disagrees with the requirements in both the Brazilian and the ring tests. But, at a given time, a similar concept started to be applied for less symmetrical grains. Nowadays, it is commonly used in discrete modelling, for example, as a method to calibrate the model of single breakable grain: McDowell and Harireche (2002); Cheng et al. (2003); Laufer (2015); Cantor García (2017). To highlight the specific character of granular materials, it was

[4] In other words, for a full cylindrical shape the stress concentration factor becomes $K(0) = 1$.

often called the *vertical compression* instead. Many researchers used the vertical compression to estimate the tensile stress in the grain $\sigma_t = F/d^{D-1}$ in D-dimensional analysis. As presented in the section 2.2, in the numerical modelling many of breakage criteria have been built upon this relationship. Since, the ring is a perfectly symmetric, the vertical compression is not an adequate term. To address those studies, we will refer to it mainly as *uniaxial radial compression* (URC).

3.3.1 Identification of parameters based on the experimental campaign – uniaxial radial compression tests

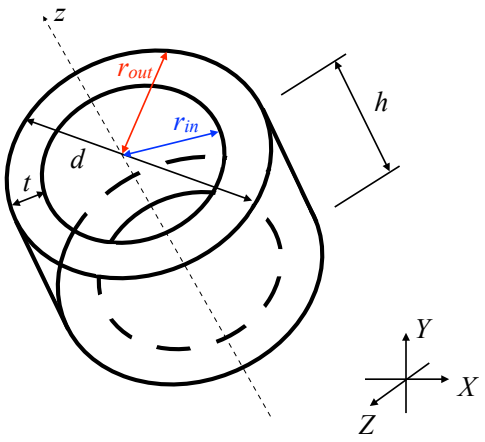

Figure 3.8 : A notation of shell dimensions was based on the assumption that its axial direction (z) is the leading one. Then, h is the height of the shell following the axial direction, t is a tube thickness and a ring (cross-section) has the external diameter d. With the last two, one can easily compute an internal r_{in} and an external r_{out} radius.

A number of uniaxial radial compression tests have been performed on two different shell sizes: *d18* and *d20*. In fact, the notation of those sizes characterises the manufacturing diameter, which is slightly bigger than our measurements of diameter d given in **Table** 3.1.

Two other dimensions (h and t) were distinguished to fully describe the shell geometry as demonstrated in the **Figure** 3.8 and given by the **Table** 3.1. The enhancement of shell fabrication has been an ongoing work, and therefore, we tested two various populations of shells (MP1 and MP2). The average measurements did not vary significantly, but the population MP1 presented stronger geometrical imperfections like the axial buckling or the flattening of the cross-section (an oval-like deformation). However, the shells of the population MP2 were visibly closer to the ideal tube.

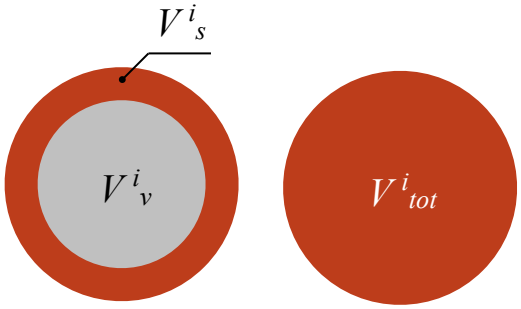

Figure 3.9 : 2D view of the shell – a scheme showing the division between the solid V_s^i and the void V_v^i used to calculate the shell void ratio E_0 or the shell porosity P_0.

In **Table** 3.1 also two dimensionless descriptors of shells are given: the mean relative radius $\bar{r}$ and the void ratio E_0 at the shell scale, not for the continuant material. The geometrical intrinsic exclusion, *i.e.*, the internal void, has a volume V_v^i (**Figure** 3.9). Moreover, V_v^i summed up with a volume of the solid V_s^i gives, what we call, a total shell volume V_{tot}^i. Then, $E_0 = V_v^i/V_s^i$ is a void ratio within the contour of a single shell. If one prefers, a shell-porosity $P_0 = V_v^i/V_{tot}^i$ can be given instead such that $P_0 = 0.479$ for *d20* and $P_0 = 0.502$ for *d18* (based on the average dimensions). The volumes of the void and the solid are of the same order. Bigger shells consist of slightly more material, which is to be found of greater importance on the macro-scale.

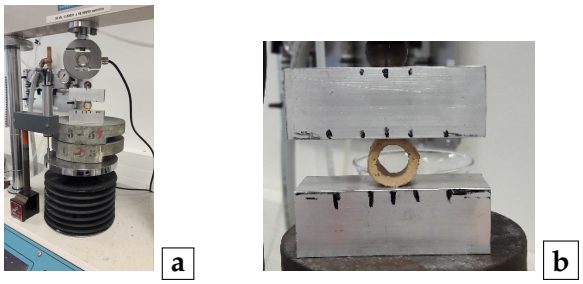

Figure 3.10 : a – The final experimental settings for uniaxial radial compression of a shell and **b** – a zoom on the shell.

Figure 3.10**a** shows a sample installed on the press, to be diametrically compressed

Shell size	Population	No. of samples	h (mm)	d (mm)	t (mm)	$\bar{r}$	E_0
$d18$	MP1	33	17.4±1.3	16.5±0.4	2.4 ± 0.1	0.709	1.011
	MP2	18	17.1±0.2	16.4±0.3	2.4 ± 0.1	0.707	1.000
$d20$	MP1	50	18.4±1.5	18.2±0.4	2.8 ± 0.1	0.692	0.920

Table 3.1 : A geometrical description of compressed shells. h, d and t are the shell dimensions as shown in the **Figure 3.8** and there are two-dimensional shell characteristics: $\bar{r}$ – a mean relative radius, and $E_0 = V_v^i / V_s^i$ – a void ratio of one shell (**Figure 3.9**).

(**Figure 3.10b**). Although a constant press velocity was imposed (0.02 mm/min), its vertical displacement was registered during each test. Finally, those measurements were assumed to be the diametrical reduction Δd (**Figure 3.6**). Besides displacement, the force was also recorded up to its final value F_I[5].

Two experimental observations require some comments before discussing the results. Firstly, the breakage was of highly dynamic nature in each test. Although one can expect an instant failure characteristic of brittle material, the ring geometry seems to intensify the "explosive" response. Secondly, we must discuss the nature of the breakage. **Figure 3.11a** shows how the majority of shells broke, namely into 4 parts. The shells split not only in the vertical direction of loading (as expected from **Figure 3.7**), but also in the perpendicular direction – horizontally (**Figure 3.11b**). A similar manner of breakage was observed by Mellor and Hawkes (1971) who showed that the manner of breakage changes with the value of the relative radius. For its low values, only the axial splitting appears, and therefore, it was suggested to treat the vertical cracks as primary breakage and the horizontal ones as secondary breakage. Plausibly the "explosive" response favours the appearance of the secondary cracks. The ring is less stiff than a full disc, thus it is more vulnerable to high dynamics of breakage. Yet it is not possible to distinguish the force when the primary crack initiates experimentally, and the force of the ultimate failure is measured instead. On the other side, the secondary cracks should also initiate in tension. The boundary conditions impose the requirement of uniform contact along the length of the specimen called the height of the shell (**Figure 3.10b**). To this end, each shell was wired out to ensure two contact surfaces to be as parallel as possible (**Figure 3.11c**).

Figures 3.12a and **3.12b** show the mechanical responses (force-displacement curves) of shells *d18* and *d20*, respectively. The diversity of the mechanical response is obvious. The variability of ultimate load results both from the geometrical variability of the tubes and from the material heterogeneity. Some internal flaws such as tiny minerals or air bubbles trapped in the crude clay were introduced when the shell mass was formed. In **Figures 3.12a** and **3.12b**, each shell has a nonlinear force characteristics. Initially, there appear discrepancy from the linear elasticity, typically as-

[5] The limit of the sensor was $2\,500 \pm 1$ N

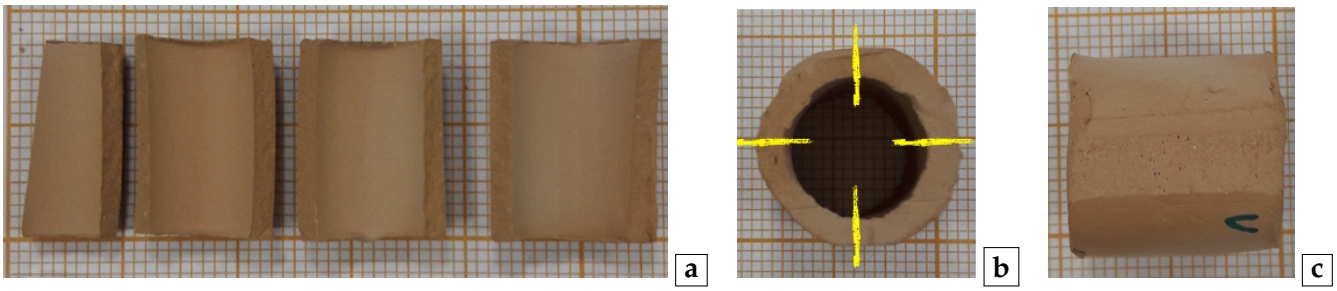

Figure 3.11 : **a** – The shell usually breaks into 4 fragments as a result of URC (yellow lines in **b** show the localisation of the cracks). **b** and **c** – show a shell before the test.

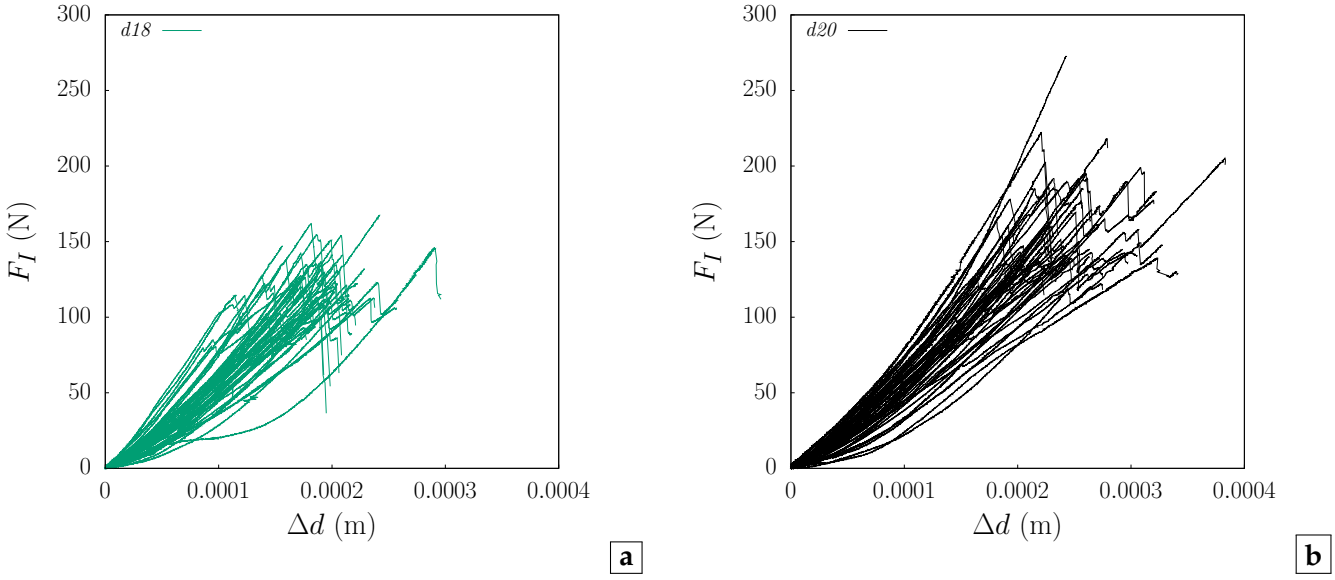

Figure 3.12 : Diametrical load *vs.* vertical displacement curves resulting from radial compression test performed on two sizes: **a** – *d18* (combining MP1 and MP2) and **b** – *d20* (see **Figure** 3.6).

sumed in the modelling and the theoretical approaches. Two types of deviation from the linear response can be observed. First one is an initial curvature in the zone of low forces ($\sim 0.2F_I$). In the literature, similar behaviours have been reported in cases of different materials like sand Cheng et al. (2003) or the clinker particles (Vallet and Charmet, 1995). According to the latter authors, the initial curvature as a result of the contact area flattening. For example, the irreversible changes of the contact zone might arise from the crushing of local asperities. Despite the surface treatments, we did not meet the challenge of extracting the perfectly parallel surfaces. Even if the non-linear phase has not been avoided, it is believed to be reduced. Once the contact has been adjusted by applying sufficient load, the curve entered the linear/elastic part. Also in some cases, the intermediate drop of force occurred in the curve. This temporary loss of energy corresponds to the work required for the crack initiation. Soon after, the continuous increase of the force was renewed and continued up to the final failure. We were not able to spot the onset of the crack in the majority of tests.

The *Weibull* distribution is reported to be adequate for statistical analysis of particles strength (Weibull, 1951; McDowell and Amon, 2000; Cheng et al., 2003; Laufer, 2015). If P_f represents the cumulative possibility of failure, then the possibility of survival P_s is equal to $(1 - P_f)$. Using the *Weibull* cumulative distribution function (*cdf*), one can obtain:

$$P_s = \frac{1}{e^{(\frac{x}{x_0})^m}}, \tag{3.13}$$

where m is a *Weibull's* modulus and x_0 is the scale parameter. Note that Weibull's modulus is a shape parameter controlling the "inclination" of the cumulative distribution curve. The higher is m, the thinner is the range of variation of results. In other words, m controls the width of Weibull distribution. The value of x_0 is the characteristic stress at which $1/e \sim 37$ % of samples survive. Equation (3.13) combines an exponential law with a power law. The use of logarithmic space linearises the trend:

$$\ln \circ \ln \frac{1}{P_s} = m \ln x - (m \ln x_0). \tag{3.14}$$

The linearised trend is convenient while determining the scale and shape parameters of the function (3.13). Then, m is the slope of the line and x_0 is related to the y-intercept.

Figures 3.13 and 3.13**b** confirm that the probability of shells failure is Weibullian both for size *d18* (3.13**a**) and *d20* (3.13**b**). The insets of plots

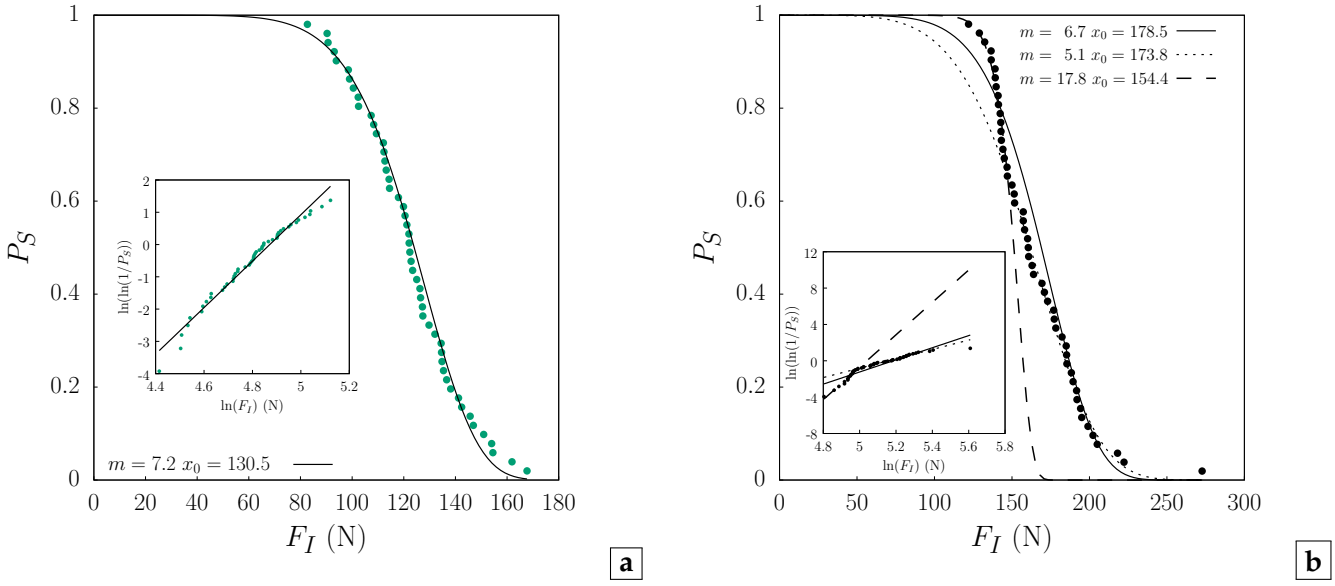

Figure 3.13 : Probability of shell survival P_s while being diametrically compressed by the critical force F_I for two shell sizes: **a** – *d18* (combining MP1 and MP2) and **b** – *d20*. The points show the experimental data and the curve is a trend function according to equation (3.13) with parameters found from fitting equation (3.14) in a logarithmic space as shown in the insets.

present the linearised trend in the logarithmic scale, as explained hereinbefore. Whereas for smaller shells the function (3.14) fits full range adequately, it was less sufficient for size *d20* (solid curves). To verify the tendency, the force range has been divided into two sub-domains: $\langle 120\ \text{N} : 150\ \text{N}\rangle$ (dotted line) and $\langle 150\ \text{N} : 280\ \text{N}\rangle$ (dashed lines). This division helped us to obtain more precise fits, with no accurate physical justification. Fitting in the second subdomain provided a comparable result as the global fit (m and x_0 of the same order). In the literature, it is rare to find Weibull's modulus higher than 10, especially for brittle materials, which is the case of the lower subdomain ($m = 17.8$). Perhaps there exist some intrinsic defects, a change in the mineralogical composition of clay-stone or the manufacturing process inconsistency leading to this locally narrow distribution. Similar deviations can be observed, for example, in the study of McDowell and Amon (2000), but usually, they are disregarded since the Weibull distribution was proven to be successful by many. Moreover, the multiple fits are not practical in terms of implementing the strength variability in the future DEM model acting in favour of using only the global fit. Comparing the shell sizes, the global fits have similar variability defined by comparable m (**Figures 3.13a** and **3.13b**). The scale parameter x_0 must vary as the force is size dependent variable.

Figure 3.14 presents a direct comparison of the two sizes plotting the ultimate force with respect to the final reduction of diameter. For both sizes,

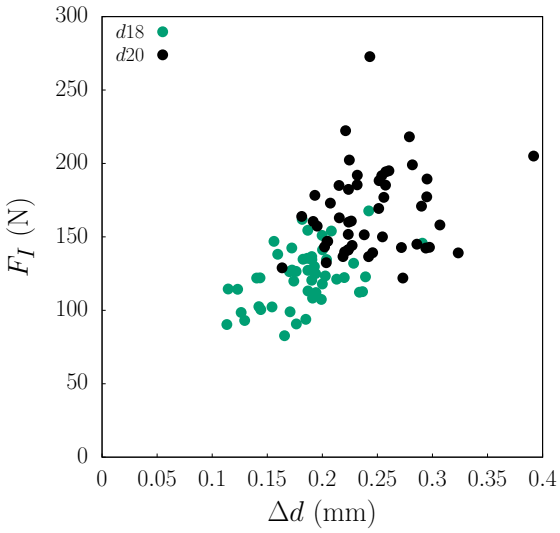

Figure 3.14 : Force causing ultimate breakage F_I *vs.* the corresponding displacement Δd for two shell sizes. Loading condition: uniaxial radial compression.

data are spread randomly rather than form a clear tendency. Although the two sets overlap slightly, the results confirm fairly well the size dependency of force. Thus, in **Figure 3.15** the same data has been converted to the measures unrestricted by the dimensions.

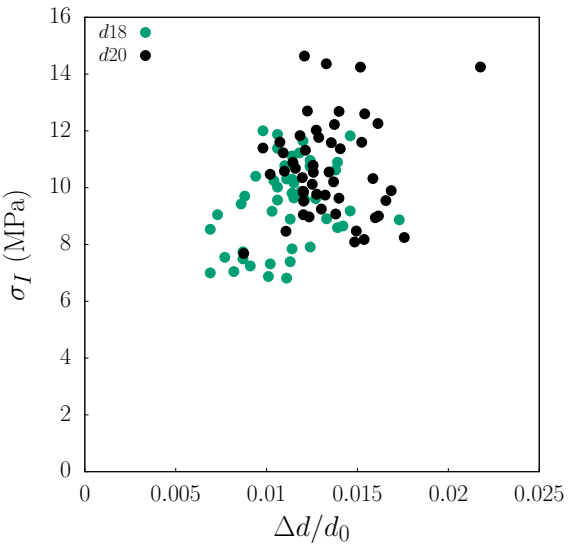

Figure 3.15 : Tensile stress as a function of the vertical strain. σ_I is calculated using equation (3.12). A dimensionless deformation equals $\Delta d/d_0$ according to small strain formula. Loading conditions as shown in **Figure 3.6**.

Despite the fact that the true tensile is unknown, we currently rely on the theoretical background and tensile stresses have been calculated using equation (3.12) with the simplified formula for stress concentration factor K proposed by Hobbs (1964): $K = 6 + 38\,\bar{r}^{\,2}$. Even if the "predicted" stresses mismatch reality, one can treat it as an estimation and benefit from the simplicity of the formula. Any other more complex formula, *e.g*, (Chianese and Erdlac, 1988; De-Lin, 1990; Mellor and Hawkes, 1971), confirms that K is a function of the ring thickness t (most often replaced by the relative radius $\bar{r}$). Yet we were not able to validate any of them due to lack of knowledge of material properties. The horizontal axis in **Figure 3.15** refers to a vertical strain according to the small strain concept. As is seen, the sets merged more than in **Figure 3.14**, but still, there exist partial division. Note that Δd includes the non-linear plastic adjustment phase, which enlarges the final strain randomly.

Above results showed that, on the average point of view, the force depends on the shell size. The scattering of the particle strength is a commonly acknowledged phenomenon (Vallet and Charmet, 1995; McDowell, 2001; Laufer, 2015). Herein, we attempt to describe this effect by means of the power law:

$$F_I = k d^{\alpha}. \tag{3.15}$$

One must remember that it is possible because the relative radii of sizes $d18$ and $d20$ are of the same order. The scheme to fit power law is equivalent to fitting Weibull distribution. The linearisation of trend is expected in a double logarithmic space. **Figure 3.16a** shows that in fact, we do not deal with a line but a "linear band", which thickness depends on the deviation of results. Therefore, coefficient k changes but the power α remains constant. Note that α stays in a good agreement with the empirical Bond's law with $\alpha = 2.5$ or $\alpha = 1.5$ found by Vallet and Charmet (1995). **Figure 3.16b** presents the same plot in the standard $F_I \leftrightarrow d_0$ space. The solid line shows the trend that matches the average strength, such that a prediction divided by the average experimental force gives 0.97 ($d20$) and 1.01 ($d18$). The dashed lines present the limits obtained by varying the value of k as shown in the **Figure 3.16b**. Although the range of size was not that wide, the results prove that the scattering of force can be determined with the approach already applied for brittle materials.

3.3.2 Adjustment of the numerical parameters using DEM

The experimental shell breakage under the uniaxial radial compression URC has been successfully characterised. Now, the physical response needs to be adequately reproduced numerically by means of discrete models. To this end, hereinafter, the cluster model approach will be tested. As was explained in the section 3.2, there exists a number of numerical parameters that need to be adjusted. Experimental campaign not only gives us a reference response that is aimed, but also helps to bridge the numerical parameter with the numerical response.

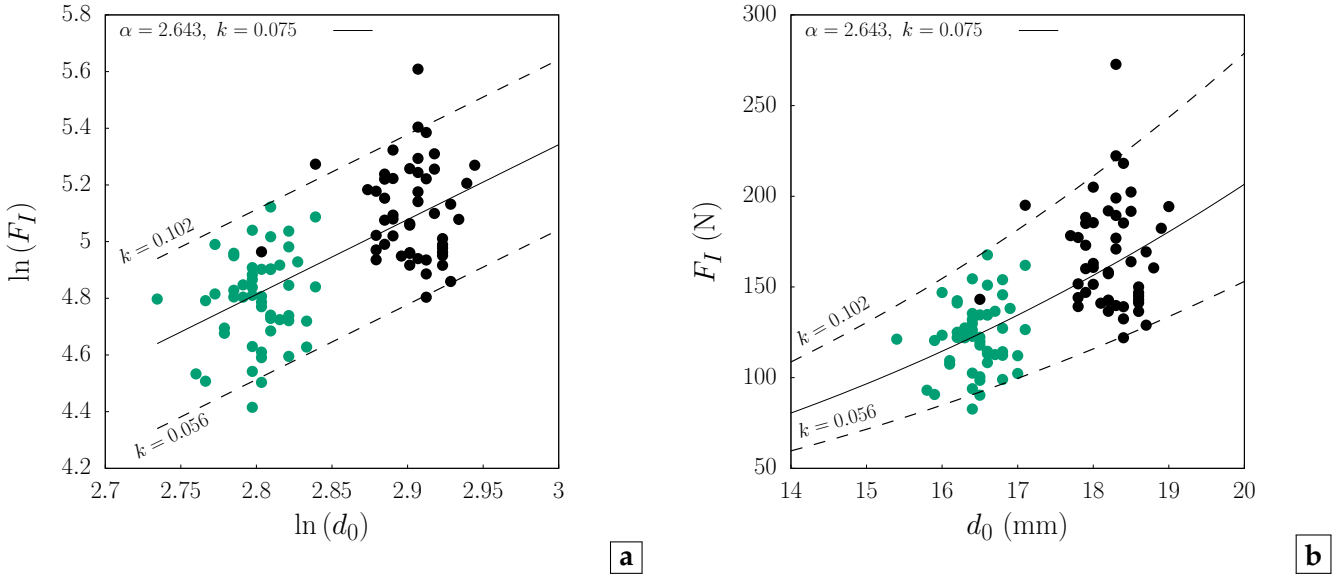

Figure 3.16 : Insight into the scattering of the force F_I with respect to the initial shell diameter d_0: **a** – linearisation of result applying double logarithmic space and **b** – The scaling of force can be described with function (3.15). The average trend presented by solid line. The variability of force is enclosed between two limits (dashed lines) are characterised by different k in equation (3.15) but keeping the power α.

First calibration for shells *d18*

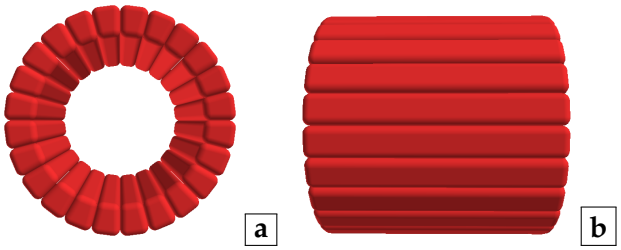

Figure 3.17 : Cluster shape *d18*-S6 with dimensions nearly equal to the average experimental measurements ($d = h = 17$ mm and $t = 2.4$ mm): **a** – $N^{\star}_{circ} = 24$ and **b** – $N^{\star}_{axial} = 1$.

From now on, the *cluster* can have only the tube shape which is a numerically equivalent to the real intact shell. Onwards, once the tube-shaped cluster breaks, the resultant pieces are called the *fragments*, the *parts* or, occasionally, even the *sub-clusters*. Note that fragment does not have any specific geometry assigned to it and ultimately, it is made of a single sector. First of all, the choice of shape discretisation needed to be made. We have made the primary calibration on the shell size *d18* using 24 sectors with a discretisation shape denoted as S6[6]. As shown in the **Figures 3.17a** and **3.17b** this model does not include the axial slitting, which is irrelevant to the breakage manner in the URC (recall **Figure 3.11a**).

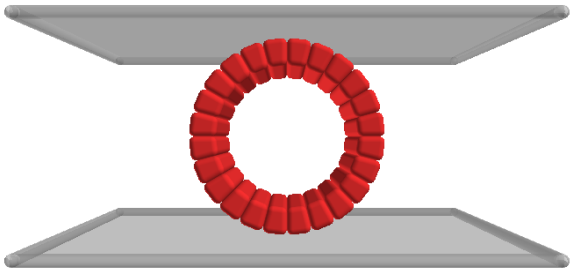

Figure 3.18 : Numerical cluster before the URC test. Only circumferential division with 24 sectors – cluster shape *d*18-S6. Rigid walls used as the boundary.

Figure 3.18 shows the cluster placed between two rigid plates. The bottom plate was motionless, whereas the top one was moving downward with a constant velocity 10 mm/s (we recall that the experimental velocity was $5.5 \cdot 10^{-4}$ mm/s). The force F_I was measured for the top plate, and Δd was an actual reduction of vertical diameter.

Table 3.2 presents the parameters used in the modelling. They concern the breakage criterion and force laws described in sections **3.1** and **3.2**.

[6] All the cluster shapes are described in **Appendix A.1** (see **Table A.1**).

Note that this is the final set of parameters established from a small parametric study, but their adjustment will be explained in more details later on.

Links		Frictional contacts	
k_I	1.1 10^7 N/m	k_n	1.1 10^7 N/m
k_{II}	1.1 10^7 N/m	k_t	1.1 10^7 N/m
$f_I^\star$	85 N	μ_{shell}	0.36
$f_{II}^\star$	250 N	μ_{wall}	0.36
q	2		

Table 3.2 : Parameters used in the simulation of URC on cluster shape d18-S6. The parameters are explained in sections **3.1** and **3.2**.

Figure 3.20 shows comparison between the non-linear experiments and perfectly elastic modelling (red curve). As explained in the section **3.3.1**, the experimental non-linearity originates from contact adjustment. Our model is not able to represent this effect, but we include it indirectly by aiming the average experimental displacement Δd. For the loading configuration shown in **Figure 3.18**, only the normal interaction forces act between the plates and the cluster. They are determined thanks to linear elastic force law, thus $F_I \leftrightarrow \Delta d$ relationship must be linear. The ultimate breakage into 4 pieces (**Figure 3.11a**) was reproduced numerically but in two steps. The tube firstly broke in the axis of the load (first force peak in the **Figure 3.20**). This vertical breakage occurred for higher load[7] $F_I = 123.6$ N which is consistent with the mean experimental value $F_{I\ true} = 122.5$ N. Experimentally, the failure happens so rapidly that it is impossible to reliably distinguish what mechanisms are occurring. A DEM insight also suggested that horizontal breakage has a secondary character – the second force peak in the **Figure 3.20**. As commonly accepted, the occurrence of breakage requires some amount of energy, and therefore, the drop of force must have appeared with the primary breakage. Then the system was re-stabilised and the force mounted up again, yet the half-ring fragments behaved less rigid. The link (local) stiffness k_I rules the slope of the $F_I \leftrightarrow \Delta d$ line but it also depends on purely numerical or geometrical model characteristics such as number and size of sectors. In contrast, the true shell stiffness depends on the material and also on the geometry of the tube. Breakage modifies the shell geometry from full ring to half-rings, and perhaps, the loss of adhesive material bonds leads to a less stable support and makes the fragments behaviour less rigid. Recording experimentally the large growth of Δd, after primary breakage, is not feasible due to high dynamics of response. Therefore, we are not able to fully state if it is a realistic result or the model requires an adjustment of k_I to the new geometry. Note that in terms of energy release the numerical breakage is also highly dynamic and both damping approaches had to be used simultaneously (viscous and Cundall damping) to "secure" the DEM computations.

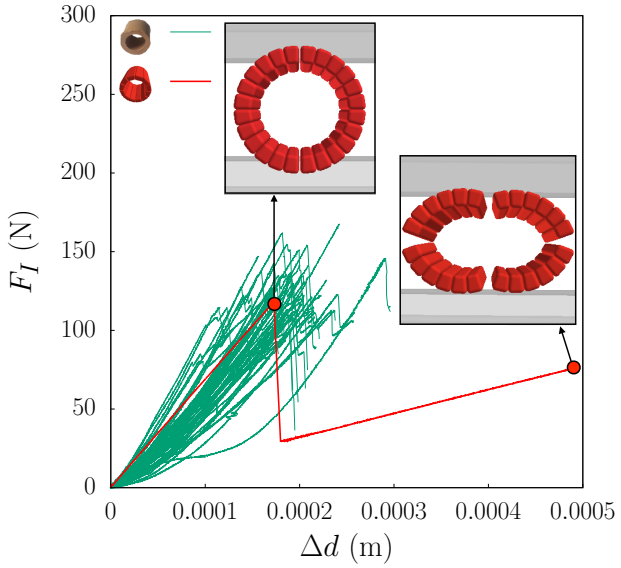

Figure 3.20 : URC test was strained controlled (velocity of plate 10 mm/s). Set of green lines represent the experimental force: displacement curves and the red line shows the numerical reflection of mechanical behaviour. Insets present the localisation of primary and secondary cracks.

Looking at the type of forces within the cluster and half-ring fragments, in **Figure 3.19** the compressive and the tensile interaction forces are distinguished. They are marked by red and green lines, respectively. **Figure 3.19a** confirms that there exist tensile force (causing opening of links) at the point of primary failure as predicts the theory (**Figure 3.7**). Note that the force distribution

[7] In the current section, F_I refers to DEM result.

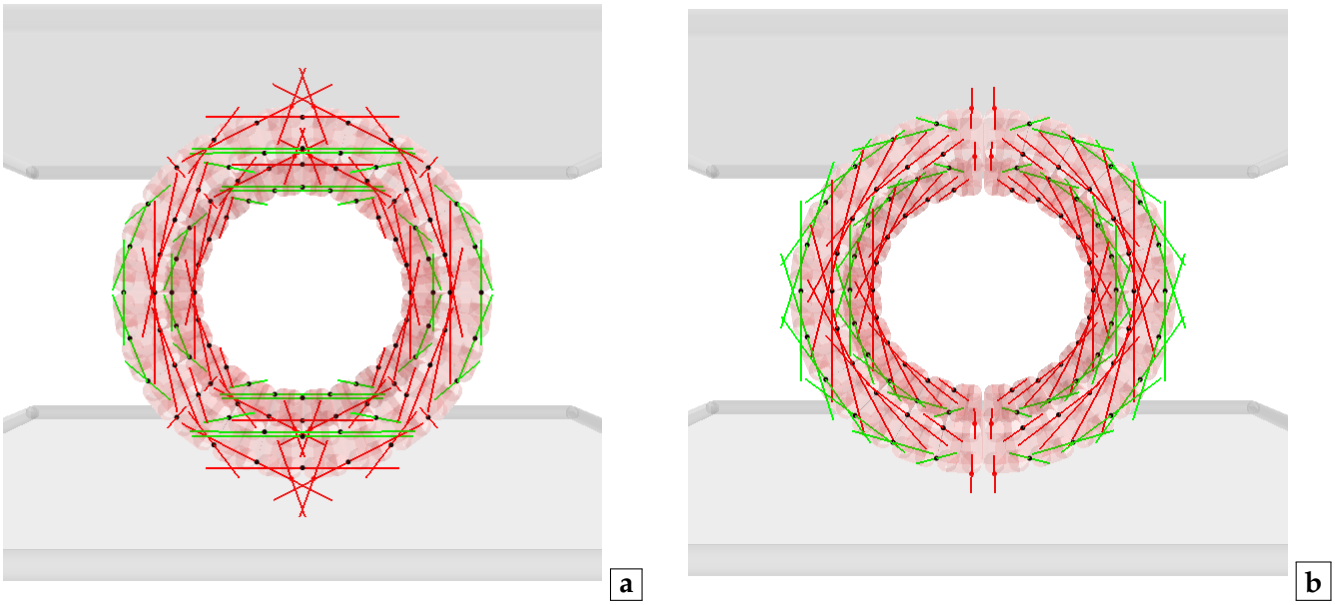

Figure 3.19 : The compressive (red) and tensile (green) contact forces causing **a** – the primary and **b** – the secondary cracks in URC tests.

is displayed just before breakage such that all the intra-clusters breakable interfaces still hold (black dots). But for the configuration **Figure 3.19b**, just before horizontal breakage, the corresponding interfaces have been disrupted, which in fact is the failure of 4 links (per interface). Furthermore, it is clear that the secondary breakage is also triggered by the tensile force. At the scale of bonded interactions, both tensile interaction forces ($f_I = -84.91$ N for the vertical cracks and $f_I = -84.95$ N for the horizontal cracks) almost met the tensile yielding limit $-f_I^\star = -85$ N. Considering the failure criterion (3.10), the tensile force contributed to the failure in 99.9 %. Failure in tension was confirmed by simple 2D modelling by means of Finite Element Method (see **Appendix A.2**). If both failures occur in tension, then taking into account the ultimate experimental force is acceptable. On the contrary, in the analysis of modelings, we focused only on the primary breakage.

To summarise, it is possible to correctly model the uniaxial radial compression with fairly large polygonal constituents. This part provided a successfully calibrated model capable of reflecting not only the mechanical response but also the breakage manner. Whereas the numerical behaviour is consistent with the experiments, the distribution of the internal forces agrees with the theoretical predictions. Still, we refer to this part of the work as "primary calibration", because it provides only one of the possible choices for the cluster model. At this point, the reader is missing the understanding of the parameter roles in the behaviour and the degree of model complexity caused by the discretisation into polyhedral bodies. Furthermore, strength variability requires implementation into the DEM model. Hereinafter, we will address those concerns.

Contact and link stiffnesses

As mentioned, hereinbefore, the link stiffnesses rules the slope of force-displacement curve, numerically. Here, we show to what extent the discrete stiffness influences the linear elastic response of the cluster to URC load. In **Figure 3.19** one can distinguish both the cohesive sector-to-sector (black dots) and the frictional sector-to-plate (red dots) interactions. Thus, we deal with the inter-sectors k_I, k_{II}) and inter-clusters (k_n, k_t) contact stiffnesses, so-called link and contact stiffnesses, respectively. We have probed three different values varying them by a factor of 10 in nine different combinations of stiffnesses in order to characterise their numerical influence (**Table 3.3**). For the sake of simplicity, the ratio between the nor-

mal and tangential stiffnesses was fixed to one ($k_I/k_{II} = k_n/k_t = 1$).

No.	k_n (N/m)	k_I (N/m)	Δd (m)
1	10^6	10^6	0.002064
2	10^7	10^6	0.002070
3	10^8	10^6	0.002066
4	10^6	10^7	0.000189
5	10^7	10^7	0.000191
6	10^8	10^7	0.000191
7	10^6	10^8	0.000019
8	10^7	10^8	0.000019
9	10^8	10^8	0.000018

Table 3.3 : The values of a normal contact stiffness between two sectors k_I and between the sector and the wall k_n (**Figure 3.18**), with $k_{II} = k_I$ and $k_I/k_{II} = k_n/k_t = 1$

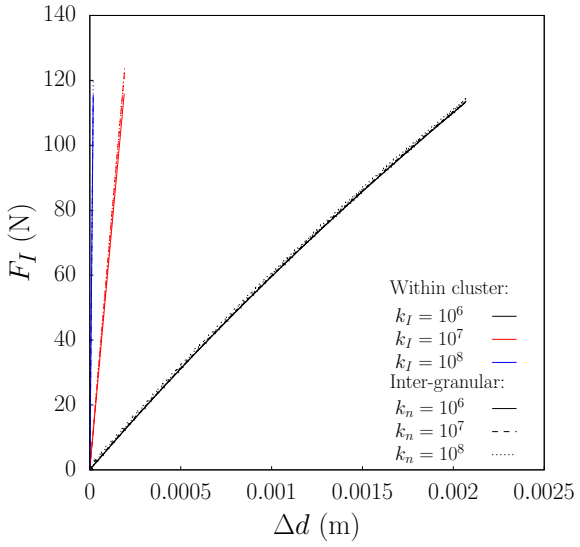

Figure 3.21 : The influence of the contact stiffness inside cluster (link k_I) and between clusters (contact k_n). An identical line colour is meant for the same k_I and an identical line type is meant for the same k_n. Combination from **Table 3.3**.

In **Figure 3.21** the mechanical responses are shown by taking into account all the combinations (No. 1 – No. 9) form **Table 3.3**. In the plot, k_I is colour-coded whilst k_n is distinguished by the same type of line. As is seen, the influence of the inter-cluster stiffness k_n is negligible. In contrary, the contact stiffness k_I limits the maximum value of displacement Δd. **Table 3.3** exposes that the increase of k_I by a factor of 10 resulted in an increase of Δd by the same factor. Thanks to this, the stiffness k_I can be adjusted so that the numerical value (for primary breakage) stands in the agreement with the mean experimental value.

Tensile strength – yield tensile threshold $f_I^\star$

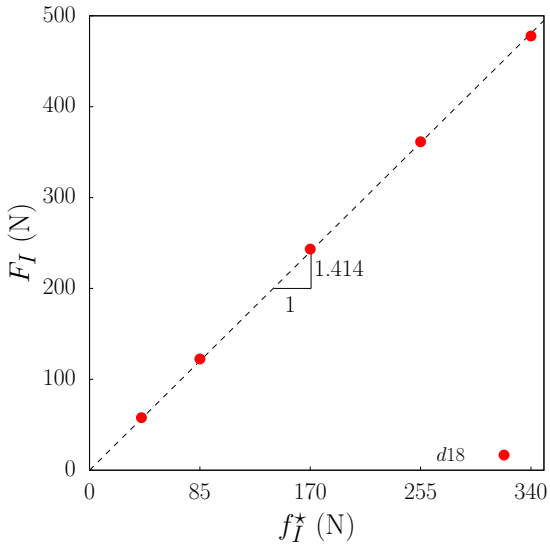

Figure 3.22 : Linear relationship between global force at failure F_I applied on the shell during URC and the yield normal force $f_I^\star$ in the link (with $f_{II}^\star = 450$ N).

The yield threshold of the normal link force $f_I^\star$ has been modified, while keeping the tangential force threshold $f_{II}^\star$ at its high value[8]. **Figure 3.22** shows that there exist a linear relationship between the tensile limit and the critical load. The increase of F_I is proportional to $f_I^\star$ such that ratio $F_I/f_I^\star = 1.414$ for the shell size *d18*. Note that for shells *d*20, $F_I/f_I^\star$ was found at 1.660. The strength scattering due to the size of internal hole has been mentioned in the literature. For example, Hudson (1969) implied a relationship between F_I and $\bar{r}$, governed by a power law, with a small variation above $\bar{r} > 0.2$. Both sizes *d20* and *d18* have a relative radius $\bar{r}$ higher than 0.2 ($\bar{r} = 0.699$, and $\bar{r} = 0.718$, respectively). Since *d20* has a bit lower relative radius (the ring is slightly more thick), observations of Hudson (1969) may justify the slight increase of the slope.

[8] $f_{II}^\star = 450$ N maintains the contribution of shearing forces negligible.

$N^{\star}_{circ}$	$N^{\star}_{axial}$	m_i (kg)	k_I (N/m)	$f^{\star}_I$ (N)	F_I (N)	Δd (m)
24	1	$1.469\ 10^{-4}$	$1.1\ 10^{7}$	85.0	123.4	$1.74\ 10^{-4}$
16	1	$2.228\ 10^{-4}$	$7.5\ 10^{6}$	85.0	122.2	$1.67\ 10^{-4}$
12	1	$2.966\ 10^{-4}$	$5.5\ 10^{6}$	85.0	121.3	$1.69\ 10^{-4}$
12	2	$2.966\ 10^{-4}$	$5.5\ 10^{6}$	42.5	122.2	$1.70\ 10^{-4}$
8	1	$4.344\ 10^{-4}$	$4.2\ 10^{6}$	85.0	121.9	$1.67\ 10^{-4}$
Experimental data		-	-	-	122.5	$1.65\ 10^{-4}$

Table 3.4 : A summary of numerical parameters (mass of the sector m_i, normal contact stiffness k_I, normal yield force $f^{\star}_I$) resulting in the mechanical state at failure: F_I and Δd.

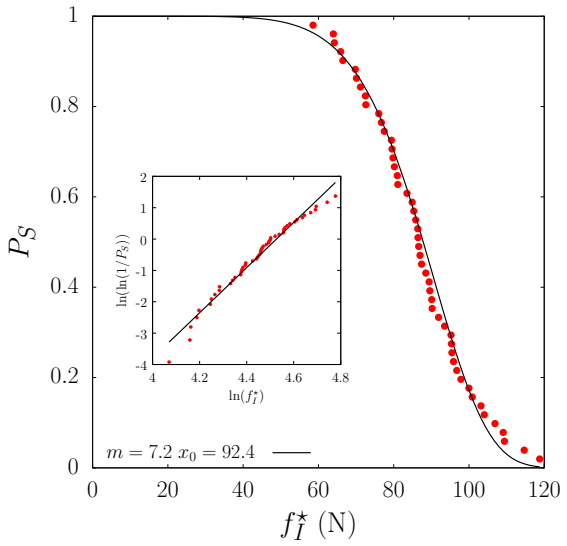

Figure 3.23 : Probability of survival as Weibullian function for various yielding tensile strength of the shell (equation 3.13). Points show data and the curve is a theoretical trend with the Weibull modulus m and the scale parameter x_0. Inset: linearisation of trend in the logarithmic space (equation 3.14 in section **3.3.1**).

Using this linear relationship, any experimentally measured F_I can be converted to the numerical input $f^{\star}_I$. Furthermore, one can classify its variability using Weibull distribution. **Figure 3.23** demonstrates it on the shell size *d18*. The original force distribution shown in **Figure 3.13a** (in section **3.3.1**) had the scale parameter $x_0 = 130.5$ N and the Weibull modulus $m = 7.2$. Due to the proportionality, m remains the same for $f^{\star}_I$. The scale parameter found from the fit ($x_0 = 92.4$ N) is equal to the estimation made from the linear relationship, shown in the **Figure 3.22**, and the experimental scale parameter ($130.5/1.414 = 92.3$ N). For size *d*20, Weibullian distribution of $f^{\star}_I$ is characterised by parameters $m = 6.7$ and $x_0 = 107.7$ N.

Summarising, $f^{\star}_I$ governs the ultimate applied load F_I in a straightforward, linear manner. One can benefit from the fact that $f^{\star}_I$ can be easily estimated using a simple experiment. Furthermore, relying on the validity of Weibull distribution for particle strength in granular material, even with small amount of tests the variability might be characterised and introduced in the model.

Number of sectors

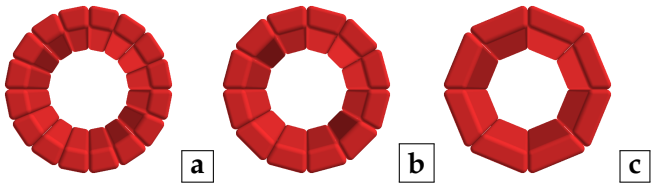

Figure 3.24 : The clusters composed of $N^{\star}_{circ}$: **a** – 16 (*d18*-S3), **b** –12 (*d18*-S1)and **c** – 8 (*d18*-S7) sectors. $N^{\star}_{axial} = 1$ (see **Appendix A.1**).

The computation time in case of URC on a single shell is not a problematic issue, but it gains on the importance while thinking of the big picture – an assembly of 2 000 shells or even bigger FEM×DEM model. Therefore, an attempt to reduce the number of sectors per cluster has been considered. **Figures 3.24a**, **3.24b** and **3.24c** present the cluster shapes with circumferential division lower than 24 sectors, but keeping the experimental dimensions. The URC has been simulated for each of this cluster structure, and a quite similar mechanical response was obtained. The mechanical curves are not presented graphically, but they are compared in **Table 3.4** providing the values of F_I and Δd. It is a fair method as all the curves presented a linear response.

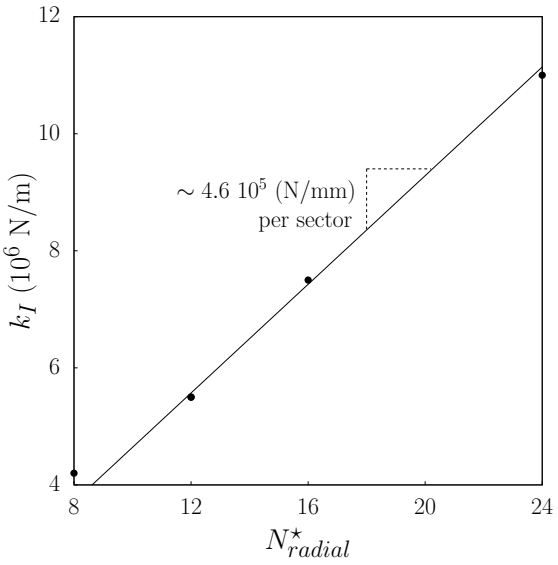

Figure 3.25 : DEM URC. The link normal stiffness k_I dependency from the circumferential discretisation number, and thus, the size of sectors.

One must notice that the stiffness of the links has been modified between the modelings as shown in the **Figures 3.25**. The bigger is the sector, the lower is k_I. If $N^\star_{circ} = 24$ is a reference, k_I can be estimated from the relationship $k_I \approx (k_I^{(24)} N^\star_{circ})/24$. It was sufficient to keep the tensile limit of normal interaction force $f_I^\star$ constant for all those simulations.

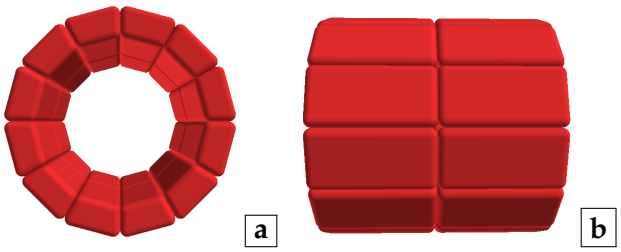

Figure 3.26 : Cluster shape *d18*-S2 with dimensions nearly equal to the average experimental measurements ($d = h = 17$ mm and $t = 2.4$ mm): **a** – $N^\star_{circ} = 12$ and **b** – $N^\star_{axial} = 2$.

Less attention was paid to the axial division, but even the brief analysis provided us some useful observations. Axially the shell was split into two rows of sectors as shown in the **Figures 3.26b**. As shown in **Table 3.4**, the true response to URC was reproduced for the same contact stiffness k_I as used in case of a shell with 12 radial sectors but no axial split ($N^\star_{axial} = 1$ in *d18*-S1). The manner of breakage has remained identical, but it was necessary to lower $f_I^\star$. Because the number of cohesive links to break was doubled, the threshold $f_I^\star$ needs to be multiplied by $N^\star_{axial}$ (**Table 3.4**). In other words, $f_I^\star$ stands in an inverse proportion to the number of breaking links. Using less sectors per cluster increases their size and, consequently, the mass of a sector m_i (given in **Table 3.4**). The critical time can be estimated from relation $T_c = \pi\sqrt{m_i/(N_{link}k_I)}$, where N_{link} is number of links between two sectors. The bigger the sector mass, the bigger is T_c, and consequently the time step [9]. Then, ΔT can be potentially but reasonably enlarged to speed up the computations time. In the case of large assemblies, the reduction of sectors number brings more benefits. Despite some numerical tricks, the computations of forces, the integration of many equations or the updates of the neighbourhood list can be highly time-consuming procedures. Fewer sectors mean fewer forces to compute and fewer elements to verify and update the neighbourhood list. Thus, using less sector makes the calculation less time-consuming.

Concerning this part of the study, one must remember the following conclusion. Whereas the circumferential discretisation modifies k_I, the axial discretisation modifies the interaction force threshold $f_I^\star$ for URC.

Imposing loading and the shear contribution to the failure

Pure shear force is extremely difficult to extract experimentally, thus, a numerical attempt to estimate the level of tangential yield force $f_{II}^\star$ has been considered. Up to this moment, the sectors were connected such that the bonded interaction appeared in the point of tensile failure (**Figure 3.27a**). Then, the tangential interaction force f_{II} acting in the broken interaction was negligible (*e.g.*, $f_{II} \sim 1/100$ N for *d18*-S6). To activate more tangential forces in the failing link, the cluster was rotated as presented in the **Figure 3.27b**. Drawing special attention to the plate-sector contact, one can see that the cluster cannot break where the maximum tensile force appears. Moreover, the radial failure

[9] Recall that the time step ΔT is proportional to T_c throughout the inverse of time steps number $N_{\Delta T}$.

$N^\star_{circ}$	$N^\star_{axial}$	α (°)	F_I^∞ (N)	a	b	$f_I/(-f_I^\star)$
24	1	82.5	130.3	-0.073	1.080	0.904
12	1	75.0	177.3	-0.115	1.448	0.848
8	1	67.5	268.0	-0.203	2.118	0.767

Table 3.5 : Shear force contributions in uniaxial radial compression for different radial division of clusters $N^\star_{axial}$ (**Figure** 3.27**b**). Rotated configuration has failure plains inclined at α. F_I^∞ is applied diametrical load for very high tangential yield force $f^\star_{II}$. a and b are fit parameters of function drawn in **Figure** 3.28. An example of level of tensile force contribution $f_I/(-f_I^\star)$ for $f^\star_{II} = 50$ N in the failure (see equation 3.10.

planes are inclined at an angle α with respect to the horizontal axis. In **Table** 3.5 one can observe how α changes with number of sectors ($N^\star_{circ}$), and therefore, with the size of sector. The radial distance from the vertical axis is also of great importance.

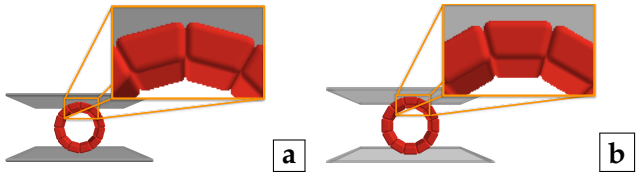

Figure 3.27 : A type and the geometry of shell-plate contact have been modified from **a** –sphere-face to **b** – face-face contact.

Change of $f^\star_{II}$ influenced the results of uniaxial radial compression on rotated configuration (**Figure** 3.27**b**) for each $N^\star_{circ}$, as is presented in the **Figure** 3.28. In fact, the normalised values were used in the plot such that:

- load at failure F_I as a proportion of experimental average force $F_{I\,true}$ demonstrates the degree of "deviation" from the experiment,
- and thresholds ratio $f^\star_{II}/f^\star_I$ shows the balance between the shear and tensile material strengths.

The load F_I causing breakage increases nonlinearly as a function of $f^\star_{II}$. When the tangential threshold is very high ($f^\star_{II} = \infty$), the F_I tends to its limit, notated as F_I^∞. In this study, we assume that F_I^∞ was met for $f^\star_{II} = 400$ N. The relationship from the **Figure** 3.28 was described by function $f(x) = a/x + b$, where a is a shape parameter ($N^\star_{circ}$-dependent), and b is essentially the value $F_I^\infty/F_{I\,true}$. One can see that the fit was more sufficient for a higher number of sectors, while for $N^\star_{circ} = 8$ slight discrepancy can be stated. The parameters from fitting are given in the **Table** 3.5. It is clear that if $f^\star_{II}/f^\star_I < 1$, the tangential force rules the breakage because the shearing strength is lower than the tensile one. The trend mounts up rapidly showing high sensitivity to the change of the yield shear threshold in this regime. When $f^\star_{II}/f^\star_I$ becomes larger than 1, the shear strength is higher than the tensile one, and the shell will crush mainly due to the tensile stress. Therefore, a plateau of $F_I/F_{I\,true}$ must appear in **Figure** 3.28 once the test becomes as insensitive to shear as possible, which occurs faster in the case of the more inclined slope, *i.e.* when the failure plane radially closer to the true failure point.

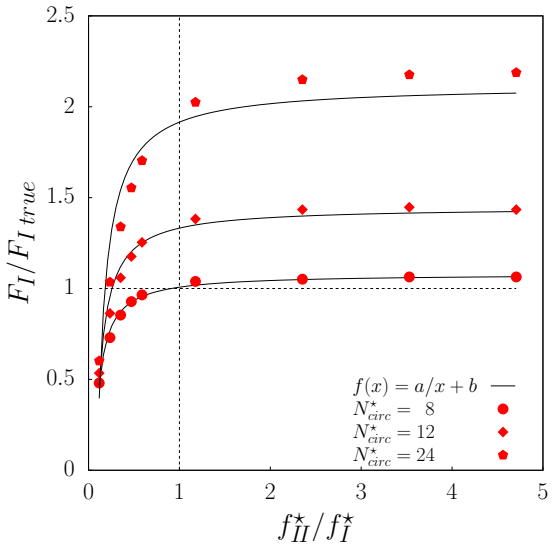

Figure 3.28 : Importance of tangential yield threshold $f^\star_{II}$ in uniaxial radial compression of the shell. Tests made on the configurations shown in the **Figure** 3.27**b**. Dots present data, while the line stands for a fitted function.

Looking at the interaction force it was confirmed that the rupture of links also involved more shearing between the sectors than before,

and thus, higher tangential forces were activated (*e.g.*, $f_{II} = 14.7$ N for *d18*-S6). Let us assume that an acceptable strength balance is $f^\star_{II}/f^\star_I = 0.59$, *i.e.* $f^\star_{II} = 50$ N. **Table 3.5** shows that the breakage was always governed mainly by the tensile force, but the failure was not in pure tension any longer. The lower the inclination (α), the lower is the contribution of tensile force $f_I/(-f^\star_I)$. That is due to the internal stress state in the ring. The tensile stresses fade with radial distance as confirmed by simple FEM modelling in **Appendix A.2**. Therefore, if the failure plane is located in higher radial distance from the loading axis (as it is for bigger sectors), the tensile force must decrease until the transition to the attractive force happens (for $\alpha \approx 50°$). For larger sectors, due to the tensile force distribution, a higher critical load F_I is required to trigger adequate tensile force f_I, and thereby, an adequate proportion $f_I/(-f^\star_I)$.

To conclude, the radial division into 8 sectors is too rough of an estimation, which already may significantly mismatch the experimental results for this very basic calibration. An increase in the number of sectors leads to a more reliable outcome. $N^\star_{circ} = 24$ appears to be most appropriate discretisation, among the tested ones, for which shearing is of secondary importance from $f^\star_{II} = 50$ N. However, including the previous study of axial splitting the final recommendation is $N^\star_{circ} = 12$. For a large assembly, we would reduce the radial division in favour of axial one, if necessary.

3.4 Verification of the model on a single crushable grain

The uniaxial radial compression has been of multiple uses, both to find the true strength (including its variability) and to adjust the numerical parameters. Despite our best efforts to include in the calibration as many aspects as possible, the uniaxial radial compression is characterised by the simplest boundary conditions. Such a simple loading is not really expected to occur within packing, thus we attempt a brief verification of the model by slight increase in the complexity of loading conditions. As shown in the **Figure 3.29**, the boundary conditions have been modified such that the horizontal radius remains constant in the process of vertical compression by a pair of forces F_V. Hence, we provoke a biaxial compression of the shell[10], even if the horizontal force is not an imposed load but a consequence of strain constrains.

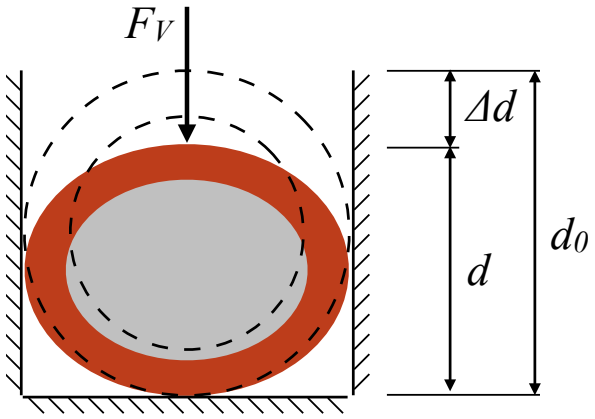

Figure 3.29 : 2D view of biaxial radial compression (BRC) on a single shell. Dash lines show the contour of the initial ring with an initial diameter d_0 reduced of Δd while being compressed diametrically by a vertical force F_V.

One must remember that this small modification still provides a simple plain stress loading path. On one side, the boundary conditions remain quite simple and bear some significant similarities to the ring test. On the other side, doubling the number of supporting contacts reduced the deviatoric load and makes the loading condition more realistic, though not as complex as expected within an assembly. Hereinafter we will refer to the test as Biaxial Radial Compression (BRC).

Experimental test of biaxial radial compression

Additionally, 15 BRC experiments were performed for the boundary conditions presented in **Figure 3.29**. Despite the change of the boundary conditions, the preparation and the test protocol were as in the experimental campaign of

[10] It is actually an oedometric compression of a single shell. To avoid confusion with the macroscale, at which the oedometer test is simulated on an assembly, the name the term "oedometer" has not been employed.

URC, thus one can find the description in section 3.3.1. The experimental setup prior to the compression is shown in **Figure** 3.30**a**. A small metal piece was constructed to prevent horizontal deformation. One can see that its span could be adjusted to the variability of shell dimensions given in the **Table** 3.6. Note that the average measurements were consistent with previously tested shells (**Table** 3.1).

Size	No.	h (mm)	d (mm)	t (mm)
$d18$	15	17.0 ± 0.3	16.4 ± 0.4	2.3 ± 0.1

Table 3.6 : The geometrical description of shells tested in BRC. h, d and t are shell dimensions given **Table** 3.6 (recall also **Figure** 3.8).

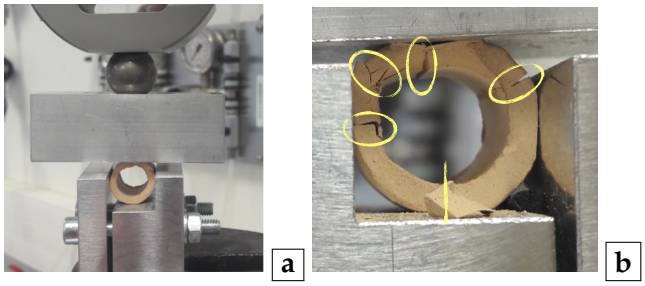

Figure 3.30 : BRC with blocked horizontal deformation of the shell: **a** – a final experimental settings, and **b** – the breakage manner at an advance load stage.

Figure 3.30**b** shows the localisation of breakage after the test. As is seen, the damage was more extensive and more complex crack patterns have developed. One can see that the lateral walls provided additional support for the shell, such that the damage was located mainly in the upper part of the ring cross-section. Although we still deal with brittle fracture, the lateral wall also prevented the explosive behaviour observed in URC experiments. Most often the cracks caused the radial slicing as shown in the **Figures** 3.31**a** and 3.31**b**, but some local crumbing or/and axial crushing were also observed, as shown in the **Figures** 3.30**b** and 3.31**b**. The primary breakage was consistent with breakage in URC. In other words, the first splitting appeared in the vertical axis (maximum load) with its initiation at the point of maximum tensile stress. A similar experimental observation was made by Salami et al. (2017) who investigated the effect of coordination number while compressing discs. Furthermore, the authors also observed the cracks located in the upper part of the disc for conditions equivalent to our BRC.

Figure 3.32 shows the evolution of the top vertical force F_V as a function of the press displacement. Similarly to mechanical response to URC (**Figure** 3.12), each line has two phases: a nonlinear adjustment of the contact zone followed by a linear behaviour. The intermediate drops appear when new cracks occur. Due to the support of the lateral walls, one can observe an arching effect, and therefore, the force was transmitted even after multiple breakages. More contacts per shell led to an increase of shell resistance, such that the average force measured gives $F_{V\,true} = 671.7 \pm 123.0$ N, which is ~ 5.5 times higher than in URC.

Validity of model

Links		Contacts	
k_I	$0.55\ 10^7$ N/m	k_n	$0.55\ 10^7$ N/m
k_{II}	$0.55\ 10^7$ N/m	k_t	$0.55\ 10^7$ N/m
$f_I^\star$	85 N	μ_{shell}	0.36
$f_{II}^\star$	100 N	μ_{wall}	0.00 or 0.15
q	2		

Table 3.7 : The parameters used in the simulations of BRC with the horizontal constraints. The mechanical response is shown in the **Figure** 3.32. The parameters are explained in sections 3.1 and 3.2.

Also the numerical loading procedure has not been modified so we refer to its description given in section 3.3.2. The cluster of 12 sectors (only circumferential divisions) has been tested (inset of **Figure** 3.32) with the set of parameters given in **Table** 3.7.

Figure 3.32 compares the numerical behaviour with the experimental response. Two modelings presented slightly different mechanical responses showing that the cluster-wall friction μ_{wall} gains the importance of more complex loading conditions (with respect to the modelling of URC). The frictionless configuration has lower ultimate force $F_V = 538.2$ N because at a given point the sliding of cluster-wall contact occurred and the fragments rotated ending the test without any secondary breakage. To prevent sliding, the friction was activated. Consequently, the top force rose up

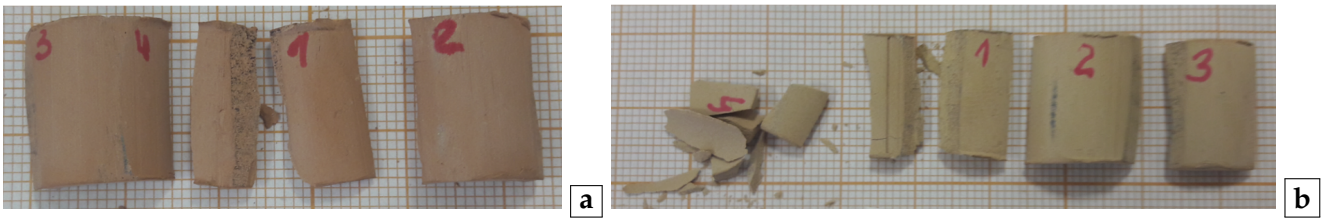

Figure 3.31 : The breakage manner in the biaxial radial compression: **a** – splitting in only only radial planes and **b** – a mix of purely radial cracks and some local crumbing.

to $F_V = 705.3$ N, and the BRC modelling finished with crushing into multiple parts.

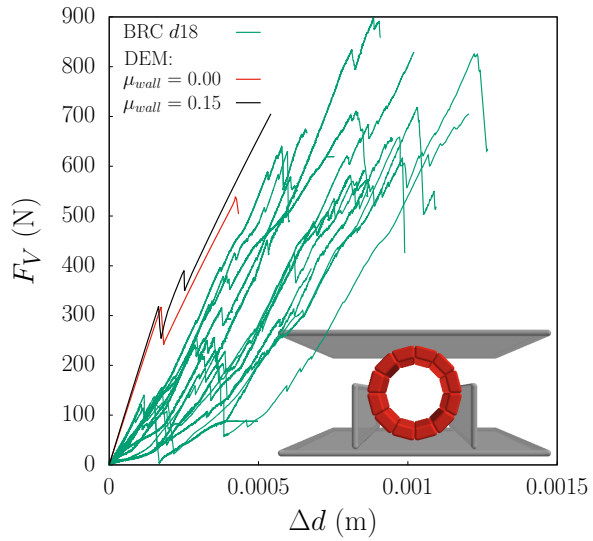

Figure 3.32 : The vertical force (applied on the top of the shell) F_V *vs.* corresponding displacement Δd curves. Loading condition: biaxial radial compression with no horizontal deformation as shown in the **Figure 3.29**. Green curves show the experimental tests, while red and black lines present the DEM modelling for friction and frictionless interactions between cluster and the plates.

This outcome proved us that the selection of the numerical parameters was a successful process. The average strength of the shell is comparable to the numerical result $F_V / F_{V\,true} = 1.05$. Due to the perfect elasticity, the model mismatches the experimental displacement Δd. In other words, the model did not capture the imperfections of lineic contacts in the experiments. Yet it is remarkable to see that the inclination of numerical lines corresponds to the linear part of experimental curves.

3.5 Summary

This section has been dedicated to the micro-scale study of tube-shaped shells both experimentally and numerically. In order to model complex geometry and to reflect the shell breakage, a suitable model using an efficient number of constituents was generated. A cluster model used in this study subdivides a tube-shaped shell into a number of sphero-polyhedral rigid sectors (presenting the sub-grains as clumps) connected together through the cohesive sphere-to-sphere links. Each link is an interaction point for which the standard force laws have been designed such that two parameters correlated with a shell strength were included. The numerical parameters controlling shell strength ($f_I^\star, f_{II}^\star$) were extracted from the experimental campaign of uniaxial radial compressions. Bellow, we summarise the most important observations:

- The ultimate diametrical force F_I presents a strong variability due to the geometrical and material heterogeneities. The cumulative distribution function of F_I at the point of shell failure is Weibullian for both sizes: *d18* and *d20*. Those distributions can be easily converted to Weibullian cdf of the numerical yield threshold of the normal interaction force $f_I^\star$ and can be implemented in DEM simulations.
- The force F_I depends on the shell size. The scattering of average force follows the power law. If one wishes to take into account the deviation from the mean value, a determination of the limiting power laws is possible.
- Adding horizontal constrains to the vertical compression leads to biaxial loading of

the shell. With respect to the uniaxial radial compression, the resistance of shell was enhanced and the top vertical force F_V was 5.5 times higher than F_I. The horizontal support levelled down the deviatoric loading such that we have observed hardening due to the increase of the coordination number.

Afterwards, the work has been continued with DEM simulations:

- Small parametric study allowed the adjustment of the numerical parameters. The normal contact stiffness k_I controls the slope of linear elastic response with small or large deformations. The ultimate force F_I is modelled by a local parameter $f_I^\star$ causing a tensile opening of links. Both parameters depend on the scheme of shape discretisation, which is an important part of the numerical model. Whereas the radial discretisation number implies the modification of k_I, the change of the axial discretisation number requires a modification of the link force threshold $f_I^\star$. The rotation of the sector allowed us to estimate the importance of yield tangential force $f_{II}^\star$ and its minimum level required in the uniaxial radial compression.
- Different number of sectors per cluster has been considered. The importance of axial subdivision was found of secondary importance in the case of shell diametrical compression. Focusing on the circumferential division, $N_{circ}^\star = 24$ provided the most accurate results, but for the sake of calculation efficiency, the final discretisation with $N_{circ}^\star = 12$ has been chosen as an adequate optimal choice to be probed using a large assembly.
- In both uniaxial and biaxial radial compressions, the vertical splitting was a primary breakage, and other cracks horizontal or/and inclined were found to make the second appearance.
- We successfully calibrated our cluster model such that a linear elastic response of model correctly reflects the experiments.
- Verification of parameters was performed on the example of biaxial radial compression constrained horizontally. The experimental average critical force and the slope of linear elastic part stand in good agreement with DEM model. Thus, the force thresholds $(f_I^\star, f_{II}^\star)$ and the stiffnesses (k_I, k_{II}) were considered as well adjusted.

Preparation of an assembly of the tube-shape grains

Contents

Introduction

Both experimentally and numerically, to study the mechanical behaviour of the granular material, first of all, a sample needs to be assembled from the constituent particles. Not only the experimental mechanical behaviour is affected by an initial sample state, but also the numerical simulations in quasi-static loading conditions are sensitive to it. All the more reason why one should reflect the "natural" structure of sample numerically. To this end, the method to compare both assemblies needs to be selected *a priori*.

Each granular material creates a characteristic material structure, called also fabric. Many studies follow the definition of Brewer (1964) who described the fabric of granular matter simply as a spatial arrangement of the solid particles and the associated voids. Then, it is referring to a specific combination of variables such as density, grains and contact orientations, number of contacts and others. In such a framework, also scalar quantities like void ratio or coordination number provide some information about the material structure. Therefore, in this study, among many possible internal variables we took advantage of those that can be estimated from reality. The numerical and experimental samples were compared using: a number density n and a coordination number Z.

Furthermore, fabric depends on the material itself – characteristics of grains such as shape and angularity – and the preparation technique, *e.g.*, gravity deposit or isotropic compression (Radjaï and Dubois, 2011). Thus, a preparation protocol was carefully chosen, hereinafter.

Oda (1972) suggested that "*the concept of fabric of granular mass should include at least two main subconcepts,* e.i*, (1) orientation of individual particles, and (2) position of the particle and its mutual relationship to each particles*." In the domain of discrete element modelling, the fabric is characterised by the second subconcept and refers to contact orientation throughout fabric tensor (Radjai et al., 2012). This study employed the first subconcept and used the distribution of grain orientation as a reference to numerical sample structure.

Section **4.1** concerns the experimental measurement and estimation of internal variables. This section includes our experimental measurement of the density and coordination number performed at the fabrication plant where the VMC segments are pre-casted. Moreover, the estimation of surface friction angle and mortar strength were done providing some of the input parameters required in the future DEM modelling.

Section **4.2** presents a definition of shell orientation and the statistical analysis of real samples acquired using X-ray imaging techniques. The analysis tool, called 3DShellFinder, was developed for this study to efficiently detect the shells on the 3D image obtained from the X-ray scanning. As will be discussed, this is an alternative algorithm to overcome the issues arose during the classical watershed segmentation for this particular material.

Section **4.3** is dedicated to the numerical assemblies of shells. Thus, in section **4.3.1** the numerical preparation protocol was described. Also, a small parametric study was carried out to determine the influence of inter-granular friction on the state of prepared samples. This led to the preparation of more samples as presented in the section **4.3.2**. Thereafter, the samples were compared with the experimental ones. Thanks to DEM, an influence of rigid boundary was studied, and as a result, the samples with the preferential orientations of shells were generated.

List of symbols

Symbol	Explanation
Section 4.1	
cdf	Cumulative density function
α	Angle describing a geometry of pyramid-like system of 3 shells (°)
ϕ	Angle of friction considering between shell extrados (°)
μ_{surf}	Experimental estimation of friction coefficient for surface-surface contact
μ_{shell}	Numerical inter-cluster (two clusters) and intra-cluster (two sectors) friction coefficient
ρ_m	Mass density (kg/m^3)
D	Diameter of cylindrical sample (m)
d	Diameter of ring in the shell cross-section (mm)
$d18,\ d20$	Fabricated sizes of shells distinguished by a target diameter $d \sim 18$ mm and d~ 20 mm
H	Height of cylindrical sample (m)
$F_1,\ F_2$	Loading gravitational forces (N)
F_S	Shear force of cemented joints between shells (N)
F_T	Tensile force of cemented joints between shells (N)
L	Loading arm (m)
L	Large sample size
M	Mass of sample (kg)
m	Weibull's modulus
m_{mortar}	Mass of cement coating per sample (kg)
m_{shell}	Mass of one shell (kg)
N	Number of shells / clusters
N_n	Number of neighbours
n	Number density (m^{-3})
P_S	Probability of survival
S	Small sample size
V	Volume of sample (m^3)
x_0	Scale parameter of Weibull distribution
$Z_\bullet$	Coordination number of $\bullet$ type (specified at in the text)
Section 4.2	
pdf	Probability density function
$(xyz)_{sec}$	Local coordinate system for sector
xyz	Local coordinate system for shell
XYZ	Global coordinate system for sample
ZOI	Zone of interest
α	Angle describing inclination with respect to vertical axias (°)
a_2	Anisotropy coefficient
d_{target}	Number of target zones
D_R	Reduced diameter of cylindrical sample (m)
$E(\vec{x}, \hat{q})$	Error function
e	Void ratio
H_R	Reduced height of cylindrical sample (m)
$\vec{o}$	Unit vector directing shell orientation
$N^\star_{axial}$	Discretisation number in axial direction of shell

Continued on next page...

Symbol	Explanation
$N^{\star}_{circ}$	Discretisation number circumferentially, that is in the ring cross-section of shell
n_{seed}	Number of seeds
$\vec{P}_i$	Position of search point (voxel)
$R_1,\ R_2$	Radii of circles determining the zoned of interest (voxel)
$\hat{q}_{shell}$	Set of quaternions defining shell orientation
$\vec{x}_{shell}$	Position of shell (voxel)
Section **4.3**	
μ_{shell}	Numerical inter-cluster (two clusters) and intra-cluster (two sectors) friction coefficient
μ_{wall}	Numerical friction coefficient between two cluster (shell) and wall
E_k	Kinetic energy (J)
e	Classic / overall void ratio
$e^{\star}$	Modified / inter-cluster void ratio
F_{limit}	Limit of loading force (N)
$f^{\star}_{I}$	Normal yield threshold in pure tension (N)
$f^{\star}_{II}$	Tangential yield threshold in pure share (N)
M_{max}	Impose rotational moment (kg m^2)
n_r	Relative number density
$\vec{o_0}$	Initial orientation of shell
$\vec{o_{pref}}$	Preferential orientation of shell
$\vec{v_0}$	Randomly oriented velocity vector (m/s)
Z_n	Average number of neighbours

If a symbol or an abbreviations is not distinguished in the current section, please search in the previous sections.

4.1 Characterisation of sample using experimental measurements

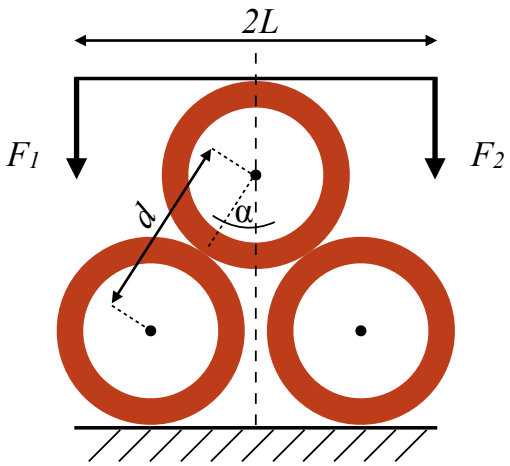

a

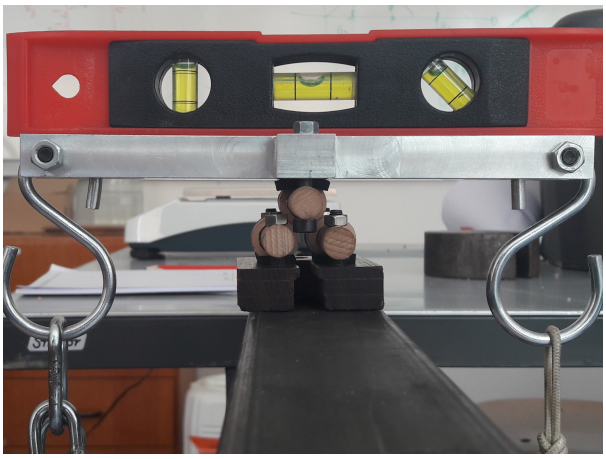

b

Figure 4.1 : Measurement of surface angle of friction ϕ for the shells made of backed clay. **a** – Scheme of set up at the starting point (equilibrium state for $F_1 = F_2$). Geometry described by size d (diameter of shells) and angle α. Both forces F_1 and F_2 act on arm with length L. Significant increase of F_2 will lead to sliding in the contact point between top and bottom shells. **b** – Experimental settings at the beginning of test (equilibrium state).

No.	F_1 (N)	F_2 (N)	ϕ (°)	μ_{surf}
1	9.8	11.2	16.81	0.30
2	9.8	11.0	14.83	0.26
3	19.6	22.0	15.08	0.27
4	19.6	22.4	17.66	0.32
5	29.4	32.9	14.28	0.25
6	29.4	32.9	14.14	0.25
7	39.2	43.8	14.18	0.25
8	39.2	42.8	10.92	0.19
9	49.0	55.3	15.56	0.28
10	9.8	11.0	15.41	0.28
11	19.6	21.6	12.39	0.22
12	29.4	34.2	19.90	0.36
13	39.2	42.7	10.63	0.19
14	49.0	54.7	14.07	0.25
15	39.2	43.0	11.54	0.20
16	29.4	31.9	10.02	0.18
17	29.4	31.9	10.03	0.18
18	19.6	20.9	8.09	0.14

Table 4.1 : Determination of surface angle of friction ϕ and corresponding friction coefficient μ_{surf} for shells baked from clay in size *d18*. F_1 and F_2 are the loading forces applied according to loading conditions shown in the **Figure 4.1a**.

Shell-shell friction

ROCKABLE requires to input a friction coefficient μ_{shell} prior to each simulation, and therefore, an experimental attempt to quantify μ_{surf} has been performed as follows. **Figure 4.1a** presents the concept that has been already introduced in case of wooden rods (Calvetti et al., 1997). Three shells were assembled in a pyramid formation as shown in **Figure 4.1a**. The bottom layer is fixed to the ground and the top shell is attached to the loading bar such that the two layers do not constrain each other. Then, the contact points between the shells are capable of mobilising friction. Technically, the shells have been fixed by means of three wooden rods passing through the internal wholes of shells (**Figure 4.1b**). The rods have been attached either to a wooden base (for the bottom shells) or to the aluminium loading part (for the top shell) using the screws placed at both ends of each rod. Two forces F_1 and F_2 are applied at the end of loading bar of length $2L$ (**Figure 4.1a**). The test starts from the equilibrium state, that is, when $F_1 = F_2$. Then, F_2 is increased in order to mobilise friction. Once the sliding appears, knowing the values of

forces and the geometry of system (d and α), the surface angle of friction ϕ can be extracted from relationship:

$$\sin 2\phi = \frac{F_2 - F_1}{F_2 + F_1} \frac{2L}{d} \cos \alpha. \tag{4.1}$$

Figure 4.1b shows the experimental setup with the geometry described by $d \approx 17$ mm and $\alpha \approx 36°$. The loading part has been constructed such that the force arm is always equal to $L = 900$ mm. The gravitational loading, *i.e.*, two masses hanged at both ends of loading bar, allowed us to determine the gravity forces F_1 and F_2 shown in **Table 4.1**.
A priori, the equilibrium state was obtained for various initial values of force F_1. Using equation (4.1) the surface angle of friction was calculated, and **Table 4.1** holds the detailed results of all tests. The average surface angle of friction was found at $\phi = 13.6° \pm 3.0°$ and corresponding friction coefficient $\mu_{surf} = 0.24 \pm 0.06$. Note that the surface of shells is relatively smooth (as for geo-materials), but the ring base of shell or angular fragments (resulting from breakage) are characterised by higher roughness. This must influence the angle of friction, yet it will not be studied hereinafter.

Packing density

Determination of density is a basic and straightforward measurement, yet it provides essential information about the material. As commonly known, the granular material might form either a loose or a dense assembly affecting the mechanical behaviour. Therefore, knowledge of density range is of great importance in the evaluation of stress-strain curves. Secondly, the density can be a reference parameter for the numerical samples. This study takes advantage of two types of densities indicated by equations (4.2) and (4.3). Mass density ρ_m measures weight of material M per unit volume V (kg/m^3), while a number density n is simply number of shells N packed in a volume unit (m^{-3}). The mass density measurement includes the coating in its value. On the contrary, the coating is ignored in the calculation of number density. Still, we profit from n while preparing numerical samples, because the comparison of n instead of ρ_m provides more reliable and robust results.

$$\rho_m = \frac{M}{V} \tag{4.2}$$

$$n = \frac{N}{V} \tag{4.3}$$

The measurements have been done at the prefabrication plant *Stradal* in Maxilly-sur-Saone, where the compressible mono-block arch-segments (VMC) are pre-casted so that the results were as reliable as possible. In **Figure 4.2** one can observe the coating process. First large portion of the shell in size *d18* has been extracted from the stock (**Figure 4.2a**), and the cement mortar containing fine aggregate (sand) was prepared using standard concrete mixer (**Figure 4.2b**). Then, the shells and the mortar were combined and mixed further until the coating was accurately distributed among shells (**Figure 4.2c**).

Figure 4.2 : a and **b** – Photos showing the coating process done at *Stradal* plant. **c** – Material used in density measurements – shell in the size *d18* with the coating of cement mortar (see **Table 4.3**).

Size	D (m)	H (m)	V (m^3)
L	0.16	0.32	0.00643
S	0.11	0.22	0.00209

Table 4.2 : Cylindrical sample with height H and diameter D have a volume V. Used volumes allowed us to distinguish two sample sizes: large (L) and small (S).

For the measurements two sizes of cylindrical mould were used with H/D ratio equal to 2 and the volume V, characterised in **Table 4.2**. Furthermore, we have been working both on a granular material (assembly of shells) and on a composite mixture, *i.e.*, shells with cement coating. Firstly, the material was poured into the moulds from a small dropping hight. Those samples were considered as loose ones, whereas the preparation of dense samples was continued. The mould was shaken using a small vibration table, available at *Stradal*, and the sample was completed with the material. **Table 4.3** presents the average measurements for eight types of samples being the combinations of used material, sample size and preparation protocol. Note that in the case of coated sample the weight was measured in one of three cases: fresh samples, 24 h after or 28 days after preparation. Although the number of measurements (**Table 4.3**) is limited some important tendencies can be distinguished. First of all, we have verified those measurements with data provided by Andra. Influence of sample size on mass density for volumes larger than 5.0 l has been previously determined. Since size L (with $V = 6.4$ l) fits in that range, we confirmed that average $\rho_m = 575\ \mathrm{kg/m^3}$ (shells only) remains in accordance with the previous measurements. Secondly, Andra has observed an increasing trend, that is, higher density for larger volume till a threshold density of $\sim$ 590 kg/m. In contrast, we have measured higher density in case of size S (**Table 4.3**). Yet, the small sample must be highly affected by the rigid boundary, and this size was not included in the reference measurements. In case of granular matter, the change of ρ_m need to be reflected by the change in the number density, as the shells within the sample are of the same size and have a similar mass m_{shell}. Then, naturally, the dense samples need to have a higher number of shells. When the shells are coated, this relationship vanishes. The mass density rises about 40 % – respecting the sample type, yet the number density is only slightly different. It is interesting to observe that although the coating creates adhesive links between shells the packing number is hardly influenced. Therefore, in the DEM simulation, the same numerical arrangement can be used for the simulation with and without coating. The measurements made on the loose samples will be a reference in the assessment of the numerical samples. Vibrating the samples (with Stradal's vibration table), we have tested the top limit of density. Nevertheless, it is believed that the shells typically form dense packing due to their geometry.

Finally, an attempt to assess the mortar content in the sample was made. After the measurement, two coated samples (size L) have been cleaned and left to dry. Each sample has been weighed twice such that the mass difference provides us the mass of mortar m_{mortar}. **Table 4.4** shows the mass quantity ($\sim$1 g) of coating that is attributable to each shell. Note that the average mass of shell has been found at 3.77 ± 0.09 g for shell size *d18*. Assuming that a typical density of cement mortar is about 2 000 kg/m^3, the measured shell density (density of backed clay) was found at the level. Consequently, the mass proportion of mortar and shell is equivalent to volume proportion, such that 23 % of solid volume should refer to the coating.

Type	m_{mortar} (kg)	m_{mortar}/N (kg/shell)
Dense	1.2373	0.00114
Loose	1.1132	0.00118

Table 4.4 : An estimation of the mass of mortar in the samples performed on the samples of size L (**Table 4.2**).

Shell connectivity

Coordination number Z is a commonly used dimensionless variable describing the average number of contacts (neighbours) per particle. For materials in which the grains breakage is most likely to appear, Z is of great importance because it modifies the potential for a particle to crush. A low number of contacts leads to high deviatoric forces acting on the particles, whereas the particles with many contacts are believed to be more isotropically loaded, and therefore, less prone to break.

Material	Size	Type	ρ_m (kg/m^3)	N_{config}	n (m^{-3})	N_{config}
Shells	L	Loose	575.0 ± 0.0	1	151 384 ± 1 319	2
		Dense	610.1 ± 0.0	1	166 538 ± 1 868	2
	S	Loose	580.8 ± 9.3	2	155 129 ± 3 952	6
		Dense	649.6 ± 18.5	5	171 806 ± 4 894	5
Coated shells	L	Loose	806.1 ± 58.9	5	148 223 ± 1 092	3
		Dense	846.7 ± 41.5	2	168 636 ± 0	1
	S	Loose	779.6 ± 5.6	2	155 448 ± 1 353	2
		Dense	915.1 ± 0.0	1	-	-

Table 4.3 : Mean mass ρ and number n densities for the samples prepared in the prefabrication plant *Stradal*. Size of samples is presented in the **Table** 4.2. To obtained dense packings, the samples were subjected to vibration.

As shells breakage rules the behaviour of our assembly, we found it beneficial to estimate the coordination number collated, afterwards, with a numerical model. To this end, one of the large coated sampled has been disassembled shell by shell, keeping only one requirement: the contact must be capable of transferring the force between two shells. Whether the shells actually touch or a mortar bridge appears was disregarded for two reasons. Firstly, the verification is a strongly person-dependent process. Secondly, such a distinction does not exist in the model either. Experimentally, each contact point was registered with a specification of its appearance, either at the shaft, *i.e.*, external convex surface, or at the base of the shell. Thus, we could not only calculate the coordination number of all the neighbours Z_n but also establish the contribution of base and shaft contacts throughout Z_{base} and Z_{shaft}, respectively. Equation (4.4) presents a simple formula to calculate coordination number using existing neighbours N_n and a total number of shells N.

$$Z = \frac{2N_n}{N} \tag{4.4}$$

One more remark needs to be made concerning the volume range of the measurement. Instead of full volume, only top (T) and bottom (B) layers were included. The layers had a height of around 9 cm and 5 cm, that is, $\sim$ 43 % of total sample volume was analysed. The results are shown in **Table** 4.5. As is seen, the sample was assembled into a uniform structure, such that the results from the top and the bottom parts are consistent with each other. One can observe that fewer contacts appear at the bases of the shell, such that the shaft contacts are more than doubled. Note that, for a full cylinder with $d = h$, the ratio of the shaft to bases surfaces (A_{shaft}/A_{base}) equals 2. On an average point a view, there exist 6.7 contacts per shell. Naturally, it is hard to state the validity of this measure, yet one can compare it with typical values of Z known from Discrete Element simulation (DEM) on 3D grains. For example, an arrangement of spheres exhibits $Z = 6$ in the case without friction and between $Z \in \langle 3 : 4 \rangle$ for frictional spheres. For 3D grains with complex shapes, *i.e.*, non-spherical shapes, Z can reach 12 when there is not any friction. As a consequence, $Z = 6.7$ for our frictional coated shells seems like a reasonable value.

Layer	T+B	T	B
N	406	261	145
Z_n	6.71	6.78	6.58
Z_{shaft}	4.69	4.71	4.65
Z_{base}	2.03	2.08	1.93

Table 4.5 : Coordination number Z calculated for N shells taking into account: all the types of contact Z_n, only the side surface contact Z_{shaft} and only ehe contacts with the ring bases Z_{base}. T and B denote top and bottom part of sample, respectively.

Mortar joints

Within sample with coating, the mortar joints are created between the shells such that the strength of each contact is enhanced. The cement mortar can either complement the shell-shell contact or form a bridge between shells (the shells are not actually touching). Due to the arrangement of shells

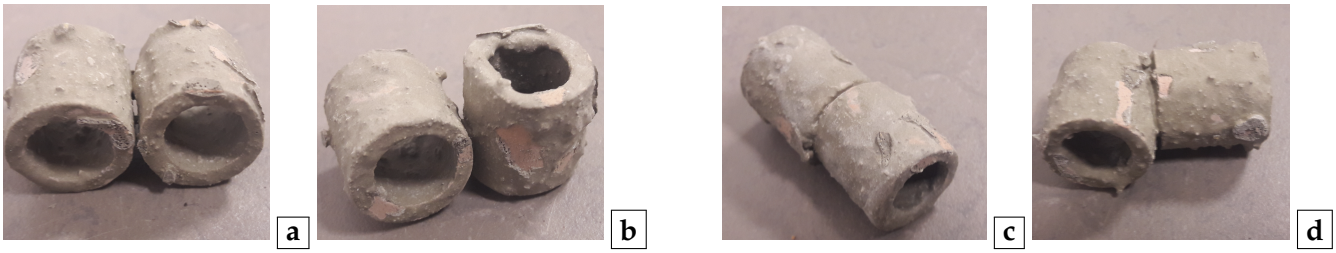

Figure 4.3 : Most basic types of contacts observed while disassembling the sample S after 24 h of drying: **a** – shaft to shaft with parallel alignment, **b** – shaft to shaft with angular (90°) alignment, **c** – base to base contact, and **d** – shaft-base connection.

we distinguished four basic type of contact shown in the **Figures 4.3a** to **4.3d**. As is seen, the mutual alignment will create different types of contacts with various amount of mortar, and therefore, various strength of links. The pairs of shells, seen in the **Figure 4.3**, have been extracted from the small sample (S) after 24 h from the preparation. The cement coating has congealed enough to create the stable links between shells, but still weak enough to disassemble the sample into the smaller clumps. Once the cement bonds are fully developed (after more than 28 days) we have tested the joint's resistance. This will serve a future DEM model of shells with inter-granular cohesion (model of the coated sample). It is worth recalling that the mortar joint will be represented by a bonded contact (see section **3.3.1**). This type of contact requires two parameters related to the tensile F_T (**Figures 4.4a**) and shear F_S (**Figures 4.5a**) strengths of the joint. To this end, simple tests were performed in order to estimate the average strength and variation. For the simplicity of the experimental setup, the types of contact were limited to most basic geometry. The experimental setup allowed us to test the shaft to shaft contacts (**Figures 4.3a** and **4.3b**) in traction, but a shaft-base contact (**Figures 4.3d**) was included in the shear test. In both cases one of the shell has been fixed (**Figures 4.4b** and **4.5b**), while the other was attached to a loading mass. Once the mortar joint failed the mass was registered, and a gravitational force (F_S or F_T) was calculated. **Figures 4.4b** presents the experimental settings used in traction test including the *KERN* hanging balance with

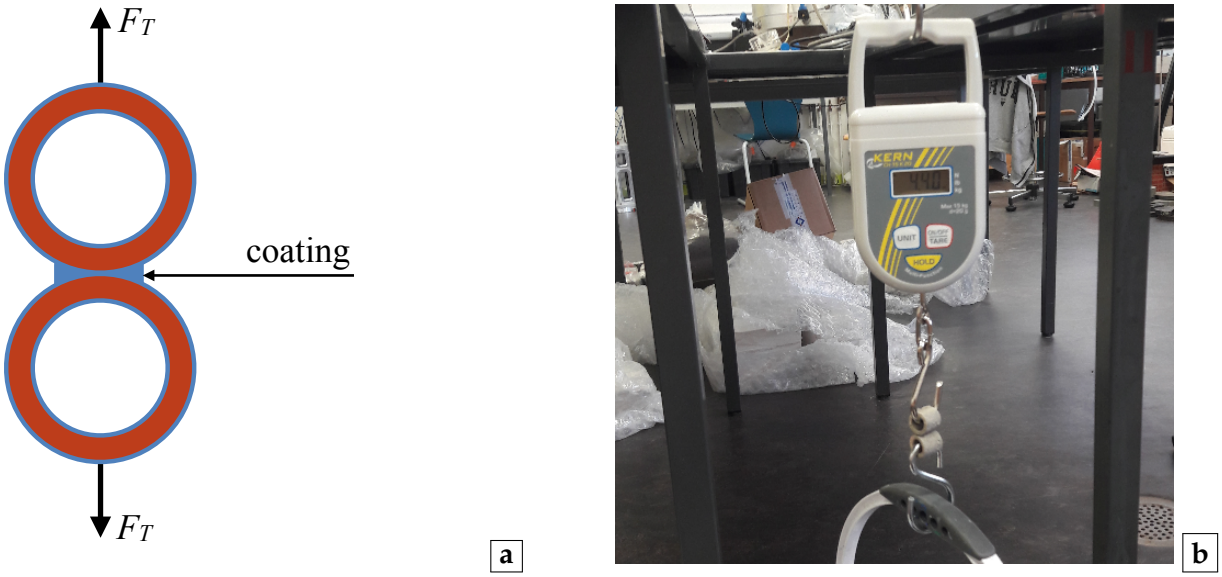

Figure 4.4 : Experimental determination of tensile strength of mortar joints. **a** – Scheme of loading conditions, and **b** – the experimental setup testing shaft-shaft contacts (**Figures 4.3a**).

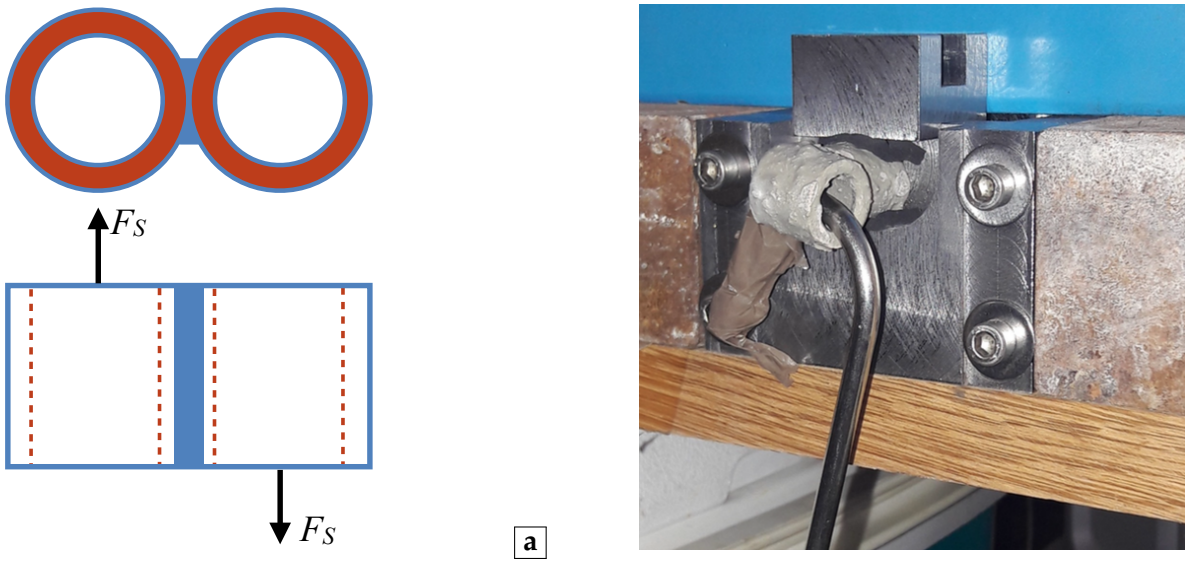

Figure 4.5 : An experimental attempt to extract the shear strength of mortar joints. **a** – Scheme of loading conditions, and **b** – the experimental setup presented in the case of base-shaft joint (**Figures 4.3c**).

limit of 15 kg and accuracy of ±20 g. The small experimental campaign was followed by statistical analysis. Since cement mortar is classified in the family of the brittle materials, we successfully verified the distributions as Weibullian (**Figures 4.6**). The probability of survival P_S in tension has been presented in **Figures 4.6a** using 30 traction tests. Linear relationship was found in the logarithmic space (inset of **Figures 4.6a**) allowing us to determine the Weibull modulus $m = 2.8$. Recall that low parameter m characterise a wide distribution, such that, one can observe that the ratio between maximum and minimum force reaches ~ 4 in this case.

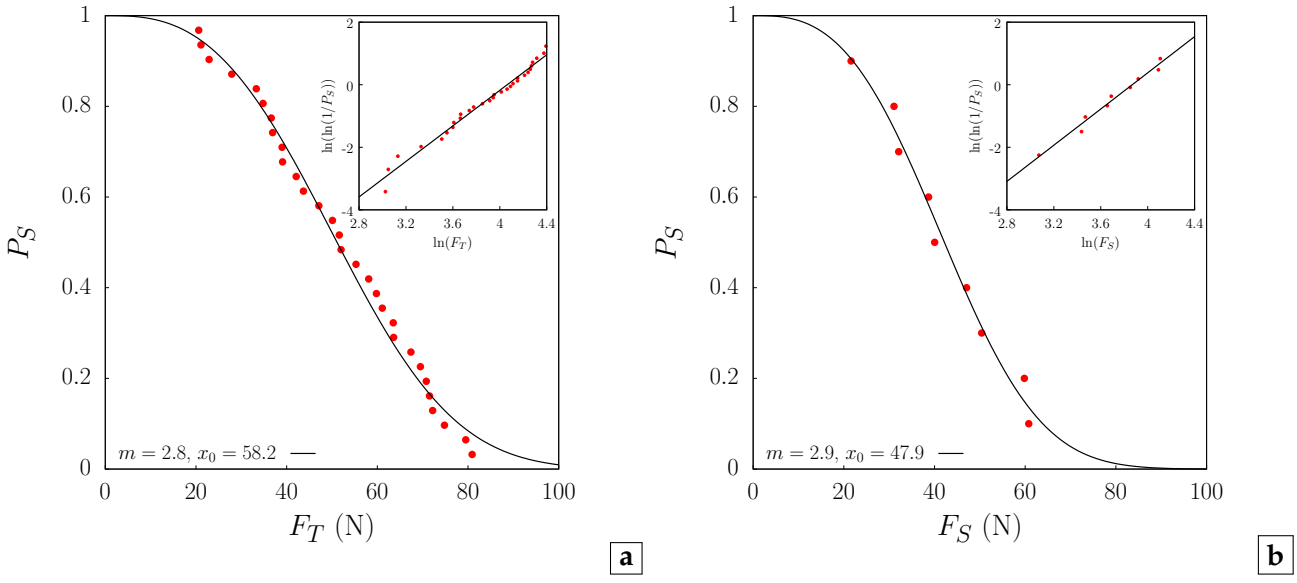

Figure 4.6 : The probability of the cement links survival. Weibull distribution $P_S = 1 - cdf = e^{-(x/x_0)^m}$ was found with scale x_0 and shape m parameters for: **a** – tension and **b** – shear strengths. Red points shows data from experiments and solid curve is an adjusted fit function P_S. Inset: Linear relationship in ln-ln space simplifies the determination of parameters x_0 and m.

An attempt to shear a single shell only has previously shown that it is difficult to secure the loading condition for shearing setup. The fix did not provide the desired loading conditions. Thus, cautiously, only 9 trial tests (red points) were performed in the shear condition (**Figure 4.5b**). This amount cannot provide reliable statistical distribution, yet it serves well the estimation. **Figure 4.6a** shows the statistical analysis of F_S. A wide distribution ($m = 2.9$) has been found for shear, almost identical to tensile strength. Surprisingly also the scale x_0 parameter, *e.i*, the force value for $P_S = 1/\mathrm{e}$, are comparable. In other words, the values of forces F_T and F_S are enclosed in the same range, although one could expect higher shear strength. We acknowledged this result, yet the shear campaign was not carried on.

Finally, we report that there was a test in which failure of the shell instead of the cement joint occurred at $F_T \approx 100$ N. That result is consistent with the shell tensile strength determined in section 3.3.1. It shows that the maximum strength of joint cannot be determined from this test, and a fortiori, in the DEM model the shells strength should not be constrained by this exact distribution. Summarising, those tests actually indicate the bottom limit of mortar strength.

4.2 X-ray Computer Tomography (CT)

Figure 4.7a shows a large specimen acquired from the mono-block tunnel segment (VMC). The compressible layer was composed of cement-coated shells *d18* and it had thickness of around 15 cm (**Figure 4.8**). This measure includes protection, *i.e.*, $\sim$2 cm layer of cement paste, that covers the shells assembly at the extrados of the segment. The protection, located on the sides of the specimen, indicated that 80 cm is the depth of a segment, such that 40 cm is a random bowstring of tunnel ring. Firstly, the large piece has been portioned into smaller parts (**Figure 4.7b)**. Then, a cylinder with a diameter close to 12 cm was cut out using a core drilling machine shown in **Figure 4.7c**. Finally, the protection layer was removed, such that the height of the sample was reduced about 2 cm. Note that for further analysis the samples remain "upside down" with respect to their position in the tunnel segment. To avoid any confusion, the terminology is established as follows. The uneven surface of the sample was an inner interface between the compressible layer and the concrete part, but, hereinafter, it is referred to as the *top* (of the sample).

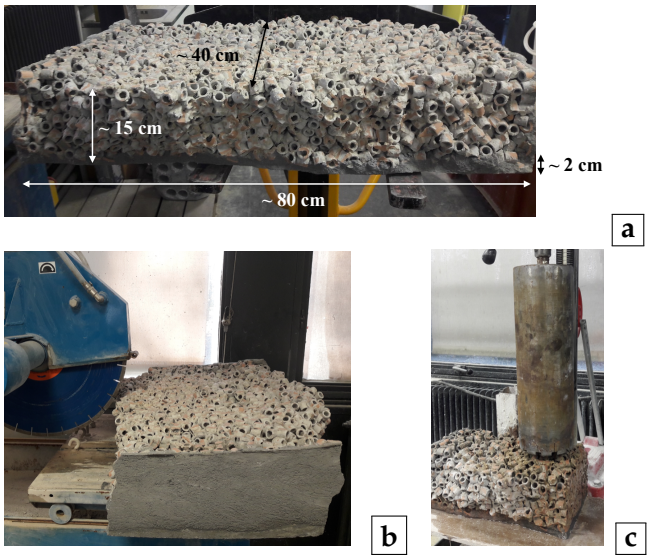

Figure 4.7 : The treatment of compressible layer extracted from the mono-block tunnel segment (VMC – see **Figure 4.8**). Thanks to this protocol the cylindrical samples of shells *d18*, in their "natural" arrangement, with the original cement coating were obtained (**Figure 4.9a**).

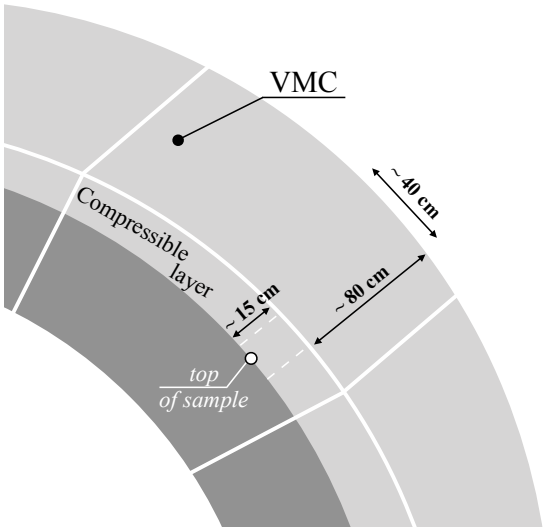

Figure 4.8 : Sketch of VMC segment relates the dimension of extracted part to the compressible layer and shows the "upside down" orientation of sample (**Figure 4.9a**) with respect to in-situ location.

Thus, the flat surface, this is the *base/bottom* of the sample, in arch-segment was located at the exterior of the tunnel.

Figure 4.9a presents one of the extracted samples. The drilling is a complex and invasive method, especially in case of the brittle shells. Unintended sample damage has been reported on the top due to lack of constraints on the free surface. In **Figure 4.9a** one can observe the remaining fragments of broken shells. Also, the intact shells have been detached from the top surface because of the cement bond failure, and thereby the surface gaps were created. Furthermore, while making a core, the water needed to be constantly poured, and therefore, the cement-coating was partially washed out in the boundary zone. Finally, only some of the preparation attempts finished successfully, and the geometry of just two samples have been approved for X-ray tomography.

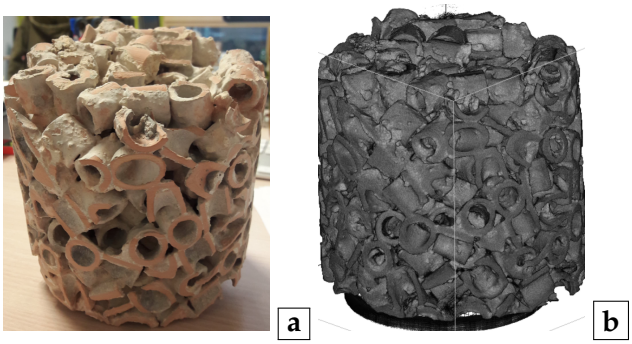

Figure 4.9 : Cylindrical sample ST-SC-1 (**Table 4.6**) composed of cemented shells and acquired from a tunnel segment: **a** – photo, and **b** – volume reconstruction from X-ray radiographies.

The radiographs have been acquired using RX-Solutions scanner administrated by Laboratoire 3SR. One can find its detailed description given by Doreau-Malioche (2018) or Papazoglou (2018). An "indirect" flat-panel Varian PaxScan® 2520V detector and Hamamatsu Corporation L8121-03 source are embedded in this device allowing to apply following image acquisition settings. A voltage equal to 135 kV and a current of 500 μA were selected. To capture the structure pattern and whole volume of sample, the spot size[1] was set to "large"[2] and the spatial resolution (voxel size) was kept at 100 μm. Consequently, the size of the image was 1400×1400×1400 voxels. The vertical 2D projections of the sample have been acquired at 1440 different angular positions by averaging 6 scans, captured with frame rate 5. Then, the Filtered Backprojection (FBP) analytical method, incorporated in X-Act software, allowed to reconstruct the X-ray attenuation field in 3D as presented in the **Figure 4.9b**.

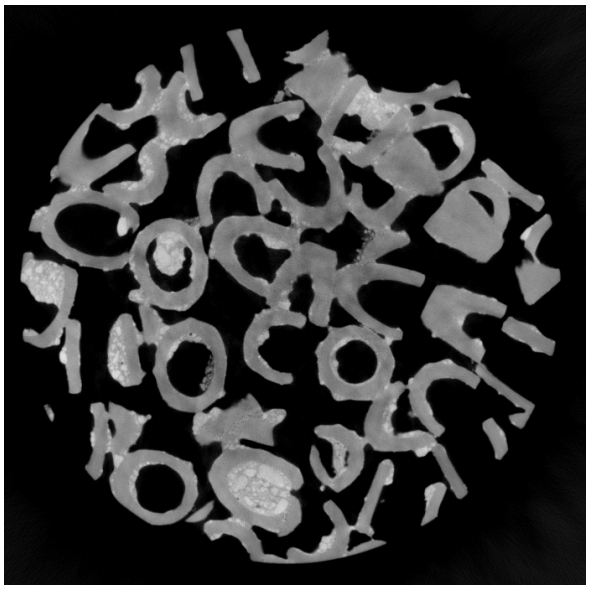

Figure 4.10 : 2D horizontal slice located in the top part of sample ST-SC-1 (**Figure 4.9**). 16-bit image obtained from X-ray CT.

Figure 4.10 presents a typical horizontal slice subtracted from the reconstructed volume (**Figure 4.9b**). X-ray CT provided us insight into the interior of sample exposing the non-uniform distribution of cement coating. Firstly, it can be observed that the internal void geometry was modified by the mortar on different levels: from shells fully filled with mortar, throughout partially penetrated ones, to shells with a thin layer of coating. All this cases can be distinguished in **Figure 4.10**. Secondly, it seems that inter-granular free space is relatively less occupied by cement mortar. As expected, the coating forms the shell-to-shell bridges that are clearly outlined for various shapes and amount of mortar. Often, the shells do not touch each other in the contact point. In the image, one can intuitively distinguish different shells, as well as separate the shells from

[1]The spot is a starting point of the X-ray beam.
[2]The largest available distance between the X-ray source and the specimen allowed to capture full sample.

the coating. From the technical aspect, it is not a straightforward task. Once the X-ray beam crossed the matter of sample, its attenuation is recored by a detector, measuring the final intensity of an X-ray beam. In the image, the attenuation of beam is represented by a greyscale. Since, we operated on 16-bit images, the grey level can range from 0 to $2^{16} = 65536$. Various types of material might absorb the beam differently, and therefore, one can clearly see that the sand particles outstand within the solid matrix (**Figure 4.10**). A specific grey level is assigned to each voxel in the 3D image, thus, the various phases can be extract from the distribution of grey level. **Figure 4.11** shows the histogram of grey level recorded for both samples. Those results take into account the entire volume of sample. Two peaks are clearly marked in both cases. First one, for a low grey level, characterises the voids (air). Second peak at higher grey level corresponds to the bulk. Two vertical doted lines indicate a manually determined thresholds for sample TS-SC-2. Note that those values varied slightly for the sample TS-SC-1, but for the sake of transparency only TS-SC-2 was marked in **Figure 4.11**.

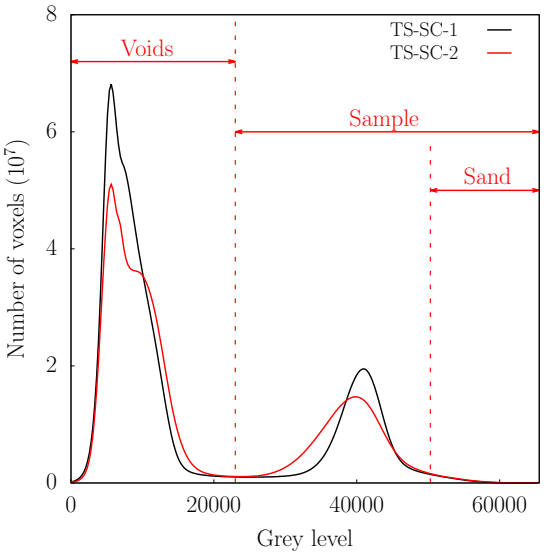

Figure 4.11 : Histogram of the grey level calculated for 16-bit images. For each sample results take into account whole volume of the sample.

Thanks to first threshold, appearing between two peaks, we distinguished two phases: voids and solid. But, the analysis of solid matrix is more complex. The coating is composed of a cement paste and a fine aggregate. The aggregate can be easily recognised because the sand particles absorbed X-ray more intensively than the rest of material. To this end, **Figure 4.11** demonstrates another threshold, at the end of second peak downfall (found at 50 300), above which we defined the sand particles. Owing to the fact that the cement paste causes similar X-ray attenuation as backed clay, it is impossible to extract full volume of coating simply by using another threshold. This leads to major difficulties with the classic image analysis. Note that also specific tube-shaped geometry increase the degree of analysis complexity. As explained by Guida et al. (2018), the intra-porosity causes major difficulties in watershed segmentation employed in labelling the constituent particles. One final remark is that each horizontal slice is charactered by its own histogram of grey level. In other word, the two thresholds of grey level are not homogenous within the 3D image. Whereas, void phase threshold is quite robust, the aggregate phase limit varies significantly between top and bottom of the sample. Therefore, the image analysis has begun using threshold that includes the coating in the solid phase.

Sample	H (cm)	D (cm)	H_R (cm)	D_R (cm)	e
TS-SC-1	12.15	12.86	10.55	12.60	1.283
TS-SC-2	11.55	12.86	9.55	11.70	1.013

Table 4.6 : Sample dimensions extracted from X-ray CT: H – height and D - diameter. Due to damage during preparation for calculation of void ratio e the size of cylinder has been reduced: H_R and D_R.

Table 4.6 presents precise sizes (diameter D and height H_0) of samples measured from the images. Due to the boundary damage and the axial tilt (evident for sample ST-SC-2), the measurement of void ratio e was conducted to reduced volume: H_R and D_R. Thanks to that approach, the overestimation of void volume has been avoided. To measure e, first of all the image have been converted to binary one using the solid-void threshold. Within 3D image array, one can easily calculate the number of voxels assigned to void (grey level = 1) and solid (grey level = 0). Then, the ratio of those num-

bers provided us the value of e as presented in the **Table 4.6**.

The characterisation of shells

Identification of shells and determination of their angular position are most challenging tasks yet provide most valuable informations. To this end, a special image analysis tool, called 3DShellFinder, has been developed aiming this peculiar material. This C++ tool operates on a compressed 3D binary image. Three different sets of input parameters need to be established concerning:

- the shell size and its discretisation,
- the zone of interest (ZOI),
- and the seeding of search.

For the first set of parameters, let us begin with the assumptions regarding the single shell. Firstly, the geometry is represented by an ideal tube (black dashed line in **Figure 4.12a**), and therefore, the height h and two radii (inner r_{in} and the outer r_{out}) must be defined in voxel units. In order to ensure a correct detection of the shells and to account for their actual size variabilities, the dimensions were chosen with some offsets from the contour of the "most-representative" shell-size as shown in **Figure 4.12a**. Nevertheless, this still leads to some limitations. 3DShellFinder cannot detect the shells with strong geometrical imperfections, *e.g.*, egg-shaped cross-section. Also detection of shells located at the sample border, that have been partially cut during mechanical treatment, is less feasible but somehow doable as we will see. Secondly, the search is of a discrete nature. In other words, instead of full shape only number of points are provided for the search as presented in the **Figure 4.12b**. As a consequence, two more dimensionless numbers need to be specified such that $N^{\star}_{circ}$ points are evenly distributed in the radial plane and $N^{\star}_{axis}$ points are located along the axial direction z. These points are referred to as the *search points* $\vec{P}_i, i \in [0, N^{\star}_{circ} \times N^{\star}_{axis}]$. Whereas $N^{\star}_{circ}$ and $N^{\star}_{axis}$ were selected arbitrarily, the shape parameters were adjusted respecting to actual geometry of shells. The average shell dimensions measured during the experimental campaign were selected as the most-representative one, and they were decreased and converted to voxel unit using the spatial resolution of 100 μm. Afterwards, many primary detections were made to find the optimal choice (in terms of correct detection and acceptable search duration) given in the **Table 4.7**.

For the second set of parameters, we move to the scale of sample size where a cylindrical do-

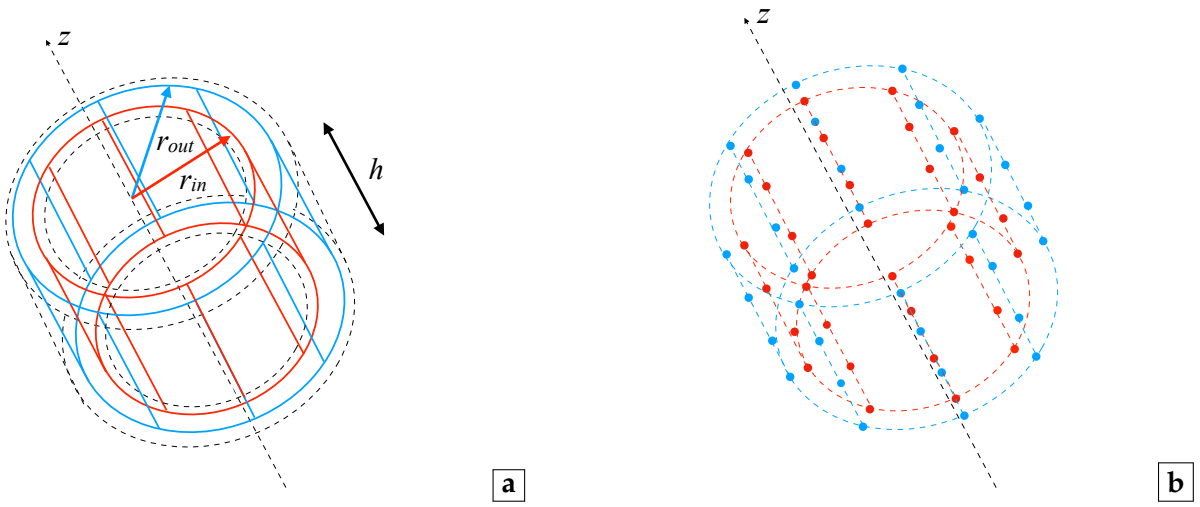

Figure 4.12 : Scheme of tube shape discretisation in 3DShellFinder tool. **a** – First step consists in adapting the dimensions of two layer internal grid: the height h and two radii (for inner r_{in} and outer r_{out} layers). **b** – Then, search points are distributed on the grid such that $N^{\star}_{circ}$ points are evenly distributed in the radial plane and $N^{\star}_{axis}$ points are located along the axial direction z – as presented on above sketch for $N^{\star}_{circ} = 8$ and $N^{\star}_{axis} = 4$.

main needs to be specified; it corresponds to the drilled carrot. Technically, it is achieved by defining two horizontal circles with radii $R_{1,2}$ and position ($X_{1,2}$, $Y_{1,2}$, $Z_{1,2}$). They correspond to bottom and top bases of cylindrical sample. This results in higher efficiency of computation as only actively occupied part of image is taken into account, but more importantly it improves the finding of sawn shells by ignoring the search points that could be placed on the outside during the search procedure.

Name	TS-SC-1	TS-SC-2
h (voxels)	120	120
r_{in} (voxels)	70	68
r_{out} (voxels)	80	78
$N^{\star}_{circ}$	18	18
$N^{\star}_{axis}$	30	30

Table 4.7 : The shape parameters specified as an input in 3DShellFinder: the height h, the inner r_{in} and the outer r_{out} radii. Parameters responsible for discretisation of hollow cylinder into nodes: $N^{\star}_{circ}$ and $N^{\star}_{axis}$. They distribute the points evenly in the radial plane and along the axial direction, respectively.

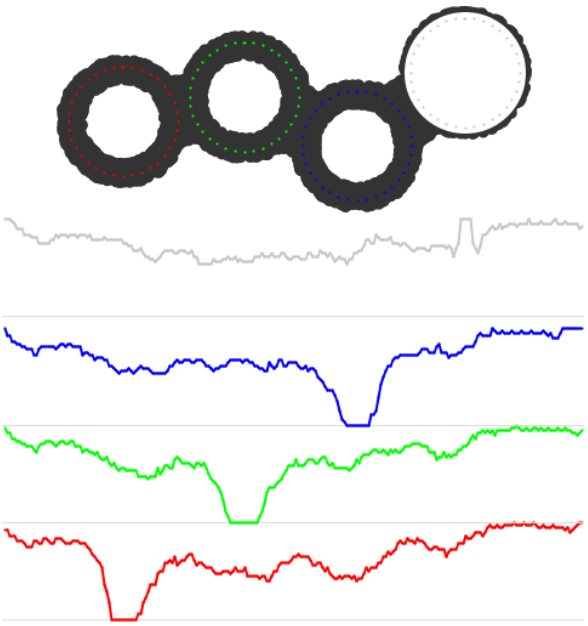

Figure 4.13 : A 2D illustration showing the error spans over the space (colour curves). The search points are placed on the corresponding shell (with identical colours). The shell on the right, masked in white, has already been found. The error depends only on the x-coordinate (the horizontal axis); for the sake of simplicity the y position is known. For each curve, the error varies between 0 (bottom line) and 1 (top line).

Before addressing the third set of parameters, let's look at the procedure in more detail. The algorithm to find a shell is based on the minimisation of an error function parametrised by the position (vector $\vec{x}_{shell}$) and the orientation (quaternion $\hat{q}_{shell}$) of the search points $\vec{P}_i$. By using voxels as length unit, this error function can be written as follows:

$$E(\vec{x}_{shell}, \hat{q}_{shell}) = 1 - \frac{1}{N_{ZOI}} \sum_{i \in ZOI} \mathcal{I}\left(\vec{P}_i(\vec{x}_{shell}, \hat{q}_{shell})\right), \tag{4.5}$$

where $\mathcal{I}$ is the scanned 3D-image that has been binarised so that each voxel is 0 for the "voids" or 1 for the "solid phase", and N_{ZOI} is the number of search points that stand within the ZOI.

If this minimisation is performed with random position and orientation as starting guess, the chance of finding all the shells would be really low. So, the procedure involves several requirements: (1) a shell that has been found can no longer be found again, (2) error wells that tend to trap the minimised solution must be distinguished from really deep wells with near-zero errors, and (3) the position and orientation of cut shells at the boundary of the drilled carrot should be found as far as possible.

Figure 4.13 illustrates how these requirements are dealt with on a simplified 2D case with ring shaped shells, the error function of four shells as a function of their x-position (the y-position being set to the correct value). The right most shell has already been found, and a "patch" with zero-values was then placed at its position so that no deep well can exists anymore (see top curve compared with the other curves). This is how the first requirement is satisfied. In the same figure, the deep wells can clearly be distinguished, but for the minimisation procedure can be trapped inside the smaller wells. To reach the deep wells, cubic target zones having nearly the size of a shell are placed on the ZOI, and each of these zones contains a number of *seed positions* that will serve as initial guess for several minimisations. To be considered as found, the admissible error must then be extremely small – typically less than 1 %. This multiple-seed solution is technically achieved by defining the size of the target zones d_{target} and the number of seeds per target zone n^3_{seed}.

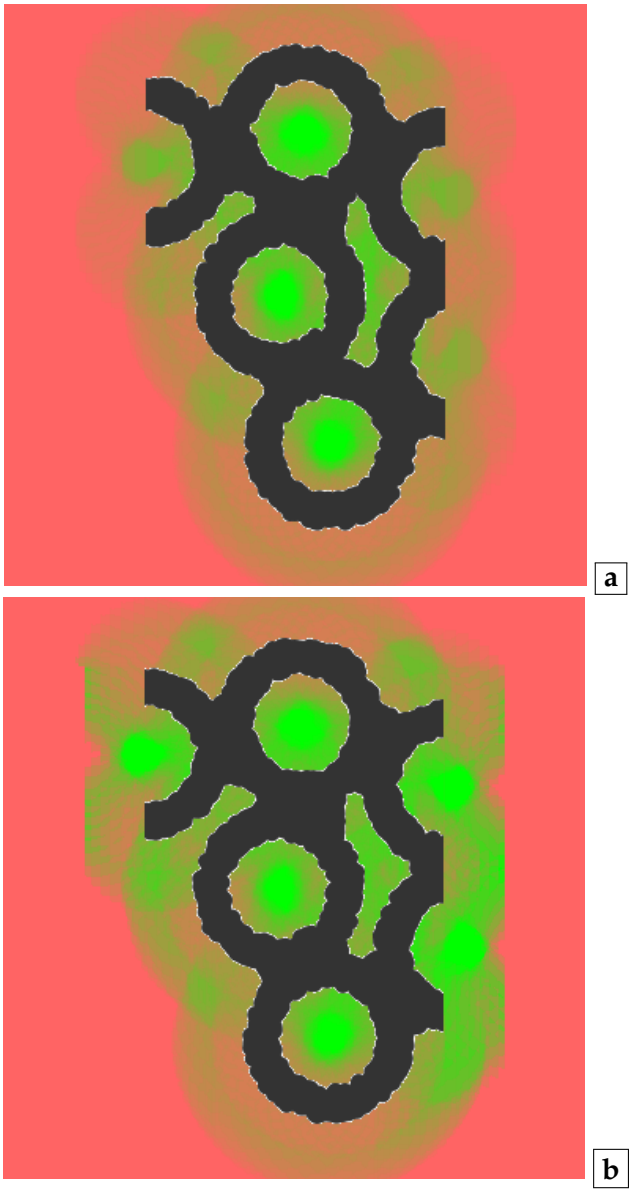

Figure 4.14 : Map of errors from 0 (green) to 1 (light red). The zone of interest (ZOI) is a vertical band in the middle of the image. **a** – Error function with a constant number of search points, **b** – error function as defined in equation (4.5).

The fulfilment of the third requirement is ensured by the error function itself, equation (4.5), because it accounts for the number of search points that stand inside the ZOI rather than a constant number. That way, the the depth of the wells for the cut shells are very deep with nearly zero error, even if the shell is located outside the ZOI. **Figure 4.14** illustrates the cases where the error function accounts or not the ZOI.

We now focus on the settings related to the minimisation seedings that involves two parameters: the size of the target zones d_{target} and the number of seeds per target zone n^3_{seed}. Assuming that each target zone seeks a single shell location, the parameter d_{target} was set at 180 voxels corresponding to the typical shell size. Because the volumes of the two samples were different, and consequently of the volumes of the ZOI, 273 targets were established for sample TS-SC-1 and 221 for sample TS-SC-2. Using the average number density (for large volume samples) equal to 148 223, we have estimated the shell number as 234 and 222, respectively. As is seen, for TS-SC-1 the number of targets is overestimated, whereas for TS-SC-2 the two values are comparable.

The higher the number of trials n^3_{seed}, the higher is the number of successfully detected shells – as presented in the **Table 4.8** – although the computation becomes more time consuming. The best choice for n^3_{seed} is therefore a matter of compromise between the duration of the search and the number of shells effectively identified. A saturation of the number of identified shells is observed, which suggests that not many additional shells will be detected for higher values of n^3_{seed}.

n^3_{seed}	Identified shells
27	47
343	136
1 000	165
3 584	209
25 947	229

Table 4.8 : Influence of the number of trials n^3_{seed} on the number of detected shells by 3DShellFinder.

In summary, the search procedure loops over the target zones. For each trial within a target zone, different positions and orientations of shell are tested where each search point is assigned to a voxel position. It is recalled that in a binarised image, only two possible grey levels exist for each voxel, with the following convention: 1 for solid phase and 0 for voids. If the all search points are perfectly aligned with the image of shell, the value of grey level at each voxel must be 1, resulting to an zero error. The Powell's method is employed to find the position and orientation that give the minimum value of the error function, but a shell is considered as successfully detected only if the

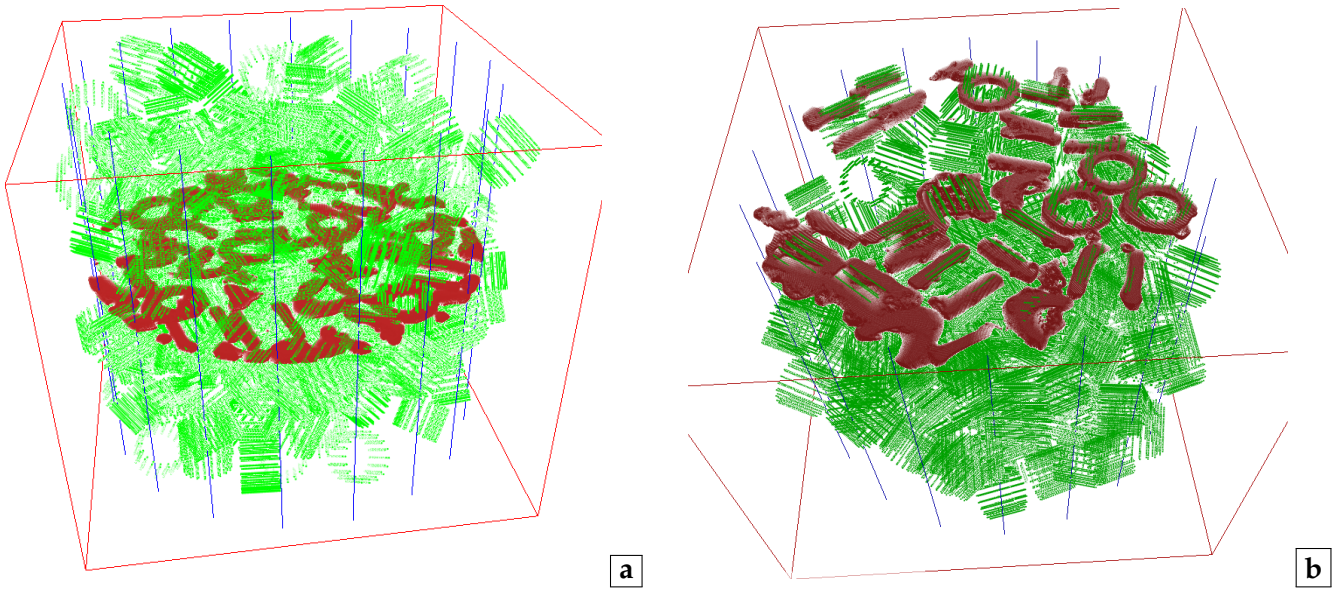

Figure 4.15 : 229 and 199 shells were detected from X-ray scans of coated shells extracted from tunnel segment for sample TS-SC-1 (**a**) and TS-SC-2 (**b**), respectively. Green points present the search points of successfully localised shells. The binary image is represented by the slices, where red zone stands for the solid phase. Whereas red box marks the border of full size image, the zone of interest is shown by blue vertical lines. 3DShellFinder tool.

lowest error found is below 1 %.

For such constrains, 229 shells were identified for sample TS-SC-1 as presented in **Figure 4.15a**. Detected positions and orientations stay in a good agreement with the image. Nevertheless, only in 84% of targets the shell was detected. Considering the average number of shells, 98 % of them were identified in the image, but there are shells that have not been identified. The majority of missing shells are located at the boundary. This is partially caused by the fact that some shells were highly chipped or badly cut during the carrot extraction by sawing. Yet, there can be found shells with full geometry that have not been detected in the image. Similar result were obtained for sample TS-SC-2, for which 199 shells have been identified. That provides around 90 % of successfully identified shells as shown in the **Figure 4.15b**.

Shells orientation

In a fixed coordinate system, an orientation of particle is defined as inclination of its characteristic axis with respect to the reference axes. First and foremost, one need to specify the maximum or/and minimum axis of each grain within the granular matter. For example, Wiebicke et al. (2015) based their method on the moment of inertia tensor using its eigenvectors as characteristic axes of sand particle.

In this study, a different approach was chosen. Taking advantage of peculiar and consistent shell geometry, the characteristic axis z is determined in advance. In **Figure 4.16a** the concept of shell orientation is explained in case of the intact tube-shaped shell. Each shell is described by a local coordinate system xyz related to a global coordinate system XYZ throughout a rotation arisen during preparation. The local orthogonal system is constructed such that a longitudinal direction of sector, *i.e.*, direction of dimension h, follows axis z, whereas the plane xy includes the ring cross-section of tube. Axis z is of great importance, since the inclination of load with respect to this axis activates different mode of fracture – mechanism of failure (section 3.3.1). To profit therefrom, it has been chosen as the shell characteristic axis. Note that, this concept is valid both experimentally and numerically, and therefore, the method will be to quote afterwards. Whereas experimentally it works only for the intact shells, in the numerical model it is more comprehensive. As a consequence of numerical discretisation, each sector

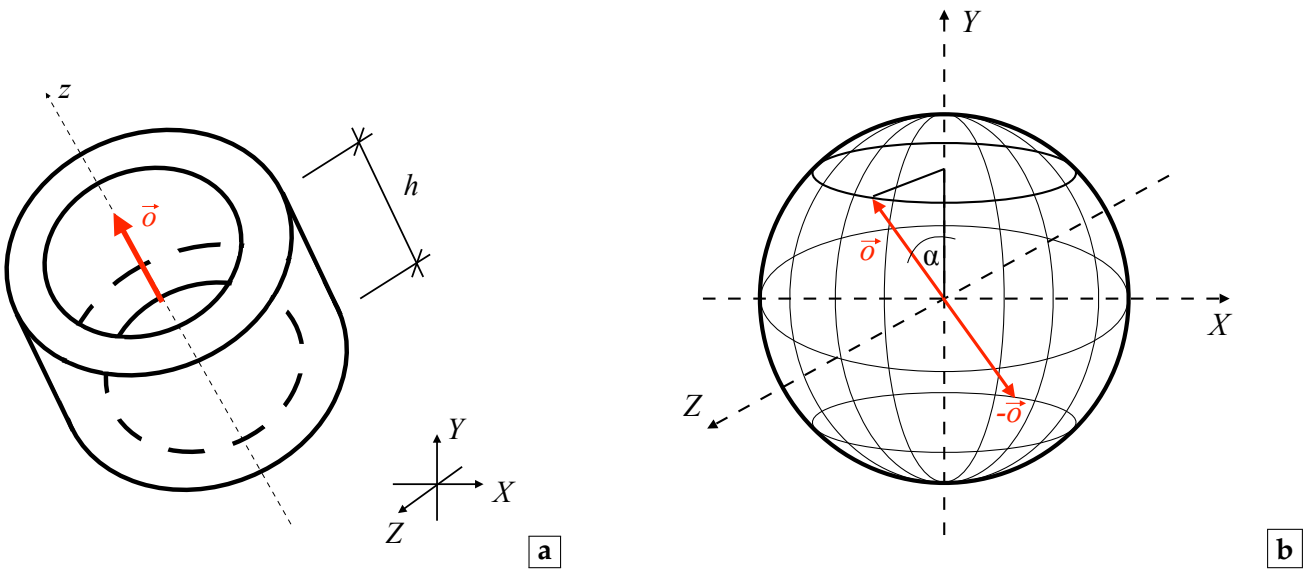

Figure 4.16 : a – A local axis z of intact shell is formed as tube is presented in XYZ space by an unit vector $\vec{o}$. In a similar fashion, $\vec{o}$ describe direction of orientation for a sector in local coordinate system. **b** – Within a global coordinate system, any possible orientation vector $\vec{o}$ can be inscribed inside a sphere with an unit radius. Angle between the vector $\vec{o}$ and vertical axis Y, denoted as α, is a measure of shell or sector orientation.

has another coordinate system denoted as $(xyz)_{sec}$. Yet, z_{sec} must have identical direction as axis z (see section 4.3.1). Since, the axis z_{sec} for each sector in not influenced by the breakage, this concept can be applied despite the fragments size.

As is seen in **Figure 4.16a**, an unit vector $\vec{o}$ describes the direction of axis z. Full 3D analysis should take into account inclination of orientation vector $\vec{o}$ with respect to all of the reference axes. In practice, for the sake of simplicity, the number of reference axes is reduced like in study of Doreau-Malioche (2018). Likewise, we took the advantage of the axial symmetry in the cylindrical sample. Also, the fact that this work aims one-dimension compression in the axial direction supports the choice to limit the analysis to only one axis. Therefore, herein, the orientation is defined as an angle α between vector $\vec{o}$ and vertical axis Y as shown in **Figure 4.16b**. In XYZ space, a point crated from the components o_X, o_Y and o_Z belongs to the surface of sphere with radii equal to $|\vec{o}|$=1 (**Figure 4.16b**). All the orientation vectors $\vec{o}$ pointing to the same parallel of sphere are characterised by the identical value of α (**Figure 4.16b**), and consequently, its values range in $\langle 0 : \pi \rangle$, with $\alpha = 0$ for vertical orientation. Within an isotropic three-dimensional fabric, a high prevalence of horizontally oriented grains occurs naturally. An implicit analysis can be applied using the cosine function to level this geometrical tendency. Since, $\cos\alpha$ is an even function such that $\vec{o}$ and -$\vec{o}$ are equivalent, the $|\cos\alpha|$ ranges from 0 to 1.

For a perfectly isotropic structures, the *pdf*(x) is uniform. Any deviation from the uniform distribution exposes the heterogeneity of the variable x. Therefrom, the statistical analysis needs to be complemented with an assessment of the anisotropy. A number of studies concerning granular media have already used Legendre polynomials to probe the anisotropy of fabric. This method has been successfully applied both in case of particle orientation (Doreau-Malioche, 2018) and the contact anisotropy (Khalili, 2016).

The series of Legendre polynomials (orthogonal polynomials) can play the role of the "coordinate system" for some functions such that those functions can be defined as linear combinations of the polynomials. Herein, we attempted to construct a fit function combining only even orders Legendre expansion $P_{2n}(\mathrm{x})$ into a sum:

$$pdf(\mathrm{x}) = \sum_{n=0}^{\infty} a_{2n} P_{2n}(\mathrm{x}), \tag{4.6}$$

where the coefficients a_{2n} are related to the moments of the function such that they characterised its shape. Limiting the sum of polynomials to the the 4^{th} order reflects the trend of *pdf*(x) accurately as mentioned by Radjaï and Dubois (2011). By keeping the low order, the amount of parameters to adjust is reduced without any deterioration of the result. Then, the general formula form equation (4.6) can be rewritten as:

$$pdf(x) = 1 + a_2(3x^2 - 1) + a_4(35x^4 - 30x^2 + 3), \tag{4.7}$$

with $x = |\cos\alpha|$. Then, the value of coefficients a_2 quantifies the deviation from the isotopic state:

$$a_2 = \frac{15}{4}\left(\langle x^2\rangle - \frac{1}{3}\right), \tag{4.8}$$

where $\langle x^2\rangle$ is a second moment of function (4.7). The isotopic state is given by $\langle x^2\rangle = 1/3$, and therefore, $a_2 = 0$. Thus, the lower the anisotropy coefficient $|a_2|$, the more homogenous is the distribution.

We highlight that in following case *pdf*(x) has strictly limited number of set due to low number of data points. To account for all data points into the fit, it is possible to operate on the cumulative density function *cdf*(x) which resolves this limitation. Keeping the framework of the Legendre polynomials *cdf*(x) is transformed to the following relationship ($cdf(x) = \int pdf(x)$):

$$cdf(x) = x[1 + a_2(x^2 - 1) + a_4(7x^4 - 10x^2 + 3)] + c. \tag{4.9}$$

Figure 4.17 presents the statistics of the orientation of shells found in the samples extracted from tunnel segment (**Figure 4.15**). For the sake of reliability, 428 shells, identified in separate samples, were combined in a common data set. Probability density function *pdf*(x) shows a heterogenous arrangement with high dominance of horizontal shells ($\cos\alpha = 0$). As the shell orientation tends to be vertical ($\cos\alpha = 1$), the distribution seems to become more homogeneous. The solid line presents the function (4.7) for the parameters a_2 and a_4 obtained by fitting the *cdf*(x) (equation 4.7). Although Legendre polynomials are reported to work well in case of sand samples assembled by dry pluviation, they suit the cemented shells distribution only partially. The distribution obey the trend for $\cos\alpha > 0.3$, whereas the peak results in change of distribution shape.

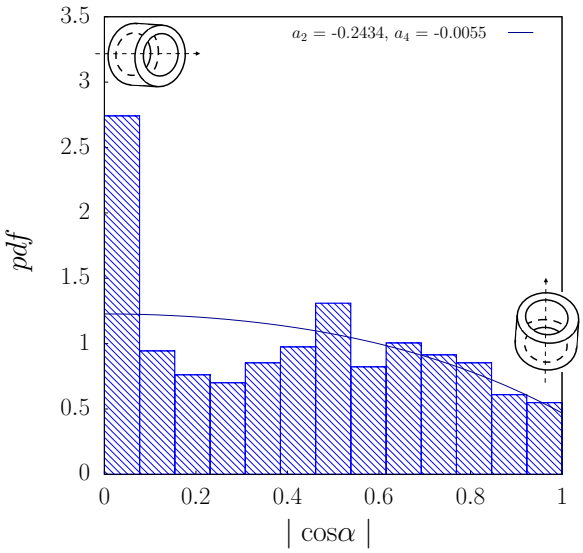

Figure 4.17 : Probability density function *pdf*(x) of shells orientation in the sample cut out of a compressible layer around a tunnel segment (*VMC*). Orientation of shells with respect to vertical axis are described by cosines of angle α such that $\cos\alpha$ is 0 when shell is horizontally oriented and for vertical shells $\cos\alpha$ is equal to 1.

This might be the concrete arch-segment affecting the compressible layer like a rigid boundary (4.7). Nevertheless, it provides as an estimation of anisotropy degree, *e.g.*, comparing with the sand assemblies exhibiting high level of anisotropy for $a_2 \approx 0.3$. Finally, this results describe the reference state to be targeted in the preparation of DEM samples.

4.3 Numerical preparation of a sample

4.3.1 Procedure using DEM

To build a numerical sample, we have simply imitated the preparation procedure from reality by DEM. The procedure consisted of two steps:

- 1^{st} – gravitational deposit of shells,
- 2^{nd} – numerical relaxation.

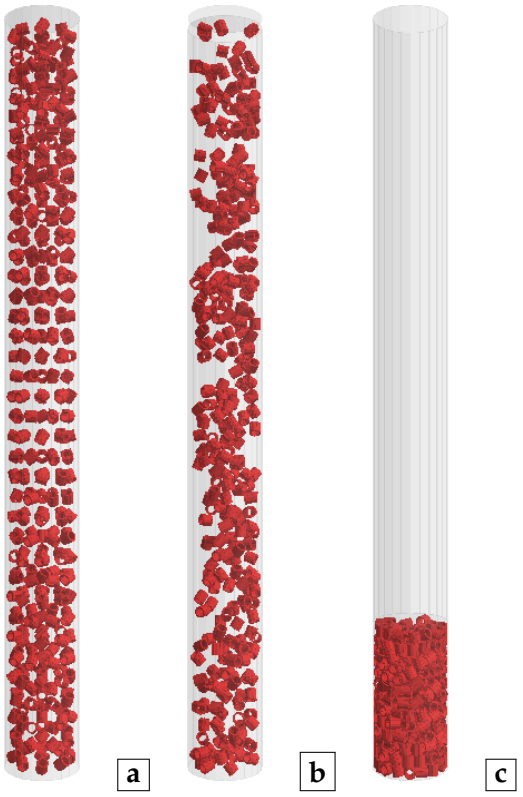

Figure 4.18 : Sample 11×22: **a** – 333 random orientated shells suspended in space on a cylindrical grid without any interactions, **b** – beginning of gravitational downfall with off-grid shaking and **c** – sample under equilibrium.

Firstly, a number of shells was distributed on the grid such that there was not any interaction between them. The assembly suspended in the air was surrounded by an airtight set of rigid walls in order to prevent the shells from floating in the space (**Figure 4.18a**). In case of a sample prepared for oedometer test, a cylindrical mould and a flat plate were used, but for cubic samples 6 separate flat walls were the boundaries (see section 6.3). Then, a movement of shells was imposed by two different factors: a gravitational acceleration and an initial velocity (**Figure 4.18b**). The gravity provided movement downwards, while the shells displace off the grid due to randomly oriented velocity vectors $\vec{v_0}$. The direction of velocity vectors varied for each shell, but all of them had the same magnitude. For the samples that have not been "shaken", it was possible to observe a local zone of highly heterogenous fabric, especially in case of high inter-granular friction. To create flat sample surface, the top plate was allowed to fall down with velocity adjusted automatically. More precisely, its was controlled at each time step such that the force measured on the wall did not exceed the imposed limit F_{limit}. Once all clusters embed on the bottom of the mould, the sample rested until the equilibrium state was reached (**Figure 4.18c**). At this stage Cundall damping was employed as an additional method of energy dissipation. Until the sample became well balanced, a high value of force thresholds $f_I^\star$ and $f_{II}^\star$ prevented the breakage of shells.

Aiming realistic results, the measurements performed at *Stradal* company (section 4.1) were a benchmark. Then, to verify the numerical protocol the size of sample was identical as the physical one – diameter D equal to 11 cm and height H_0 of 22 cm. For this size, 333 bonded clusters suspended in the air were shaken by means of velocities vectors with the magnitude of 1 m/s. The value of F_{limit} was set to 5 N that resulted with an axial stress equal to 520 Pa.

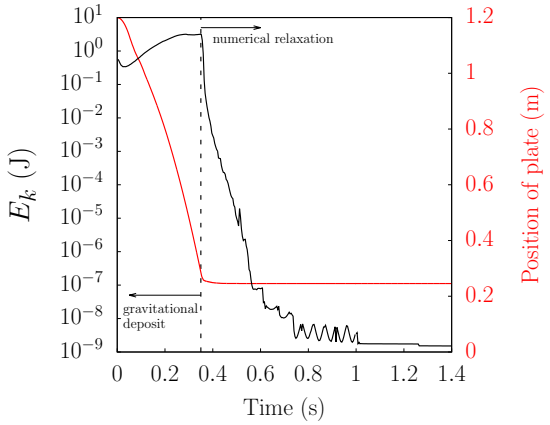

Figure 4.19 : Evolution of kinetic energy E_k for the process of sample preparation. A downwards movement of top plate is presented by red line. The vertical dashed line shows the transition between two stage of preparation (gravity fall and relaxation).

Figure 4.19 shows the evolution of kinetic energy in the course of the deposit (black line). Initially, the sample gains the kinetic energy E_k, when shells are falling. The gravitational downfall is demonstrated also by fast decrease of plate vertical position (red line). Then, as the sample settles on the bottom, the assembly looses the kinetic energy gradually but non-linearly. The decrease is

rapid at the start and slows down while approaching the plateau. Even though the plate remains motionless, one can observe strong fluctuations of kinetic energy. Those oscillations vanished after the activation of Cundall damping (time of 1s), and as a consequence, the equilibrium state was stabilised more efficiently.

First challenge encountered in numerical modelling is the preparation of representative sample. There exists a number of internal variables allowing to judge the quality of numerical samples as recounted in Radjaï and Dubois (2011). One can select many of them to assess the numerical heterogeneity/anisotropy of sample. Yet, currently, not many among them can be quantified experimentally in a fast and straightforward manner in order to be compared with DEM. Herein, a priority was given to the number density n (equation 4.3) having those advantages. Its true values were easily measured and it can be compared directly with the DEM outcome. Then, the average number of contact and the statistics of orientations were verified.

Numerically, the fabric is influenced by friction. To establish how it affects the shell arrangement a parametric study has been carried out. A number of deposits were simulated varying the inter-granular friction coefficient μ_{shell} every 0.25 in the range between 0 and 1 and using frictionless walls ($\mu_{wall} = 0$). For each value of μ_{shell} five different deposits were done following foregoing protocol. **Table 4.9** holds data describing the samples at the end of deposit. It is clearly demonstrated that the number density n and coordination number Z_n can be controlled by μ_{shell}. The higher the friction, the looser the sample and the less contacts appearing. The decrease of density is exhibited also by the increase of two void ratios e and $e^\star$. In both cases void ratios are the proportion of voids volume V_v to solid volume V_s, but the way to calculate V_v is different. Whereas, e takes into account a total volume of voids, *i.e.*, inter- and intra-granular, the modified version $e^\star$ is the inter-granular void ratio disregarding the internal void of the shell.

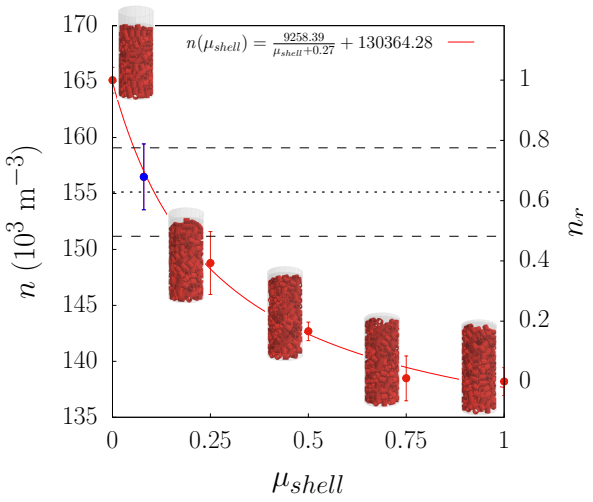

Figure 4.20 : Trend (solid red line) between number density n and inter-granular friction coefficient μ_{shell} for sample size 11×22 cm. The points are the mean values with corresponding standard deviation showing the variability of five different simulations for each value of μ_{shell} used. The experimental range (both the mean and the standard deviation) are shown by black dotted and dashed lines. $n_r = (n - n_{min})/(n_{max} - n_{min})$ is a relative number density.

Figure 4.20 shows the obtained trend that describes n as a function of inter-granular friction coefficient for a sample of size 11×22. Applying friction $\mu_{shell} \simeq 0.08$, the number density n levelled the experimental one ($n \approx 155\,129 \pm 3\,952$ m^{-3}). Note that the most dense samples, with n_{max} of

μ_{shell}	n (m^{-3})	$e^\star$	e	Z_n
0.00	165 121 ± 1 155	0.570 ± 0.011	2.403 ± 0.024	7.03 ± 0.16
0.08	156 489 ± 2 944	0.657 ± 0.031	2.591 ± 0.068	6.12 ± 0.07
0.25	148 788 ± 2 814	0.742 ± 0.033	2.777 ± 0.071	5.27 ± 0.06
0.50	142 679 ± 828	0.816 ± 0.023	2.938 ± 0.023	4.64 ± 0.07
0.75	138 479 ± 2 006	0.872 ± 0.027	3.058 ± 0.059	4.43 ± 0.10
1.00	138 193 ± 1 246	0.875 ± 0.017	3.066 ± 0.036	4.35 ± 0.06

Table 4.9 : Initial state of samples described by: a diameter of sample D, a height of sample H_0, a number density n, an total void ratio e and an inter-granular void ratio $e^\star$.

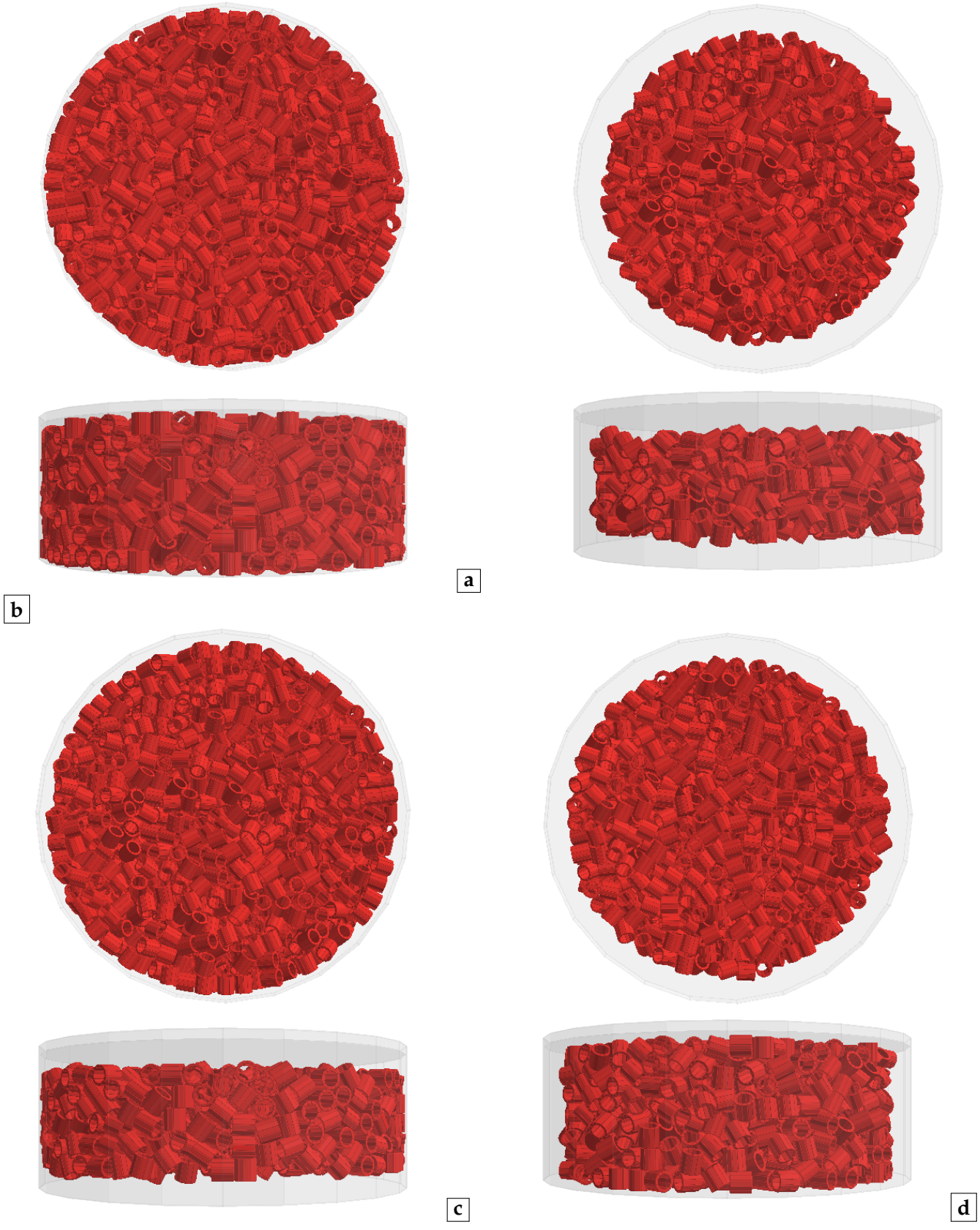

Figure 4.21 : Sample C_35×12_d_01_A composed of: **a** –1 947 shells (100 %), **b** – 1 006 shells building the inside core without the full boundary zone (52 % of shells), **c** – 1 272 shells after extracting horizontal boundary layer (66 % of shells), and **d** – 1 525 shell after extracting radial boundary layer (79 % of shells).

around 165 121, were obtained for totally frictionless simulations (**Table 4.9**). Ignoring higher value of inter-granular friction coefficient, it is assumed that for $\mu_{shell} = 1$ a minimum density n_{min} is reached. Then, the relative number density can be determined as $n_r = (n - n_{min})/(n_{max} - n_{min})$ for any intermediate n. For $\mu_{shell} = 0.08$, the sample has quite dense packing with $n_r \approx 0.68$. The average coordination number found at $Z_n = 6.12$ in numerical samples is an adequate result to the experimentally determined $Z = 6.71$. Ignoring the value estimated experimentally (section **4.1**), $\mu_{shell} = 0.08$ was used for further sample preparations. Nevertheless, we would like to stress out that it is an empirical value employed in the preparation protocol. Once we proceeded to the simulations of mechanical behaviour under uniaxial compression, the experimental estimation had been used (**Table C.1** in **Appendix C**).

4.3.2 Numerical samples

Onwards, the cylindrical samples are denoted as: C_$(D \times H)$_(*aimed density*)_*i*_(*options*).
This manner describes a cylindrical sample (C) with a diameter D and height approximate to H_0 (both in cm). The friction coefficient was applied during deposit such that l – loose, d – relatively dense or D – dense sample was obtained. Repetition of deposits with the same input parameters resulted in different shell arrangement for configurations *i*. Any other changes – *options* – are underlined by additional notation employing capital letters such as shape of shell (A to F) or preferential orientation of shells (H, V). All the samples, discussed hereinafter, has been presented in details in **Appendix B**.

With established preparation procedure, a consecutive step was to assemble larger samples. New sample named C_35×12_d_01_A (see **Table B.1**), was generated (**Figure 4.21a**). As a consequence of depositing 1 926 bonded clusters, the height of assembly H_0 was stabilised at 12.2 cm. Higher number density was obtained in case of this larger volume using the same $\mu_{shell} = 0.08$. This indicates that the change of geometry, and therefore the boundary zone, has modified the relationship from **Figure 4.20** (see section **5.1.2**). Nevertheless, one can expect that the relative density n_r will remain of the same order, that is of around 0.68. Then, the sample is still distinguished as a dense packing with n equals 164 139 (m^{-3}) and two void ratios: $e^\star = 0.579$ (inter-

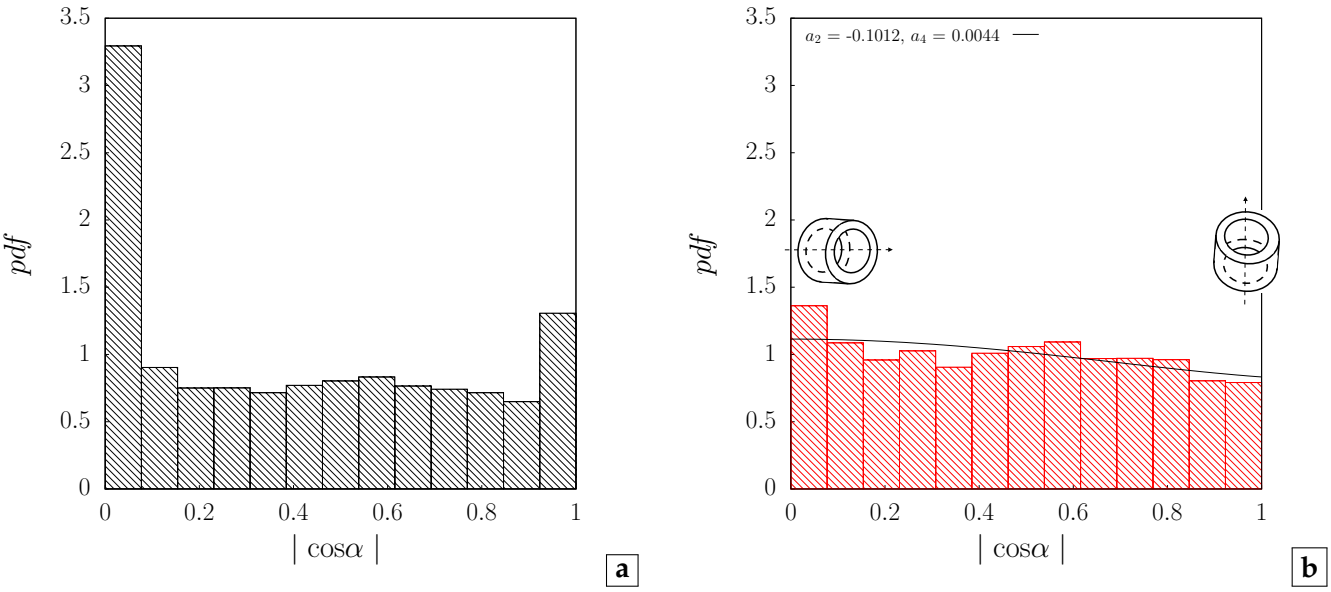

Figure 4.22 : Distribution of sectors orientation for the initial state of sample C_35×12_d_01_A. *Pdf* calculated using sample: **a** – of all the shells (see **Figure 4.21a**), and **b** – without layer at the boundary (see **Figure 4.21b**). Note that α measures inclination with respect to vertical axis such that $|\cos\alpha| = 0$ for horizontal shell and $|\cos\alpha| = 1$ for vertical shell. Solid line presents Legendre polynomial fit with low anisotropy coefficient a_2 (equation 4.7).

granular) and $e = 2.423$ (overall). Averagely, each shells has ~ 6.2 contacts with neighbouring shells. Such structured arrangement has been analysed for shells orientation using approach described in section 4.1.

Figure 4.22a shows the statistics of orientation to be compared with experimental results (**Figure 4.17**). *Pdf* has an overall trend shaped similarly to real samples but with one significant exception. The distribution in **Figure 4.22a** clearly shows that the horizontally orientated shells are dominant within whole assembly. Then, for $|\cos\alpha| \in \langle 0.1 : 0.9 \rangle$ (the range of intermediate orientations) the orientations seem to be more isotropically distributed. In contrast with experimental observations, a superior presence of vertically oriented shells is observed – lower peak marked at $|\cos\alpha| = 1$. The background of this heterogeneity was investigated numerically aiming the rigid boundaries effect as a cause. To this end, the statical analysis was repeated for the core of sample, *i.e.*, shells that do not remain in the neighbourhood of the walls (**Figure 4.21b**). The boundary zone is created throughout a geometrical criterion. Using an offset from wall equal to shell diameter d the boundary zone is determined, such that all the shells with at least one sector located inside the layer belong at the boundary. In this way a data set was limited to 52 % of shells which corresponds to 1 006 shells (or 12 072 sectors). **Figure 4.22b** confirms that the anisotropy exhibited by the two peaks for vertical and horizontal directions in the **Figure 4.22a** were triggered by the rigid boundary. This also shows that the walls have a short-length influence on the shell orientations. In the core of the sample there is no preferable orientation. Also the heterogeneity coefficient $a_2 = -0.101$ extracted from Legendre polynomials proved the low anisotropy level with slight tendency towards horizontal positions (negative value).

Another type of statistical representation is seen in the **Figure 4.23a**, which collates cumulative density function (*cdf*) for both experimental and numerical samples. Therefore, one can directly notice already discussed differences. Blue dots recall the real fabric, indicating the boundary effect in tunnel segment. Red point shows almost isotopic core of sample, while red continuous line presents the fit of equation (4.9). Black dots stand for numerical sample showing heterogenous fabric of full sample. The accumulations of hori-

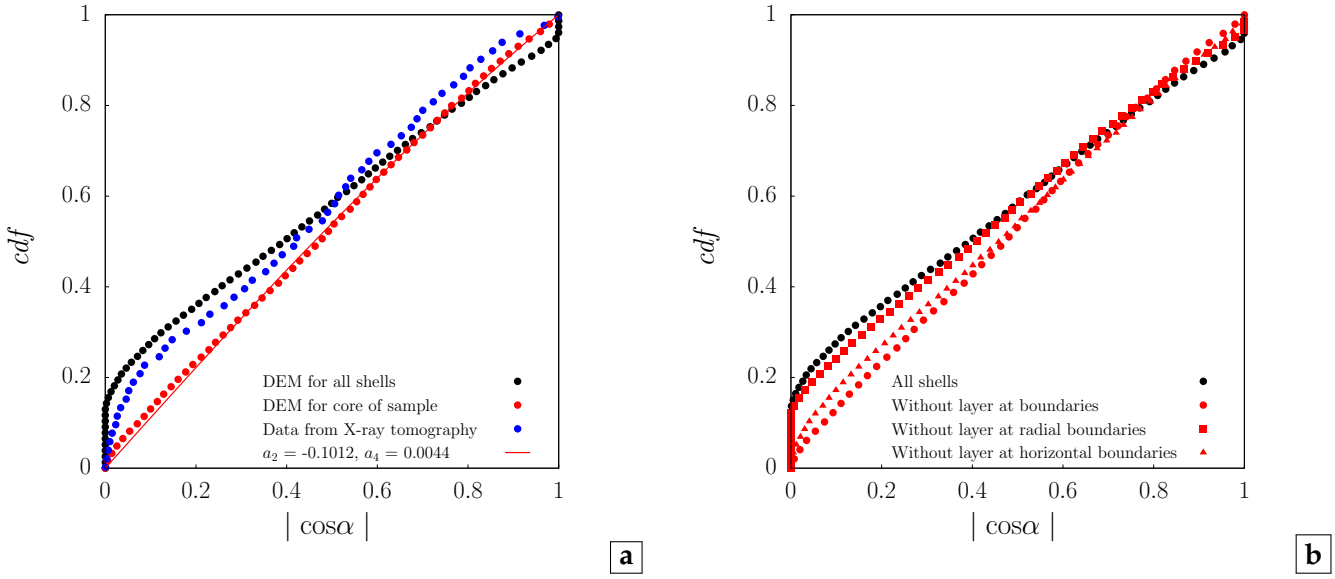

Figure 4.23 : Statistical analysis of shell orientation for large sample C_35×12_d_01_A. Numerical sample analysed for different ranges as shown in the **Figures 4.21**. **a** – comparison of numerical and experimental results. Legendre polynomials were adjusted to reflects the *cdf* and provide anisotropy level with a_2 (equation 4.9). **b** – The study of boundary effect and its origin.

zontal and vertical shells are exhibited by locally steep increases of *cdf*. This complex shape of numerical distribution cannot be properly reflected with the Legendre polynomials due to the steep extremes. Yet, it has been studied further and **Figure 4.23b** investigates the influence of shells localisation within the boundary zone on their orientations. To this end, the shells at the boundaries have been divided into two groups composed of the shells next to the:

- 1^{st} – horizontal plates at the top and bottom (▲),
- 2^{nd} – vertical circular wall (■).

Then, either first or second group was extracted from the assembly providing 1 272 and 1 525 shells for the statistical analysis, respectively. Note that the "corner" shells belong to both groups. In total, 48 % from 1 926 shells within the assembly are located at the boundary. 36 % is located in the neighbourhood of horizontal plates (**Figure 4.21c**), but only 21 % belong to radial boundary layer as seen in the **Figure 4.21d**. This is a reasonable division as it is influenced by the $D/H_0 = 2.87$. **Figure 4.23b** shows once more the statistics of orientation for entire sample (**Figure 4.21a**) by the black points. Red colour is reserved for the samples with limited number of shells. It is proven that the anisotropy of shell orientations is imposed by the flat horizontal plates for the sample size 35×12. The radial wall did not contribute to boundary effect, most possibly, due to the curvature of wall. This results will diverge with significant change of D/H_0 for different sample sizes.

Method to impose the orientations

Up to now, for each sample the arrangement of the shells was an outcome of gravitational fall with no control over the grain orientation. Despite the homogenous core of the sample, the preferential orientations were detected within fabric. Thus, it is interesting to investigate the behaviour of highly heterogeneous arrangements. To this end, the preparation protocol of numerical assemblies was enhanced. **Figure 4.24a** presents the concept of redirecting the orientation of shell during the deposit to preferred direction. In XYZ coordinate system, an unit vector $\vec{o_0}$ is an exemplary orientation vector randomly assigned to shell at the beginning of the deposit. To impose selected direction marked by vector $\vec{o}_{pref}$ an additional rotational moment M_{max} acts on each shell. Note that the frequent collisions between the shells might counteract the movement towards the preferential orientation. The higher the rotational moment, the faster the extorted shell rotation in time. Therefore, the magnitude of M_{max} must have been adjusted not only because of the time of downfall but also due to the occurring collisions. Then, it is clear that the final distribution is still not fully controlled.

Varying the angular moment M_{max} (**Table 4.10**), 5 new samples were assembled aiming either strongly vertical (V) or strongly horizontal (H) orientation of shells (**Figure 4.25**). For all those samples, the preparation process started from the same initial configuration suspended in air. The sample size has been reduced to 25×13 cm such that assembly was composed of 1 047 shells. The reason for this size limitation is dis-

Sample	M_{max} (kg m^2)	n (m^{-3})	$e^\star$	e	Z_n
C_25×13_d_01_AV	0.0001	160 452	0.651	2.502	6.07
C_25×13_d_02_AV	0.0002	161 602	0.604	2.477	6.01
C_25×13_d_03_AV	0.0005	156 488	0.656	2.590	5.40
C_25×13_d_01_AH	0.0001	161 324	0.606	2.483	6.21
C_25×13_d_02_AH	0.0005	159 707	0.623	2.518	6.19

Table 4.10 : Description of samples with imposed orientation characterised by number density n, standard e as well as modified $e^\star$ void rations and coordination number Z_n. The higher was M_{max}, the stronger was the anisotropy of shells orientation towards preferential orientation. The preferential orientation can be V for vertical or H for horizontal.

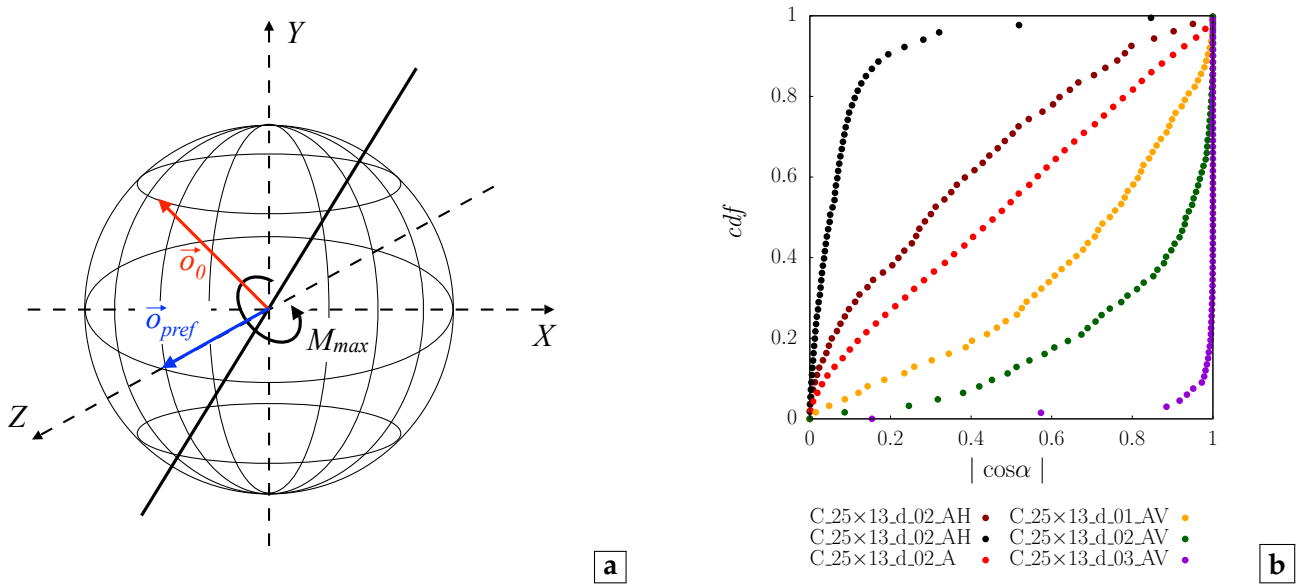

Figure 4.24 : a – The concept of redirecting the initial $\vec{o_0}$ orientation of shell. An angular moment M_{max} rotates the shells towards the desired direction $\vec{o_{pref}}$. **b** – Distribution of shell directions within preferentially oriented assemblies: vertically (V) or horizontally (H). Different rotational moment were applied with order of magnitude 10^{-4} (**Table 4.10**). The isotropic state with randomly oriented shells C_25×13_d_02_A , obtained for zero angular moment, is presented in red.

cussed thereafter. More detailed description of the samples can be found in **Table B.1** (see **Appendix B**), yet their state is briefly summarised in **Table 4.10**. As suggested, with increase of M_{max} the assembly tends to be looser. The coordination number varied slightly with density but always remained close to the experimental observation ($Z = 6.71$). **Figure 4.25** clearly shows that in the horizontal (XZ) plane the distribution of shell orientations is not axially symmetric, which contradicts the assumptions of the statistical framework proposed hereinbefore (see **Figures 4.16**). Recall that the mechanical response of the shell is material oriented due to the shell geometry. Then, the vertical and horizontal orientation with respect to Y can balance the consequences of such XZ anisotropy in the sample under oedometric compression. Thus, the statistical analysis has been carried out focusing on the inclination with respect to vertical axis α despite the inconsistency in the XZ distribution. The anisotropic fabric is statistically characterised by cumulative density functions shown in the **Figure 4.24b**. They are compared with randomly oriented sample C_25×13_d_02_A for which angular moment was not imposed ($M_{max} = 0$). Note that presented *cdf* was calculated ignoring shells located within the layers at horizontal boundaries such that one can directly observe strong deviation from the almost isotropic state (red points).

4.4 Summary

This section discussed the experimental and numerical preparation of the samples. First, the shells with and without coating were the subject of different experimental measurements. They were (*i*) the reference parameters targeted in numerical assemblies and (*ii*) supplementary numerical parameters or estimation of parameters for the DEM model.

- First measurements done at the prefabrication plant *Stradal* allowed to determined "natural" density, its maximum limit and coordination number.
- Sample extracted from tunnel segment were scanned using X-ray CT. A special image analysis tool was created to detect shell including their spatial orientation. Afterwards

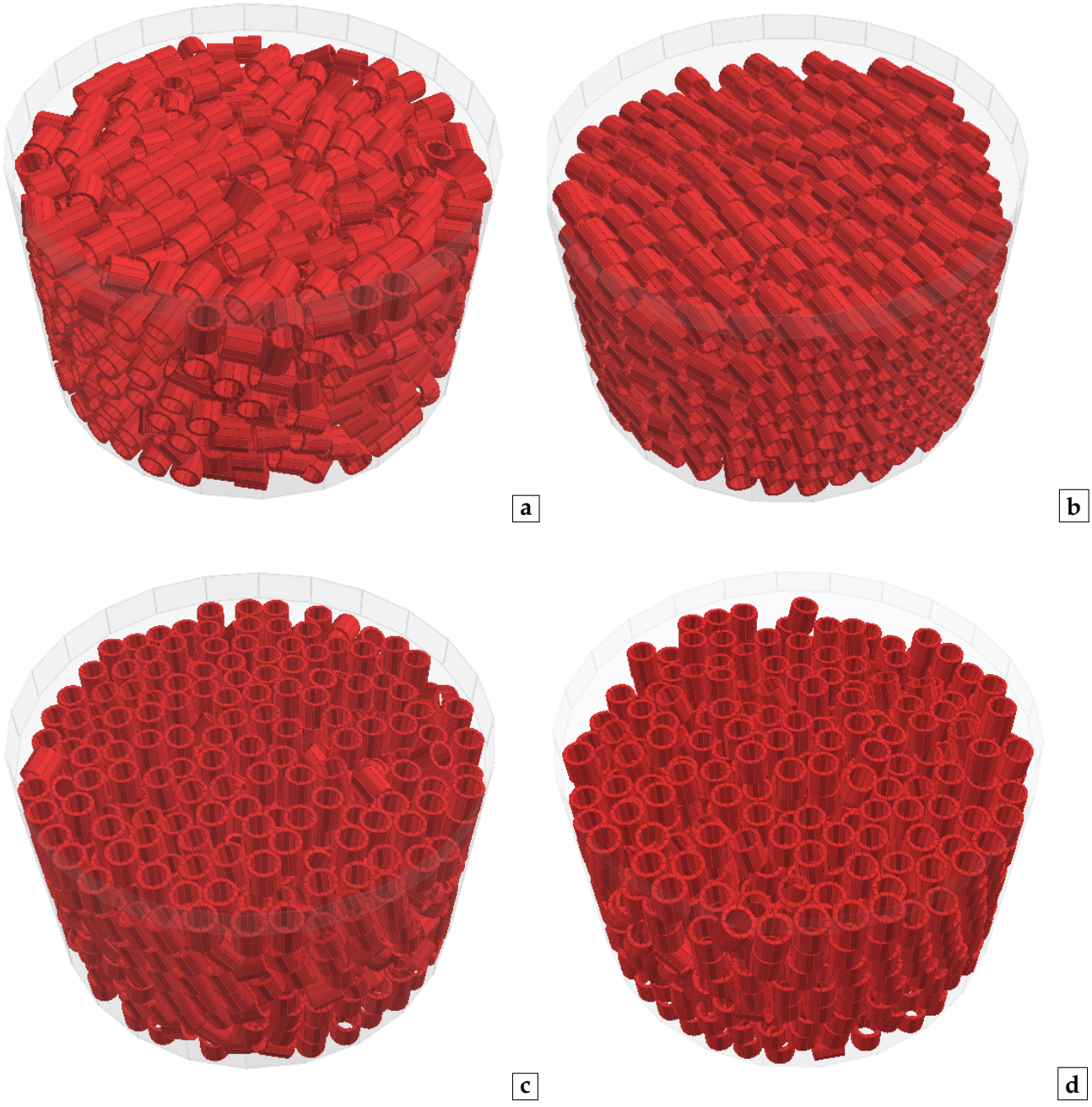

Figure 4.25 : View of samples in size 25×13 with preferential orientation (**Figure 4.24b**). The samples with horizontal shell anisotropy: **a** – C_25×13_d_01_AH, and **b** – C_25×13_d_03_AH. The samples with vertical shell anisotropy: **c** – C_25×13_d_023_AV, and **d** – C_25×13_d_03_AV. The sample states were described in **Table 4.10**.

the statistical analysis provided insight into the anisotropy of fabric using framework of Legendre polynomials.

- The level of cemented joints strength was estimated for pairs of shells extracted from coated sample (prepared at *Stradal*). The distribution of minimum strength was verified as Weibullian. Those results will be useful in the adjustment of numerical parameters in the DEM model.
- The surface angle of friction was found at low level. This estimation provides us another input parameter required by DEM model.

Then, various numerical samples were prepared to reflect true samples fabric as accurately as possible:

- The numerical protocol was established including two phases: gravity deposit and numerical relaxation.
- Parametric study were performed allowing to characterise an influence of inter-granular friction on the number density of assembly. The study were performed on sample size matching the experimental measurements. Thanks to this study, the inter-granular friction coefficient μ_{shell} was selected to generate a representative numerical sample.
- The larger samples were assembled aiming the 1D compression. A comparison with the real samples was done taking into account: the number density, the coordination number and the statistics of shells orientation.
- The boundary effect was probed, such that we have found almost isotropic core of the sample. The horizontal rigid plates caused the orientation anisotropy at the boundary.
- Finally, the preparation protocol was slightly modified in order to build strongly anisotropic assemblies with preferential orientations of shells. The cumulative density function showed that it has been successfully used to modify the fabric of numerical samples.

Shell assemblies under uniaxial loadings

Contents

Introduction

Chapter 4 finished with the preparation of representative assemblies, ready to be submitted to a uniaxial loading, but estimations of few parameters have been provided in the process. Probably the most fruitful experimental contribution can be found in chapter 3 (section 3.3.1) showing the assessment of tensile strength and its variability.

At that point, there remained nothing else to do but to probe those parameters in the simulation of oedometer test. In section 5.1.1, the first attempt has been shown and discussed. We have juxtaposed the primary numerical response *versus* the experimental result, and there was still room for improvement. Prior to the comprehensive analysis, model calibration was required to secure the results.

Firstly, section 5.1.2 presents the sample size independence addressing mechanical behaviour. The analysis acknowledged the boundary effect exhibited by the shells orientations. "Size independence" has been reported also experimentally (tests on the different initial height of samples), but numerically one can gain from possible size reduction by limiting the computational costs.

The understanding of numerical macroscopic curves are, in fact, the understanding of parameter roles and the assessment of their importance. Thus, the parametric study continues in this direction. By many, breakage has been reported of great importance to compressible behaviour (Coop and Altuhafi, 2011; McDowell et al., 1996). Section 5.1.3 focuses on the numerical parameters involved in the classic plastic law in the contact without the cohesion (μ), the link elasticity (k_I, k_{II}) and its breakage criterion ($f_I^\star$, $f_{II}^\star$ and q). Such that one can understand the influence of the external contact forces applied on shells, transmitted to links, and eventually lead to breakage, respectively.

Section 5.1.4 comments the influence of the initial state of samples. By initial state, we refer to the density of packing, expressed by the number of shell per unit volume (n), and the statistical distribution of shell orientations with a specific degree of anisotropy. The experimentally determined density was either increased or decreased. Similarly, the shell orientations were directed towards either horizontally or vertically oriented anisotropy.

This study needs to rise to the challenge of the complex shape. On one hand, we already deal with the tube-shaped shell. On the other hand, the model bears the burden of highly sophisticated discretisation – complex structure/shape of the sector. The ability to break is crucial, and therefore, the size of the sector needs to be small enough for the sake of representative breakage, but large enough to reduce the computation time. To this end, in section 5.1.5, firstly we test the influence of the number of sectors used to discretise a shell. Note that we only varied the number of sectors per shell. Then, section 5.1.5 presents the variations around the thickness of shell t. This closes this partial parametric study.

The understanding of parameter roles helped us establish their final set. Once more, the best numerical curve was compared with the experiment in section 5.1.6. The simulations of unloading and reloading (UR) cycles were followed by a comprehensive analysis of interactions evolution. Finally, we reproduced numerically the experimental difference in the compression curves between shell size: *d18* and *d20*. This part served the purpose of reliable reproduction of the samples numerically.

List of symbols and abbreviations

Symbol / Abbreviation	Explanation
Sections from **5.1.1** to **5.1.5**	
cdf	Cumulative Density Function
pdf	Probability Density Function
α	Inclination of sample strong axis with respect to vertical axis (°)
ε_a	Axial strain of a cylindrical sample (%)
κ	Dimensionless stiffness parameter
μ_{shell}	Friction coefficient of a shell-shell contact
μ_{wall}	Friction coefficient between the shell and rigid boundary
σ_0	A typical macroscopic stress (MPa)
σ_a	Axial stress in case of a cylindrical sample (MPa)
ν	Poisson ratio
a	Typical size of particle (m)
b	Primary breakage level
D	Diameter of a cylindrical sample (m)
$d18, d20$	Fabricated sizes of shells distinguished by a target diameter $d \sim 18$ mm and d$\sim$ 20 mm
E	Young modulus (GPa)
E_{oedo}	Oedometer modulus (MPa)
e	Total void ratio
e_0	Initial void ratio
F_I	The ultimate force in the uniaxial radial compression (N)
$f_I^\star$	Normal yield threshold in pure tension (N)
$f_{II}^\star$	Tangential yield threshold in pure share (N)
H	Height of a cylindrical sample (m)
H_0	Initial height of a cylindrical sample (m)
I	Inertial number
I_{ij}	Breakable interface
$\sum I_{ij}$	Current number of breakable interfaces in the cluster
$(\sum I_{ij})_0$	Initial number of breakable interfaces in the cluster
K_c	Kinetic energy per cluster (J)
k_I	Normal contact stiffness in the cohesive contact – link (N/m)
k_{II}	Tangential contact stiffness in the cohesive contact – link (N/m)
k_n	Normal contact stiffness in the contact (N/m)
k_t	Tangential contact stiffness in the contact (N/m)
m	*Weibull's* modulus / shape parameter of Weibull distribution
n	Number density (m^{-3})
N	Total number
N_{config}	Number of deposits in specific sample size
$N^\star$	Number of sectors per cluster
$N_{circ}^\star$	Number of sectors in axial the direction per cluster – along height of shell h
$N_{axial}^\star$	Number of sectors in the radial plane (ring) per cluster
N_{broken}	Number of broken broken cluster (at least one link broken)

Continued on next page...

Symbol / Abbreviation	Explanation
N_μ	Number of non-cohesive contacts in the sample
t	Shell thickness (mm)
q	Shape parameter of the yield surface
V_s	Volume of solid phase in the assembly (m^3)
V_{tot}	Total volume of sample (m^3)
V_v	Volume of voids and pores in a sample (m^3)
v_{load}	Velocity of the loading plate (m/s)
x_0	Scale parameter of Weibull distribution
Z_n	Coordination number of neighbours
Section **5.1.6**	
UR	Unloading–Reloading cycle
f_n^0, f_t^0	Normal and tangential components of contact force before unloading (N)
f_n^{unload}	Normal component of contact force after unloading (N)
$f_t^{unload-el}$	Tangential component of contact force after elastic unloading, without sliding (N)
$f_t^{unload-pl}$	Tangential component of contact force after plastic unloading, sliding (N)
M_{oed+}, M_{oed-}	Oedometric modulus during reloading and unloading, respectively (MPa)
M'_{oed}, M''_{oed}	Oedometric modulus at the beginning and at the end of the uniaxial compression, respectively (MPa)
$N_{\mu-max}$	Number of sliding contacts per sample
Z_c	Coordination number of contact pints
Z_n	Coordination number of neighbours

If a symbol or an abbreviations is not distinguished in the current section, please search in the previous sections.

5.1 Oedometer tests on the cohesion-less shells

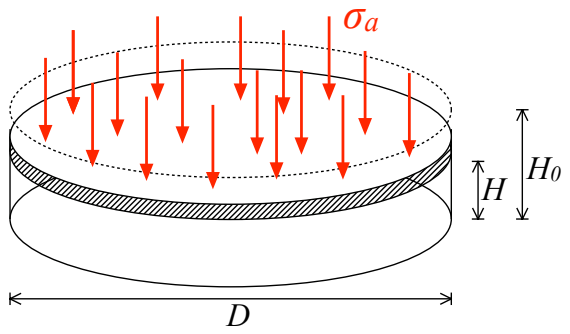

Figure 5.1 : Oedometer test is a one-dimensional compression providing the plain strain conditions in the remaining directions. Classically, the cylindrical sample loaded by an axial stress σ_a experiences a reduction of the initial height H_0 to a current value H.

Soil compressibility refers to its capability to decrease its volume while being subjected to a compression loading. In the laboratory conditions, the soil compressibility is observed with a one-dimensional compression test, commonly known as an oedometer compression test. **Figure 5.1** gives a sketch of the oedometer test on a cylindrical sample submitted to an axial loading σ_a [1]. This test provides an axial symmetry by using a sample formed as a cylinder. Therefore, one can distinguish an axial direction following the height of the sample H and the radial directions in the circular cross-section with a diameter D. The boundary conditions prevent any radial deformation (D = constant) and as a consequence the volumetric changes are ruled by the axial strain ε_a. In case of highly compressible soils, for which large strains are expected, the true strain is defined as suggested by Hencky (1928) but with a soil mechanics convention, *i.e.*, $\varepsilon_a > 0$ for compression:

$$\varepsilon_a = -\int_{H_0}^{H} \frac{\delta h}{h} = \ln\left(\frac{H_0}{H}\right), \tag{5.1}$$

where $H_0 > H$.

The compressibility of soil derives from grain rearrangements and thus from the filling of free space, *i.e.*, voids. In soils mechanics, it is common to quantify voids with a parameter called the void ratio e. Considering the total volume V_{tot} and the volume of solid phase V_s, the classical definition of e is the ratio of void (V_v) and solid volumes:

$$e = \frac{V_v}{V_s} = \frac{(V_{tot} - V_s)}{V_s}. \tag{5.2}$$

In the case of crushable shells, a decrease of e originates not only from the rearrangements of constituents but also from the shell breakage. Despite the fact that the overlaps between two clusters exist in DEM, the concept does not apply to the experiments. Thus, the overlaps are always ignored in the calculations of the void ratio.

5.1.1 DEM–Experiment comparison: a first attempt

Experimental oedometer tests

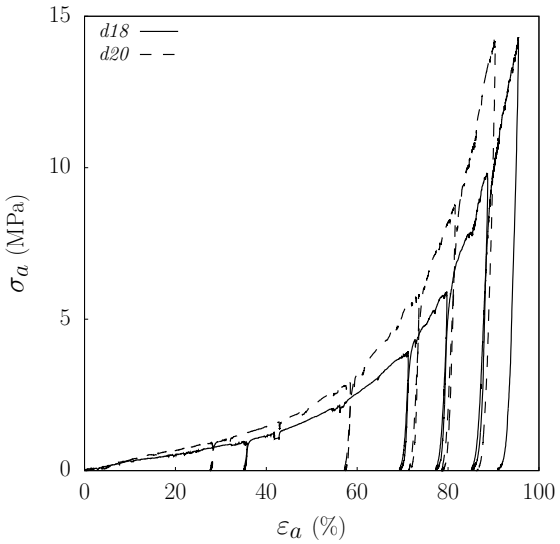

Figure 5.2 : The experimental oedometer tests. The mechanical responses of samples made of shells $d18$ and $d20$. The quasi-vertical lines correspond to the unload-reload cycles. With the courtesy of *Euro-Géomat-Consulting EGC* (Ly, 2018).

An experimental campaign was performed by *Euro-Géomat-Consulting EGC* in Orléans. The oedometer tests were performed on the samples composed of the shells in the sizes $d18$ and $d20$,

[1] On the contrary to the sample preparation, friction between the walls and the sample is present in further DEM modelling as it is in the reality.

separately. The cylindrical samples had the following characteristics: a diameter $D = 35$ cm and an initial height $H_0 \approx 13$ cm. The tests were conducted with a stress-control of σ_a. During the loading, the piston displacement was measured to obtain the evolution of the axial strain ε_a. The typical mechanical responses ($\sigma_a \leftrightarrow \varepsilon_a$) for sizes *d18* and *d20* are shown in the **Figure 5.2**.

On one hand, the observed mechanical responses have some classical features, the oedometer modulus E_{oedo} increases with the increase of σ_a, even if E_{oedo} is almost constant for $\varepsilon_a < 40\%$. On the other hand, the final true strain can be very large, reaching around 100 %. Note that, according to the natural strain formula, 100 % corresponds to a hight reduction close to $2/3^{rd}$ of H_0 ($H_0/H \simeq 3$). This is one of the main characteristics of this granular material: its capability to undergo a huge volume change. The two tests shown in **Figure 5.2** are performed on two different samples: one is made of $d18$ shells and the second one is made of $d20$ shells. It is then observed that for the same stress level, the sample made of shells $d18$ shows a larger vertical strain, just like its strength was weaker than for the other sample. This observation can be explained by the fact that the shells $d18$ break for $F_I = 121$ N, whereas the shells $d20$ break for $F_I = 167$ N, as shown in the **Chapter 3** section **3.3.1**. At the scale of the gain, the grains break with the increase of the loading. As an example, **Figures 5.3a** and **5.3b** are the snapshots of broken shells for a small strain and for a large strain, respectively. Our objective is now to see whether this experimental mechanical behaviour can be reproduced by means of DEM.

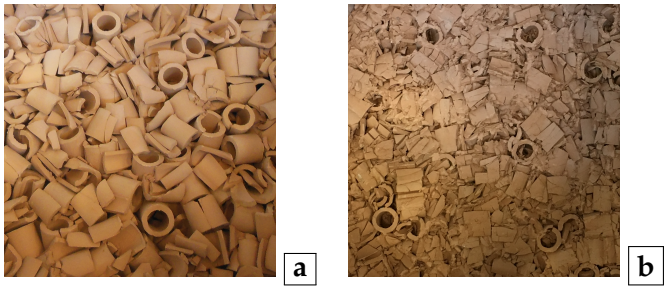

Figure 5.3 : A snapshot of broken shells in the top part of the oedometer cell for: **a** – $\sigma_a \simeq 0.4$ MPa and **b** – $\sigma_a \simeq 6.8$ MPa.

[2] $a = 0.02$ m for the shells

A first attempt of DEM modelling of an oedometer compression

A sample was generated with the dimensions respecting the experimental ones, *i.e.*, $D = 35.0$ cm and $H_0 = 12.2$ cm, as mentioned in the section **4.3.1**. **Figure 5.4a** shows an assembly of shells prior to the test, represented by 1 926 numerical clusters (breakable shells). Each shell is composed of 12 sectors that are rigid clumps of 26 sub-elements, which give 23 112 sectors and 600 912 sub-elements in this sample. **Figure 5.4b** presents the sample state after the oedometric compression, when all the shells were crushed due to a high stress level as σ_a reached 18.2 MPa – simulation Oedo_first (**Appendix C**).

As seen in the section **3.1**, the particles interact with each other through the contact points. At each contact point, a normal elastic compressive force and an incremental tangential force (with a *Coulomb* threshold) are computed, Cundall and Strack (1979); Radjaï and Dubois (2011). Both contact laws need stiffnesses here denoted k_n and k_t. The normal stiffness k_n was estimated using the dimensionless stiffness parameter κ suggested by Roux & Chevoir, *e.g.* in Radjaï and Dubois (2011). Assuming an elastic normal contact law,

$$\kappa = k_n/(a\sigma_0), \tag{5.3}$$

where a is the typical size of the particles[2] and σ_0 is the typical stress applied on the granular matter. For Hertzian contact laws, κ can be express with the young modulus E and the Poisson coefficient ν of the matter:

$$\kappa = \left[\frac{E}{(1-\nu^2)\sigma_0}\right]^{2/3}. \tag{5.4}$$

For COx, $E = 4$ GPa and $\nu = 0.29$. With $\sigma_0 = 1$ MPa, it can be shown that $\kappa \simeq 267$. Thus, assuming the elastic contact law (in the normal direction), one can obtain $k_n = 5.2\ 10^6$ N/m, which is observed to be of the same order as the value obtained for k_I. Whereas it is commonly admitted that $k_t = k_n$ is a good approximation, for sake of simplicity, we arbitrarily used uniform stiffness coefficients: $k_n = k_t = k_I = k_{II}$. The other parame-

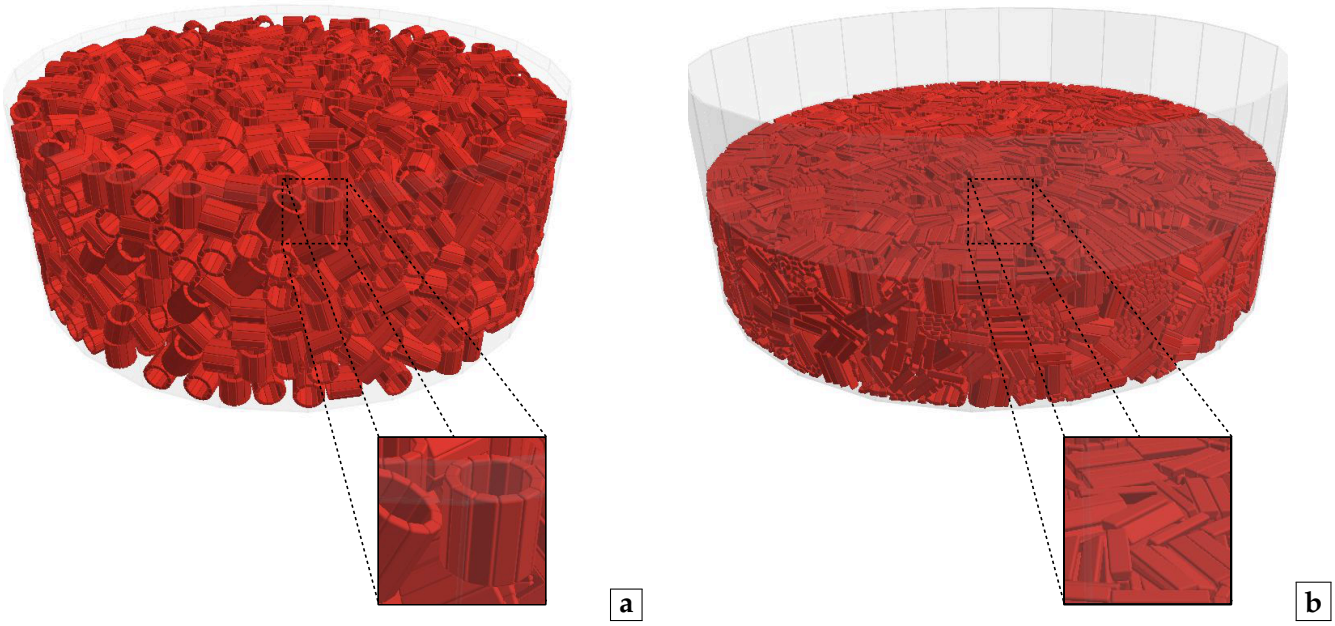

Figure 5.4 : Cylindrical sample (C_35×13_d_01_A) with a diameter 35.0 cm and a height 12.2 cm composed of 1 924 shells of size *d18*. Each cluster consists of 12 sectors such that the total number of particles equals to 23 112. **a** – The sample before the oedometric compression and **b** – the sample at the end of test for $\varepsilon_a = 60$ % and $\sigma_a = 18.2$ MPa.

ters were estimated using either the experimental tests ($f_I^\star$ and μ_{shell}) or the numerical simulations like $f_{II}^\star$ (section **3.3.2**). This simulation was performed with a primary estimation of parameters shown in **Table 5.1**[3].

Links		Elastic contacts	
k_I	5.5 10^6 N/m	k_n	5.5 10^6 N/m
k_{II}	5.5 10^6 N/m	k_t	5.5 10^6 N/m
$f_I^\star$	85 N	μ_{shell}	0.36
$f_{II}^\star$	50 N	μ_{wall}	0.15
q	2		

Table 5.1 : The parameters used in the primary modelling – Oedo_first (see **Figure 5.6**). Whereas, I and n represent normal direction of the links and the contacts, respectively, II and t indicate tangential direction (more details in sections **3.3.1** and **3.2**).

Two types of friction coefficients are distinguished: when two shells interact μ_{shell} and when the shell is in contact with rigid boundary μ_{wall}. The friction coefficient μ_{shell} was estimated experimentally as shown in the section **4.1**, yet the range of friction was measured for the "smooth" surface, *i.e.* curved extrados. The values of μ_{wall} was chosen arbitrarily yet respecting the numerical sensitivity and a sense of physics.

Whereas experimentally, the tests were stress-controlled, the majority of DEM simulations were strain-controlled. However, using either strain- or stress-control the equivalent mechanical behaviours were obtained under the quasi-static conditions. The strain-controlled test was achieved by imposing a constant velocity for the upper plate v_{load}, *e.g.*, in our modelling $v_{load} = 0.05$ *m/s*. This velocity was chosen such that the quasi-static conditions can be assumed. One way to verify it is to compute the inertial number I:

$$I = \frac{v_{load}}{H_0}\sqrt{\frac{m}{\sigma_a d}}, \tag{5.5}$$

where d is the outer diameter of the shell considered as the typical size kept constant. σ_a starts from 0 and reaches large value at the end of the compression test. Thus, I quickly decreased from 0.937 10^{-3} and was reduced to 0.440 10^{-4} by the end of test. Note that a quasi-static critical state regime corresponds to $I \leq 10^{-3}$ as reported by Cruz et al. (2005). In this case the analysis of the

[3] More details can be found in **Appendix C** (**Tables C.1** and **C.2**)

inertial number gives a very generic sense of the kinematics but, additionally, in **Figure 5.5** an evolution of the average kinetic energy K_c (computed over all the shells) along the simulation shows a decreasing trend. K_c clearly declines initially, when the breakage has not yet occurred, and finally, when most of the shells were already broken. In between the onset of breakage and the landmark at which around half of the shells have been broken, the energy oscillated randomly yet in a constant range. In other words, the breakage is highly dynamic and constantly adds to K_c. Though, the average kinetic energy always remains of small order, especially in the final phase when K_c tended towards 10^{-6}.
Many other numerical parameters can be discussed: damp coefficient, time step, period of update of the neighbourhood list, *etc.* It is here proposed not to present all the work that led us to their optimums. Nevertheless, the reader must know that these parameters were chosen carefully to obtain optimal computation time and numerical stability for the simulations.

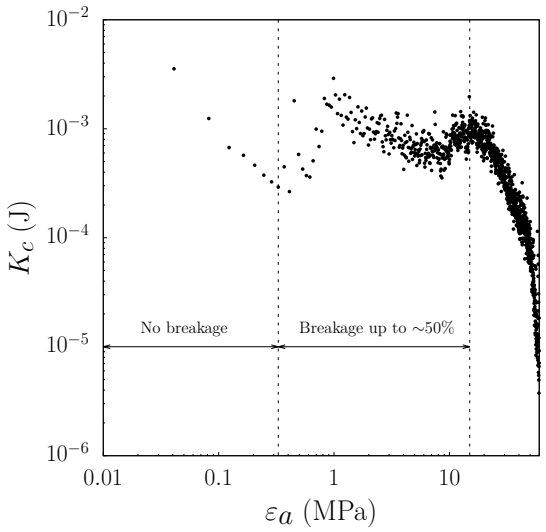

Figure 5.5 : An evolution of the kinetic energy per cluster with respect to the axial strain during the oedometric compression.

Figure 5.6 presents the mechanical response to an oedometric loading of both experimental and numerical samples. Even if the mechanical behaviour obtained numerically shows the same features as the experiment, there remain noticeable differences between the experiment and the modelling. The main one is the capability of the model to reach as large ε_a as the experimental one. This can be easily explained by the observation of the shells at the end of the compression test (**Figure 5.3b**). Whereas experimentally, shells are transformed into powder, numerically, shells can only break into 12 segments that can not fill the space as efficiently as the powder (**Figure 5.4b**). Unable to produce as small particles as the experimental ones, the numerical model limits the macroscopic strain range.

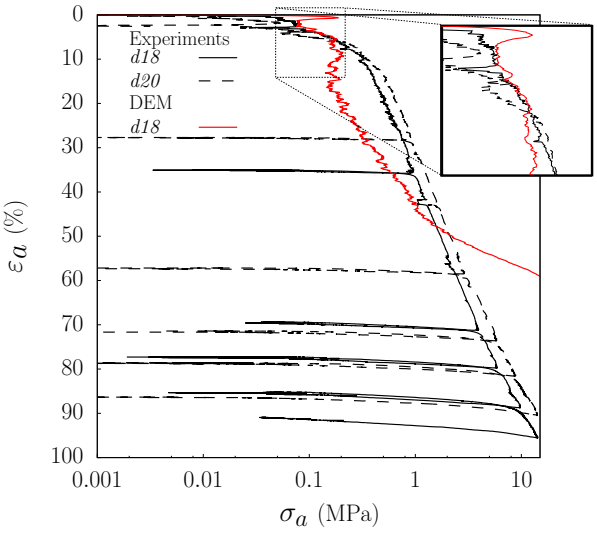

Figure 5.6 : The mechanical responses to one-dimensional compression. A comparison between the experimental results (black lines) and a numerical simulation (red line). The experimental tests were carried out on two sizes of the shells (section 3.3.1), while the modelling was performed for sample shown in the **Figure 5.4** (*d18*).

Considering the stress evolution, another discrepancy between model and experiment should be pointed out. One must notice a slight initially peak followed by a softening due to which the curves converge (inset of **Figure 5.6**). This can be the result of the initial numerical density combined with the idealised geometry and the lack of plastic deformations in the model. The curves diverged once more in the phase of isotropic hardening when the compression curves evolve linearly in semi-logarithmic scale.The numerical curve exhibits softer "hardening", *i.e.*, the stresses arise

slower, with many fluctuations. It can be seen as a consequence of breakage, that was accompanied by the intense release of energy, but it still remains an open issue to be investigated, hereinafter. Despite the limitation, the same character of the stress-strain curve was obtained both numerically and experimentally. The macroscopic behaviour is ruled by grain breakage that enables high densification of the sample. More elaborated explanation can be also found in **Chapter 6** in section **6.1** dedicated to the influence of shells breakage.

To sum up, a primary DEM simulation of oedometric compression was performed on sample of real size, with the same number of shells as experimentally.

- Previously, the validation of a single shell model has been proceeded for its uniaxial radial compression (section **3.3.2**). Enlarging the number of shells in the simulation of odometer test not only employs new numerical parameters such as a friction coefficient, but also some of already tested parameters might be of a greater importance within an assembly. For example, the contribution of the tangential contact force was minor in the validation, whereas more complex loading conditions can activate higher shearing within cluster. Then, the tangential force threshold $f_{II}^{\star}$ and shape parameter q might gain the importance and significantly influence the mechanical response of sample.

- Using a large sample composed of approximately 2 000 shells respects experimental condition and provided a sufficient number of particles in the modelling, but a high number of sectors made the computations highly time consuming.

Many ideas can be considered to enhance the numerical modelling such that it fits better the experiments. One of them is to investigate the influences of micro-mechanical parameters that were not directly assessed experimentally (*e.g.*, $f_{II}^{\star}$, and many others). This is the topic of the following section.

5.1.2 Sample size dependency

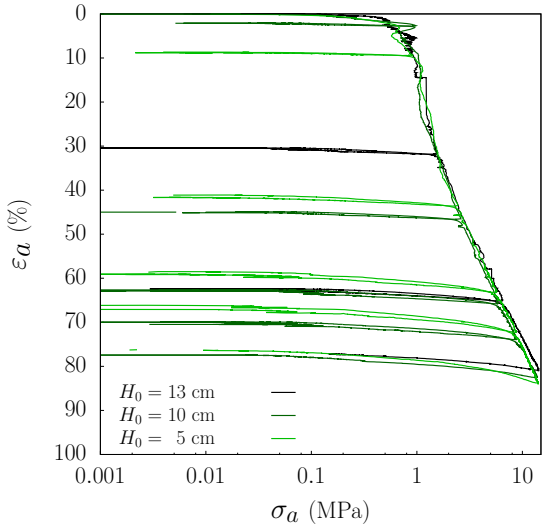

Figure 5.7 : The experimental macroscopic response does not depend on the initial height of the sample. The experimental campaign of the oedometer tests made on the shells *d18* with the cement coating. Data from *Euro-Géomat-Consulting EGC* (Ly, 2018).

The fact that the mechanical response of assemblies of shells does not depend on the initial high H_0 of the sample is an important result observed experimentally (Ly and Robinet, 2017; Ly, 2018). This can be observed in the **Figure 5.7**. Hence, a similar study was carried out by means of DEM. There are a few reasons for this. First, this important experimental feature that ensure that the mechanical test are not size dependent must be numerically reproduced. Secondly, it is an interesting alternative to reduce the computation time[4]. The reduction of sample size corresponds to a decrease of the shell number, and therefore, it leads to a reduction of the computation time. The goal was also to (*i*) identify the smallest sizes usable in a simulation, and (*ii*) to probe the boundary effects on the macroscopic response.

Herein, DEM simulations of oedometric tests were performed for samples with different sizes, varying either the diameter or the height of the sample. Six different sizes of the sample (referred

[4] 1 month on 8 cores for ∼2 000 shells

Sample	H_0 (cm)	N_{config}	N	$NN^\star$	n (1/m^3)	e_0	Z_n
C_35×12_d_01_A	12.20	6	1 926	23 112	163 582 ± 751	2.435 ± 0.160	6.25 ± 0.05
C_35×10_d_01_A	10.09	6	1 579	18 948	162 266 ± 469	2.463 ± 0.010	6.18 ± 0.05
C_35×7_d_01_A	7.34	6	1 105	13 260	157 885 ± 954	2.559 ± 0.022	5.99 ± 0.04
C_35×5_d_01_A	5.10	10	790	9 480	161 061 ± 212	2.488 ± 0.005	5.89 ± 0.09
C_25×13_d_01_A	13.08	7	1 047	12 564	162 499 ± 1 088	2.458 ± 0.023	6.18 ± 0.03
C_25×13_d_01_A	13.45	20	203	2 436	155 669 ± 1 846	2.610 ± 0.043	5.86 ± 0.15

Table 5.2 : The initial state of samples described for different size of sample $D \times H_0$: a number density n, an initial standard (total) void ratio e_0 (as defined in equation 5.2) and a coordination number of neighbours Z_n. Note that $NN^\star$ indicates a total number of sectors in the sample.

to as their sizes: diameter $D\times$ initial height H_0) were tested. The number of clusters ranged from 203 to 1 926. In the table 5.2, the sample characteristics are presented by three chosen internal variables averaged over a number of samples in a given size: a number density n, an initial standard void ratio e_0 and a coordination number Z_n[5].

One can observe that although all the samples were prepared with the same protocol, their density depends on their sizes. Note that in this study the decrease of density is connected to the decrease of coordination number. The smaller the size, the loser is the packing. This observation can be related to a very common rigid boundary effect. This phenomenon was already studied for the biggest sample size 35 × 12. On the other side, the stronger influence of boundaries for the reduced sizes is expected, as a natural consequence of isotropic sample core getting relatively smaller with respect to the boundary zone. The distinction between boundary zone and the sample core was given in section **4.3.2**. For all the sample size, the distribution of shell orientations has provided a better insight into the influence of boundaries on the parameters in **Table 5.2**. **Figure 5.8** shows the statistical analysis following the procedure already introduced in the section **4.3.1**. One must keep in mind that if the distribution of orientations is isotropic, then the *cdf* is a linear function of $|\cos\alpha|$ with a slope of 1. For all the samples, one can observe in **Figures 5.8a** and **5.8b** a dominancy of horizontal shells (quick increase of the *cdf* from 0 to 0.15 for $|\cos\alpha| = 0$). A similar but less pronounced effect can be noticed for vertical shells (vertical increase of the *cdf* from 0.9 to 1 for

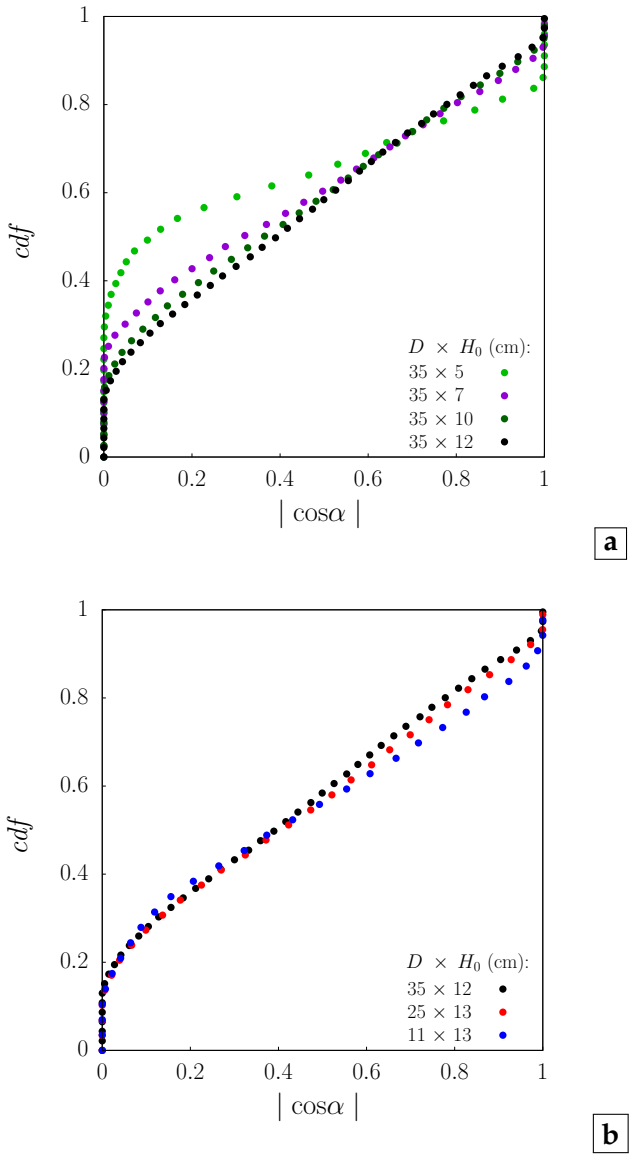

Figure 5.8 : The statistical analysis of the shells orientations separated for samples with various: **a** – the initial height H_0 or **b** – the diameter D. For vertical shell $|\cos\alpha| = 1$ and for horizontal shell $|\cos\alpha| = 0$.

[5] The coordination number is computed from all grains, including the rattlers

$|\cos\alpha| = 1$). The linear increase in between these two limit indicates the isotropy of the sample core. When samples is not high enough ($H_0 < 7$ cm), the shells are mainly anisotropically oriented with respect to the vertical axis (**Figures 5.8a**). In **Figure 5.8b**, one can observe the statistics of shells orientation when the sample diameter is reduced. Similarly, when the sample became significantly thin, the anisotropy of shell orientation increased, and it was more probable to have horizontal or vertical shells. The boundaries affect mainly the zones located close to the horizontal plates (section 4.3.1), and therefore, the reduction of H_0 had a stronger impact.

In **Figure 5.8b** one can observe that only size 11×13 diverge in the region of vertical shells (for $|\cos\alpha| > 0.6$). Similarly, the reduction of the height by half does not affect the distribution significantly. Firstly, the horizontal anisotropy was deepened as seen in the distribution of sample with $H_0 \approx 7$ cm. Then, **Figure 5.8a** exposes that smallest size 35×5 experienced the strongest boundary effect. Due to the large area of plate and the small height, the zone at the boundaries outbalanced the isotropic core consisting of only 16% of shells in the assembly (35×5).

Figure 5.9 shows the stress-strain relationship for different sample sizes submitted to the oedometeric compression. Even if the range of axial strain varies slightly, no tendency concerning the size of the sample is observed. The differences in mechanical response are mainly related to the initial arrangement of the shells. The mechanical behaviours follow common tendency, but the smaller the number of shells the more fluctuations from the trend can be observed. In other words, the higher the number of shells, the smoother the compression curve. It is evident in case of sample of size 35×5 represented by the green solid line in **Figure 5.9a**. Few local peaks can be distinguished on the curve showing high oscillations during stress growth. Indeed, the high probability to have a "chain" of vertical shells[6] influences the mechanical behaviour since these shells can support high loading, and therefore, the stress rises rapidly.

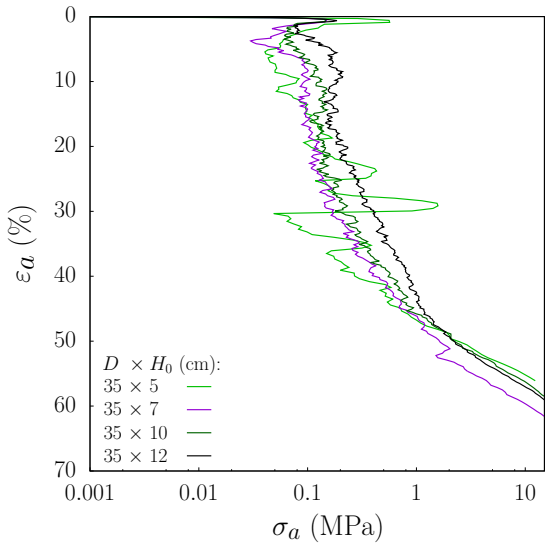

a

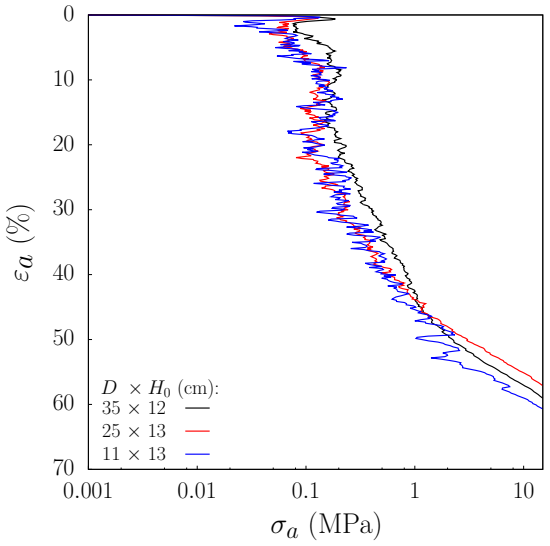

b

Figure 5.9 : The influence of the sample size on the mechanical response to the oedometric compression. The sizes were created varying either **a** – the initial height H_0 or **b** – the diameter D.

It is remarkable to observe that we have succeeded in reproducing the experimental size independency on the mechanical response regarding the initial sample hight. Furthermore, the DEM simulations supplemented the experiments, and we have also stated the lack of influence while reducing the diameter. On the other hand, there exists a minimum number of shells required to conduct a reliable compression test. This number must depend on the rigid boundary effect. In

[6] One vertical shell must be in the contact with the horizontal wall

this work, a specific range of sample sizes, *i.e.* always smaller than experimental, has been tested employing rigid boundaries. The smooth evolution of compression curve and the avoidance of boundary effect as much as possible were two primary goals, referencing the state for experimental size (35×12). Then, from above analysis followed a conclusion that at least 1 000 clusters need to be used in the simulations. Sacrificing a bit the quality of curve ∼800 shells are also sufficient, but, herein, lower amount of shells is not being advised. Note that introducing of periodic boundaries most possibly will enable to reduce the number of shells as well.

In the next section, the work moves to the parametric studies. To this end, size 25×13 has been chosen as an optimal, providing a good compromise between a representative behaviour and the computation time[7]. Ultimately, the sample size can be slightly reduced to cut the computation time.

5.1.3 Influence of the parameters controlling the force laws

As presented in section 3.2, a number of parameters are employed in the force laws: force thresholds, stiffnesses, shape parameter and friction coefficient. Herein, an influence of those parameters on the mechanical behaviour is presented. This parametric study serves the calibration of the model, as well as provides the indications to better understanding of mechanisms involved in the response of material. All the simulations discussed in this section were conducted on sample of size 25 × 13 changing only one parameter at the time. Shell breakage is classified of the utmost importance, and therefore, greater attention was paid to the constants assigned to the bonded contacts throughout the failure criterion, recalled:

$$\frac{f_I}{f_I^\star} + \left(\frac{f_{II}}{f_{II}^\star}\right)^q = 1. \tag{5.6}$$

The shear strength of shell

The force threshold in the pure shear $f_{II}^\star$ is one of the parameters describing the strength of material and, consequently, the strength of shells. Since the value of the shear force threshold could not be found using the experimental observations, it was adjusted numerically for a single shell compressed uniaxially in its radial direction. To verify this adjustment, the parametric study has begun by varying the shear force threshold $f_{II}^\star$ while the limit for the tensile force was kept constant, at $f_I^\star$ = 85 N. The results are presented in the context of tensile force threshold *versus* shear force threshold ratio $f_I^\star / f_{II}^\star$, hereinafter shortly referred to as thresholds ratio. The reference simulation (Oedo_$f_{II}^\star$-50), performed for $f_{II}^\star$ = 50 N, is presented by black solid line in **Figure 5.10**. The mechanical responses of samples with bigger threshold ratio are shown with red and blue lines and correspond to higher values of $f_{II}^\star$ (Oedo_$f_{II}^\star$-250 and Oedo_$f_{II}^\star$-85).

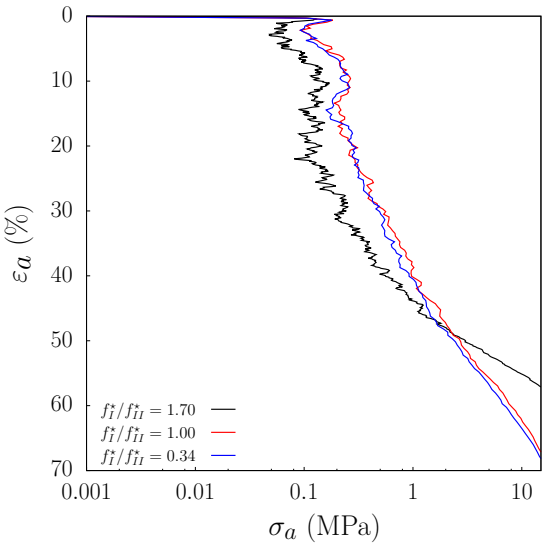

Figure 5.10 : Influence of shell shear strength on the mechanical behaviour for sample of size 25 × 13. The tensile yield limit $f_I^\star$ was kept constant at 85 N.

One should notice that when $f_I^\star / f_{II}^\star$ is smaller than 1, the mechanical behaviour is barely modified. The main difference in the mechanical behaviour occurs after the inclination point. Whereas the oedometer modulus E_{oedo} does not seem to depend on the threshold ratio for ε_a ranging from 0 % to 35 %, E_{oedo} increases significantly for $f_I^\star / f_{II}^\star = 1.7$ for $\varepsilon_a > 35$ %. Similar tendency

[7] 1 week on 8 cores for ∼1 000 shells

was observed in case of a uniaxial radial compression of shell (section 3.3.1), where $f_I^\star / f_{II}^\star > 1.17$ (smaller $f_{II}^\star$) was reported to lower the force at rupture. As the shear strength is low for a high value of threshold ratio, the loading leads to premature shell breakage if the tangential force acts in the failing bond. Analogous conditions might occur during oedometric compression within the assembly. Focusing on the shell orientations, one might expect that horizontally oriented shells will fail due to the high contribution of normal force f_I in the link, while the failure of vertical shells will be ruled by tangential forces f_{II} (equation 5.6). If this assumption is correct, too low threshold $f_{II}^\star$ would: (*i*) increase the contribution of shearing in the failure for horizontal shells and (*ii*) decrease the strength for the vertical shells as it directly depends on $f_{II}^\star$. In both cases, increasing $f_{II}^\star$ prevents the premature breakage. A delay of shells breakage, for ratio lower than 1, results in lower compressibility of the structure at a given time. Then, the strain range increases and the local softening, clearly visible on the black curve between 10 % and 25 % of deformation, is smoothed. In other words, we obtained better, tighter packed assembly.

The study showed that threshold ratio smaller than 1 is not suitable for larger scale simulations. For the sake of representative results, the thresholds ratio equal to 0.34 was established as an adequate value for future simulations. This choice was supported by the rough results of vertical (axial) compression of single shell.

The shape of yield surface

The contribution of shear in failure is not only determined by the limit of the force $f_{II}^\star$ but also by power q. The **Figure 5.11** shows the manner how *shape parameter* q changes the yield surface in $f_I : f_{II}$ space. If q equals 1, a linear relationship will be observed alike the classical linear Mohr-Coulomb criterion. When q tends to ∞, the yield surface/line resembles more criterions such as von Mises. It is important to notice that q does not play a role in the plastic flow rule. In **Table C.1** detail information about used parameters can be found for tests: Oedo_q-2, Oedo_q-3 and Oedo_q-5 (see also **Appendix C**).

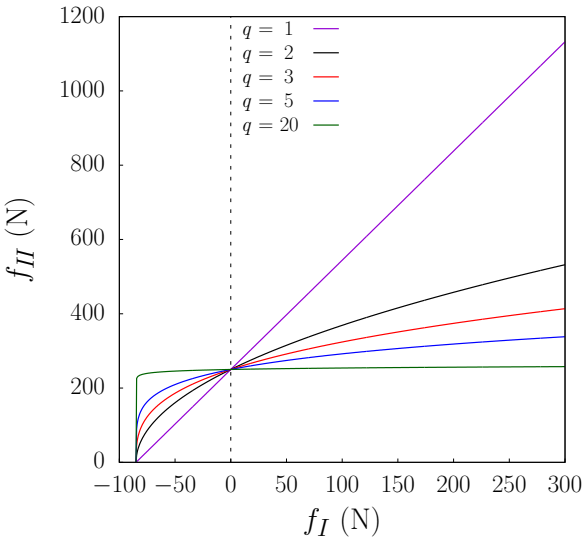

Figure 5.11 : The yield surface for various shape parameter q. Graphically, the failure criterion (equation 5.6) is symmetric with respect to f_I axis.

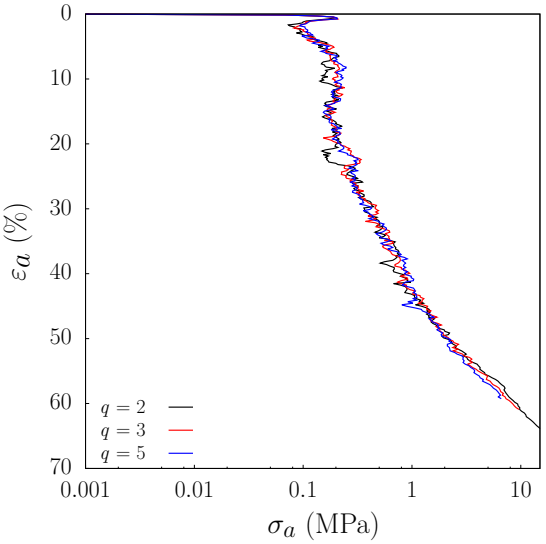

Figure 5.12 : Oedometer test. Influence of the shape of yield surface (**Figure 5.11**)/the parameter q (equation 5.6) on the mechanical response. Sample size 25×13 with an identical initial state.

Although the modification of surface is significant, the trend on the stress-strain curve remains unaffected as shown in the **Figure 5.12**. Then, a parabolic shape with $q = 2$ has been used in most of the simulations presented afterwards, but in the final result $q = 5$ is suggested.

The tensile strength of shell

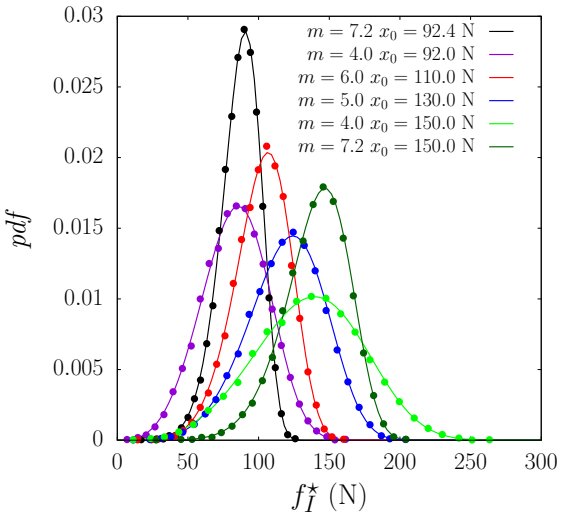

Figure 5.13 : The statistical distribution of tensile strength. The solid line presents the applied function, whereas the points present the *pdf* of Weibull distribution calculated form data used in the modelling (equation 5.7).

Experimentally, it was observed that the strength varies from one shell to another due to the material inhomogeneities. The variation of tensile strength can be described by Weibull distribution with shape parameter $m = 7.2$ (section **3.3.1**). Hence, Weibull statistic distribution was applied to rule the tensile threshold of normal force $f_I^\star$ within the oedometer sample. The scale parameter x_0 was experimentally found equal to 92.4 N. An average force needed to break shell corresponds to $F_I = 92.4\,1.41 \simeq 130.3$ N. **Figure 5.13** explores the influence of shape and scale parameters, using simulations denoted as Oedo_$f_I^\star$-x_0_Wm-m, for various x_0 and m (see **Appendix C**, **Table C.1**). Probability density functions of Weibull distribution (equation 5.7) for different couples of parameters are drawn with solid lines in the **Figure 5.13**.

$$pdf = \frac{m}{x_0}\left(\frac{x}{x_0}\right)^{m-1} \mathrm{e}^{-(x/x_0)^m} \qquad (5.7)$$

The lower the shape parameter m (Weibull's modulus), the wider is the distribution. Since the scale parameter x_0 corresponds to the force threshold allowing $1/\mathrm{e} \approx 37\%$ of shells to survive, the increase of x_0, *i.e.*, the tensile strength of shells, in this case, should result in the rise of sample strength. The dot points in **Figure 5.13** verify that the force limit was correctly distributed in the links for each simulation.

Figure 5.14 shows the mechanical behaviour for different distributions and compares them with the simulation Oedo_$f_I^\star$-85 for which all the links were characterised uniformly by the average strength (brown curve). Although the Weibull distribution properly simulates the natural differences of shells strength (black curve), **Figure 5.14** presents a slight difference in the stress-strain relationship between assemblies composed of variously and uniformly strong shells. The two curves diverge only in the final phase of the test in which the sample with Weibull distribution behaves stiffer, that means, the axial stress increases faster. Most possibly the sample becomes stiffer as there is a lower possibility that breakage occurs due to a high strength of link and the arrangement of parts with respect to the load. Then, breakage is a secondary factor.

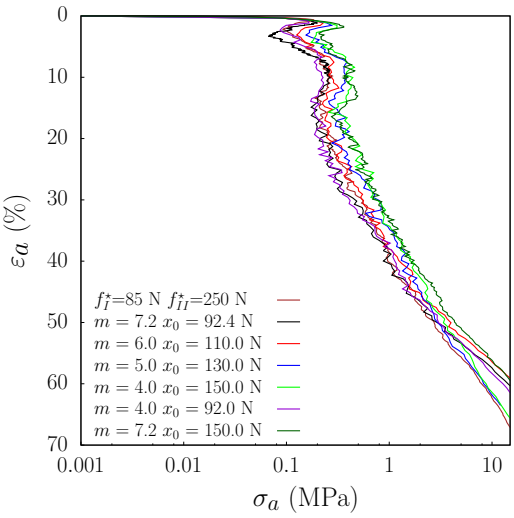

Figure 5.14 : The influence of tensile strength variability on macroscopic response to uniaxial compression, using Weibull distributions from **Figure 5.13**.

Figure 5.14 confirms that the scale parameter x_0 is ruling the strength of sample as with higher x_0 the shells get stronger. The curves sharing the

same scale parameter follow the same trend as long as breakage remains crucial to the mechanical response ($\varepsilon_a < 40$ %). Still, it is remarkable to observe that the range of strength is insignificant in those simulations. These results indicate that the arrangement of shells already introduced diversity in the loading condition of shells such that the material inhomogeneities played a secondary role in the evolution breakage within the assembly. Hence, the study of tensile strength was carried on varying the average strength of shells, yet without applying any distribution. Simultaneously, the shear force was increased, such that the thresholds ratio was kept constant, at 0.34. The mechanical responses presented in **Figure 5.15** are consistent with the previous results (**Figure 5.14**). As expected, it can be observed that the sample bearing capacity rises as the shells are stronger. **Figure 5.15** also demonstrates that the post-inflexion behaviour is stiffer for weaker assemblies. Finally, more resistant sample accesses lower strain limit. However, among modelling applying Weibull distribution, there are acceptation from this observation, possibly explained by the arrangement and size of parts.

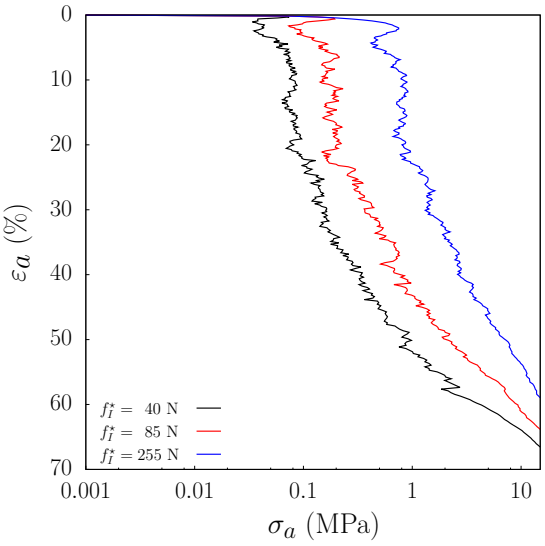

Figure 5.15 : The influence of shell tensile strength on the mechanical response. $f_I^\star$ is constant between shells.

Summarising, the implementation of the variability of strength neither prevented the softening of stress during intensive breakage nor increased the strength of the sample. Yet higher tensile strength got the numerical behaviour closer to experimental results. For this reason $f_I^\star$ was increased temporally up to 150 N and ultimately up to 190 N.

The variability of shell stiffness

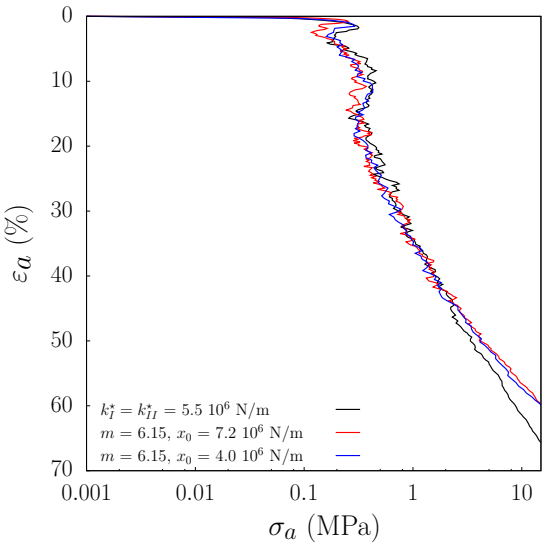

Figure 5.16 : A mechanical behaviour for the various stiffnesses of shell structure. Weibull distribution (equation 5.7 in section **3.3.1**), with shape m and scale x_0 parameters, was employed to introduce the variability of $k_I = k_{II}$.

Normal and tangential stiffnesses are commonly used in the calculation of the contact forces. In this work, the value of tangential stiffness was always equal to the normal one, both in the links $k_I = k_{II}$ and in the contacts $k_n = k_t$. Herein, only the first type of contacts is analysed. Experimentally, it is observed that the elastic properties of shells differs from a grain to another, since it emerges from both geometrical and material aspects, burden with the imperfections and heterogeneities. This has been observed throughout various inclinations of force F to displacement δ curve in the experimental campaign (section **3.3.1**). Since the stiffness rules the increase of contact forces, to reflect the shell stiffness (the slope of $F \leftrightarrow \delta$ relationship) the link stiffnesses needed to be adjusted in the DEM model. For the same reasons, those stiffnesses need probing within assembly. In order

to include the variability of shell stiffnesses, we relied on the Weibull distribution (equation 5.7). Using the slope of experimental curves, a rough estimation of k_I has been done using the uniaxial radial compressions of shells in size $d18$. Cumulative density function allowed finding Weibull modulus and the scale parameter: m = 6.15 and x_0 = 7.2 10^6 N/m. These values were used in the modelling Oedo_k_I-7e^6_Wm-6. For simulation denoted as Oedo_k_I-4e^4_Wm-6, another Weibull distribution of contact stiffnesses was applied. In this case, the scale parameter was lowered down to x_0 = 4.0 10^6 N/m. Detail parameters of modelling can be found in **Table C.1** (**Appendix C**). In **Figure 5.16**, the mechanical behaviours are compared with response of assembly of identically stiff shells. Although the constituent shells can experience higher deformation before the breakage, the macroscopic strain range has been reduced just slightly. No change in the character of mechanical response has been reported in the phase of intensive shell crushing, that is when the parameter is used most actively. That result remains consistent with the observation from single-shell uniaxial radial compression. If the stiffnesses in the links remain of the same order of magnitude, the results vary negligibly. Onwards, most often the primary choice of stiffness k_I = 5.5 10^6 N/m was kept in the modelling.

The inter-granular and boundary friction

Once a shell is broken, the type of contact between the parts becomes the classical frictional contact, like the interactions between two shells (clusters). Since in the tangential direction the force is limited by the Coulomb's friction, the friction coefficient μ is an input parameter. Two contacts can be distinguished: wall-shell (at the boundary) and shell-shell (inter-granular). Initially, the parameters were set to μ_{wall} = 0.15 and μ_{shell} = 0.36 (modelling Oedo_μ_0 in **Table C.1**). Then, each one was increased separately for the simulations Oedo_$\hat{\mu}_{shell}$ and Oedo_$\hat{\mu}_{wall}$.

As shown in the **Figure 5.17a**, the inter-granular friction affects the mechanical relationship more than the "boundary" friction between the wall and the shells. Higher μ_{shell} leads to a higher stress level experienced by the sample during full test. Initially, the difference stands out less but it increases as the loading rises.

Figure 5.17b provides an insight into the evolution of cohesion-less contacts N_μ as a portion of all the contacts N. Note that N_μ cumulates both

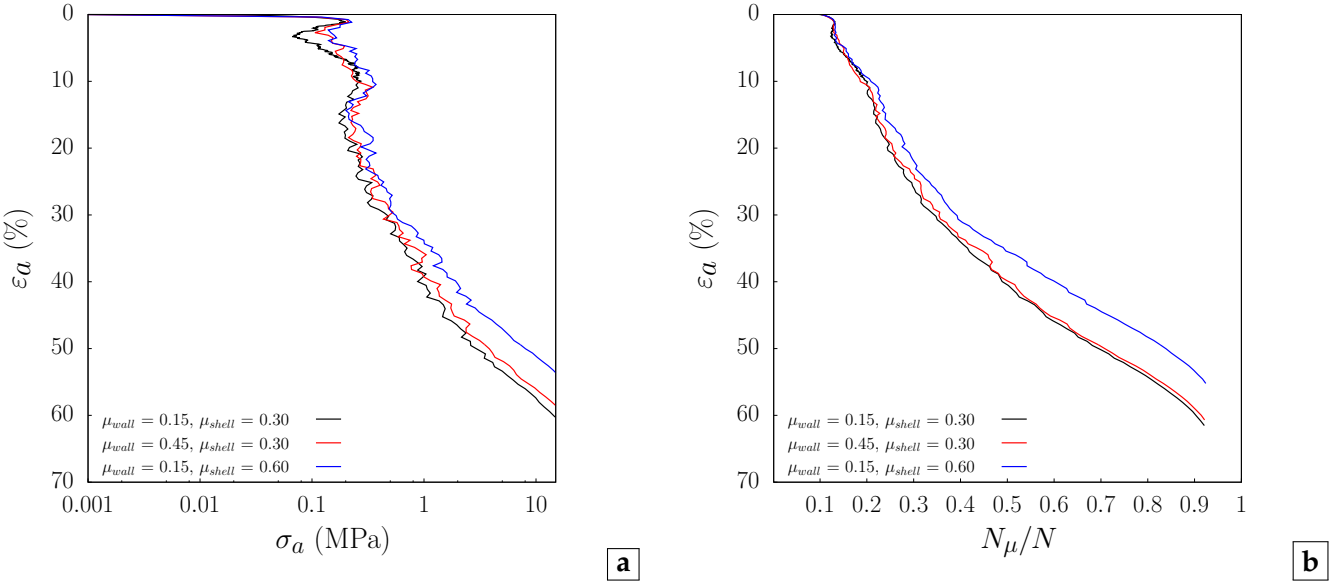

Figure 5.17 : a – The mechanical behaviour of one-dimensional compression for different values of inter-granular friction coefficient μ_{shell} and the friction between the shell and the rigid wall μ_{wall}. **b** – The evolution of number of contacts N_μ normalised by the number of all the interactions N (the links and the contacts).

the shell-shell and the shell-wall contacts. Initially, only $\sim$ 11% of all the interactions were recognised as frictional, but this ratio must increase non-linearly as a consequence of (*i*) breakage and (*ii*) densification (an increase of the coordination number). Since higher tangential forces can act in the contact points, the shell breakage occurs faster, *i.e.*, for the lower value of axial strain. This was manifested only for the simulation with a higher inter-granular friction, most possibly, due to the fact that μ_{wall} affects fewer shells. It is observed in **Figure 5.17b** that, initially, the curves follow the same trend suggesting that the breakage progress evenly. The higher the difference in the number of frictional interactions, the more the macroscopic response deviate from each other as shown in the **Figure 5.17a**.

Numerical parameter influence: a synthesis

Current part of parametric study has concerned only selected numerical parameters related to the failure criterion and the force laws. Although the stress-strain relationship still diverge from the experimental behaviour, that was the first step to accurate understanding of macroscopic response. The simulations have contributed to our understanding of parameter roles and to the assessment of their importance. One must remember that material strength parameters $f_I^\star$ and $f_{II}^\star$ rule the behaviour most efficiently, and the variations of the remaining constants were often of negligible influence. For a given initial geometry (the density, the coordination number, the shell orientations, *etc.*) the shear strength ($f_{II}^\star$) modifies the compressive behaviour only to small extent, whereas the tensile strength ($f_I^\star$) always remains influential. This is an important observation because $f_I^\star$ is a unique parameter that can be measured easily. It is interesting to observe that lack of $f_I^\star$ variability resulted in almost identical mechanical behaviour. Finally, these modelling provides many data for comprehensive analysis of macroscopic response (section **6.1**).

5.1.4 The influence of the initial state

The initial state of an assembly can be characterised by several internal parameters. Two main parameters can be distinguished: the packing fraction and the coordination number. For example, Roux and Chevoir (2005); Emam et al. (2006); Combe and Roux (2017) have shown that these two parameters can be independently controlled during the DEM sample preparation, which is not possible experimentally. It has been reported that two samples of similar packing fraction can have very different mechanical behaviour, if their contact connectivity is very different.

Here, the initial state is obtained after a gravitational deposit and a relaxation phase to reach the equilibrium state. The samples can be characterised by the number density n which is the counterpart of the packing fraction. In this work, the coordination number was not controlled due to the sample preparation process (a deposit under gravity without an energy injection). Then this parameter was not specifically controlled. But, unlike classic DEM studies on the spherical particles, our shells are material oriented and their strength strongly depends on the loading direction. Thus, another important internal parameter is the shell orientation anisotropy, *i.e.*, the anisotropy of statistical distribution of shells orientations.

The numerical recipes to control the arrangement of shells during the sample preparation are described in sections **4.3.1** and **4.3.2**. It is worth remembering that those ways allow us to control the arrangement of shells indirectly by means of the input parameters, like initial oriented velocity. Then, the sample state is not imposed but rather tends to a preferable one.

Those preparation methods helped us compose samples such that the influence of both number density (Oedo_l, Oedo_d and Oedo_D) and shell orientations (Oedo_h, Oedo_H, Oedo_v and Oedo_V) were studied.

Initial density n

There exist two additional motivations to study the influence of the density n. Firstly, it has been observed that the larger is the size of the sample the denser it is, although the procedure was identical. Therefore, the numerical samples were denser than the experimental ones. Secondly, the experimental measurements showed that the

coated samples are less dense. Since the cement is modelled as a *bond* in one of the interaction points, and its volume is ignored, ultimately, the sample needs to be loose. Still, in the first order simulation without cement bonds were performed.

Sample	μ_{shell}	n (m^{-3})	e_0	Z_n
C_25×13_l_01_A	0.90	140 388	3.002	4.244
C_25×13_d_02_A	0.08	161 084	2.488	6.177
C_25×13_D_01_A	0.00	171 450	2.277	7.088

Table 5.3 : The initial state of samples used in the characterisation of density influence. (See **Appendix B**).

Table 5.3 describes the initial state of 3 samples studied here after[8]. Using the inter-granular friction coefficient $\mu_{shell} = 0$, the highest density can be obtained. In the case of sample dimensions 25×13, the density was found at 171 450 shells per meter cube. Although this value would vary slightly between configurations, it indicates a level of maximum density (numerically). Note that the densest sample generated in size 11×22 had $n = 166\,913$ m^{-3}. Due to the boundary effects, the limit is size dependent as suggested by the results in sections **4.3.1** and **5.1.2**.

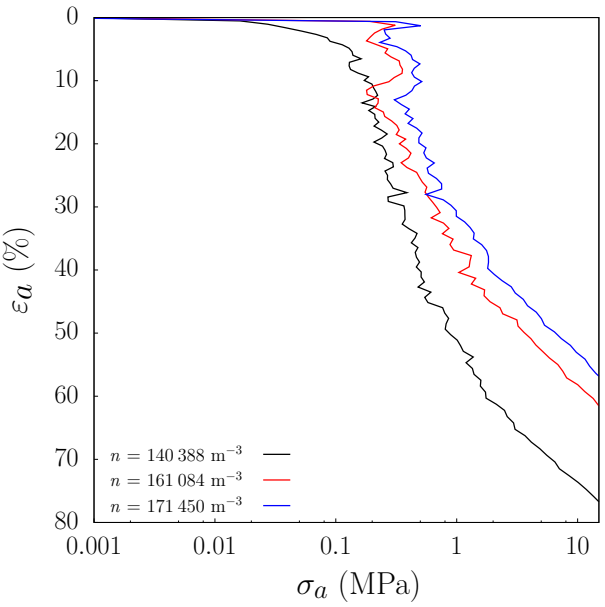

Figure 5.18 : Oedometer test. The influence of the initial density on the compression curves. The number density n is equivalent to the packing fraction, such that higher n stands for denser samples.

The average number of contacts decreases linearly with n (with trend: $Z_n = 9.2\,10^{-5}n - 8.75$). By definition, as the density increases, the void ratio e must decrease as the following relationship indicates: $e = N/(nV_s) - 1$. The number of shells N has been kept identical, and automatically, neither the volume of solid V_s varied between the simulation. Therefore, the difference in e_0, between 2.277 and 3.002, originates from the volume of inter-granular voids. This explains why the range of axial strain was reduced for denser samples, *i.e.*, the smaller initial volume of inter-granular voids (**Figure 5.18**). The mechanical response for the looser sample evolved with a smooth uprise of stress. More precisely, the initial peak and the local stress softening (at ∼5% and ∼15% of ε_a), characteristic for denser samples, did not appear for the loose packing. The behaviour of sample C_25×13_l_01_A (Oedo_l) resembles more the experimental curve, but the stress capacity of sample is lower.

Effect of shell orientations

The samples studied this far presented the heterogeneity in shells orientations due to the rigid boundaries. But within the samples core the shells are rather isotropic oriented just as in the reference sample C_25×13_d_02_A (used in modelling Oedo_r). Herein, we extend the study of orientation heterogeneity with modelling assuming strong (Oedo_h, Oedo_v) and highly strong anisotropy (Oedo_H, Oedo_V) also within the core of the sample. Those simulations make use of samples that have been already characterised in section **4.3.1** by the statistical distribution of shells orientations (**Figure 4.24b**). The initial state parameters were summed up in **Table 4.10**. The influence of shells orientations is shown in the **Figure 5.19** for the oedometer test. The mechanical responses demonstrate that the axial strain experienced by the sample depends not only on the initial density but also on the orientations of shells or fragments of shells (see also **Figure 6.11** in section **6.3**). For any given stress, the assembly with a vertical preferential orientation can be compressed less, *i.e.*, exhibit a lower strain, than the assembly

[8] More details about the initial state and the numerical parameters can be found in **Appendices B and C**, respectively.

of horizontally orientated shells. Furthermore, the breakage of vertical shells results in higher fluctuations from the stress-strain trend (Oedo_V in **Figure 5.19**). The shear resistance of links $f^{\star}_{II}$ is the most requested component for axial loading of a shell. $f^{\star}_{II}$ is higher than $f^{\star}_{I}$, and therefore, more energy can be accumulated during the compression and later released during shell crushing. The release of energy corresponds to the drop of stress on the mechanical curves. Also, there is no variability introduced[9] in the shear limit $f^{\star}_{II}$ such that for the perfectly axially compressed shell the links break at once. It is interesting to observe that the initial peak disappears for the looser sample but only for the arrangement of horizontal shells.

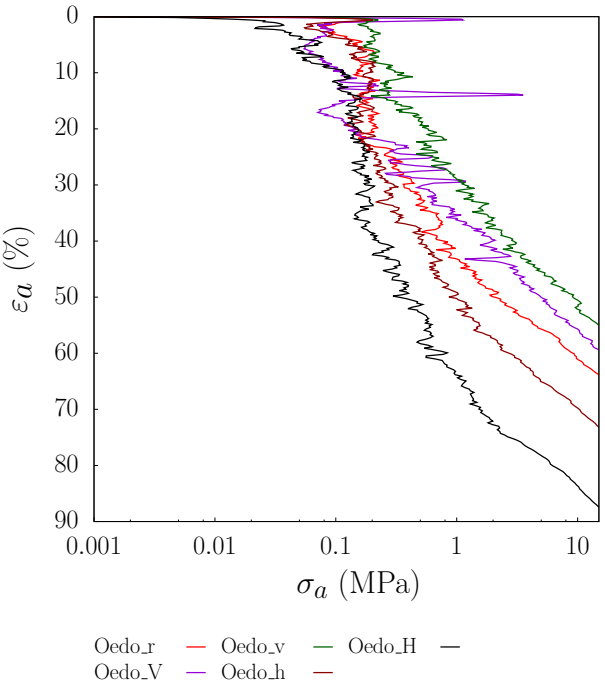

Figure 5.19 : Change of mechanical response due to strong anisotropy in the orientation of shells. The preferential orientation can be either v, V – vertical, or h, H – horizontal. Notation includes small and capital letters which refer to lower and higher anisotropy level, respectively.

Summary

The study of initial state has shown that the change of sample density results in significant changes in mechanical behaviour. To reflect experiments, a sample with a lower number density needs to be used. Also, the orientation of shells in the model plays an important role. Extreme anisotropy of orientations affects the stiffness and strength of the sample because the manner of breakage may vary within assembly due to loading conditions of constituent shells.

5.1.5 The predefined slicing of shells

As already discussed, the discretisation of shells into the sectors causes some limitations of the model and its maximal compressible capability. As presented in section **3.3.2**, we have characterised the discretisation of shell by two values: $N^{\star}_{axial}$ and $N^{\star}_{circ}$. They stand for a number of sectors into which the shell was divided in its axial and radial directions, respectively. Whereas the circumferential slicing of shell into the sectors is suitable and sufficient for the uniaxial radial vertical compression on the single shell, it raises the concerns about the breakage manner in the context of the assembly. Within this section, we investigate those matters.

The circumferential and axial slicing of shell

Different values of $N^{\star}_{axial}$ (1 or 2) and $N^{\star}_{circ}$ (12 or 16) were used to generate the model of shell *d18*. Because the external dimensions of shells remained unchanged, the initial state of sample did not vary significantly[10]. The exact values of the void ratios and the coordination number can be found in **Appendix B** for the samples: C_35×12_d_01_A, C_35×12_d_07_B, C_11×13_d_01_A and C_11×13_d_21_F.

Increasing the circumferential number of sectors $N^{\star}_{circ}$ does not lead to any improvement of mechanical behaviour as shown in the **Figure 5.20a**. The isotropic hardening stands out less for the smaller sectors (Oedo_$N^{\star}_{circ}$-16), whereas the strain range has not been affected. On the contrary, doubling the number of sectors in the axial direction (**Figure 5.20b**) has increased the final strain

[9] *e.g.*, Weibullian variability

[10] The sample cannot be exactly the same. Due to an increase of the sector number, the arrangement of the contacts between two shells will change. Thus, slight modifications in the shells position are need to reach equilibrium state.

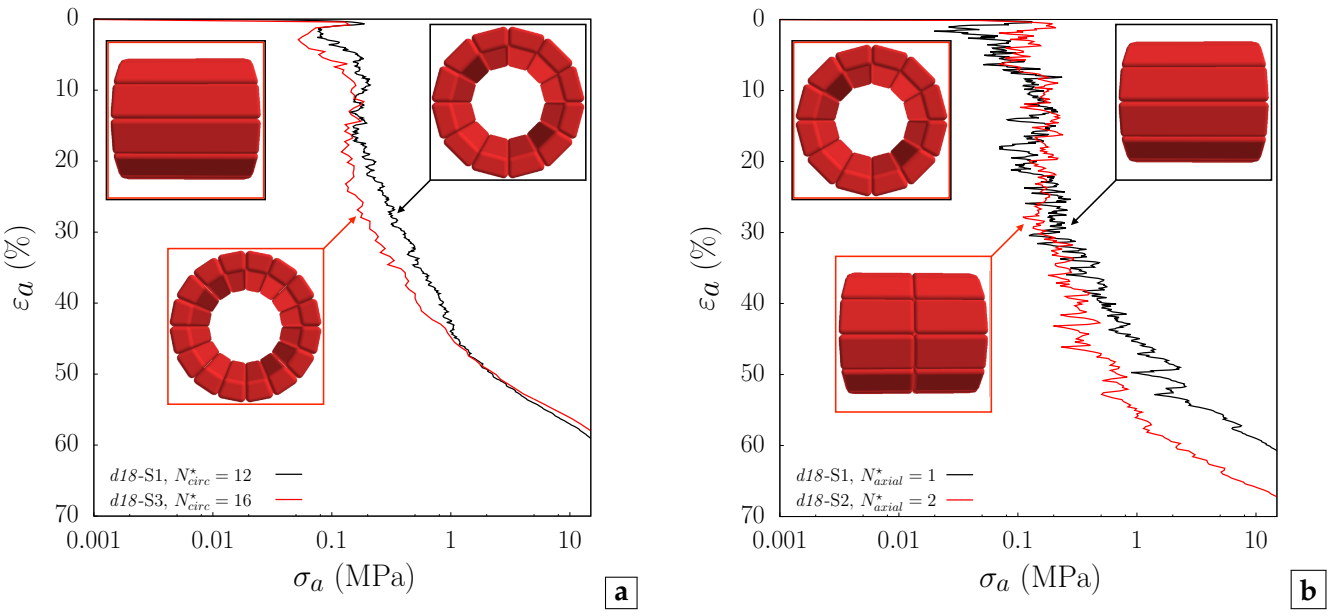

Figure 5.20 : In the uniaxial compression, three shell shapes were used: *d18*-S1, *d18*-S2 and *d18*-S3 (**Appendix A.1**). We tested the influence of shell shape discretisation in: **a** – the ring cross-section for Oedo_$N^{\star}_{circ}$-16 (red) and Oedo_$N^{\star}_{circ}$-12 (black) and **b** – the axial direction. Modelling Oedo_$N^{\star}_{axial}$-1(black curve) made for basic shape with 12 sectors, and 24 sectors per cluster were used in Oedo_$N^{\star}_{axial}$-2 (red).

ε_a about 6.5 %. In fact, the reduction of the sector length, *i.e.*, the largest size of the sector, affected mainly the response after the inflexion point, such that the sample remained strongly compressible longer – E_{oedo} low also for $\varepsilon_a \in \langle 35\ \% : 55\ \% \rangle$. The model gained the breakage capacity, and the higher amount of links to break allowed to reduce the axial stress longer. The usage of the shorter sectors (*d18*-S2 in Oedo_$N^{\star}_{axial}$-2) indisputably extended the applicability of the simulations because it partially neutralised the model limitation ruled by the largest particle size. At the start, Oedo_$N^{\star}_{axial}$-2 presented more rigid behaviour, which contradicts the experimental behaviour more than the sample composed of longer sectors *d18*-S1 (Oedo_$N^{\star}_{axial}$-1). This suggests that the model might actually mismatch the breakage during its onset.

Variations of the shell thickness

Modelling Oedo_*t*-3.6 and Oedo_*t*-4.8 were performed using two modified shell geometries with an increased thickness t of the shell, up to 3.6 mm (*d18*-S4) and 4.8 mm (*d18*-S5), respectively. The reference simulation Oedo_*t*-2.4 employed the true geometry, that is $t = 2.4$ mm (*d18*-S1). Looking at the ring cross-section, radially the cluster has not been sub-divided, and therefore, the thickness of cluster was related to the thickness of the sector. As the volume of the shell enlarges, the shell strength must increase too. Thus, the yield threshold $f_I^{\star}$ was adjusted respecting the tensile strength of the material, namely, the tensile stress at the breakage σ_I. 2D FEM modelling has been performed with regard to this matter (see **Appendix A.2**). Then, the threshold ratio $f_I^{\star}/f_{II}^{\star}$ was kept at 0.34 for all the simulations. More details concerning the parameters used in those simulations are given in the **Appendix C**. The initial state of samples varies slightly. Rather an obvious consequence of the relative radius reduction, *i.e.*, the reduction of the internal void, is a decrease of the overall void ratio e. However, the modified void ratio $e^{\star}$ increased. In other words, for the more complete shells, the packing was looser, plausibly because the "interlocking" effect was reduced. The exact values are presented in the **Appendix B**.

Figure 5.21 shows how the mechanical response was influenced by these changes. These results highlight that the amount of internal voids is crucial to the compressibility of the material. For

the thicker shells, a larger volume of solid matter limits the accessible strain range.

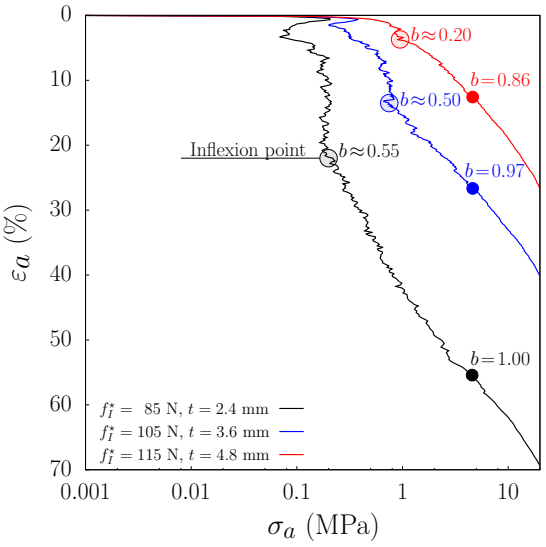

Figure 5.21 : The mechanical responses for three different shell thicknesses t: 2.4 (black), 3.5 (blue) and 4.8 mm (red). Note that with an increase of the thickness, the DEM strength parameter $f_I^\star$ also rises. The semi-transparent dots show the inflexion points, whereas the solid dots indicate the validity points (sector size to be reconsidered).

This study assumes that the strongly compressible phase appears up to an *inflexion point* marked as a semi-transparent circular zone in the **Figure 5.21**. The following remark is of great significance. In this study, we refer to the inflexion point of the material with a high internal porosity compressed in the σ_a range limited to 15 MPa. But taking into account a higher stress range, another inflexion point might be considered, especially, if the model would allow further evolution of the grain size distributions (*e.g.*, using a much smaller sector size). The second inflexion point would be characteristic for the material composed of less compressible fragments. However, in our model, the precursors of the secondary inflexion points (the full dots) are also the points at which the model starts to lose its representative quality. If the shell would not have the internal void (a relative radius $\bar{r} = 0$), in our range of σ_a the inflexion point would not be visible. Therefore, a strongly compressible phase (with a low oedometric modulus E_{oed}) exhibited by the material was reduced for the smaller voids. Hence, in the **Figure 5.21**, the inflexion point hardly stands out on the compression curve for Oedo_t-4.8 (red curve), but the inflections of two other curves are clearly visible ($\varepsilon_a \simeq 13$ % for Oedo_t-3.6 and $\varepsilon_a \simeq 22$ % for Oedo_t-2.4). Obviously, if a coarse division into the sectors might be questioned in the cases of $t = 2.4$ mm and $t = 3.6$ mm, for the larger sectors $t = 4.8$ mm, the modelling seems to lose its validity even faster. Thus, in the case of the larger t, one may consider splitting also the sector thickness. However, the change of the mechanical behaviour, shown in the **Figure 5.21**, originates not only from the model limitations. Also, in reality, the reduction of the internal porosity must lead to a degradation of the compressible capacities. An analysis of breakage can support this claim, but firstly, a degree of breakage has to be quantified.

Taking the advantage of our DE model, the breakage level can be easily established as a ratio of the shells that already broke N_{broken} *versus* an initial total number of the shells N, onwards denoted as b:

$$b = \frac{N_{\text{broken}}}{N}. \tag{5.8}$$

Due to the characteristics of ROCKABLE, all the links between the sectors i and j are assigned to a common interface I_{ij}, and therefore, the model of intact shell – *cluster* – contains a number of the interfaces $(\sum I_{ij})_0$ (recall section **3.2**). It directly depends on the chosen shell shape, that is a total number of sectors ($N^\star = N^\star_{axial} N^\star_{circ}$) constructing the intact shell:

$$(\sum I_{ij})_0 = N^\star_{axial}(2N^\star_{circ} - 1). \tag{5.9}$$

As the compression progresses, the cluster keeps separating into the smaller parts, called *subclusters*, until an ultimate breakage state is reached, *i.e.*, none of the links remains within the cluster ($\sum I_{ij} = 0$). Thus, N_{broken} is simply a number of the clusters with fewer interfaces than initially:

$$\sum I_{ij} < (\sum I_{ij})_0. \tag{5.10}$$

In the **Figure 5.21**, two values of b are marked for each compression curve. One stands for the inflexion point, where the strong compressibility has come to its end (the semi-transparent dots).

Whereas b was slightly modified between the shells with the thicknesses 2.4 mm ($b \approx 0.55$) and 3.6 mm ($b \approx 0.50$), for $t = 4.8$ mm the breakage level is more than twice times lower ($b \approx 0.20$). Furthermore, the validity of the model should be seen as the validity of the breakage manner. It is assumed that for the intact shell, the circumferential slicing is true while breaking into the coarse fragments, as was shown in the section **3.2** both for the uniaxial and the biaxial radial compressions of a single shell. Then, the validity of breakage manner is lost when $b = 1$. At that point, the importance of breakage was being redirected from the cluster to the sectors (clumps) which cannot break. For Oedo_t-2.4, the shell strength was set such that $b = 1$ occurred within the range $\sigma_a \in \langle 0 : 15 \rangle$ MPa. For Oedo_t-3.6 the point was found just at the end range ($\sigma_a \approx 15$ MPa), but in the case of the shells with $t = 4.8$ mm $b = 1$ was not experienced because it would be reached at $\sigma_a \approx 28$ MPa. Thus, for the sake of transparency, we indicated the validity points at the same stress level for all the modelling, that is $\sigma_a = 4.6$ MPa following Oedo_t-2.4. The breakage level at the validity point is lower for thicker shells. That is also explained by the higher shell (tensile) strength.

Summary

A study of the sector shape has been done to probe the limitation of our model. There is no benefit coming from the increase of the sectors number circumferentially, as long as the axial dimension is not of comparable order. Although the reduction of the height enlarged strain range, there remains a significant gap between the modelling and the experiment. In other words, doubling the number of sectors only partially reduced the limitation of the model. One must remember that the additional sectors make the computations more time-consuming.

Ultimately, a compromise needs to be done if the scale of the simulation is to be enlarged. Thus, the initial choice to discretise the shell into 12 sectors using only circumferential division has been kept hereinafter.

5.1.6 Final benchmark between DEM and experiments

Prior to this parametric study, three objectives have been established. First two – the understanding of the contributions of the parameter and the assessment of their importance – have been fulfilled. Addressing the parametric study, one must remember that:

- The tensile strength of the shell, ruled by the parameter $f_I^\star$, controls the macroscopic stress-level.
- The initial density n, linked to the average number of the neighbours Z_n, serves the adjustment of the strain range and can smooth the evolution of the trend (for the loose sample).
- The sector size has been compromised in favour of computation time. Finally, a coarse circumferential slicing without the axial splitting has been chosen to generate the cluster for further proceeding – shell *d18*-S1.

At this point, only one objective but of the highest importance remains – the calibration of the model. The current section shows a final comparison between the experiment and the DEM modelling and provides a primary analysis of the mechanical behaviour. Further, this section aims to:

- present a calibrated model and elaborate on the adjusted set of parameters, highlighting $f_I^\star$ and n, even if they mismatch the experimental measurements,
- show the numerical behaviour of the unloading and re-loading (UR) cycles,
- explain the response focusing on the loading and the UR cycles separately,
- reproduce numerically a difference in the compression curves between two shell size (*d18* and *d20*).

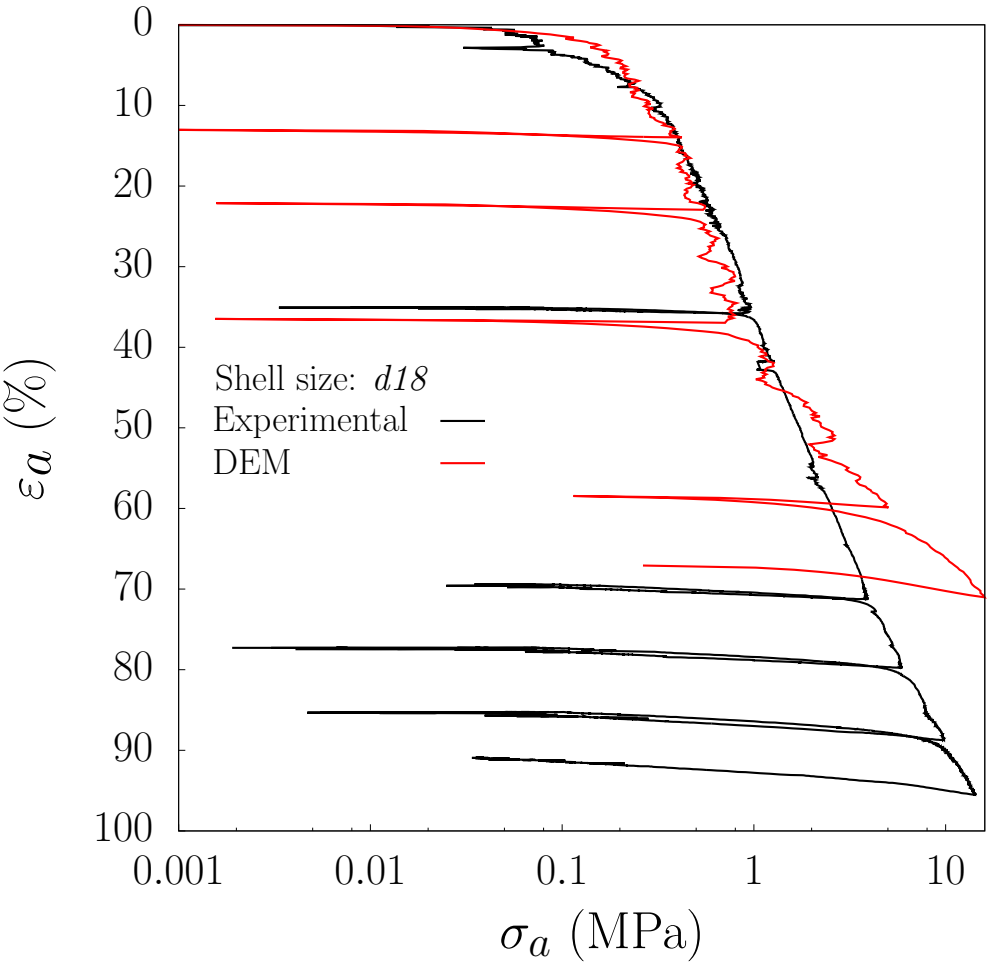

Figure 5.22 : Experiment *versus* DEM. Comparison of mechanical responses to oedometeric compressions. Numerical modelling – Oedo_Adjusted_Cyc.

Loading phase

First, we suggest to analyse only the loading parts of the mechanical behaviour. **Figure** 5.22 presents the numerical compression curve (red line) that resembles the experimental mechanical behaviour (black line) most accurately. There are three foreground remarks concerning the input of this simulation and the corresponding consequences.

Firstly, the modelling was performed on a loose sample ($n = 140\,388$ m^{-3}) not respecting the (higher) experimental density ($n = 155\,129$ m^{-3}). As a consequence, a continuous smooth increase of the axial stress was observed, without the initial peak occurring in the case of the denser sample (**Figure** 5.6). Yet the sample remained slightly stiffer at a low-stress level ($\sigma_a < 0.3$ MPa). What concerns the DEM model, the contact and/or link stiffnesses can be partially responsible for such a result.

Secondly, the force law parameters needed some adjustments in order to properly capture the isotropic hardening. The normal force threshold $f_I^\star$ was assigned to the links respecting Weibull's distribution with a scale parameter (x_0=190 N) set about two times higher than it has been determined experimentally (**Figure** 3.23 in section 3.3.1).

Finally, the large sector size reduces the ultimate strain and rules the discrepancy point, at which the numerical and the experimental curves diverge from each other ($\sigma_a = 2$ MPa).

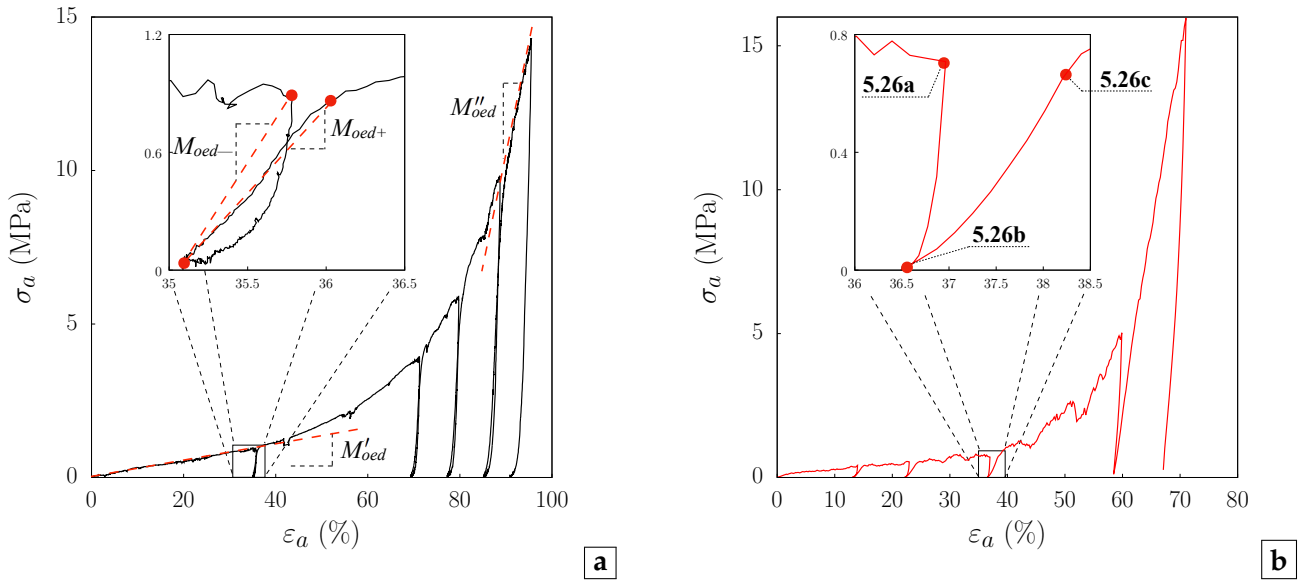

Figure 5.23 : The mechanical behaviour of 1D compression with the series of the UR cycles. A comparison between: **a** – the experiment and **b** – the numerical modelling (Oedo_Adjusted_Cyc) made for the shell size *d18*. For a selected numerical UR cycle, three sample states were selected for a detail analysis (**Figures 5.26a to 5.26c**).

Unloading-reloading cycles

Cycle	ε_a (%)	σ_a (MPa)	M_{oed-} (MPa)	M_{oed+} (MPa)
1^{st}	35.79	0.89	124	72
2^{nd}	71.11	3.91	256	167
3^{rd}	79.73	5.88	257	184
4^{th}	88.70	9.81	293	215
5^{th}	95.49	14.29	311	–

Table 5.4 : The characterisation of UR cycles using the experimental compression curves. The shells size was *d18*. The oedeomteric moduli of non-linear response are calculated as shown in the **Figure 5.23a**, separately for the unloading M_{oed-} and the loading M_{oed+}.

A comprehensive DEM modelling should fully reproduce the experiment, including the unloading steps. **Figures 5.22** and **Figures 5.23a** show that, experimentally, a classic over-consolidated behaviour was observed characterised by a much stiffer hysteresis-like stress path. From each unloading-reloading cycle (UR), two elastic modulus are measured: a secant oedometer moduli M_{oed-} for the unloading and a secant oedometer modulus for the reloading M_{oed+}[11]. The inset of **Figure 5.23a** illustrates these two elastic moduli and their values in the cases of all the successive UR curves are given in the **Tables 5.4** (experimental) and **5.5** (numerical).

Cycle	ε_a (%)	σ_a (MPa)	b (%)	M_{oed-} (MPa)	M_{oed+} (MPa)
1^{st}	13.96	0.42	30.8	46	21
2^{nd}	22.94	0.54	51.8	64	23
3^{rd}	36.96	0.71	78.7	150	38
$(3^{rd})'$	36.96	0.71	78.7	117	131
4^{th}	59.88	5.03	98.5	344	142
5^{th}	71.02	16.00	100	399	–

Table 5.5 : Description of numerical UR cycles for initially loose sample (**Figure 5.23b**). The starting points (the unloading) are characterised by the axial strain ε_a, the axial stress σ_a and the breakage ratio b. For each cycle, oeodometric modulus was calculated twice: for the unloading M_{oed-} and the reloading M_{oed+}. The $(3^{rd})'$ cycle has been performed as a parallel to (3^{rd}) cycle but with a high friction coefficient $\mu = \mu_{wall} = \mu_{shell} = 100$.

Following the experimental protocol, the UR cycles have been repeated several times during the 1D compression. Numerically, the sample was unloaded at five different stress states as described in

[11] $M_{oed} = \Delta\sigma_a / \Delta\varepsilon_a$

the **Table** 5.5. The unloading points were selected aiming various degrees of breakage.

The inset of **Figure** 5.23**a** presents a typical experimental behaviour focusing on the selected unloading–reloading hysteresis. Despite the lower stiffness, the numerical modelling (**Figure** 5.23**b**) correctly reflects the character of over-consolidated soil. In both cases, the initial rapid drop of the stress suppresses gradually and non-linearly during the unloading. Further, one can observe a fast augmentation of the loading up to the consolidation stress, above which the inclination of the stress-strain curve returns to the starting point. Two main observations can be pointed out concerning the oedometric moduli of the UR curves. Those remarks are valid for both the experiment and the DEM modelling. But although the experimental and numerical responses are similar, the numerical sample has presented much softer behaviour (M_{oed} are respectively lower), due to the numerical parameters. Firstly, M_{oed-} was higher than M_{oed+} with one numerical acceptation[12] (**Tables** 5.4 and 5.5). In other words, the samples behaved stiffer during the unloading than during the reloading. Secondly, the UR behaviour was becoming stiffer as the stress level was rising. This observation can be explained by the change of the sample structure. As a consequence of shell-crushing, the fragments became stiffer due to their geometry. Also, the grain size distribution became less uniform, thus the fragments were packed in denser assembly. For all these reasons, the assembly became less compressible.

Herein, we supplement the analysis of the mechanical curves with some observations at the grain scale. **Figure** 5.24 presents the evolution of the average number of contacts Z. Although two colliding clusters constitute only one neighbour for each other, they can interact throughout multiple contacts. Therefore, we acknowledged two variables: the average number of neighbours in contact Z_n and the average number of contact points Z_c. In both cases, the coordination number maintained an upward tendency with respect to the growth of the breakage level b. Naturally, more fluctuations were observed in the case of the contacts, whereas the evolution of contacts was more steady. An opening of contact is not equivalent to the loss of neighbour. Furthermore, two phases can be distinguished in **Figure** 5.24 with either a slow ($b \leq 0.95$) or a rapid evolution ($b > 0.95$).

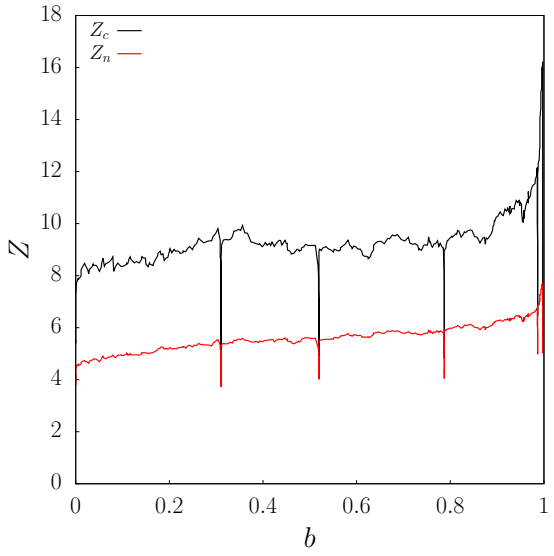

Figure 5.24 : Numerical oedometer test. The evolution of the coordination number for both neighbours Z_n and the contacts Z_c. The compression curve has been shown in the **Figures** 5.22 and 5.23**b**. Note that breakage level b rises with increase of stress level in non-linear manner.

An intensive shell breakage releases the access to a large amount of the inner voids trapped in the shells (a passive free space). Consequently, the parts can rearrange freely, and not only the contact network but also the neighbours' network can be significantly modified. The breakage also reduces the typical size of the parts, which is usually thought to lower the number of possible contacts. However, the release of the inner surface can balance this tendency in the case of the tube-shaped geometry. Those phenomena can explain the slow growth of both Z when the primary breakage is intense ($b \leq 0.95$). Once the majority of the shells were broken ($b > 0.95$), the small volume of the free space within the sample did not allow any significant rearrangements, and the coordination numbers began to mount rapidly due to strong

[12] The cycle $(3^{rd})'$ is to be discussed soon afterward.

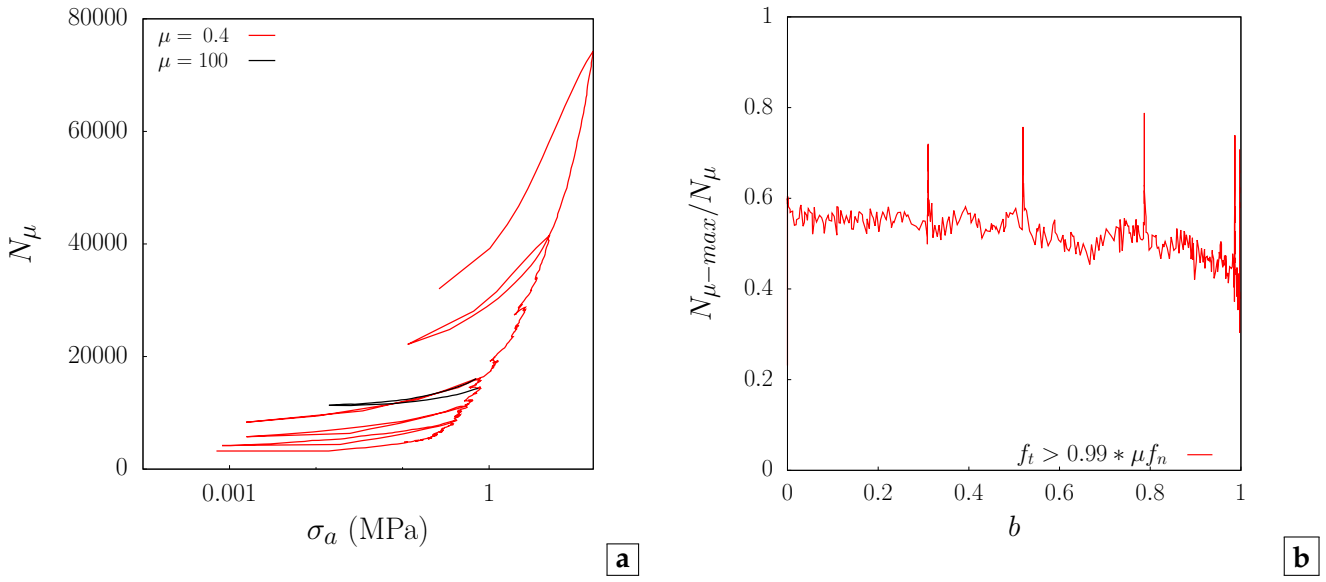

Figure 5.25 : a – Loss and gain of the contacts. An evolution with respect to macroscopic loading σ_a. N_μ is a number of contacts. The UR cycles are specified in the **Table 5.5**. **b** – The percentage of the sliding contacts presented with respect to the breakage level. $N_{\mu-max}$ is a number of sliding contacts (according to the criterion $f_t > 0.99\mu f_n$).

densification. **Figure 5.24** exposes that breakage did not occur during the UR cycles (b is constant). Thus, one can observe the vertical drops during each cycle. For the unloading, the contact opened intensively, and therefore, Z_c decreased significantly. With the opening of the last contact, also the neighbour was lost, but this led to a relatively smaller drop of Z_n.

Figure 5.25a presents a non-linear evolution of the number of contacts N_μ (excluding the cohesive links) during the uniaxial compression. The loss of contacts during each unloading is clearly demonstrated by the decreases of N_μ. The reloading resulted in the creation of new contacts once more. The processes presented a hysteresis-like trend each time which indicated the irreversible changes in the contact network. Initially, the evolution of N_μ was slow, such that only 18.2 % of the total growth was reached at the point of the 3^{rd} unloading ($b = 0.787$). At the beginning of the 4^{th} cycle corresponding to $b = 0.985$, N_μ reached 58.8 % of its final value. This proves that mainly the densification contributed to the creation of new contacts. **Figure 5.25b** quantifies how many of those contacts approached the sliding, *i.e.*, satisfied the criterion $f_t > 0.99\ \mu f_n$. The ratio of sliding interactions $N_{\mu-max}$ with respect to the total number of contacts N_μ evolved as a function of the breakage. Due to the sample preparation, the sliding was present in only 23 % of the contacts. A rapid jump of about 40 %, once the loading began, might have been caused by the modification of the equilibrium of the forces. On the overall point of view, the contribution of the sliding interactions decreased non-linearly from 0.6 to 0.37 – slowly at the beginning and more rapidly above $b \approx 0.9$. Since the contacts with the large normal forces are less capable of sliding, the contribution of $N_{\mu-max}$ decreases for the high-pressure. When the breakage began to stop, the sample densified significantly, and therefore, the contact openings were less likely to appear due to the compaction of the sample. As is seen in the **Figure 5.25b**, the trend demonstrates a high peak each time the UR was performed (for $b =$ constant). This plastic response has been further investigated as shown in the **Figures 5.26a** to **5.26c**. The analysis was dedicated to the status of the contact (elastic or sliding) and its modification during the UR cycle, as shown on the example of the 3^{rd} UR (**Table 5.5**). Three different states (**5.26a** to **5.26c**) have been already marked on the

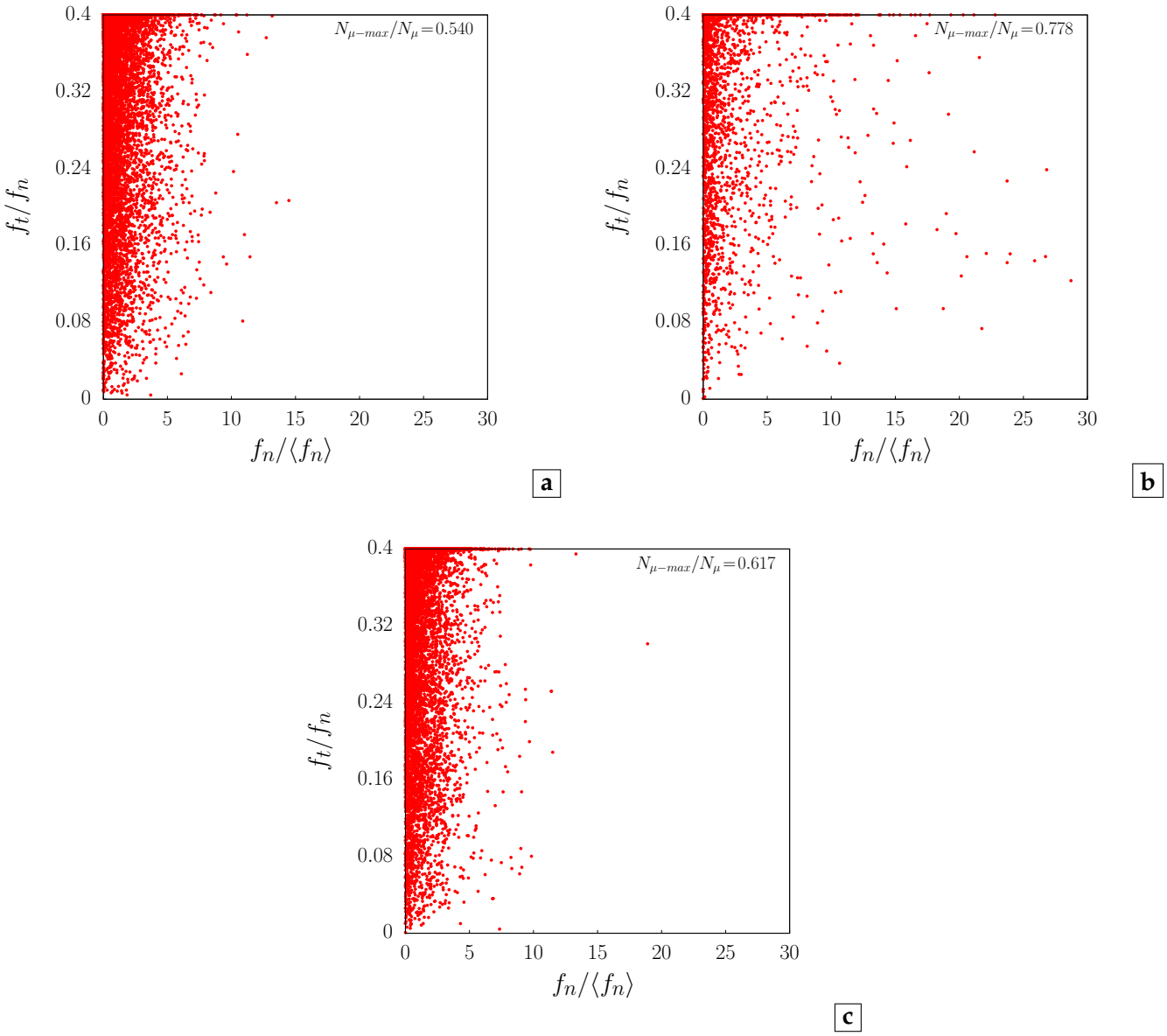

Figure 5.26 : Uniaxial compression. The status of the contacts: **a** – before the unloading, **b** – after the unloading and **c** – after the reloading in the case of the third UR cycle (see **Figure** 5.23). The simulation were made imposing a low angle of friction. The proportion of the contacts with a mobilised friction is given by $N_{\mu-max}/N_\mu$.

compression curve – the inset of **Figure** 5.23**b**. It is worth recalling that *Coulomb's* model of friction has been incorporated in the force laws, and therefore, the mobilised friction cannot exceed the friction coefficient set at $\mu = \mu_{wall} = \mu_{shell} = 0.4$ (modelling Oedo_Adjusted_Cyc see **Table** C.1). The normal contact force has been normalised by the average normal force acting between two parts $\langle f_n \rangle$. What concerns **Figure** 5.26:

Figure 5.26**a** – Before the unloading, the contacts were spread between the critical state and the elastic domain rather evenly. At this point, the sliding occurs in 54 % of all the contacts.

Figure 5.26**b** – Within the unloaded assembly, there still exist numerous elastic contacts, yet their contribution decreases in favour of the sliding contacts. The ratio $N_{\mu-max}/N_\mu$ rose up to 77.8 %. On the plot, the sliding points are visibly concentrated in the neighbourhood of the horizontal line $f(x) = \mu = 0.4$.

Figure 5.26**c** – Due to the reloading, $N_{\mu-max}/N_\mu$ decreased to 61.7 %, but it remained slightly

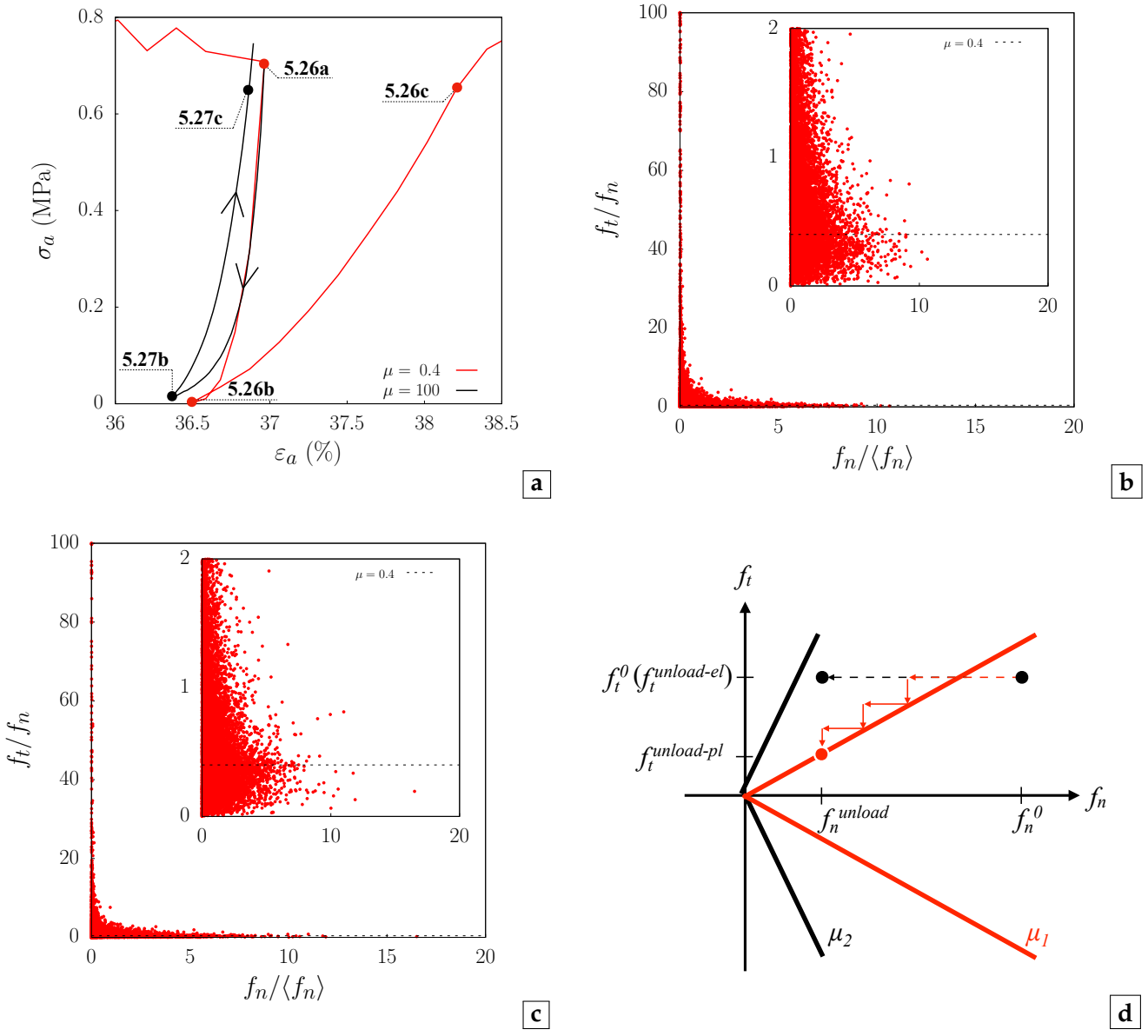

Figure 5.27 : a – The comparison of the mechanical responses to the UR for a low and high friction μ. **b and c** – The evolutions of contacts during the elastic unloading and reloading, respectively. The results for modelling with low angle of friction at the equivalent states were shown in the **Figure** 5.26**b** and 5.26**c**. **d** – A sketch explaining the influence of the friction coefficient ($\mu_2 > \mu_1$) on the micro-scale behaviour. The initial contact (f_n^0,f_t^0) can experience two various responses – either a plastic (red) or an elastic (black) unloading.

higher than the initial (unloading) value. Although the network has been modified, the contact balance between the elastic and sliding states has been restored to the starting point fairly close (**Figure 5.26a**). Those results clearly demonstrate that the sample responds to UR with some irreversible changes. Thus, the final step was a numerical repetition of the UR cycle with a high (unphysical) friction. **Figure 5.27b** shows that the $(3^{rd})'$ UR cycle has begun at the same compression state as the 3^{rd} cycle (**Table 5.5**). The friction coefficients have been risen up to $\mu = \mu_{wall} = \mu_{shell} = 100$, such that the angle of friction $\phi = 89.4°$. This approach serves two objectives: (*i*) a comparison of the mechanical behaviours and (*ii*) the observation of an enforced elastic response. **Figure 5.27a** shows the change in the stress-strain relationships focusing only on the 3^{rd} UR range. Initially, the same rapid stress drop was observed, but the curves diverged before the end of the unloading (in the non-linear phase). In **Figure 5.25a** (black curve) we observed that the number of contacts initially decreased with the same manner both for $\mu = 0.4$ and $\mu = 100$. At a given point, the number of contacts stabilised for the higher friction, such that the contact opening finished sooner. The shape of the elastic unloading curve (black curve), with a higher curvature, resemblances the experimental behaviour more accurately (the inset of **Figure 5.23a**). M_{oedo-} decreased towards more realistic value (**Tables 5.5** and **5.4**). Therefore, a higher elastic strain was recovered using a large angle of friction (about 26% more comparing to $\mu = 0.4$). On the contrary, the reloading phase exhibited too stiff behaviour. M_{oedo+} was so high that the consolidation stress was under-estimated. However, this proves that the response can be adjusted by a modification of the friction coefficient, which is believed to be highly inhomogeneous in the different parts of the shells (or the fragments) because of the strong variations of surface roughness. The black points in **5.26a** indicate the stress-strain states for which the analysis of a mobilised friction is shown in the **Figures 5.27b** and **5.27c**. As is seen, they correspond to states **5.26b** and **5.26c** of 3^{rd} UR (**Figure 5.26**). The dotted lines recall the previous low sliding limit $\mu = 0.4$. Since the starting point is identical as for the low friction, the initial status of the contact network shown in the **Figure 5.26a** is valid also in this case. Note that $\mu = 0.4$ is now a part of the elastic domain, *i.e.*, none of the contacts reached the sliding limit ($N_{\mu-max}/N_{\mu} = 0$). **Figure 5.27b** presents the state of affairs after the elastic unloading. The majority of the contacts remained within the elastic domain of the Coulomb's cone. In some rare cases, Coulomb's criterion has been satisfied, yet the amount of the sliding contacts was lower than $1‰$. In **Figure 5.27b**, the distribution of the points presents a decreasing tendency as the normal component of the force rises. In other words, the high friction is triggered mainly in the less compressed contacts. Although many of the tangential forces were high, the low friction coefficient $\mu = 0.4$ still stands out as a clear landmark, which is a display of the loading history[13]. **Figure 5.27c** confirms the elastic reloading of the sample. The spreading of data points has been hardly influenced by the increase of the macroscopic load. Those results combined with the observation from **Figures 5.26a** to **5.26c** suggest that mainly the normal component of the contact force decreases during the unloading. **Figure 5.27d** explains this concept. The black and red lines present the projection of Coulomb's failure surface for a high and a low friction coefficient ($\mu_2 > \mu_1$) in 2D $f_n \leftrightarrow f_t$ space. Initially, the point (f_n^0, f_t^0) lies within the elastic domain (before the unloading). Since the normal contact force is calculated using the actual contact geometry (based on the overlaps), f_n decreases with the unloading towards a possible separation ($f_n = 0$). Thus, the point migrates from f_n^0 towards f_n^{unload}. Due to the fact that the tangential force is calculated as an increment, the shear component remains almost constant. In the case of low friction (red line), the point drifts to the plastic domain as shown in the **Figure 5.27d**. At this point, thanks to *Coulomb's* model of friction, the interaction gets assigned to the critical state line (or a failure surface in 3D) such that $f_t = \mu_1 f_n$. If the unloading is carried on, this procedure is constantly repeated (a step

[13] Recall that before the UR cycle μ was set to 0.4

path in **Figure 5.27d**) till the interaction reaches a final state ($f_n^{unload}, f_t^{unload-pl}$). In other words, the elastic contacts reach the sliding (red point) only due to the decrease of f_n. For the high friction, the interaction remains within the elastic domain (black point), although f_t maintains its value constant $f_t^{unload-el} \approx f_t^0$.

The assemblies of shells *d18* and *d20*

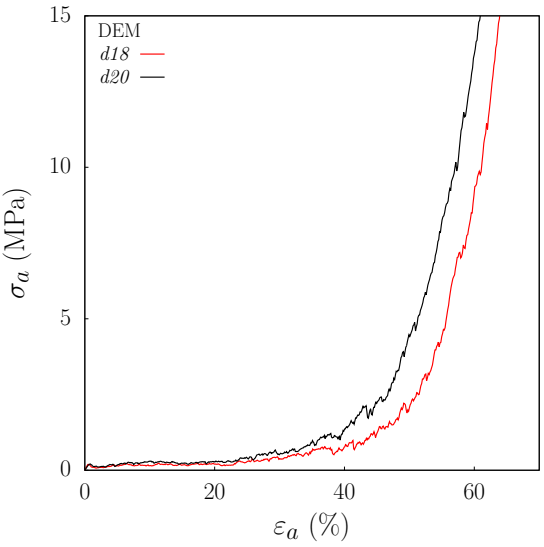

Figure 5.28 : The influence of a shell size. The mechanical behaviours were obtained using DEM simulations, but the experimental results for the assemblies consisting of the identical sizes were presented in **Figure 5.6**.

Figure 5.28 compares the mechanical behaviours for two dense packings of a different shell size: *d18* and *d20*. Note that **Figure 5.2** presented the equivalent experimental curves. The numerical parameters has been adjusted such that the true micro-mechanical aspects, *e.g.*, a shell strength, were captured representatively (see **Table C.1** for the modelling Oedo_*d18* and Oedo_*d20*). The experimental and numerical compression curves diverge (similarly as in the **Figure 5.6**). Since those discrepancies have been discussed hereinbefore, we addressed only the tendency resulting from the shell size. For a normally consolidated state, the oedometric modulus was calculated twice: at the beginning M'_{oed} and in the final phase of the uniaxial compression M''_{oed} (**Figure 5.23a**). The results are given in the **Table 5.6**. Initially, the sample composed of the bigger shells *d20* exhibited a higher stiffness, *i.e.*, M'_{oed} was higher. In this phase, the breakage is a crucial mechanism ruling mechanical behaviour. Thus, the stronger shells, crushing for the higher stress level, behave less compressible. M'_{oed} was 26.9 % bigger than the one found for the size *d18*. A similar observation concerns the discrete modelling with the difference of 41.2 %.

Shell size	M'_{oed} (MPa)	M''_{oed} (MPa)
Experiments		
d18	2.6	78.2
d20	3.3	70.6
DEM		
d18	1.2	118.0
d20	1.7	100.2

Table 5.6 : The evolution of compressibility depending on the shell size for 1D axial compression of a dense sample. The initial M'_{oed} and the final M''_{oed} moduli were marked in the **Figure 5.23a**.

Once the primary breakage of shells was highly advanced ($b > 0.95$), the breakage of the parts could progress but it required a fairly high stress level. Therefore, mainly the reduction of the inter-cluster void ratio was present within the assembly. The higher is ε_a, the lower is the discrepancy between the mechanical responses (**Figure 5.28**). Numerically, the difference (*d18 vs. d20*) of the moduli M''_{oed} decreases to 17.8 %, and experimentally to 10.8 %. Although all the shells were crushed in both cases, the differences between the arrangements and the size distributions should naturally occur. Thus, M''_{oed} were still not fully equal for $\sigma_a = 15$ MPa. For a respectively higher stress level, those moduli should finally even out each other. That is to happen when the mechanical response will depend only on the stiffness of the backed clay, and the deformation will approach the physical strain limit (the breakage of the fragment does not appear any longer).

5.2 Summary

The current section discussed the mechanical response to a medium-pressure oedometric compression. The parametric study allowed us to adjust reliably the numerical parameters, test the in-

fluence of the initial state of a sample and discover the model limitations due to the geometry of the sectors:

- The computation time has been reduced by the use of smaller sample size, and thereby, the total number of sectors in the sample.
- Among all the force law parameters, two yield thresholds $f_I^\star$ and $f_{II}^\star$ controlling the shell strength occurred to be of the greatest importance to the mechanical behaviour. The average strength of shells controls the sample strength, whereas the variability of strength plays a secondary role.
- Denser samples presented initial stress peak unless a stress-controlled loading was applied. Despite the strain-control, in the loose samples, this initial local peak has not been observed, presumably, due to shell rearrangements.
- The vertically oriented shells caused high oscillation in the mechanical response (more precisely, in the stress evolution). On the contrary, horizontal shells seemed to arrange into a rather loose assembly, which presents a smooth mechanical response.
- Generating the model with more sectors in the axial direction of the shell increased the strain range enhancing the model validity but making the computations more time-consuming. The increase of the circumferential number of sectors did not bring any other benefit, however, we believe that it is more fruitful when combining both the more detail axial and more detail circumferential discretisation at the same time.
- A significant change in the shell geometry need to be accompanied by a generation of adequate sector size.
- The model correctly reflects the experimental shells size dependency. It is supported by the analysis of the oedometric moduli for the shells *d18* and *d20*.
- We successfully managed to reproduce the macro-mechanical response to 1D compression, but the model mismatch the experimental estimations of the micro-mechanical parameters and the true initial density.
- The final modelling included the unloading and reloading cycles. UR cycle correctly reproduced the character (the shape and the tendencies) of the response, but the values of the friction coefficient during UR should vary between the normally consolidated and over-consolidated states to fit the real UR oedometric moduli. A deeper DE analysis showed that the contact openings during the unloading lead to an increase of sliding contacts in the model.

Oedometer: from micro observations to macro analytical model for stress-strain predictions

Contents

Introduction

Grains breakage is known to be of great importance for understanding the mechanics of granular materials for a long time.
" [...] in order to understand the physics of the strength and stress-strain behaviour of soils and to devise mathematical models that adequately represent such behaviour, it is important to define the degree to which the particles of an element of soil are crushed or broken."
Following this statement, Hardin (1985) discussed quantifying the breakage of particles with a relative breakage B_r – a parameter calculated using the grain size distribution. Since then, the concept of relative breakage has been modified and applied in other studies as summarised by Einav (2007a). In the case of one-dimensional compression, grains breakage contributes to the reduction of volume, especially in highly porous materials. Bolton and McDowell (1997) presented the volumetric changes as a consequence of grain breakage in aggregates of uniform brittle grains. More recent studies, *e.g.*, the numerical investigation made by Laufer (2015), also demonstrated that the landmarks on the stress–stain relationship correspond to a certain amount of breakage. Therefore, the lack of breakage representation in the model leads to the deviation of mechanical response from the reality (Karatza, 2017). Section **6.1** relates to those aspects. Firstly, the mechanical behaviour is commented in the context of breakage evolution. Secondly, the growth of breakage in one-dimensional compression is presented as a function of shell strength including the effect of anisotropy caused by the orientation of shells.

Section **6.2** investigates the evolution breakage in detail using grain size distribution (GDS). The numerical GDS framework has been adapted in order to be compared with the experimental result. The importance of micro-mechanics for the macroscopic evolution of breakage has been determined. Finally, more detailed analysis of GDS supplements the experimental observations.

The evolution of fabric anisotropy using only shell and parts orientations has been presented in section **6.3**. The major difficulty of fabric analysis using the contact network has been discussed taking into account the model characteristic. As a consequence, the alternative analysis of micro-stress applied to the fragments instead of contact forces has been performed.

Section **6.4** focuses on high compressibility of breakable shells. The attention has been dedicated to the evolution of the consolidation curves, *i.e.*, the void ratio as a function of axial stress (in semi-logarithmic scale). The reduction of voids was also shown with respect to the axial deformations. Then, the geometric exclusions accounted for the necessity of defining a modified void ratio $e^\star$. Within this new framework, the modified consolidation curves presented non-classic evolution with a temporary increase of void volume. Therefore, the large volume of internal "pores" explained the highly compressible response.

Those results have actually led to an attempt of predicting the inter-granular void ratio in section **6.5**. This section has been organised in two parts **6.5.1** and **6.5.2** dedicating the prediction model separately to strain and stress (respectively). Whereas the predictions based on the strain evolution are rather discarded, many researchers attempted to build a constitutive model, acknowledging the breakage of constituent particles, to foresee the classic consolidation curve (Bauer, 1996; Einav, 2007b; Hu et al., 2011). In section **6.5.2**, we have attempted to relate to the constitutive model proposed by Bauer (1996) and show its applicability range in the case of shells.

List of symbols and abbreviations

Symbol / Abbreviation	Explanation
Section **6.1**	
ε_a	Axial strain (MPa)
σ_a	Axial stress (MPa)
B_r	Relative breakage (used in the literature)
b	Primary breakage level
$f_I^\star$	Normal yield threshold in pure tension for link (N)
$f_{II}^\star$	Tangential yield threshold in pure share for link (N)
Section **6.2**	
cdf	Cumulative Density Function
GDS	Grain Size Dsistribution
pdf	Probability Density Function
$\sum I_{ij}$	Number of breakable interfaces in the tube-cluster/sub-cluster
d	Diameter of ring in the shell cross-section – typical grain size (mm)
F_I	Critical diametrical load causing the tensile breakage (N)
h	Heigh of shell in the axial direction of tube (mm)
$\langle m_{d18} \rangle$	True average mass of shell in the size $d18$
Section **6.3**	
α	Inclination of sectors with respect to global vertical axis Y (°)
β	Inclination of sectors with respect to global horizontal axis X (°)
$\Delta\beta$	Rotation of grain orientation towards the horizontal axis (°)
$\varepsilon_x, \varepsilon_y, \varepsilon_z$	Macroscopic strain in X, Y, Z axis (%)
$\gamma_{xy}, \gamma xz$	Macroscopic shear strain in XYZ coordinate system (°)
$\boldsymbol{\sigma}_i$	Stress tensor of the cluster (or the sub-cluster) i (MPa)
$\check{a}$	Power in the law used for the low local stresses
$\hat{a}$	Pre-factor of variable in the exponential law used for the high local stresses
a_2	Anisotropy parameter for the assembly (Legendre's polynomials)
$(a_2)_0$	Initial anisotropy parameter
$\vec{f}_n$	Contact/link force (N)
$\vec{l}$	Branch vector (m)
l_n	Normal scalar component of branch vector (m)
l_t	Tangential scalar component of branch vector (m)
$\vec{n}$	Unit vector in normal direction of interaction
p	Mean pressure of the cluster (or the sub-cluster) (MPa)
$\vec{r}$	Position of a contact and/or link (m)
$\vec{t}$	Unit vector in tangential direction of interaction
V_i	Volume of the constituent i: a shell or a fragment (m^3)
Section **6.4**	
μ	Inter-cluster friction coefficient
e	Void ratio (standard definition)
$e^\star$	Inter-shell void ratio (modified definition)
V_s	Volume of solid phase in the assembly (m^3)

Continued on next page...

Symbol / Abbreviation	Explanation
V_{tot}	Total volume of sample (m^3)
V_v	Volume of voids and pores in a sample (m^3)
$V^\star$	Volume of all the intrinsic voids in intact tube-shells (m^3)
Section **6.5.1**	
b	Primary breakage level
E_0	Microscopic void ratio analysing only shell
e	Void ratio (standard definition)
e_0	Initial void ratio
$e^\star$	Inter-shell void ratio (modified definition)
N	Initial total number of shells
N_{broken}	Current number of broken shells
V_s^i	Volume of the solid of tube per shell (mm^3)
V_v^i	Volume of internal void of tube (mm^3)
$(V_{tot})_0$	Initial total volume of sample (m^3)
Section **6.5.2**	
$\hookleftarrow$	Super-script of variable referring to behaviour before the inflexion point
$\hookrightarrow$	Super-script of variable referring to behaviour after the inflexion point
Δe	Maximum reduction of void ratio in oedometr test
σ_b	Axial macroscopic stress when any b is reached (MPa)
σ_{50}	Axial macroscopic stress at the inflexion point (MPa)
σ_{peak}	Axial macroscopic stress for the peak of $e^\star \leftrightarrow \sigma_a$ curve (MPa)
σ_{ref}	Reference axial stress – scale parameter for b-evolution (MPa)
$\breve{a}$	Linear slope (for the $\sigma \leftrightarrow F_I$ relationship)
e_0	Initial void ratio
e_{fin}	Final void ratio
h_s	Soil hardness
m	Shape parameter (primary breakage evolution)
n	Shape parameter (compression curve)

If a symbol or an abbreviations is not distinguished in the current section, please search in the previous sections.

6.1 Study of mechanical behaviour as a consequence of grain breakage

Among all performed simulations, the analysis of breakage focuses mainly on two uniaxial compressions performed on:

- initially loose sample with parameters adjusted such that the macroscopic behaviour reflects properly the experiment. Yet the microscopic strength of shells found in the experimental campaign was ignored – Oedo_Adjusted,
- sample with number density determined experimentally. Although the strength thresholds applied in the modelling respect the true values, the mechanical behaviour diverges from experiment one – Oedo_True.

Contributory observations will be presented using other simulations, yet, their analysis is of supplement character.

Figures 6.1a and **6.1b** present the non-linear evolution of breakage level b (red curves) as a function of axial strain ε_a for loose and dense sample, respectively. **Figures 6.1c** and **6.1d** show the same growth of breakage degree, yet, with respect to the axial stress σ_a using a semi-logarithmic space. The black lines recall the compression curves.

Naturally, the value of ultimate accessible strain is affected by (*i*) the density of initial arrangement and (*ii*) shell breakage. Therefore, the evolution of breakage with respect to axial strain is of great interest. The analysis was based on breakage parameter b, which is a function of only intact shells breakage. In other words, the secondary breakage of smaller particles, that are not tube-shaped any longer, has been ignored. Note that the breakage level has been already introduced in section **5.1.6** by the equation (5.8). The evolution diverges from dense to loose packing, yet it rises with a similar trend – a rapid increase (phases Ⓘ and Ⓘ) followed by slower non-linear transition towards threshold $b = 1$ (phase Ⓘ).
For axial stress equal to 15 MPa, the axial strain are about 6.7 % lower in case of the dense sample (**Figures 6.1b**). Almost half of the strain difference arises in the initial phase Ⓘ corresponding to the onset of breakage with $0 \leq b \leq 0.05$. Note that phase Ⓘ in **Figure 6.1b** corresponds to phase ① in **Figure 6.1d**. As is seen, the initial stress peak, in dense packing, appears during this initial phase. Low inter-granular space limits the re-arrangements of shells, and therefore, the stress mounts up rapidly. The significant breakage begins when an adequate amount of energy is accumulated in the sample. Due to higher initial stiffness, the energy triggering the shell breakage is accumulated faster in dense configuration – for almost five times lower strain. As breakage releases the energy accumulated in shell, the sudden and dynamic breakage causes stress softening, when entering phase Ⓘ. Although experimental samples are classified as dense, the stress peak has not been observed in mechanical behaviour. Plausibly, there exist some plastic deformations known to dissipate the energy as well. The shells might experience some local damage in the contact zone like crumbling. Yet, the model is incapable of representing this type of local, surface damage or the contact adjustment. It also does not take the plastic flow into account. A similar observation has been already pointed out for the mechanical response to single shell compression.

In zone Ⓘ, the progress of breakage is uniform and quite proportional to increase of axial strain. A straight line with slope, equal to 0.022, has been found to successfully describe the trend both in *adjusted* and in *true* samples. Averaging the tendency (over many simulations), 1 % of axial deformation corresponds to increase of breakage ratio of 2 % despite different initial densities. This suggests that the macroscopic strain in this phase is quasi-fully ruled by the breakage. The strain growth is affected equally due to the fact that the amount of released void volume (locked within the intact shell) is of the same order.
Phase Ⓘ starts when the breakage rate begin to decrease gradually. $\sim$ 25 % of shells in the case of loose sample and only 10% for the denser sample were still to break. The transition progress

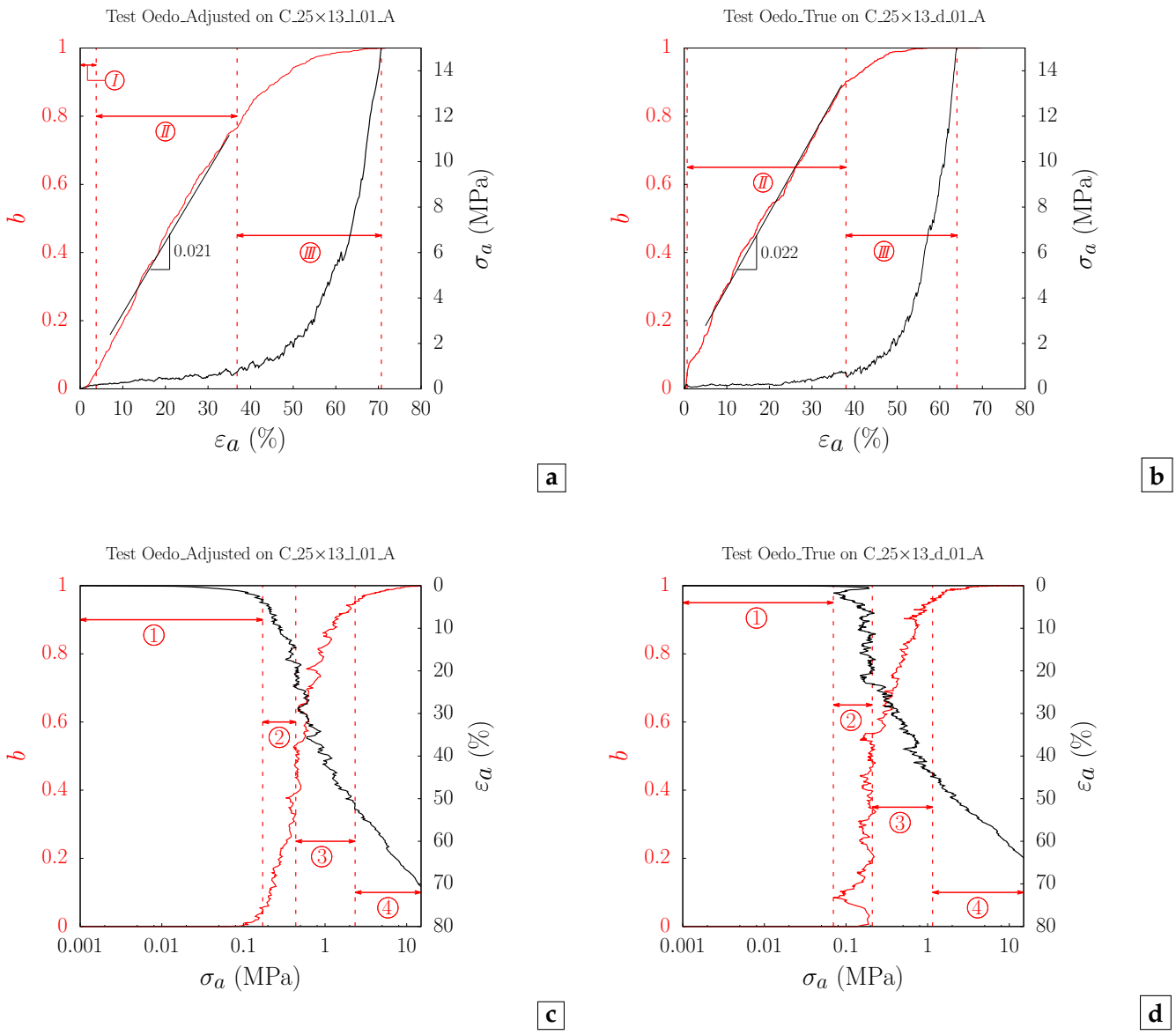

Figure 6.1 : Influence of broken shells ratio b on the mechanical behaviour for the loose (**a** and **c** – Weibull distribution such that $f_I^\star = 190$ N for $cdf(f_I^\star) = 0.37$) and dense (**b** and **d** – $f_I^\star = 85$ N) samples.
a and **b** – Three phases were distinguished for the axial strain as a reference: Ⅰ – the lack or the onset of breakage, Ⅱ – a linear growth, and Ⅲ – a non-linear inhibition of breakage.
c and **d** – Four breakage zones were considered for σ_a as a reference: ① – $b \leq 0.05$, ② – $0.05 < b \leq 0.5$, ③ – $0.5 < b \leq 0.95$ and ④ – $0.95 < b \leq 1$.

faster in a dense configuration. Yet, this difference might originate from higher average shell strength and wide Weibull distribution imposed in the adjusted modelling (**Figure 6.1a**). Essentially, the plot proves that breakage controls the large strain in the oedometric compression and significantly influences the compressibility of this material. Intense breakage with almost linear trend results in low but constant stiffness of the sample while loading (see the analysis of M_{oedo} in section **5.1.6**). Yet, when it slows down non-linearly, also the mechanical behaviour of samples gradually tends towards the stiff response. The macro-mechanical behaviour of crushable granular matter has been reported as a consequence of breakage over the decades. Bolton and McDowell (1997) have com-

mented on the shape of compression curve using clastic mechanics base on fractal fragmentation (Turcotte, 1986). More recent DEM study, made by Laufer (2015), provides similar numerical observations. Bolton et al. (2008) showed the DEM simulations of sand aggregates with and without particles crushing, thereby highlighting the necessity of modelling breakage once more. Nowadays, also the experimental work supplements the numerical study, *e.g.*, Guida et al. (2018). All those examples referred to uniaxial compression, and each of them has presented similar behaviour using compression curve in a semi-logarithmic scale as we presented, hereinbefore, in **Figures 6.1c** and **6.1d**. To demonstrate the influence of axial stress on the evolution of breakage four different breakage phases has been marked in the **Figures 6.1c** and **6.1d**. They have been established using three characteristic values of b: 0.05, 0.50 and 0.95 (presented by vertical dotted lines). Note that those values are approximation among many numerical simulations.

① – The onset of breakage caused by the failure of the weakest shells within the assembly. Since the tensile strength is the lowest of material resistances, the shells are expected to fail in tension. It is referred to as *clastic yielding* after Bolton and McDowell (1997). It has been detected due to a visible decrease of hardening rate and it has been determined at the average $b \approx 0.05$. The sample densified mainly due to the reduction of the inter-granular void volume. Thus, the mechanical behaviour in this regime is strongly influenced by the initial state of assembly.

② – The material presents an inherent variation of tensile strength (recall **Figures 3.13** and **5.14**). Thus, this phase begins when the macroscopic loading σ_a creates a microscopic load leading to the breakage of many shells. Therefore, the parameter b mounted up rapidly with an exponential manner. Then, many internal voids initially blocked in the shells, became accessible. As a consequence, the inter-granular free space was constantly enlarged and its highly compressible behaviour of material was triggered in this regime. A *clastic hardening* is clearly visible in case of the loose sample, whereas for dense packing the hardening rate was lower, such that rather a plateau was formed. This term is equivalent to plastic hardening, yet underlines that fact that the irreversible behaviour is a result of grains crushing. The constant and monotonous increase of stress is a result of both higher shell strength (guaranteed by survival probability) and increase of coordination number of the packing **Figure 5.24**).

③ – A transition between phase ② and ③ can be referred to as an *inflexion point*. We have estimated it for $b \approx 0.5$ alike in the study of Laufer (2015). Experimentally, for example, Guida et al. (2018) have found it at 0.4 for LECA with highly porous grains. The inflexion point in some cases might be successfully determined within the small range of b, depending on the strength variability and the shell arrangement within the assembly. Once the inflexion stress is reached, the trend of breakage curve $b \leftrightarrow \sigma_a$ is modified (the convex part of the curve) and the breakage develops less rapidly. Due to the increase of the coordination number, the particles should be more isotopically load, and therefore, less prone to break. Those changes are reflected by the mechanical response that also starts to change. The clastic hardening evolves non-linearly increasing the hardening rate. This indicates that the frictional interactions become more and more significant.

④ – Last phase starts, approximately, when b is equal to 0.95. The breakage of shells is of secondary importance to mechanical behaviour as the end comminution is approached. The small amount of voids does not affect the current sample density. The sample presents high stiffness as it is composed mainly of small resistant parts (sub-clusters) and "rigid" unattached sectors. Due to sector size and ultimate size distribution, the model will tend asymptotically to its limit.

Focusing on the first aspect, the comparison curves from **Figures 6.1c** and **6.1d** indicates that stress level for which the specific amount of breakage b is reached depends on the strength of constituent shells. This observation has been tested further using initially loose assembly for different normal force threshold $f_I^\star$ without its variation. Simultaneously, the equivalent modelling was performed on dense samples (see **Fig-**

ure 5.15). Among those simulations, **Figure 6.2** presents the growth of breakage ratio for selected modelling made on initially:

- loose samples (l) – Oedo_l_$f_I^\star$-85, Oedo_l_$f_I^\star$-150 and Oedo_l_$f_I^\star$-225
- dense sample (d) – Oedo_$f_I^\star$-40.

Detailed numerical parameters are enclosed in **Table C.1** (**Appendix C**).

As is seen, despite the peculiar shell shape, the breakage phenomena ruling mechanical behaviour is rather a standard response presented by many granular materials used in geotechnics. The differences in compressive behaviour originate from the material properties – the shell strength and the ability of the assembly to compresses.

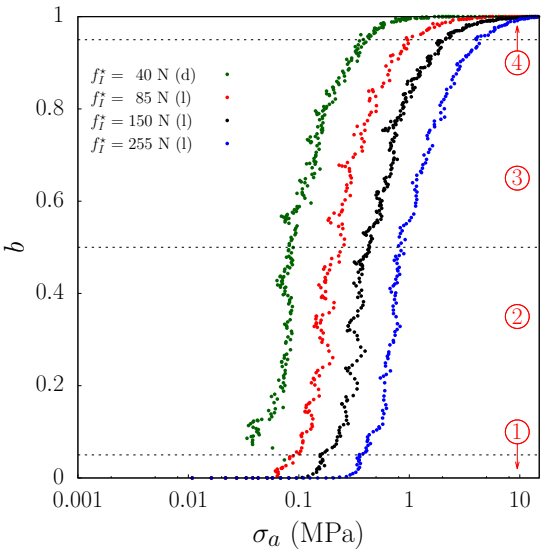

Figure 6.2 : The evolution of primary breakage is influenced by the tensile strength of the shell, which is controlled by the limit of normal force $f_I^\star$. She shear strength of shells was established by the proportion: $f_I^\star / f_{II}^\star = 0.34$. Introduced notation: (l) – loose and (d) – dense configuration.

In **Figure 6.2**, one can observe that the breakage grew with similar rate up to $b = 0.95$ in all the cases. There exists a standard evolution with the trend shape separated into two parts: (*i*) concave – an increase of breakage rate before the inflexion point $b \approx 0.5$, and (*ii*) convex – slowing down of breakage rate after the inflexion point. The curves are just horizontally shifted towards higher stresses when the strength of shells increases. Therefore, the onset of breakage, the inflexion point and the comminution limit are the functions of shell strength. Also, a constitutive model of Bauer (1996) has employed the soil hardness h_s (stress at the inflexion point), and accompanying Gudehus (1996) has stated that it is proportional to the strength of constituent particles. Then, in phase ④ there is a visible growth-inhibiting, such that the suppression of breakage is slower for "stronger" samples. However, the semi-logarithmic representation distorts the proportion. Practically, composing the layer of stronger shells makes it more suitable for very high loads since its compressibility is active for a wider loading range. Although **Figure 6.2** only indicates the following observation, the evolution of breakage with respect to stress ($b \leftrightarrow \sigma_a$) has been found independent of initial density. Similarly, in the continuum breakage mechanics (CBM) model presented by Einav (2007b) the growth of $B_r \leftrightarrow \sigma$ is material strength dependent.

As is presented in section **4.3.2**, the initial density is not sufficient to describe the initial state. Hence, the analysis has been carried on by taking into account more anisotropic arrangements[1] (**Figure 6.3**). Following observations were based on the simulations Oedo_r, Oedo_v, Oedo_V, Oedo_h and Oedo_H with mechanical behaviour presented in **Figure 5.19**. Although the shells were equally strong, their orientations have affected the breakage mechanics of assembly. Firstly, horizontal shells failed at lower macroscopic stress level than vertically oriented ones as shown in **Figure 6.3a**. This tendency might originate from the fact that the tangential strength of bonded interactions $f_{II}^\star$ is much higher than normal force threshold $f_I^\star$. In other words, the shell is more resistant to shear or compression (for axial loading) than tension (for radial loading). Furthermore, the direction of microscopic loading will cause different mode of fracture. Considering assembly under oedometric compression, one can expect that major loading acts axially for the vertically ori-

[1] We refer to the anisotropy of sector orientations.

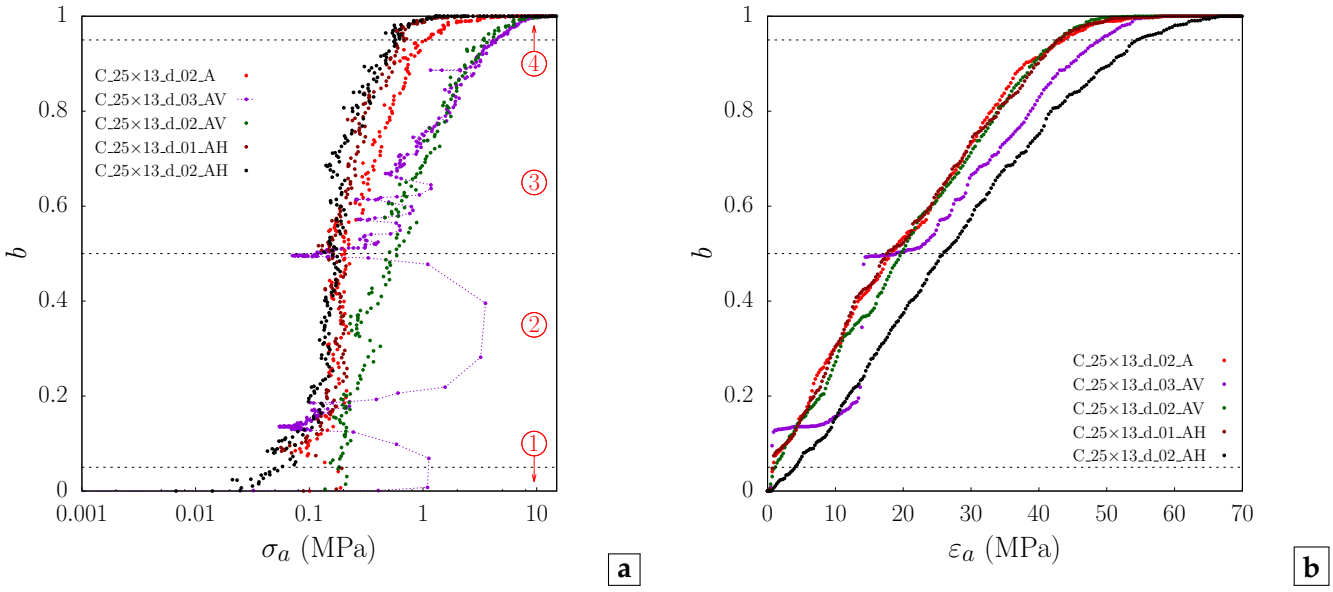

Figure 6.3 : The orientation anisotropy changes the evolution of breakage b: **a** – Horizontal preferential orientation result in higher breakage rate (C_25×13_d_01_AH, C_25×13_d_02_AH) indicating failure due to tensile stress, whereas in the vertically oriented samples (C_25×13_d_02_AV, C_25×13_d_03_AV) the breakage grows slower because shells are stronger in the axial. More homogeneous samples (with isotopic core) C_25×13_d_02_A used in Oedo_r are found in between. **b** – Evolution of breakage with respect too strain shows the influence of density and exposes the step evolution for highly vertical oriented assembly C_25×13_d_03_AV (see **Figures** 4.24 and 5.19).

ented shells, while horizontal shells will be loaded mainly radially. Then, the higher strength of vertical oriented shell assemblies is a natural consequence. Secondly, the kinematics of breakage has been modified with respect to more isotopic assembly C_25×13_d_02_A (**Figure** 6.3**a**). The breakage rate is respectively higher in case of horizontally oriented shells, and for the assembly of vertical shells, the ratio b rises slower – the breakage curve mounts up less steep. Within randomly oriented samples (C_25×13_d_02_A), the majority of shells were oriented horizontally (recall **Figure** 4.22**a**). Then, the evolution of b suggests that horizontal shells break first because the breakage evolves initially with the similar trend as for C_25×13_d_01_AH and C_25×13_d_02_AH (phases ① and ②). Afterwards, the breakage curve tends towards the behaviour of vertically oriented samples (C_25×13_d_02_AV and C_25×13_d_03_AV). That is due to the significant presence of vertically inclined shells. Finally, **Figure** 6.3**a** shows that strong vertical anisotropy – C_25×13_d_03_AV – leads to large oscillations of axial stress (for $0 \leq b \leq 0.7$). For the sake of clarity, b was shown also as a function of axial strain in **Figure** 6.3**b**. Due to the creation and sudden rupture of strong force chains formed within the sample, the breakage ratio mounts up following a step trend. Once, the brake becomes secondary to mechanical behaviour, the breakage curve develops continuously and the oscillations of stresses disappear. Similar behaviour has been reported in section 5.1.2 for sample with very low hight (35×5) as was shown in the **Figure** 5.8**a**. The variety of responses in **Figure** 6.2**b** is connected with different initial densities n (**Table** 4.10).

As mentioned, the breakage level b quantifies the primary (first) breakage of shells, which leads to release the access to the internal voids of tubes, but b ignores the progressive breakage of the fragments. This gap needs to be filled by a supplementary analysis.

6.2 Progressive breakage *via* grain size distributions (GDS)

Grain size distribution (GSD) and its evolution along the compression test provide a detailed insight into the secondary breakage throughout the fragment sizes. Sieve analysis is commonly used to characterise the size distribution of granular materials. If the grains pass through a sieve, hereinafter with a square grid, the average grain diameter corresponds to the grid size and is associated to the smallest cross-section of grains. Then, GSD is build upon the mass of a set of grains smaller than a given diameter. Whereas this approach to GSD is widely accepted to describe the size of the grains for granular geo-materials like sand, it is more questionable in the study of the GDS of broken shells. The mass of intact shell can be equal even to double mass the broken piece, although both are in the same sieve size as illustrated in **Table 6.1** for sieve size 17.0 mm (last row). For the sake of experimental simplicity, the GSD based on the grain weights was kept. Herein, the objectives are (*i*) to compare the GSDs of experimental and numerical samples all along the uniaxial compression test (respecting the axial stresses) and (*ii*) to supplement the experimental results (*e.g.*, knowing the number of broken shells), whatever the incongruity of the classical GSD analysis on broken shells with very concave shapes is.

The experimental campaign, dedicated to shell breakage in uniaxial compression, was performed at Laboratory *Navier* (Paris-Est). We have joined team CERMES to characterise shell breakage at the early stage of the uniaxial test (for at low-stress level), yet, the loading system is capable of applying the load up to 7 MPa, and therefore, more data were provided for our comparison. The samples (without coating) were prepared using the shell size *d18* with the following protocol. First, an assembly with a mass equal to 5.15kg $\pm$ 0.05kg has been measured. Then, it was poured in a mould with a diameter of 30 cm, such that the height of the sample was approximately 13.5 cm. Using an average mass of shell ($\langle m_{d18} \rangle = 0.0035$ kg), a number density n was estimated at $154\,151 \pm 1\,497$. To verify this number, n was found at 152 684. Although the estimation was burden with rather high error, both the estimation and the real value are in agreement with previous measurements $151\,384 \pm 1\,319$ (**Table 4.3** in section **4.1**). At this point, the top surface of the specimen was uneven, and therefore, it was refined using a light wooden piece, later replaced by a heavier metal platen (the influence of its weight has been balanced in the measurements).

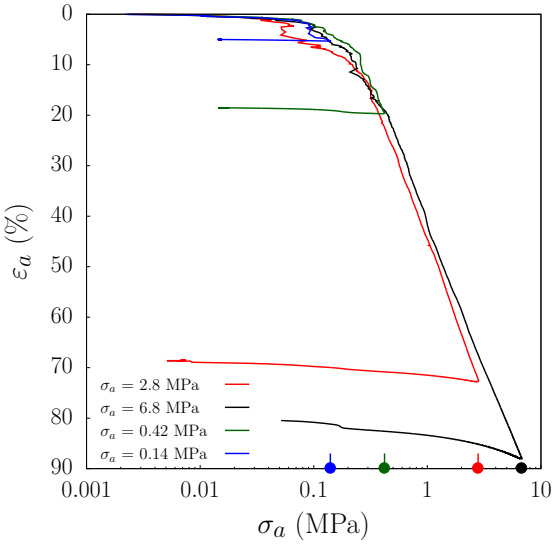

Figure 6.4 : The experimental mechanical responses to uniaxial compression. Each test was finished at a different stress level (the dots on the σ_a-axis). The experiments were conducted in Laboratory *Navier* on sample 30×13.5 (in cm) composed of shells *d*18.

The uniaxial compression was performed with stress-control, increasing force by 0.05 kN (0.7 kPa) per second. **Figure 6.4** presents at which point of uniaxial compression each test was finished (the dots on the σ_a-axis). The onset of breakage was captured at $\sigma_a = 0.14$ MPa and later for $\sigma_a = 0.42$ MPa. Once the sample has been disassembled (**Figure 6.5a**), the sieve analysis, commonly used procedure to assess the particles gradation in granular material, was performed. The material passed through a series of sieves of progressively smaller mesh size [2]: 16, 12.5, 5 and 1 mm (**Figure 6.5b**). The weight of material stopped by each sieve was calculated as a proportion to the whole sample mass, such that the grad-

[2] With the square mesh.

a

b

Figure 6.5 : The oedometer test finished at $\sigma_a = 0.42$ MPa (**Figure** 6.4): **a** – A view of the top surface after the test (in contact with the loading plate), and **b** – The fragments divided into the sieve sizes (**Figure** 6.6).

ing curves for all the tests were drawn. The evolution of GSD shown in the **Figures** 6.6**a** and 6.6**b** (point-lines) is compared it with numerical data from modelling: Oedo_True and Oedo_Adjusted, respectively (**Figure** 6.1).

Part	$\sum I_{ij}$	Sieve size (mm)
	0	4.2
	1	8.2
	2	11.7
	3	14.4
	4	16.3
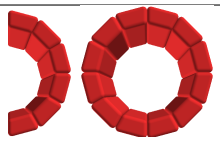	$5-11$	17.0

Table 6.1 : The numerical sieve sizes for shell with $t = 2.4$ mm and $N^\star = N^\star_{circ} = 12$ (cluster shape *d18*-S1). The sieve sizes are ruled by the number of linked sectors within the part. $\sum I_{ij}$ – is a number of the interfaces to be broken per shell/fragment (see equation 5.9).

Although we reduced measurements to only five sieve sizes, actually, the fractions include a range of possible sizes as is seen in the **Figure** 6.5**b**. Thus, the experimental GSD curves can be presented as continuous lines, or in our case the point-lines with points being the actual measurements and lines showing rough, linear interpolations (**Figure** 6.6). Construction of numerical GSD requires a basic simplification due to the discretisation of shape into sectors. Therefore, to establish the numerical sieve sizes the longitudinal size h of sectors was ignored (as if the parts passed the sieve vertically) in favour of the radial cross-section. As shown in **Table** 6.1, the sieve sizes are ruled by a number of linked sectors within the part. Then, it is a precise measurement in size (instead of the fraction) and can be successfully considered either as passing through or staying at sieve. Due to this discrete character, the zones within which an experimental measurement could be located were predicted (dashed areas in **Figure** 6.6). First of all, **Figure** 6.6 clearly demonstrates the model limitation throughout the applicable range of sieve sizes. As already discussed thereinbefore, it is due to sector size (**Table** 6.1). Whereas numerically only coarse-grained assembly can be obtained (larger or equal 4.2 mm), in the experiments also fine fraction (<1 mm) was observed (**Figure** 6.5**b**). Numerically, the focus of this section was limited to only two simulations performed with different sets of micro-mechanical parameters. **Figure** 6.6**a** shows that the results remain in a good agreement with experiments when the shell strength respect the reality, that is $f_I^\star = 85$ N (or $F_I \approx 120$ N). On the contrary, although the macro-mechanical behaviour

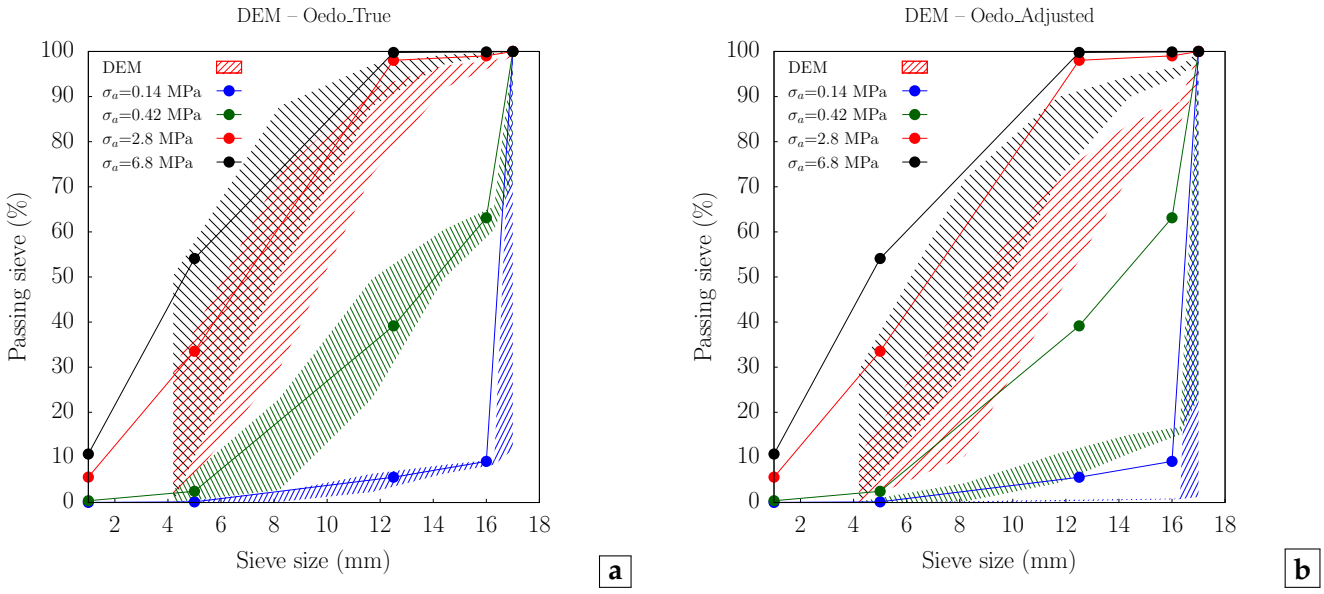

Figure 6.6 : Experimental grain size distributions for different stress states (**Figure** 6.4) were compared with the numerical data from: **a** – Oedo_Adjusted and **b** – Oedo_True (**Figure** 6.1). Experimental sieve curves are presented by the point-lines with points being the actual measurements. Whereas experimentally the GSD curves(**Figure** 6.5**b**) can be assumed as continuous lines, in the DEM model the grading curves have a discrete character. Therefore, the continuous prediction zone were created using those desecrate data.

for Oedo_Adjusted has been adapted, **Figure** 6.6**b** exposes that the micro-mechanics does not reflect the true breakage evolution. DEM sieve zones mismatch the experimental results completely. At the shell scale, the breakage appears too late (for higher axial stress), since the Weibull distribution with $pdf(f_I^\star = 190) = 1/\mathrm{e}$ has been applied. Thus, the shells are twice as strong as in reality.

To show the numerical evolution of GSD the zones were replotted respecting their discrete manner (with points) in **Figures** 6.7**a** and 6.7**b**. Note that, this time, the points were connected with dashed lines, just for the sake of transparency. 14 different breakage levels were selected between the beginning ($b = 0.00$) of uniaxial compressions and its end, when $\sigma_a \approx 17$ MPa and $b = 1.00$. Above all, it is remarkable to observe that, despite the model limitation, the GDS curves evolve experimentally and numerically in a similar manner. Initially, the sample is uniformly-

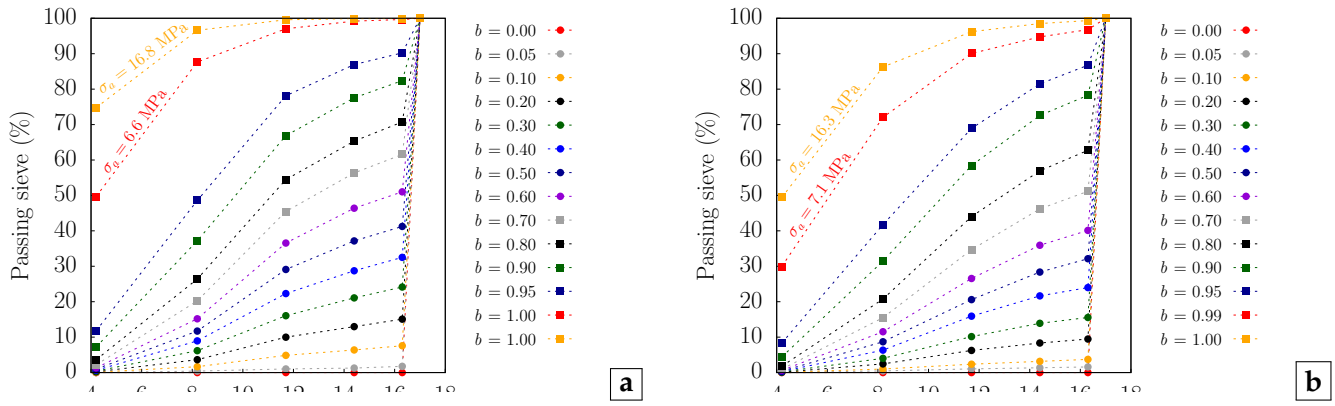

Figure 6.7 : Evolution of grain size distribution curves in the uniaxial compressions: **a** – Oedo_Adjusted and **b** – Oedo_True (**Figure** 6.1). Different primary breakage level b has been selected to show the changes within each sieve fraction.

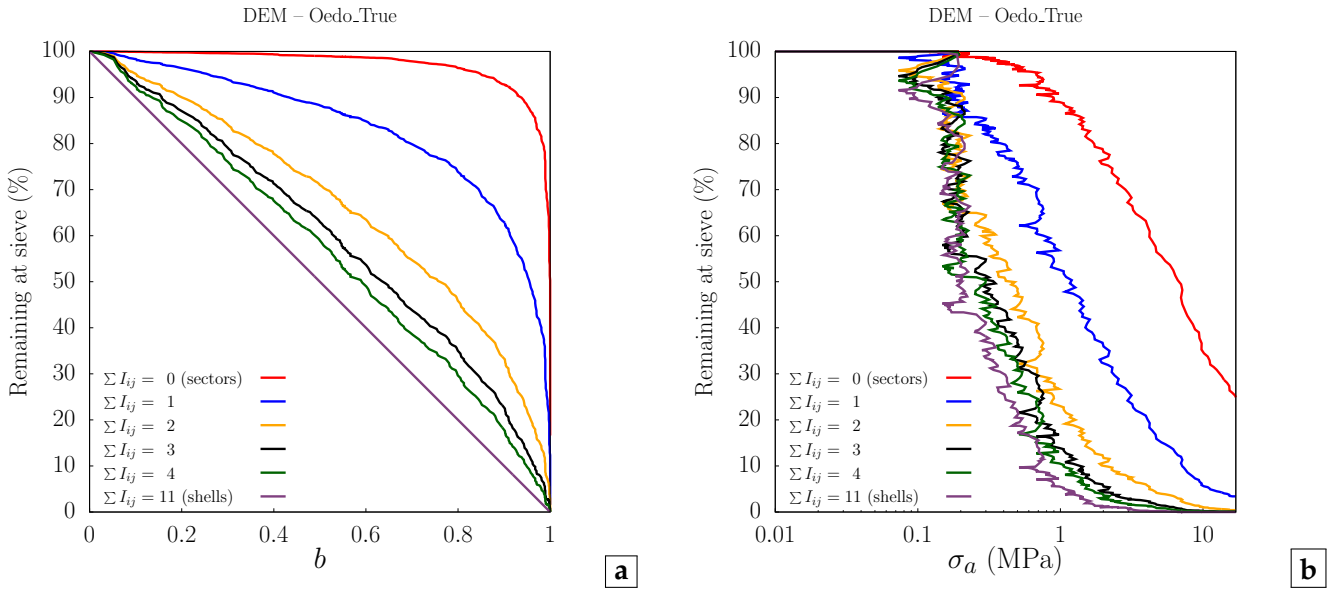

Figure 6.8 : The potential fragmentation to appear for each size concern the uniaxial compression with the micro-properties respecting the reality (Oedo_True – see **Appendix C**). The mass quantity remaining on the sieve is a function of: **a** – the primary breakage level b and **b** – the macroscopic stress σ_a. The sieve size description was presented in the **Table 6.1**. Note that $\sum I_{ij} + 1 = N^{\star}$, where $N^{\star}$ is the number of sectors per cluster.

graded with a size of $d = 17$ mm. This size-homogeneity was gradually lost. Up to the inflexion point $b \approx 0.5$, a presence of diverse sizes has arisen, but the assemblies were still rather poorly-graded. The breakage of shell led mainly to fragmentation into larger parts. In contrast, Laufer (2015) stated that in sand aggregates the small particles were first to break. A possible, explanation for this discrepancy is the initial state (uniform GDS). As the breakage kept progressing up to $b = 0.95$, the disintegration of fragments progresses more extensively, such that the GSD tended to well-graded distribution. Intensive comminution into the finest (numerical) sizes has been observed at the end of test for high axial stress, but the GDS did not become uniform again. **Figures 6.8** and **6.9** presents the potential breakage in the sample for Oedo_True and Oedo_Adjusted simulations, respectively. In both figures, the amount of parts remaining to be broken were presented separately for each sieve size (**Table 6.1**) both as a function of the primary breakage b (**Figures 6.8a** and **6.9a**) and of the microscopic loading (**Figures 6.8b** and **6.9b**). Note that the sieve sizes were described with number of interfaces to be broken $\sum I_{ij}$, which is one less than the number of sectors. Therefore, 0 stands for a single sector (red line) which is the minimum limit size. Part with 11 interfaces specifies the intact shell (with 12 sectors like *d18*-S1). The representation in **Figures 6.8a** and **6.9a** highlights the cascade type of progressive fragmentation. The violet line references to the primary breakage $(1 - b)$. Thus, there exists a linear relationship in **Figures 6.8a** and **6.9a**. When the breakage grows, the curves decline. The bigger is the part, the sooner corresponding curve begins to decrease and the sooner it reaches 0 % (no more parts existing in the sieve size). Furthermore, the curves do not interlace each other. This confirms that in first order the shells broke into bigger pieces, and then, those fragments were disintegrated into smaller ones. This process keeps repeating, and the size is reduced gradually toward a sector. This manner of gradual disintegration, we called the cascade breakage. When the primary breakage stops (b reaches 1 for the first time), the GSD still contains most of the sieve sizes. Then, the comminution progresses due to an increase of σ_a, but b remains constant, such that one can observe final vertical drops in the plots. **Figures 6.8b** and **6.9b** provides better insight at the end of test. The represen-

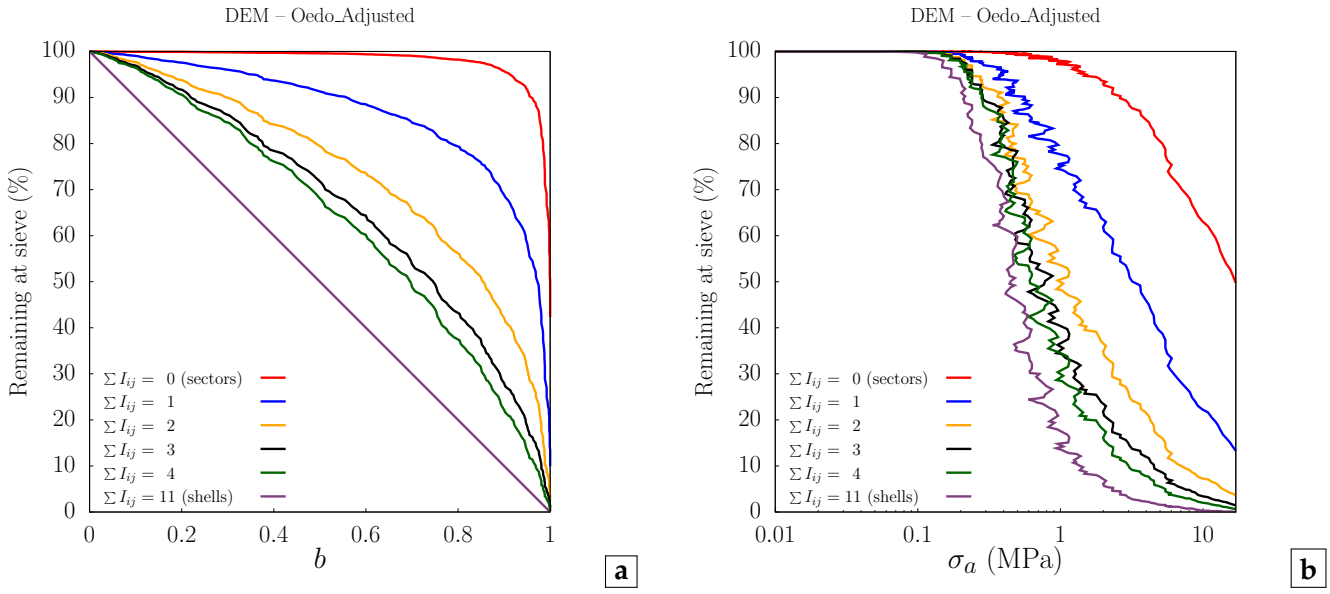

Figure 6.9 : The potential fragmentation to appear for each size as a function of: **a** – the primary breakage level b and **b** – the macroscopic stress σ_a. The shells are stronger than actual once, but the macro-mechanical response to the uniaxial compression stays in a good agreement with experiments (Oedo_Adjusted – see **Appendix C**). The sieve size description was presented in the **Table 6.1**. Note that $\sum I_{ij} + 1 = N^{\star}$, where $N^{\star}$ is the number of sectors per cluster.

tation with respect to macroscopic load has also supplemented the pieces of information about the breakage rates for each size. The change in the inclination of the potential fragmentation curve is equivalent to the change in the breakage rate. The steeper is the curve the higher is the breakage rate. Then, one can observe that each sieve size vanishes with a similar tendency. An initially flat curve has been gradually inclining till the maximum slope was reached. In other words, the onset of fragmentation into each size rose slowly at first, but afterwards, the breakage rate increased up to the maximum. The size evolutions of bigger parts were more rapid and more dynamic (higher inclinations). For each curve, there exists a point when the breakage starts to inhibit – initially slowly and then rapidly as the line approaches 0 % (non-linear final phase). It is interesting to observe that for all the sizes this inhibition point can be characterised at ∼50 % of potential breakage, which corresponds to the inflexion point of compression curves (**Figures 6.1**). **Figures 6.8b** and **6.9b** give insight into the stress level needed for each part size to break during the uniaxial compression. The breakage of bigger parts requires lower stresses than fragmentation of smaller parts. Firstly, due to the increase of coordination number, and secondly, due to the more simple shape of parts (less curved). In both cases, the disintegration of parts with more than 3 sectors requires a close range of stresses to each other (the curves interlace partially). While σ_a causing the breakage of parts containing 3 or 2 sectors had a disperse loading range (distant lines). Note that during the drop of initial stress peak (in dense assembly) the breakage was very extensive, and in fact, almost all the sieve sizes in **Figures 6.8b** experienced breakage. The comparison between Oedo_True and Oedo_Adjusted once more exposes the importance of shell strength. At the end of uniaxial compressions 25.3 % (**Figures 6.8b**) and 50.6 % (**Figures 6.9b**) of parts were still composed of multiple sectors. Whereas the weak sample has only 3 remaining sizes the, strong assembly was less uniform and contained still 5 various sieve sizes. In both cases, the distribution was not purely uniform. According to fractal breakage concept (Bolton and McDowell, 1997; Turcotte, 1986), the ultimate GSD tends to a self-similar distribution, a power law with a given exponent being the frac-

tal number. Therefore, the ultimate distribution cannot be uniform, but in the form of Pareto distribution. Numerically, GSD can get closer to uniform than experimental curves, but it is possible only due to the large size of unbreakable sectors. Nevertheless, the loading of 17 MPa does not lead to totally crushed state (assembly of separate sectors). A rough prediction indicates that $\sigma_a \approx 210$ MPa would be needed to obtained completely crushed sample. Nevertheless, the density limit before is reached before, when some non-physical overlaps appear for $\sigma_a \approx 70$ MPa.

6.3 The micro-mechanics and the orientation anisotropy during the progressive breakage

Figure 6.10 presents growth of the orientation anisotropy (using the sector "long" axis) during the numerical oedometer tests: Oedo_True and Oedo_Adjusted (**Figure 6.1**). In section **4.3.2**, one can find explanation how the anisotropy was quantified with parameter a_2 using the statistical distribution of orientations. In **Figure 6.10**, a_2 is also presented in a reduced form $\langle \cos^2\alpha \rangle - \frac{1}{3}$ (see equation 4.8), which is an actual difference from the isotopic state $\langle \cos^2\alpha \rangle = \frac{1}{3}$. The higher is the absolute value of the parameter a_2 (or its reduced form), the stronger is the anisotropy. Recall that orientation of shell, fragment or sector was consider as $\cos\alpha$, where α is measured with respect to global vertical axis Y.

A typical distribution of shell orientations prior to the uniaxial compression was shown in the section **4.3.2**. Summarising, although the rigid boundary led to local anisotropy (**Figure 4.22a**), in the core of sample the shells are rather isotropically oriented (**Figure 4.22b**). Thus, herein, the study of fragments orientation was limited to the internal core of samples, such that the analysis has started from almost isotopic state. Previously, the characterisation of boundary layer has been base on geometrical criterion – the mass centre of at least one sector within cluster must be in distance lower than 2 cm from the boundary. Yet, at the end of 1D compression, this criterion is too rigorous as it significantly restricts the number of parts (data) authorised for the analysis. Thus, the boundary layer has been redefined. Onwards, it includes two row of fragments: (*i*) all the fragments remaining in contact with rigid boundary and (*ii*) the neighbouring with them fragments. For the initial state of assembly, both definition of boundary provide comparable results.

Figure 6.10 shows the growth of anisotropy as the breakage progress. The arrangement evolved similarly for Oedo_True and Oedo_Adjusted, thus we present the statistical analysis only in case of Oedo_True. As is seen in **Figure 6.10** (right top plot), probability density function confirms almost isotopic distribution of orientations with $a_2 = -0.059$ (or $\langle \cos^2\alpha \rangle - \frac{1}{3} = -0.016$) of the initial state. Up to $b \approx 0.8$ anisotropy was constantly deepened with sectors rotating towards horizontal orientation (negative value). At this point, the anisotropy coefficient was increased around 5 times. Then, the anisotropy developed non-linearly during the final inhibition of primary breakage. The higher is the breakage level b, the steeper gets the trend. At the end of uniaxial compression ($\sigma_a = 17$ MPa) the anisotropy coefficient was almost 8.7 times bigger then its initial value for Oedo_True (and $a_2/(a_2)_0 \approx 9.2$ for Oedo_Adjusted). The core of the sample has become strongly anisotropic, and most of fragments and sectors tend to rest horizontally as presented by the statistical distribution in **Figure 6.10** (right bottom plot). The *pdf* is shaped such that the Legendre polynomials expansion (solid line) adequately reflects the numerical distribution (boxes). Finally, the manner of anisotropy growth indicates a link with the strain evolution. Charalampidou et al. (2009) has shown that the grains rotations depends mainly on the principal strain directions using 2D analogous material with rectangular particles. The authors have proven that, on the average point of view, the rotation $\Delta\beta$ of granular material follows the prediction offered by the continuum mechanics (for homogeneous strain):

$$\Delta\beta = -\frac{\gamma}{2} + \frac{\varepsilon_x - \varepsilon_y}{2}\sin 2\beta + \frac{\gamma}{2}\cos 2\beta, \qquad (6.1)$$

where $\varepsilon_x, \varepsilon_y$ are the vertical and horizontal strains respectively, while $\gamma = \gamma_{xy}$ is the shear strain. An-

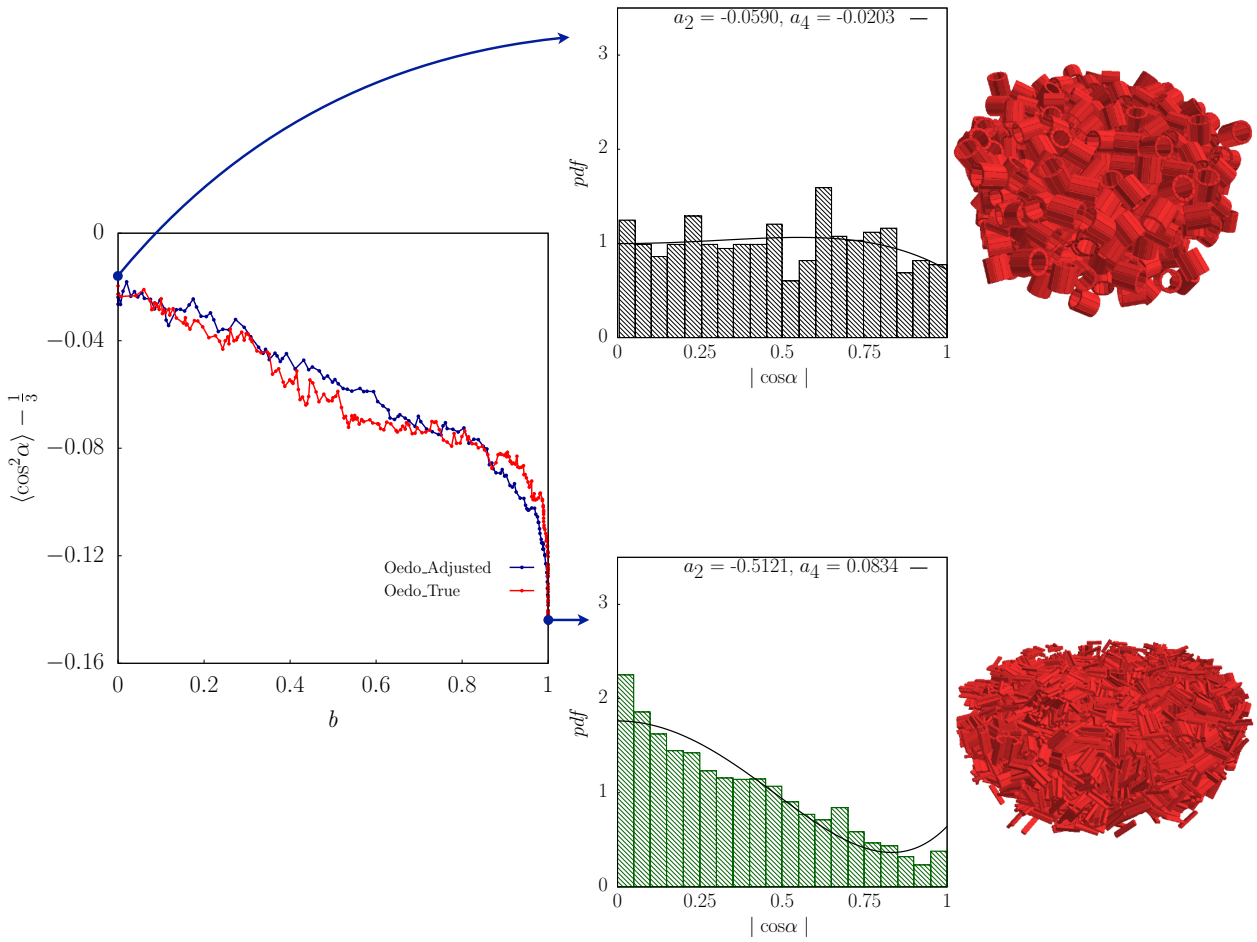

Figure 6.10 : Growth of sectors orientation ($|\cos\alpha|$) anisotropy during uniaxial compression has been characterised using anisotropy coefficient a_2 employed in the sum Legendre's polynomial expansion: $pdf(x) = 1 + a_2(3x^2 - 1) + a_4(35x^4 - 30x^2 + 3)$, where $a_2 = \frac{15}{4}(\langle x^2 \rangle - \frac{1}{3})$. Therefore $\langle x^2 \rangle - \frac{1}{3}$ is a difference from the isotopic state. Statistical analysis did not include boundary layer.

gle β was measured with respect to the horizontal axis, whereas in this study we measured the inclination with respect to the vertical axis, such that $\alpha + \beta = 90°$. Note that in a 3D case, one must include also the strain corresponding to the additional direction ε_y and γ_{xz}. However, for the uniaxial compression the boundary conditions significantly simplify the equation to:

$$\Delta\beta = \frac{\varepsilon_a}{3} \sin 2\beta. \tag{6.2}$$

Since the axial strain ε_a grows linearly[3], the prefactor $\varepsilon_a/3$ evolves linearly. Hence, one can expect a linear evolution also in the case of the orientation anisotropy with respect to the strain. The tendency of shells to rotate towards horizontal orientation during uniaxial compression has been confirmed through statistical analysis on samples with preferential orientation. **Figures 6.11a** to **6.11d** present the final distribution of orientations after uniaxial compression shown in **Figure 5.19**. For those samples, the shell orientations have been already presented in **Figure 4.24b** (section **4.3.2**), yet the probability density functions were recalled in the insets of **Figures 6.11**. An attempt to characterise the anisotropy of distribution using fourth order extension of Legendre polynomials (solid line) was successful only in some cases. Although, **Figure 6.11a** and **6.11b** clearly demonstrate the strongly anisotropic arrangements, their distributions with extremely high peak do not obey the shape of Legen-

[3] Recall that a constant velocity of the loading plate was imposed.

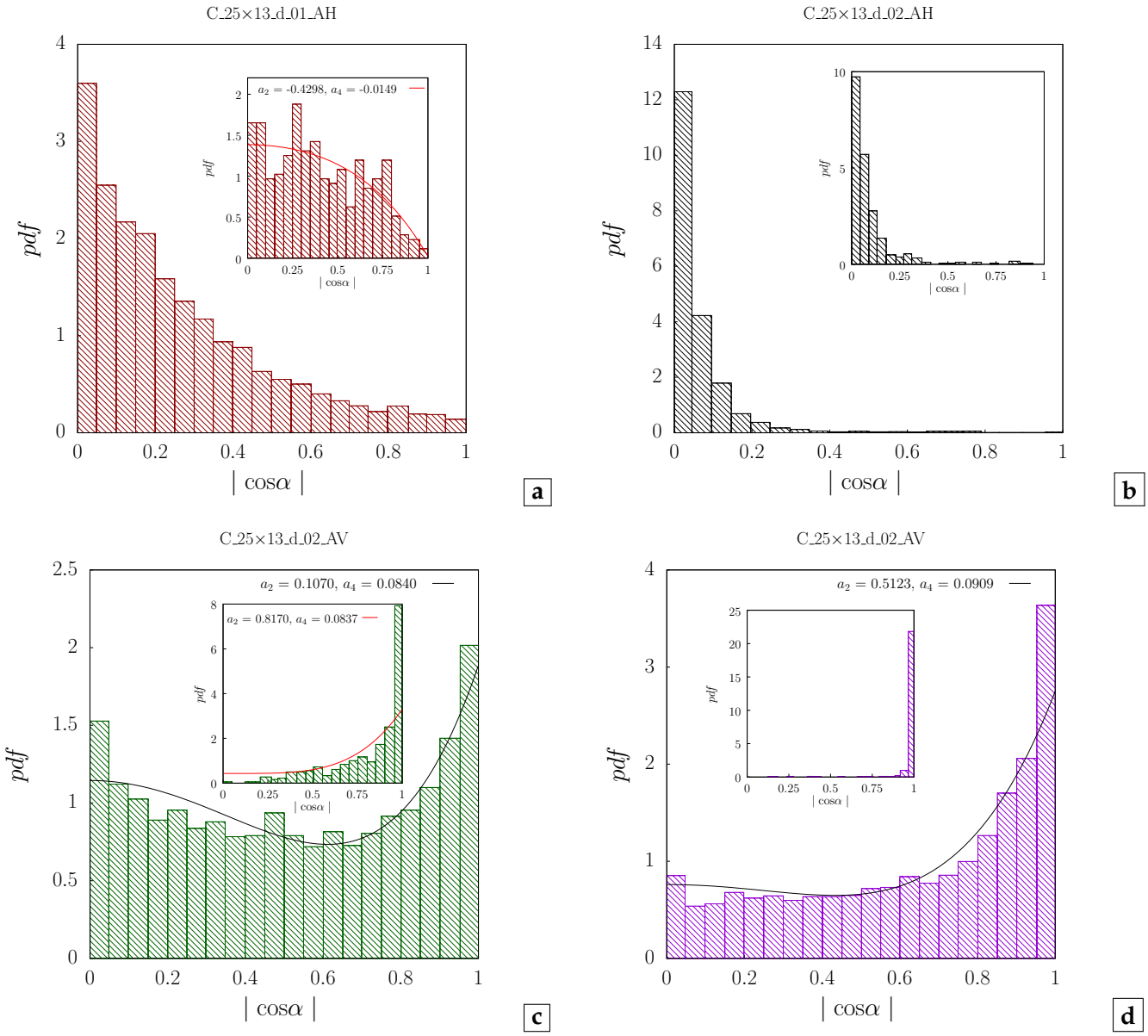

Figure 6.11 : Statistical analysis of orientations (without boundary layer) resulting from the 1D compression. The final state: $\sigma_a \approx 16$ MPa and $b = 1.0$. Initially, the majority of shells are oriented: **a** and **b** – horizontally, **c** and **d** – vertically (see **Figures** 4.24**b** and 4.25). Boxes present results of statistical analysis, and solid curve shows the fit of 4^{th} order Legendre's polynomial extension: $p(x) = 1 + a_2(3x^2 - 1) + a_4(35x^4 - 30x^2 + 3)$, where parameter a_2 quantifies the anisotropy of distribution. Inset: statistical analysis of initial shell orientations.

dre function. As is seen, the sectors always tend to rotate towards the horizontal position. Whereas for the samples C_25×13_d_01_AH and C_25×13_d_02_AH the anisotropy has been intensified, for vertical assemblies C_25×13_d_02_AV and C_25×13_d_03_AV the vertical orientation become partially balanced by horizontal rotations. **Figure** 6.11**c** shows the anisotropy coefficient decreased with respect to its initial value, $a_2/(a_2)_0 =$ 0.13 for C_25×13_d_02_AV, but the initial orientation remained dominant.

Oda (1972) has pointed out that the grains orientations should be supplemented with the mutual orientation of particles while describing the granular structure. In a basic DEM study with perfectly circular shapes in 2D or spheres in 3D, the concept of grain orientation does not appear. Then the contact network is referred to as a fabric. By

nature, an anisotropic structure characterises the contact network (Khalili, 2016), which rules material properties like the shear strength. Usually, the attention is paid to the contact normal direction $\vec{n}$. The branch vector, joining centres of two neighbouring particles, is a descriptor of the local geometry. Azéma et al. (2012) associated the branch vector $\vec{l}$ with its normal and tangential components $\vec{l} = l_n\vec{n} + l_t\vec{t}$. For 3D spheres, the position of contact lies in the direction of branch vectors ($l_t = 0$), yet it is not the case for polygonal shapes (Azéma et al., 2012; Cantor García, 2017).

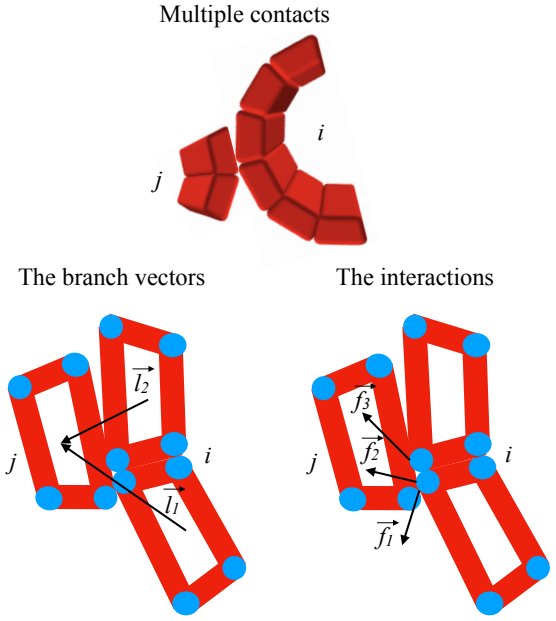

Figure 6.12 : 2D presentation of a contact with multiple interaction points. The sub-cluster is a part linking several sectors. Each sector (in 3D) is build from the spheres – the blue circles, the tubes as the edges – the red shapes, and the outer plans – not shown in 2D. This example of the contact between sub-clusters i and j involves 3 sectors and interacts in $n = 3$ contact points throughout the forces $\vec{f}_n$ ($\vec{f}_1$, $\vec{f}_2$ and $\vec{f}_3$). Two brach vectors $\vec{l}_1$ and $\vec{l}_2$ are associated to the contact.

Due to the specifications of DEM tool ROCKABLE, the analysis of contact network is more complex. First of all, a number of interactions n can be associated with one contact as is presented in the **Figure 6.12**. In other words, more than one force $\vec{f}_n$ act in the contact. Secondly, the contact may involve multiple sectors, such that there might appear more that one branch vector $\vec{l}$ in the contact (**Figure 6.12**). Consequently, analysis of the contact network and transmitted within forces was omitted in favour of the analysis of local stress. A mean pressure can be defined at the level of shell, a part or a sector i:

$$p = \mathrm{tr}(\boldsymbol{\sigma}_i), \tag{6.3}$$

where $\boldsymbol{\sigma}_i$ is a stress tensor of sub-cluster i calculated using the forces in the n contact points at the positions $\vec{r}_n$ with respect to origin of global coordinate system XYZ:

$$\boldsymbol{\sigma}_i = \frac{1}{V_i}\sum_0^n(\vec{f}_n \otimes \vec{r}_n). \tag{6.4}$$

Figure 6.13 shows the sample with prism geometry (square base 19 cm × 19 cm), prepared following procedure from section **4.3.1**. Sample P_19×17_d_01_A contained 1 000 shells *d18*-S1. It had the total void ratio equal to 2.458 and the inter-granular void ratio of 0.595. The number density n was found at 162 468. As is seen, the initial state is described by similar values as cylindrical samples. The differences concerned a lower coordination number of neighbours $Z_n = 3.6$ (or the contacts $Z_c = 5.5$) and slightly higher anisotropy of shell orientations distribution (with an isotropic core).

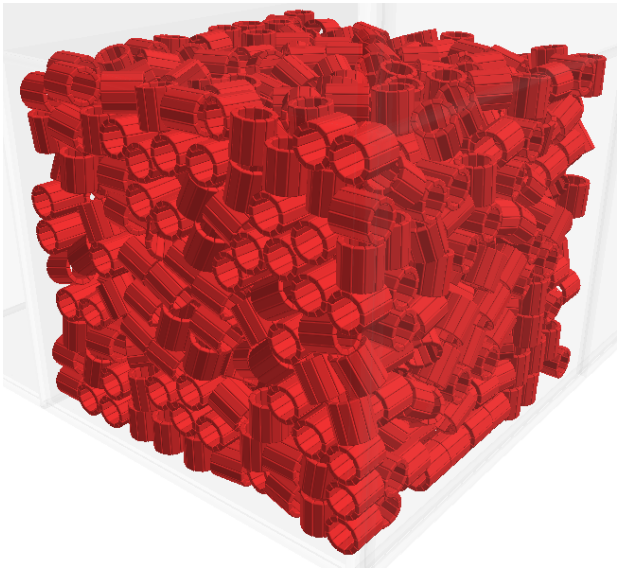

Figure 6.13 : A sample with a geometry of true prism – P_19×17_d_01_A (see **Appendix B**). The base is a square with a side size of 19 cm. The sample contained 1 000 shells *d18*-S1.

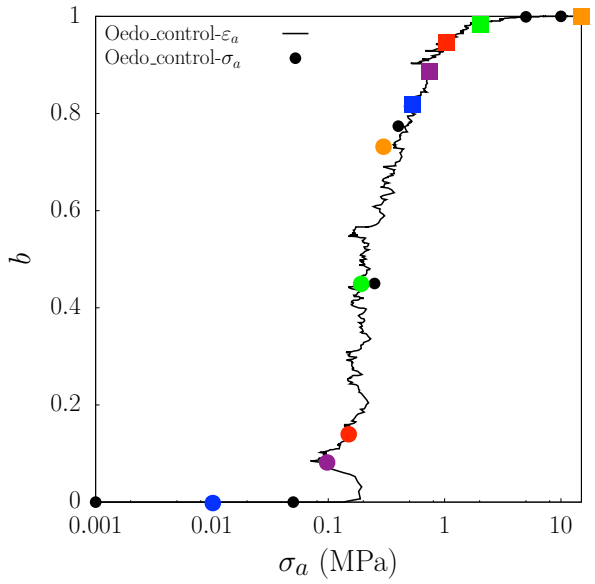

Figure 6.14 : A comparison of breakage evolution in a stress-controlled and a strain-controlled tests. The uniaxial compression was carried out on the shells *d18*-S1 with an average tensile strength set at $\langle F_I \rangle$ = 120 N (or DEM parameter $\langle f_I^\star \rangle$ = 85 N). The colourful points mark the loading steps selected for the analysis of micro-stress applied p on the constituents (**Figure** 6.16).

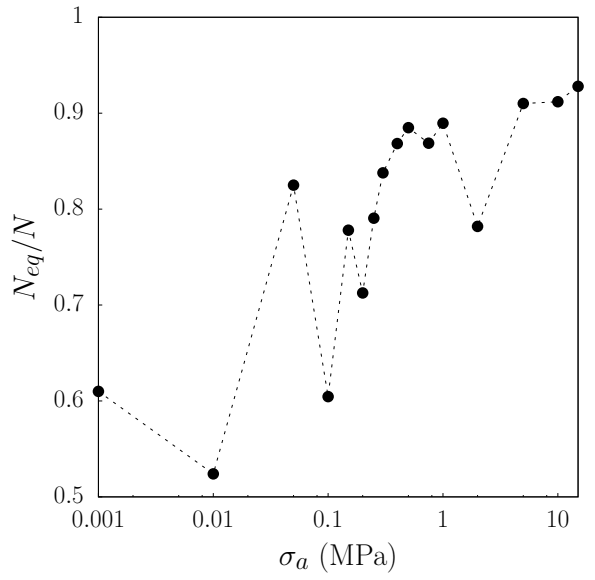

Figure 6.15 : Despite the numerical relaxation in the stress-controlled simulation, allowing to dissipate the kinetic energy in time, the equilibrium of local forces was not always verified. Thus, an analysis of the mean pressure of shells needed to be limited. The N_{eq} is a number of the constituents both under loading and well equilibrated, whereas N is a total amount of parts (including the rattlers and poorly balanced forces).

The oedometer test was simulated with the stress control (Oedo_contol-σ_a) on a gravity-free packing (see **Table** C.2). The strength parameters were used, like in Oedo_True (see **Table** C.1), such that the true micro-mechanics were respected. Despite the differences, the compression curves were consistent with each other. Similarly, the primary breakage grew with a similar trend (**Figure** 6.14).

σ_a has been increased step by step, and between each loading increment, the packing has been left to get stabilised for 0.5s (that gives 2.5 million time steps). Although globally the kinematic energy indicated steady state, locally, not all the shells were found well balanced. The force equilibrium was approved, if the ratio of the resultant force norm with respect to the norm of minimum force was lower then 0.001. The amount of poorly equilibrated shells is significantly larger for modelling with the strain control, and therefore, a less rigorous criterion would be needed. We recognised the dynamic nature of brittle breakage and the lack of the numerical relaxation phase as the causes. **Figure** 6.15 shows the percentage of shells/fragments authorised for the analysis. Note that the rattlers (floating shells) were excluded in these measures.

The colour points marked in **Figure** 6.14 shows the loading step for which the statistical analysis of local stresses were presented in **Figures** 6.16 and 6.17. The selected curves are divided into two sets, **Figures** 6.16**a** and 6.17**a** correspond to the stress states mainly up to the inflexion point, and the **Figures** 6.16**b** and 6.17**b** are dedicated to loading steps afterwards for $b > 0.8$. To compare the carves, the mean local pressure was normalised by the macroscopic load. Radjai et al. (1996) analysed the distribution of forces in 2D granular materials dividing the range into two domains: low and high forces. Although we analysed the mean pressure, similar remarks can be pointed out in case of 3D shells. **Figure** 6.16 shows that low-pressure distribution followed the power law, which gets linearised in the logarithmic scale. A line with slope $\check{a}$ clearly suits all the cases shown in the **Figure** 6.16**a**. It is clear that the peak shifted closer to $p/\sigma_a = 1$ when the inhibition of breakage begins (**Figure** 6.16**b**) and the lower sub-domain got re-

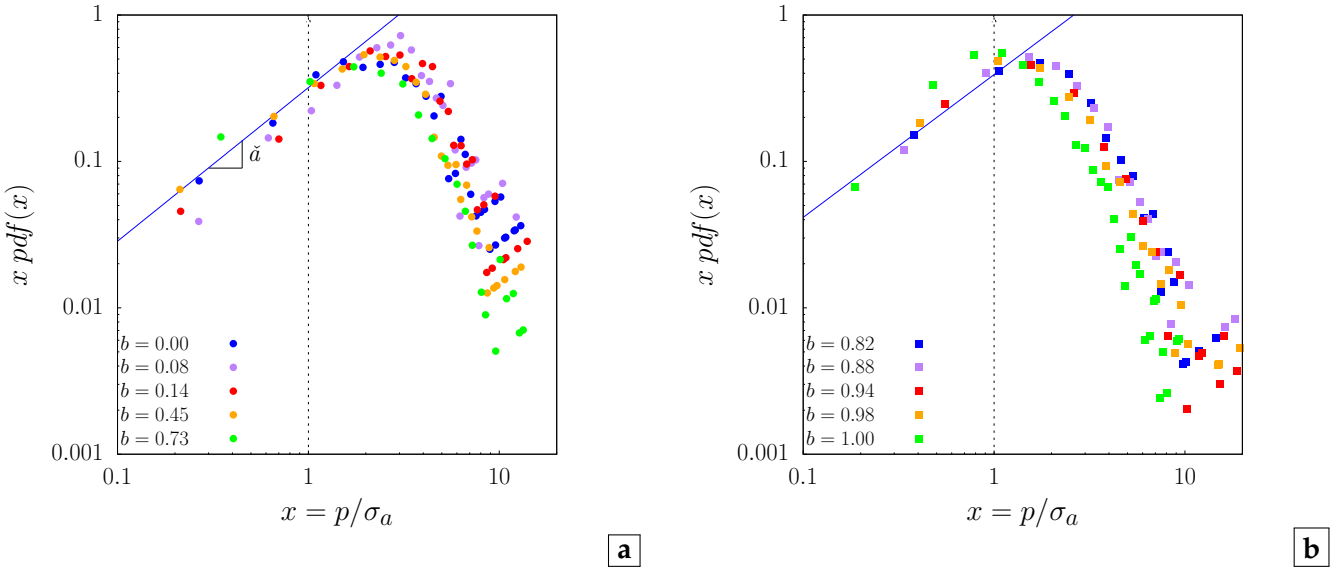

Figure 6.16 : The statistical distribution of microscopic mean pressure for the low pressure sub-domain. Mean stress applied on fragment p is normalised by the macroscopic load σ_a. the uniaxial compression performed in a stress-controlled test. The analysis were divided for the states: **a** – up to $b \sim 0.8$ and **b** – for $b > 0.8$ (points marked in the **Figure** 6.14).

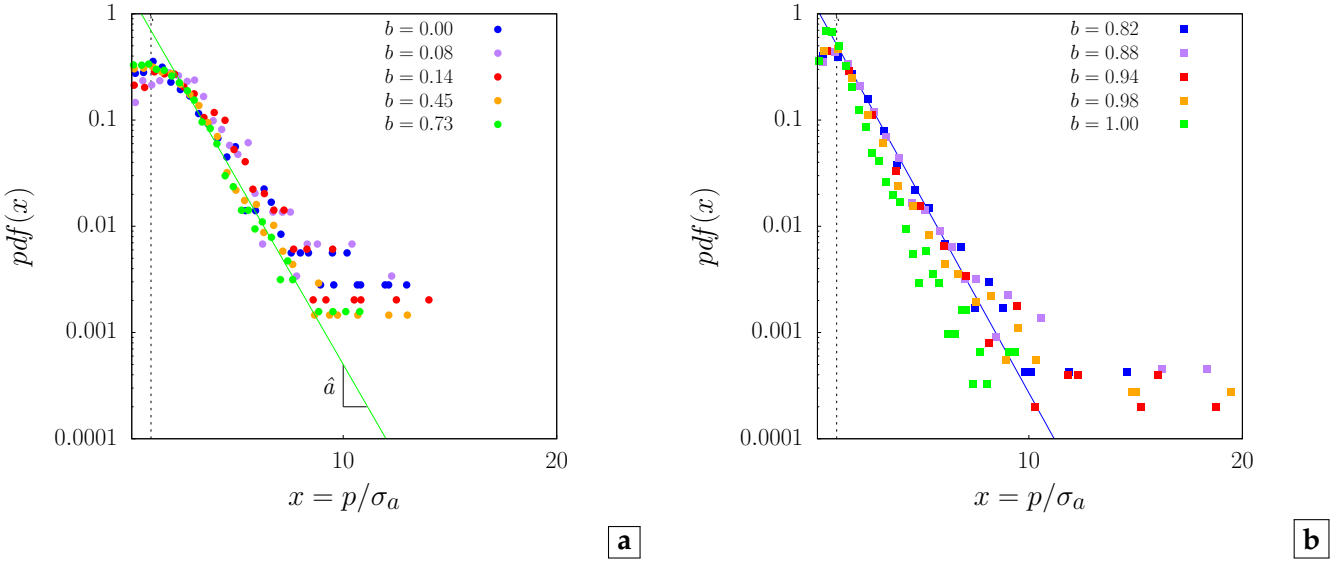

Figure 6.17 : Statistical distribution of microscopic mean pressure for the high pressure sub-domain. Mean stress applied on fragment p is normalised by the macroscopic load σ_a. Uniaxial compression performed on the stress-controlled test. The analysis were divided for states **a** – up to $b \sim 0.8$ and **b** – for > 0.8 (points marked in the **Figure** 6.14).

duced. Then, the fit is less reliable because most often only a couple of points was found in the domain of low stress. **Figures** 6.17**a** and 6.17**b** show *pdf* in the half-logarithmic space focusing on the distribution in the domain of high pressure. It is more visible that the distribution always exhibits the majority of the small stresses within the sample, such that the peak of *pdf* was always concentrated around $p/\sigma_a = 1$, but its probability rises with b. Also, the width of distribution, *i.e.*, the

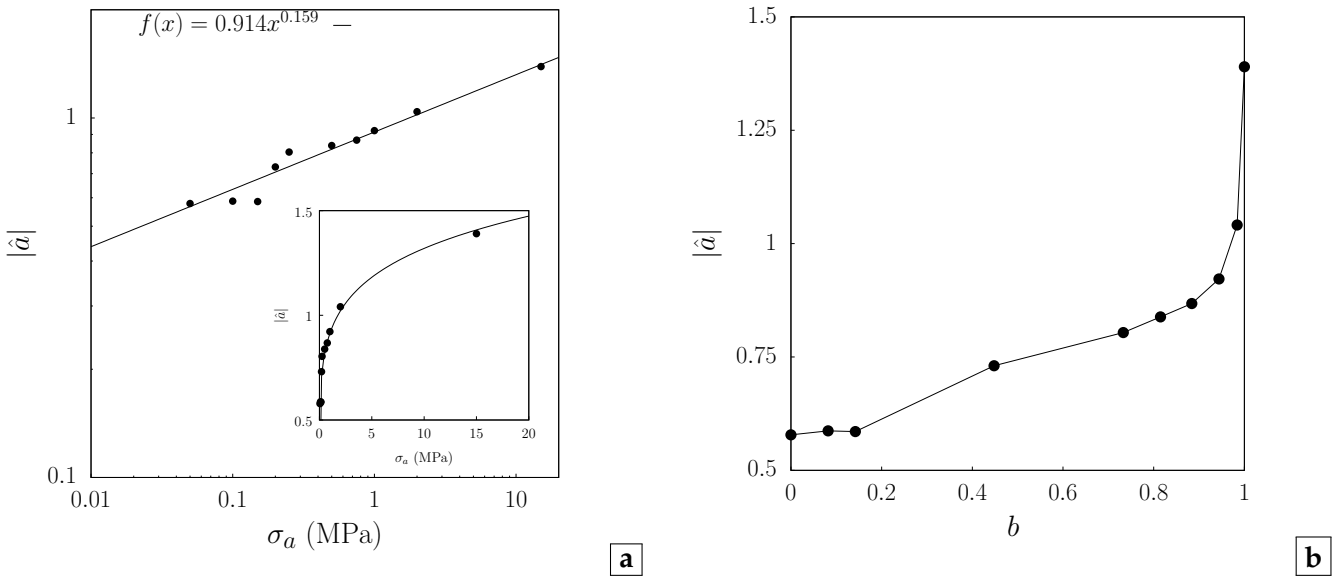

Figure 6.18 : An absolute value of parameter of exponential law $|\hat{a}|$ indicates the width of tail **Figures 6.17**. The evolution of $\hat{a}$ during uniaxial compression with respect to: **a** – the macroscopic stress and **b** – the primary breakage.

length of tail, evolved with respect to the macroscopic stress. Following Radjai et al. (1996), an exponential relationship can be determined for high pressure domain, that in the **Figures 6.17** shapes a line with a declining slope $\hat{a}$. The lower is its absolute value $|\hat{a}|$, the wider is the distribution.

Figure 6.18a presents the evolution of $|\hat{a}|$ with respect to the macroscopic load. The tendency can be reliably described by a power law, indicating that, for a high-pressure test, the width should reach a minimum limit. One can observe that, on the average point of view, the tail was always shortening. Note that it was necessary to limit the range $p/\sigma_a \in \langle 1 : 10 \rangle$, in order to obtain a robust fit. It is harder to distinguish this evolution in the **Figures 6.17a** and **6.17b** because a strong deviation from the average trend occurs at the end of each tail. To construct *pdf*, a constant number of statistical set was used, and therefore, the amount of data was very low in the final sets. This led to the flat end of the tail, which we classify as the deviation from trend. On the other side, those deviations give a sense of the maximum value of p/σ_a, which seemingly evolved due to the change of GSD, such that for more uniform grading curves the maximum p/σ_a is lower. **Figure 6.18b** shows $|\hat{a}|$ as a function of primary breakage. Once the breakage has started, the tail was shortening gradually and quite proportional to b. When the primary breakage slowed down ($b > 0.95$), the width of *pdf* became visibly narrow and a sharp increase of $|\hat{a}|$ take place. Recalling **Figure 6.7a**, mainly the evolutions of smaller fractions are present at those levels of b, such that the GDS tends to more uniform.

6.4 Analysis of compressibility through void ratios

The compressible response of the shell assembly originates from a large amount of intra-cluster space, *i.e.*, the internal voids of shells. Nevertheless, only the breakage is able to activate the highly compressible properties of samples with the brittle shells. To this end, an adequate stress level needs to be reached in order to trigger shell breakage. The strength and size of the internal void need to be combined in an optimal way such that the layer is durable and works efficiently over time. The compression curve ($\sigma_a \leftrightarrow \varepsilon_a$) can be presented in another manner replacing ε_a with the void ratio e, *i.e.*, a dimensionless parameter quantifying the proportion of voids volume V_v to vol-

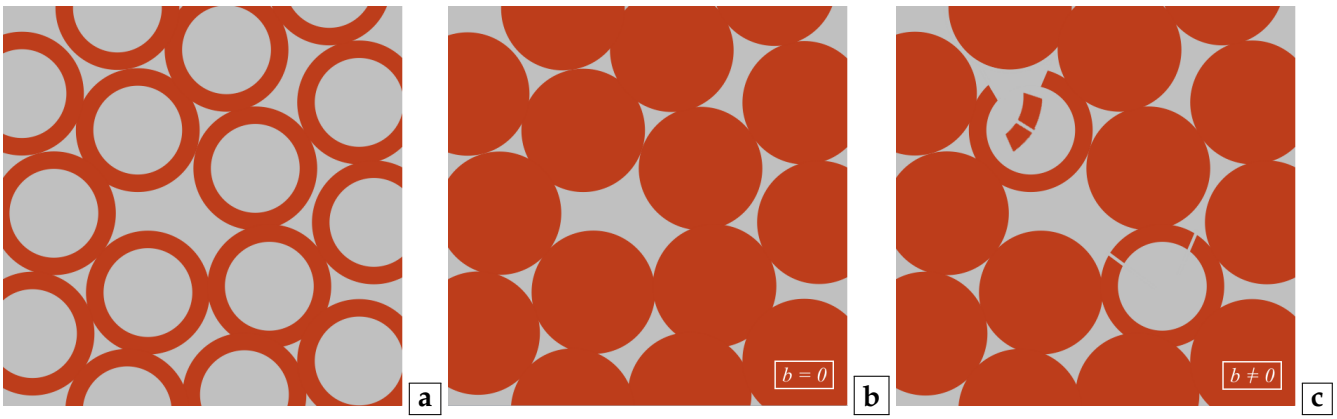

Figure 6.19 : Division into the voids (grey) and the solid (red) for 2D example. **a** – Overall void ratio e with most simple classification between void and solid that is air and backed clay. Modified void ratio $e^\star$ (the inter-granular void ratio) takes into account the accessibility to the internal voids: **b** – all shells are intact ($d = 0$) and **c** – breakage occurs ($d \neq 0$).

ume of solid V_s. A classical void–solid division into the air (grey) and the matter (red) is presented in **Figure 6.19a**. Herein, e is referred to as standard, total or overall void ratio. Considering the volume of the sample V_{tot} and the volume of the solid phase V_s (sum of the volume of sectors), the classical definition of void ratio is:

$$e = V_v / V_s = (V_{tot} - V_s)/V_s. \tag{6.5}$$

Now, the intra-cluster and the inter-cluster voids can be distinguished from the total volume of free space V_v. The peculiar geometry of a cluster disables access to the space V_v^i trapped inside it while it remains intact (**Figure 6.19b**, see also **Figure 3.9** in section **3.3.1**). Once the cluster is broken the trapped space is released as shown in the figure **Figure 6.19c**. Thus, we considered another definition for the void ratio, where $V_{accessible}$ are all the available space in the sample and $V_{inaccessible}$ is the

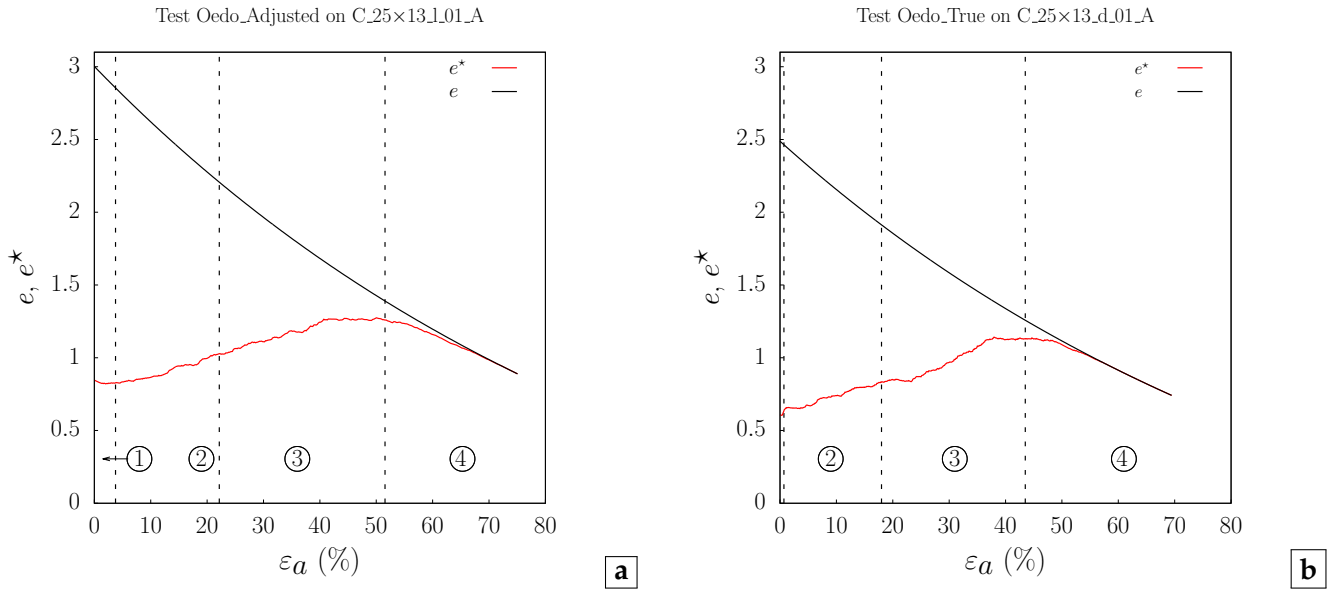

Figure 6.20 : The compression curves with respect to axial strain for the samples with **a** – adjusted and **b** – true densities and micro-mechanics. Evolution of void ratio e (black) and inter-granular void ratio $e^\star$ (red) during uniaxial compression.

space that cannot be filled by matter also because of geometric exclusions (inside intact clusters). In that way, the void ratio is accounted for:

$$e^\star = \frac{V_{\text{accessible}}}{V_{\text{inaccessible}}} = \frac{V_{\text{tot}} - (V_s + V^\star)}{V_s + V^\star}, \qquad (6.6)$$

where

$$V^\star = (1-b)\sum_{i=0}^{N} V_v^i \qquad (6.7)$$

is the volume of the hollow part of intact clusters.

In this work, $e^\star$ is called either modified or inter-granular void ratio. In **Table B.1** (**Appendix B**) the results for each prepared sample are given. The values of both e and $e^\star$ depend on the deposit protocol, and more precisely, on the friction coefficient μ controlling the inter-granular void volume (density). Averaging over the same range of densities ($\mu = 0.8$), the volume of internal voids is 3.04 times larger than the volume of inter-granular voids (with a deviation of ± 0.1). Changing friction coefficient (during the deposit), this relation varied such that for dense packing it gave 3.45 and for loose state 2.55. For the basic shape *d18*, the intra-voids had always much higher volume. Naturally, thickening of the shells ring (increasing t) reduced this proportion. Tubes with wall 50% thicker ($t = 3.6$ mm) had a ratio of 1.5, whereas doubling the thickness ($t = 4.8$ mm) results in less internal voids than inter-granular ones – volume ratio found at 0.74.

In **Figures 6.20** and **6.21**, the evolution of both standard (e) and non-standard ($e^\star$) void ratios are presented for true and adjusted set of parameters. First, the compression curves are plotted as a function of strain (**Figures 6.20a** and **6.20b**). Although the strains are imposed by the constant plate displacement, the standard void ratio e decreases non-linearly. It is simply due to the logarithm definition of strain (equation 5.1). Red lines present non-standard void ratio $e^\star$ which, in all cases, rises up to e in a non-monotonous manner. This follows from the fact that the progressive cluster breakage enables access to internal voids along with the test. Once all the clusters are crushed, $V^\star = 0$ and thus, equations (6.5) and (6.6) become identical.

Figures 6.21a and **6.21b** show the same evolution with respect to the macroscopic stress level. In the plots the breakage phases are marked as they were recognised in **Figures 6.1c** and **6.1d**, respectively. By definition, the evolution of $e^\star$ should rely on the breakage level b, and the breakage rate influences the dynamics of $e^\star$. This is valid for phases ①, ② and ③, while in zone ④ void ratio decreases despite the growth of b. The

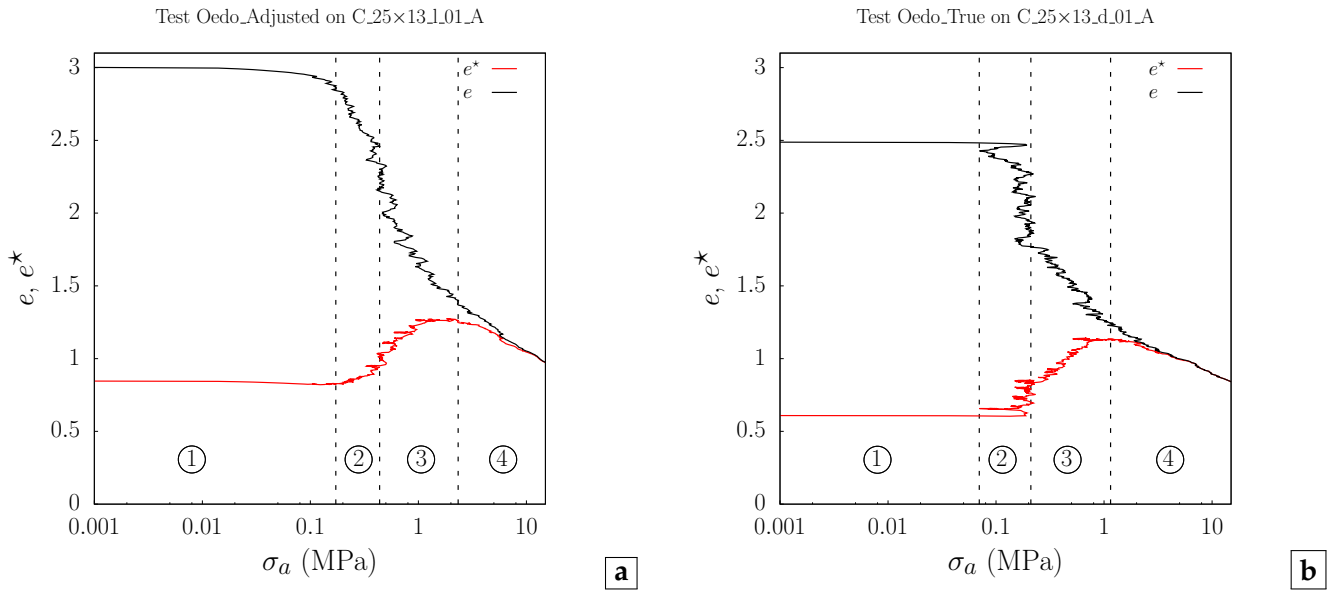

Figure 6.21 : Consolidation curves for the samples with **a** – adjusted and **b** – true densities and micro-mechanics. Evolution of void ratio e (black) and inter-granular void ratio $e^\star$ (red) during uniaxial compression.

evolution of $e^\star$ always presents a peak at $b \approx 0.95$ indicating this characteristic point as the limit of highly compressible regime. The black and the red curves must converge when all the shells are broken ($b = 1$), yet the breakage becomes insignificant and one can only observe only densification of the samples. In **Figures 6.20a** and **6.20b** those phases were marked as well, although in **Figures 6.1a** and **6.1b** different division has been established (phases Ⓘ – Ⓘ). This is to emphasise that the characteristic points ($b = 0.5$ and $b = 0.95$) play important role in the trend with respect to strain, although they have been found in the breakage to stress evolution. Evolution of $e^\star$ shows something different from the consolidation curves classically produced for fine soils in the field of geotechnical engineering. For example, Laufer (2015) distinguish overall and intergranular void ratio for sand aggregates, but the shapes of the curves remain similar. Despite similar features, the seeming consolidation slope (that increases with the stress level) relates mainly to different mechanisms related to the collapse of constituent particles. A constitutive macroscopic model dedicated to this mechanism should not be based on e directly but rather on a modified version of this variable, as we suggested by introducing $e^\star$. Finally, the plots connect the breakage and its influence on the stress level evolution with the strength of constituent particles, while the initial density remains of great importance for the strain range.

6.5 Prediction of breakage

6.5.1 Analytical model with respect to strain

Hereinafter, it is tested if the $e^\star \leftrightarrow \varepsilon_a$ plot may be predicted including the cluster breakage level $b = N_{\text{broken}}/N$ as a linear proportion to the axial strain. The linear trend followed from the first order estimation: $b = 0.022\varepsilon_a$ has been already shown in **Figures 6.1a** and **6.1b**. Considering equation (6.6) as a fraction, one can divide all the components of both its denominator and its numerator by volume of V_s. This proves that $e^\star$ is a function of total void ratio e:

$$e^\star = \frac{e - V^\star/V_{\text{s}}}{1 + V^\star/V_{\text{s}}}. \tag{6.8}$$

Then, the volume of inaccessible internal voids $V^\star$ and the volume of solid V_{s} can be easily defined as:

$$V^\star = \sum (N - N_{broken}) V_v^i \tag{6.9}$$

and

$$V_s = \sum N V_s^i. \tag{6.10}$$

where N is a total number of shell, N_{broken} counts the broken shells and V_v^i, V_s^i are void, solid volume of a single cluster i. Then, their ratio gives:

$$\frac{V^\star}{V_{\text{s}}} = (1 - \frac{N_{\text{broken}}}{N}) \frac{V_v^i}{V_s^i} = (1 - b) E_0, \tag{6.11}$$

with the cluster void ratio $E_0 = R_{\text{int}}^2/(R_{\text{ext}}^2 - R_{\text{int}}^2)$. Then, the microscopic void ratio is equal to $E_0 = 1.062$ for shells *d18* and $E_0 = 0.955$ for *d20* (see also **Figure 3.9**). Those convert to micro-scale porosity $P_0 = 51.5$ % and $P_0 = 48.8$ %, respectively. A substation of equation (6.11) into the equations (6.8) results in a general formula:

$$e^\star(b) = \frac{e - (1 - b) E_0}{1 + (1 - b) E_0}. \tag{6.12}$$

Now, both the standard void ratio and breakage evolution need to be analytically described as a function of macroscopic variable. This section was essentially dedicated to the axial strain, and therefore, at this point we focus on determination of $e(\varepsilon_a)$. Note that we have already described $b(\varepsilon_a)$ as a linear relationship limited to 1. The logarithmic strain definition, from equation (5.1), is used in the derivation of $e(\varepsilon_a)$, and for a uniaxial compression may be also re-written as:

$$\varepsilon_a = \ln \frac{(V_{tot})_0}{V_{tot}} = \ln \frac{(V_v)_0 + V_s}{V_v + V_s}. \tag{6.13}$$

The relation remains uninfluenced, once all the component are divided by V_s. Hence,

$$\varepsilon_a = \ln \frac{e_0 + 1}{e + 1} \quad \text{or} \quad \exp(\varepsilon_a) = \frac{e_0 + 1}{e + 1} \tag{6.14}$$

A simple transformation led us to the final form:

$$e(\varepsilon_a) = \frac{1+e_0}{\exp(\varepsilon_a)} - 1. \tag{6.15}$$

Note that the relation between e and ε_a needs to include the initial void ratio e_0 of the sample.

Figure 6.22 shows e/e_0 as a function of ε_a superimposed on the result of a simulation. The predictions are presented by the solid lines and the simulations with different shell thickness (recall **Figure 5.21**) are shown by dotted lines. Because the relation between e and ε_a is purely geometric, the e-curves fit perfectly. The evolution of predicted $e^\star$ follow quite well the simulated ones showing that the geometric model is actually monitored by the evolution of b with respect to ε_a. It is interesting to observe that, in the context of crushable particles that are able to "release" voids, e can be seen as an upper limit for $e^\star(b=1)$, while the natural definition of void ratio when some voids are enclosed within the particles should be $e^\star(b=0)$. The model is incapable of reproducing the decrease of $e^\star$ for $b \in \langle 0.95 : 1.0 \rangle$. Yet, the slope of linear relationship allows us to control the point at which two curves will join: either at peak (**Figure 6.22**) or for $b = 1.0$.

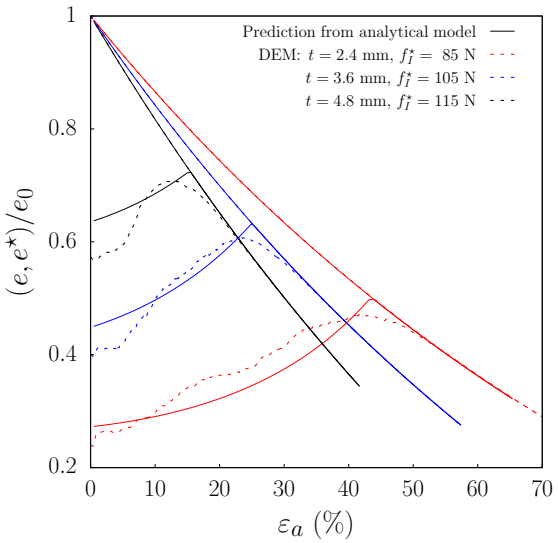

Figure 6.22 : Numerical evolution of normalised void ratios e/e_0 and $e^\star/e_0$ (dashed lines) with respect to axial strain. Compression curves (solid lines) according to equation (6.12), $b = 0.024\varepsilon_a$(red) a prediction for shells with larger holes with $b = 0.065\varepsilon_a$ (black), and $b = 0.04\varepsilon_a$ (blue).

One example of the interest of equation (6.12) was illustrated by attempting to predict the oedometric compression behaviour as a function of the hole radius of the shells in order to optimise them. Assuming a faster increase of b for smaller hole radii, the tendencies are shown in the **Figure 6.22** (black and blue curves). Obviously, the reliability of these predictions is questionable because the model still needs to include a proper evolution law for the damage-like parameter b as a function of the pressure for instance. Taking into account the simple nature of the model and a small number of parameters, the results are satisfactory despite the discrepancies exposed by **Figure 6.22**.

6.5.2 Analytical models with respect to stress

Herein, a framework to predict evolution of $e^\star$ as a function of macroscopic stress was build, and therefore, a general formula from equation (6.12) has been chosen as the starting point. Now, the challenge of constructing a model predicting modified void ratio $e^\star$ includes two tasks:

- verifying the constitutive model of standard void ratio $e(\sigma_a)$,
- and describing breakage as a function of stress $b(\sigma_a)$.

Many researchers attempted to build a constitutive model, acknowledging the breakage of constituent particles, to foresee the classic consolidation curve (Bauer, 1996; Einav, 2007b; Hu et al., 2011). Herein, the results are related to an isotopic compression law proposed by Bauer (1996) (equation 6.16) that has already been used to applied to a classical geo-materials by Laufer (2015) and Oquendo et al. (2009). Bauer (1996) presented the void ratio a function of mean pressure $3p$, hereinafter replaced by the axial stress σ_a:

$$e = e_0 \ \exp\left[-(\sigma_a/h_s)^n\right]. \tag{6.16}$$

The above relationship is ruled by three constants:

- An initial void ratio e_0 indicating the starting point of the curve, onwards, being an input.

- A so-called soil hardness h_s is a mean pressure representing the inflexion point on the compression curve ($e \leftrightarrow \sigma_a$) in semi-logarithmic scale for isotropic compression. It can be obtained also from the high-pressure oedometer test. For granular materials, it is suggested to depend on the strength of constituent particles.
- A shape parameter n related to the inclination of the compression curve.

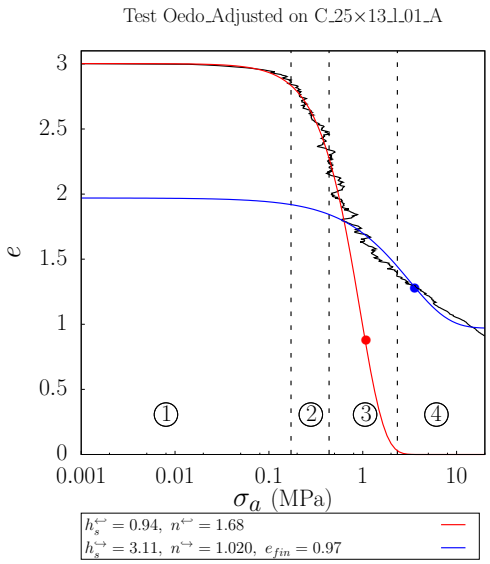

Figure 6.23 : Numerical compression curve $e \leftrightarrow \sigma_a$ (black line) follows the isotropic compression law (red line – see equation 6.16) up to the inflexion point ($\hookleftarrow$). Afterwards ($\hookrightarrow$), the trend change due to hardening of material (blue line – see equation 6.17).

In **Figure 6.23**, a typical numerical consolidation curve is compared with Bauer's law (red line). Among various attempts, the parameters h_s and n were obtained from the fit of equation (6.16) on the limited range of stress – from 0 to σ_{50}. By structure, the equation (6.16) tends to $e = 0$, which is not a physical measure. Therefore, the constitutive model and DEM simulation have to finally diverge. Yet, the point of the discrepancy between the curves is also a consequence of model limitations, and more importantly, the isotopic hardening of granular packing (both in experimentally and numerically). Note that, onwards, the set of parameters will be distinguished for ranges before and after the inflexion point, thus, $\hookleftarrow$ and $\hookrightarrow$, respectively, will mark the range in the superscript of parameters. In **Figure 6.23**, the red bullet shows the location of $h_s^{\hookleftarrow}$ found at 0.94 MPa, which is very low comparing to the values found in the literature for classical geo-materials. Bauer, himself, has suggested values between 10 and 300 MPa, and the lowest value found by Laufer (2015) is ~7 MPa. The numerical inflexion point (middle vertical line) is found at lower stress, such that $\sigma_{50}/h_s^{\hookleftarrow} = 0.47$. In **Figure 6.23**, once the inflexion point on the compression curve was reached, the trend is presented by another function:

$$e = \exp\left[-(\sigma_a/h_s)^n\right] + e_{fin}. \tag{6.17}$$

Equation (6.17) bears significant resemblance with the isotopic compression law, since it is an exponential function based on the soil hardness and the macroscopic shape parameter. At this point, it is simply assumed that the inflexion point is a consequence of the high level of material damage (breakage). The significant changes in grain size distribution lead to the change of response towards the one presented by less porous packing like sand. The experimental results of Papazoglou (2018) also indicated such a tendency. If at the inflexion point the sample would be disassembled and the packing with resultant GSD would be redeposited, the "new" initial void ratio should diminish equivalently to the lost of internal voids of broken shells. Then, one deal with a new packing with lower initial void ratio and stronger constituents, thus the parameters h_s and n need to be re-adjusted. This concepts led to modification of equation (6.16), such that the equation (6.17) ignores the "new" initial void ratio as it is irrelevant to consolidation curve. Yet, in order to avoid the limit $e \to 0$ for $\sigma_a \to \infty$, the estimated final value of void ratio e_{fin} was imposed. As is seen, the fit presented with blue line joins the numerical curve in the phase of "clastic" hardening. The soil hardness has been increased more than 3 times confirming the increase of constituents strength. The shape parameter decreases adequately to reflect the lower inclination of the curve. The denser is a sample initially, the less compressible it becomes. In other words, the lower $e_0^{\hookrightarrow}$, the smaller $n^{\hookrightarrow}$ should be found. In this framework at σ_{peak}, when entering phase ④, a recalibration of fit pa-

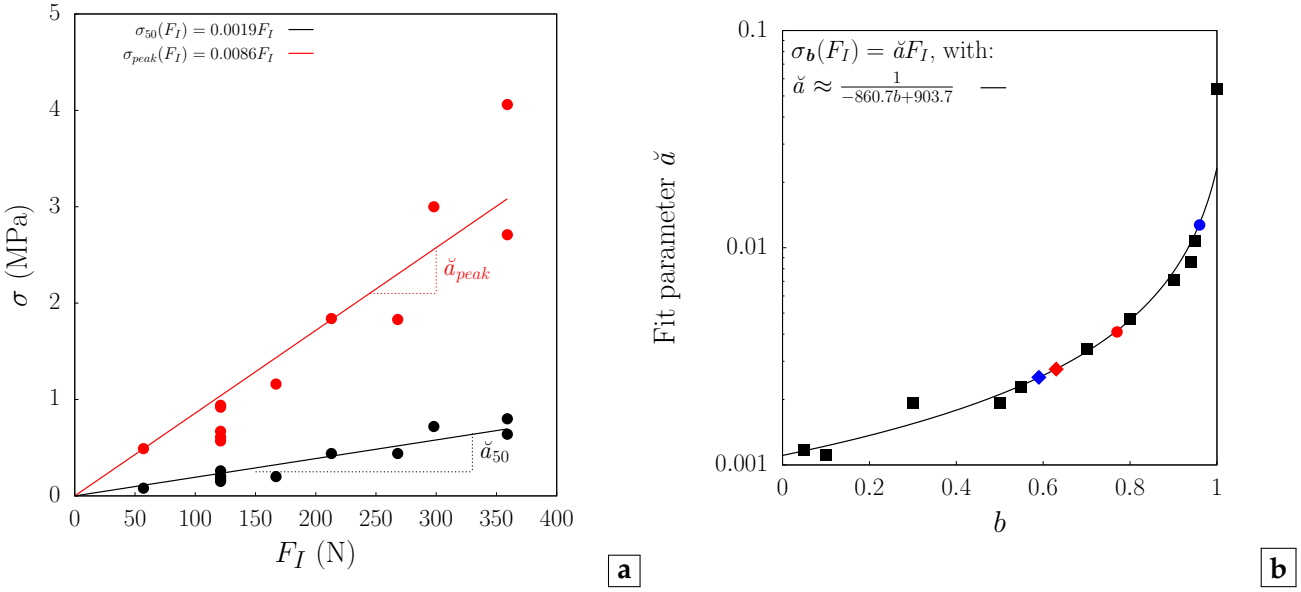

Figure 6.24 : a – Linear relationship exists between the stress σ_b at any breakage level b and the tensile strength of shells F_I. Using many simulations of uniaxial compression, the fit provides slope $\breve{a}_b$. **b** – This slope $\breve{a}$ increases non-linearly as a function of b. Thus, the breakage can be found as a function of axial stress $b(\sigma_a)$.

rameters should take place once more, yet herein, it was avoided by limiting e to e_{fin}. Following the statement of Gudehus (1996), h_s is related to the strength of shells. In this work, analysis of mechanical behaviour showed that the reflection of the curve is assigned to specific breakage level b. Combining those two observations, the axial stress at different breakage levels σ_b as a function of average tensile strength F_I was reconsidered.

Figure 6.24a presents linear relationship between the tensile strength and the macroscopic axial strain once $b = 0.5$ (σ_{50} – black line) and for $b \approx 0.94$ when the peak of $e^\star$ was reached (σ_{peak} – red line). Different slopes $\breve{a}$ have been found for those cases indicating an increase of slope for higher breakage level. Note that dots stand for data from various numerical simulations. The analysis of many breakage levels led us to the determination of trend function as presented in **Figure 6.24b**. Due to this rotational function, one can predict the linear slope $\breve{a}$, and thereby, the corresponding stress level at any b. Also, it is possible to determine the soil hardness h_s by assigning it to a specific breakage level.

Let us discuss the inclination parameters: $n^{\hookleftarrow}$ in equation (6.16) and $n^{\hookrightarrow}$ in equation (6.17). Void ratio e can be considered as a dimensional equivalent of the axial strain ε_a. Then, **Figures 6.1c** and **6.1d** indicate that n depends on the initial states of the packing.

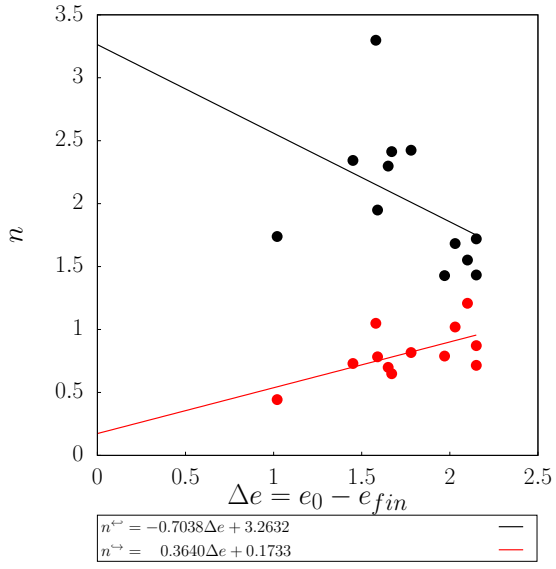

Figure 6.25 : Macroscopic shape parameter n in equations (6.16) and (6.17) control the inclination of curves predicting $e \leftrightarrow \sigma_a$ trend (**Figure 6.23**). An attempt to simplify the shape as the linear function of the initial and final state has been accepted to test the constitutive model.

Initial void ratio e_0 is the most simple scalar descriptor of initial state and is already employed as the input in function (6.16). Yet, in case of relationship (6.17) the importance of e_0 was redirected to e_{fin}, and therefore, we have attempted to combine them both and base the model on their difference $\Delta e = e_0 - e_{fin}$. The higher Δe, the more loose is the packing.

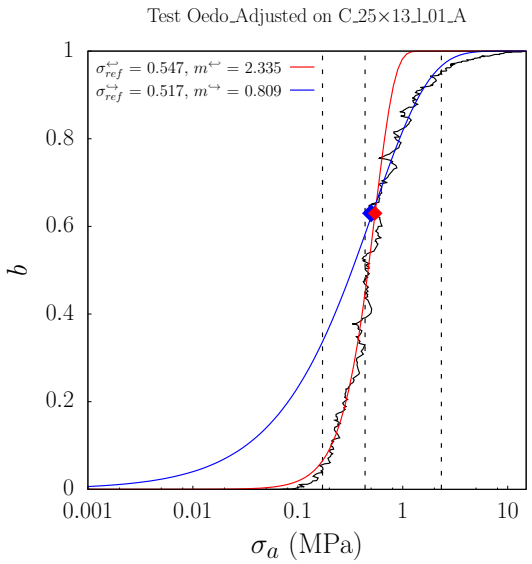

Figure 6.26 : Presenting breakage as a function of axial stress $b(\sigma_a)$ required a division of trend into two sub-domains: before (red) and after the inflexion point (blue). In the fit function $b(\sigma_a) = 1 - \exp[-(\sigma_a/\sigma_{ref})^m]$, σ_{ref} rules the stress for $b \approx 0.63$ and m rules inclination of curve.

Figure 6.26 recalls the evolution of breakage from **Figure 6.1c** in case of the initially loose assembly and adapted parameters strength (Oedo_Adjusted). Essentially, the evolution of b follows the trend described by relation:

$$b(\sigma_a) = 1 - \exp[-(\sigma_a/\sigma_{ref})^m, \qquad (6.18)$$

with scale σ_{ref} and shape m parameters. Indeed, this function provides very accurate fits, yet the complex trend of $b(\sigma_a)$ needed to be separated into two domains as for $e(\sigma_a)$: below ($\hookleftarrow$ red line) and above ($\hookrightarrow$ blue line) the numerical inflexion point. The modification of trend (its parameters) proves that the change of the response also appears at the grain scale. The inclination of trend declines as suggests the decrease of m, confirming already discussed inhibition of breakage rate (section 6.1). It is interesting to observe that the scale parameter σ_{ref} marked by for both distributions stays in good agreement with each other $\sigma_{ref}^{\hookleftarrow} \approx 1.102\sigma_{ref}^{\hookrightarrow}$ (average trend), and moreover, with the stress at the inflexion point σ_{50}. The red an blue rhomb points mark the location of σ_{ref} parameters both in **Figure 6.26** and in **Figure 6.24b**. Then, using the relationship presented in **Figure 6.24b** also σ_{ref} parameters can be predicted.

Figure 6.2 suggested that the evolution of breakage b is connected mainly to the strength of shells but is independent of the initial state of the sample. **Figure 6.27** also confirms that observation, since different initial states were taken into account. The points show parameter obtained from fitting and the horizontal lines mark their average values. Furthermore, a constant inclination parameters $m^{\hookleftarrow}$ and $m^{\hookrightarrow}$ (**Figure 6.27**) suggest the independence from the tensile strength F_I. The inclination parameter also represents the width of σ_a range causing primary breakage. The constant character is more visible in case of $m^{\hookrightarrow}$ with fewer oscillations 0.869 ± 0.061, whereas $m^{\hookleftarrow} = 2.501 \pm 0.404$ presents large fluctuations from the mean.

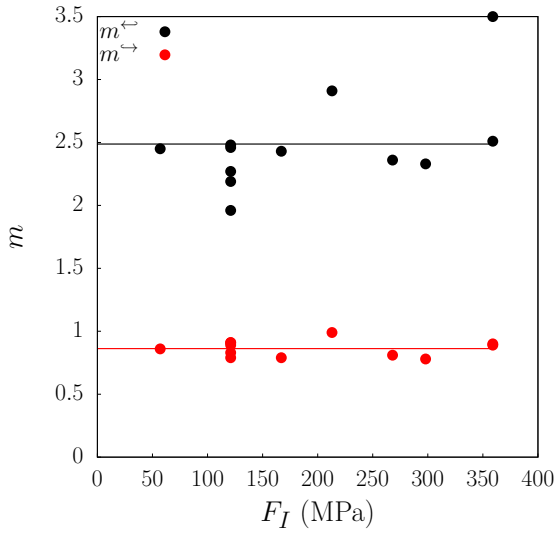

Figure 6.27 : In the relationship used to characterise the primary breakage $b(\sigma_a) = 1 - \exp[-(\sigma_a/\sigma_{ref})^m]$, m rules inclination of curve, and therefore, the width of stress range causing the breakage. If m is constant, the evolution is independent not only from the initial state but also from the strength of shells.

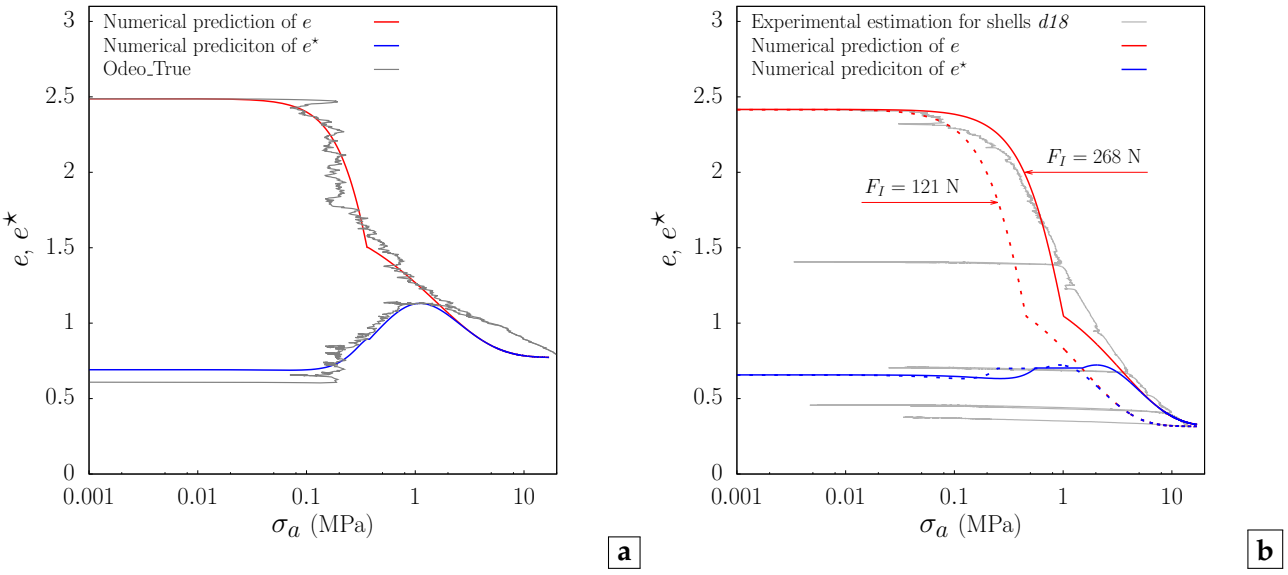

Figure 6.28 : Analytical prediction model predicting classic e (equations 6.16 and 6.17) and modified $e^\star$ void ratio (equation 6.19): **a** – a validation of the numerical implementation comparing to DEM modelling (dense packing) and **b** – a comparison with experimental curve (where e is an estimation).

To summarise, the analytical model predicting the inter-granular void ratio follows the relationship:

$$e^\star(e,b) = \frac{e(\sigma_a) - (1 - b(\sigma_a))E_0}{1 + (1 - b(\sigma_a))E_0}. \qquad (6.19)$$

A constitutive model of Bauer (1996) was used to describe $e(\sigma_a)$ up to inflexion point (equation 6.16), afterwards its modified version was introduced (equation 6.17). Both constitutive relationships have two parameters: the shape parameter and the soil hardness. First one was assumed to be a function of dimensional strain range Δe (**Figure 6.25**), while the second one was the axial stress for a specific b found as a liner function of the critical shell force (F_I) causing a tensile breakage (**Figure 6.24**). Similar scheme was used for $b(\sigma_a)$, according to equation (6.18), with a constant shape parameter and the reference stress assigned to the value of b (**Figure 6.24**). Hereinafter, we will probe this scheme. Firstly, the prediction model has been tested referencing the simulation Oedo_True as presented in the **Figure 6.28a**. The model was constructed using multiple simulations, therefore, **Figure 6.28a** validates the attempt to optimise the parameter with respect to the initial state and the average shell strength. As is seen, the analytical model has provided an equivalent behaviour, yet a few discrepancies can be pointed out. Firstly, the initial modified void ratio $e_0^\star$ is overestimated. Secondly, after e-curve and $e^\star$-curve join the prediction and the modelling start to diverge, *i.e.*, once the breakage inhibition was reached. On one side, the need to recalibrate the prediction parameters for the assembly of sectors without breakage has been highlighted once more. On the other hand, introducing another set of parameters to be adjusted would lead to higher complexity. The evolution of prediction up to peak stress for both e (recall that e is also a prediction) and $e^\star$-curves stay in good agreement with modelling. The observations of the model are consistent with the assumptions and simplifications made *a priori*, and the model seemed to be well established. Thus, **Figure 6.28b** compares model with experimental data. Note that the experimental void ratio is unknown, but we provide the reader with an estimation. 2 031 shells were assessed from the mass of sample divided by the mean mass of a shell $\langle m_{shell} \rangle = 0.0035$ kg. Using the initial dimensions of sample $H_0 = 0.135$ m and $D = 0.350$ m, e_0 was found at 2.417. From the final displacement of loading plate once can calculate $e_{fin} = 0.316$ and $\Delta e = 2.101$. Note that the

shell in size *d18* is characterised by the micro-void ratio of $E_0 = 1.06193$. The true micro-mechanics were introduced throughout $F_I = 121$ N. **Table 6.2** summaries the parameters used by the model. In case of e prediction, parameters h_s and n are compared with their experimental equivalents found from fitting the isotopic compression law (equation 6.16) and relationship (6.17). As is seen, the experimental soil hardnesses are approximately 3 times larger. The inclination parameter also shows some discrepancy. Although the experimental fit up to inflexion point was reliable, the fit above the inflexion point should be approached cautiously. Although the behaviour was reported to be less inclined (**Figure 5.22**), $n^{\hookrightarrow}$ falsely suggests higher inclination. The shells break into a smaller fraction in experiments such that the function (6.17) is less suitable for the experimental compression curve.

Parameter	Prediction	Estimation
$\sigma_{ref}^{\hookleftarrow}$	0.335	–
$m^{\hookleftarrow}$	2.488	–
$\sigma_{ref}^{\hookrightarrow}$	0.306	–
$m^{\hookrightarrow}$	0.863	–
$h_s^{\hookleftarrow}$	0.502	1.590
$n^{\hookleftarrow}$	1.786	1.333
$h_s^{\hookrightarrow}$	1.563	4.418
$n^{\hookrightarrow}$	0.938	1.556

Table 6.2 : The parameters used in the analytical model to predict the experimental $e^\star$ (**Figure 6.28b**). σ_{ref} and m correspond to the breakage (**Figure 6.26**), and h_s and n come from the isotopic compression law (equation 6.16 and **Figure 6.23**).

Focusing on the **Figure 6.28b**, one can see the prediction and experiment mismatch as much as the DEM modelling mismatch the experiment. Recalling section **5.1.6** which discussed the need to adjust micro-mechanical to obtained proper macro-mechanical behaviour, these discrepancies were foreseen. As expected from e_0, the model predicts the behaviour of dense packing. Therefore, the inclination parameter n for red curve is larger than the experimental one – grey line (**Table 6.2**). Inputting the true tensile force explained the divergence of stress at inflexion point and $e^\star$-peak. It is interesting to observe that void ratio at the inflexion point was found most adequately.

Problem with $e^\star$-peak comes from the numerical implantation. Two trends for e intersect in another point (different σ_a) than two trends for b intersect. Change of trend at inflexion point leads to the jump or in void ratio e-curve or in breakage b-curve. **Figure 6.28b** shows results where the inflexion point was adjusted such that e-curve transform smoothly. Yet, there can appear jump in predicted b-curve. To avoid it, b was kept constant (plateau) for a while such that b can only rise and never declines. But when b is constant e decrease so the model give decrease of $e^\star$. Perhaps, a point of changing b-trends should adjust separately from e, then $e^\star$ will experience a plateau as well, and $e^\star$-curve will evolve without decrease.

Summarising, the analytical prediction model was based on data from modelling, and therefore, it predicts properly the DEM simulations for various configurations. Yet, the discrepancy between DEM simulations and the experiment led the constitutive model to mismatch the experiment. At the start of this study, a simplification of the DEM model was established and resulted in this discrepancy. However, the possible future enhancements of the DEM simulations, such that the experiments are properly reflected, might be followed by the recalibration of constants in the constitutive model. Then, the prediction will reflect the experiment more adequately. Up to that moment, it is suggested to respect the true micro-mechanics of packing. It caused the under-estimation of sample macroscopic load σ_a, which is a safer approach than adapt the parameters such that for $\sigma_a > \sigma_{50}$ the models significantly over-estimate the sample strength.

6.6 Summary

Hereinbefore, the micro-mechanical response within the assemblies was analysed during uniaxial compression taking into account different aspects:

- The macroscopic mechanical behaviour is a consequence of shells breakage with respect to both axial stress and the axial strain. Nat-

urally, the evolution as a function of axial deformation is dependent on the initial state. With respect to stress breakage is ruled by the strength of constituent particles, yet the anisotropy of shell orientations is a significant contributor.

- There exists a characteristic thresholds of breakage level b that correspond to characteristic points on the compression curve: the onset of comminution, the inflexion point and the inhibition of breakage. Due to the variability of modelling, this thresholds were included in a range of breakage degree such as the inflexion point can be established as $b \in \langle 0.4 : 0.6 \rangle$. The proposed average values found in the DEM modelling are orientational landmarks rather than rigorously constrains.

- Grain size distributions were shown for different shell strength. The comparison with experimental GSD has proven that adjusting the strength lead to under the appearance of breakage. Despite the limitation of the model, a similar evolution of GSDs has been obtained numerically as experimentally.

- Analysis of each fragment size evolution has shown the cascade type of breakage evolution within an assembly. Therefore, each fraction evolves for a different range of macroscopic stress but the evolution curves have a similar character.

- The statistical analysis of local stress has shown. The majority of shells are subjected to stress in the order of the macroscopic loading σ_a. The width of distributions evolves non-monotonously as the grading, coordination number and orientation of shells change.

- The analysis of orientation shells along uniaxial compressions showed the tendency to increase the horizontally oriented anisotropy of sectors, despite the initial preferential orientation.

- The definition of void ratio e has been redefined in the framework of accessible and inaccessible space – $e^\star$. The increase of $e^\star$ as the primary breakage b progress explained that the highly compressible response of the material is activated only throughout the breakage, that is, throughout the access to the internal voids.

Finally, the construction of two constitutive models was attempted aiming mainly prediction $e^\star$ showing the potential of the assembly to compress.

- Prediction of strain was based on mainly mathematical transformations of the basic equations defining void ratio and natural strain. Still, this very basic constitutive model included the evolution of breakage and of classic void ratio as a function of strain, the initial state (e_0) and the geometrical extrusions (E_0). Although the axial strain might be considered as an incorrect reference variable, the model provides a rough estimation of compressive behaviour.

- Prediction referencing the macroscopic stress was a greater challenge since the mathematical relations are not sufficient any more. The phenomenological framework needs to be adjusted for a proper constitutive model, such as attempted in this chapter. The isotopic compression law proposed by Bauer (1996) has been used as a starting point and modified when the prediction and the modelling diverge (with parameters h_s and n). The trend function for breakage curve evolving as a function of stress also has been found (with parameters σ_{ref} and m). The model assumed the reference stresses (h_s and σ_{ref}) depend on the tensile strength of the material, whereas the inclination parameter n depends on the initial state (excluding vertical anisotropy) and m is constant. The constitutive model mismatch the experimental e in the same level that DEM simulations disagree with the experiment.

Closure of the study

7.1 Summary & Conclusions

Summarising, this PhD dissertation was dedicated to a comprehensive micro- and macroscopic investigations of unique granular material. The study had mainly a numerical character, although the series of the experimental measurements were performed to support the reliability of our model. We began at the grain scale to generate the model, continued throughout a sample deposition and finished with modelling of large assemblies.

Granular material

We studied a granular material composed of the grains shaped as the coarse-size tubes (shells) with two important characteristics. Firstly, those particles were manufactured for a specific industrial application with a necessity of being formed from an excavated COx clay-stone. The fabrication was conducted by means of the mechanical and thermic treatments, thus, we dealt with the brittle grain crushing. Secondly, the tube geometry was characterised by a high internal porosity such that the volume of the tube and a cylindrical internal void were almost equal ($E_0 \sim 1$).

DEM tool

The numerical modelings have been performed using Discrete Element Method implemented in the software ROCKABLE (Richefeu, 2016) developped for this study. This software perfectly suits our needs, since it is capable to model any complex shapes with so-called *sphero-polyhedra* and to reflect a brittle fracture thanks to the concept of the *breakable interfaces*. To generate a shell, a number of sphero-polyhedral elongated clumps, called *sectors*, were clustered together throughout cohesive links. This approach requires two user-specified parameters representing the material cohesion resistant to a pure tension ($f_I^\star$) and a pure shear ($f_{II}^\star$).

A model of breakable shell

In order to adjust the tensile failure, an experimental campaign of diametrical compressions on shells has been carried on. The critical load presented a strong variability due to the geometrical and material heterogeneities. Its cumulative distribution function was Weibullian and was easily converted to the distribution of the tensile yielding threshold ($f_I^\star$), further used in the DEM simulations. The cohesive link stiffness controlled the slope of the linear elastic force-displacement relationship, while the critical force was ruled by the tensile threshold of the links $f_I^\star$, causing their opening. Both parameters depend on the shape discretisation, which is an important choice to be made *a priori*. For the sake of calculation efficiency, the final discretisation considered only with the circumferential division into only 12 sectors, since this cluster model was then probed as a constituent in the large assembly. The verification of the cluster was successfully performed on the biaxial compression of a shell with the minor load being a consequence of the horizontal strain constraints. Thanks to the experimental results, the force law parameters for the cohesive links were successfully validated.

Sample Preparation

The sample preparation was an intermediate but crucial step to the following study of mechanical behaviour. The numerical protocol included

two phases: a gravity deposit (a reflexion of the real procedure) and a numerical relaxation (a release of the kinematic energy in time). As a result, shells belonging to the core of the assembly were randomly orientated, however at the boundary, a deviation from fairly isotopic distribution towards a preferential orientation (mainly horizontal) was observed. The initial density can be controlled by the inter-cluster friction coefficient, such that for a frictionless deposit the maximum (numerical) density was obtained. Throughout an adjustment of friction coefficient, the samples were prepared with a number density comparable to the experimental measurements. The actual orientation of shells was investigated thanks to an X-ray CT and 3D image analysis. A new tool 3DShellFinder was developed, and then, probed in the case of the true samples extracted from the original tunnel segment. The horizontal (tangent to the tunnel extrados) orientation was dominant in the in-situ configurations, although the boundary effect was expected to be negligible. The Legendre's polynomials expansion was found to be a suitable method to characterise the distribution of shell orientations and quantify its anisotropy, only if the local extreme of the distribution (steep peak) did not exist. Those study inspired us to enhance the preparation protocol such that also the samples with a strong preferential anisotropy were prepared.

Oedometer compression

The numerical investigations were limited to the uniaxial compression, know also as oedometer test. A parametric study allowed us to understand the importance of many numerical parameters, test the influence of the initial state and discover the model limitations due to the geometry of the sectors.

To obtain an agreeable mechanical curve, an adjustment of the parameters was necessary also at the macro scale. Among all the force law parameters, the normal yield thresholds $f_I^\star$ (reflecting the tensile strength of shells) one more proved itself to be of the greatest significance. For the 1D compression, if the constituents are stronger, the sample, likewise, is more resistant. Surprisingly, the heterogenity of strength played a secondary role and the use of Weibullian-like variability did not bring any obvious benefit. What concerns the tangential yield thresholds, it must exceed $f_I^\star$, since the shear strength of baked clay is higher than the tensile strength, by a natural relationship.

Internal state variables turned out to be highly influential. A standard effect of initial density has been observed, such that denser samples behaved stronger and even a local softening was observed. The investigation of the preferential orientations brought some interesting observations. The vertically oriented shells caused high oscillation in the mechanical response (more precisely, in the stress evolution). On the contrary, the horizontal shells seemed to arrange into a rather loose assembly, which presents a smooth mechanical response.

The model reproduced the stress↔strain curve from true 1D compression[1], but the input parameters mismatched the experimental estimations and the initial loose state of DEM sample was lower than the true density. Also, the model was incapable of reaching the true ultimate grain size distribution, which was caused by the initial choice of the sector size. The final modelling involved the unloading and reloading cycles. In the modelling the response of the sample less rigid, if the friction coefficient is kept constant during all the test. An increase of the friction in UR cycles led to elastic unloading at the contacts, and thus the mechanical response became more similar to the experimental one.

Analysis of compressible assembly

A more detail analysis not only provided some additional information, like the local mean pressures but also emphasised the role of grain breakage. In the case of shell assembly, the primary breakage had a major contribution to the high compressibility of material. Note that it was easy to quantify, and then, its evolution was related to the characteristics of the mechanical response. A classical consolidation curve has been obtained, if the internal voids were included in the void ratio calcu-

[1] The large scale oedometer tests were conducted both by Laboratory *Navier* and by *Euro-Géomat-Consulting (EGC)*.

lations (a total void ratio e). Looking at the inter-clusters void ratio $e^\star$ (the internal voids are seen as solid), its value rose as long as a large number of voids was being constantly released during continuous shells crushing. Once the primary breakage slowed down, the inter-cluster void ratio presented a decrease. The peak in the evolution indicated the loss of the compressible capacity of the sample.

Finally, an analytical prediction model has been constructed to foresee both the total and the inter-granular void ratios. A simple model with respect to the strain has provided rough but acceptable estimations. The more complex model was required with respect to the macroscopic stress. We attempted to characterise the classical constitutive behaviour ($e \leftrightarrow \sigma_a$) with already existing model (Bauer, 1996), yet it was only partially suitable for this case. Thus, we proposed to divide the compression curve into two sub-domains (high and standard compressibility). In both sub-domains, two types of parameters were required. The shape parameter has been presented as a function of void ratio (correlated to density), whereas the soil hardness is well known to be a function of the particle strength. To predict the inter-granular void ratio $e^\star$, also, the evolution of primary breakage had to be characterised as a function of the macroscopic loading. To this end, an exponential-power law has been used with scale parameter depending on the tensile strength of shell, but with the shape parameter insensitive to the initial state (density). Since the DEM simulations has been a foundation for model the experimental behaviour can be reflected properly until the validity point of the model.

7.2 Perspectives

Final goal – FEM×DEM model

This work is a first step on the way to the final model applicable to a tunnel lining made of compressible arch-segments (VMC). A double scale model combining FEM at the structure scale (the tunnel) and DEM at the material scale (the assembly of shells), FEM×DEM (Desrues et al., 2019) is an appealing tool for this case. The DEM model of a compressible layer can be integrated into such a solution. To this end, the DEM part has to be fully developed and explored. The compressible layer is a highly complex material which model requires (*i*) the use of the complex shapes, (*ii*) a reliable model of the breakage (the material cohesion) and (*iii*) a representation of the cement joints (the inter-granular cohesion). This work has partially addressed these complex topics, but some important enhancements and developments still need to be done.

The coating

The first and, at this point, less demanding task is to include in the model the cement bonds. A similar scheme as for the inter-sector links can be used, yet adding rolling resistance. This study already provided the estimation of cement bridge strengths, however, the model adjustment most probably will be required. If the inter-cluster bonds will be infinitesimal, *i.e.*, ignoring the volume of coating, perhaps the limitation of the model, due to large sector size, will be diminished. In other words, considering the infinitesimal bonds will improve the validity of the model.

Also, the analytical prediction model could be enhanced and rebuild within the framework of cemented shells. This approach would require the understanding of the mechanical response with the coating and knowledge of the influence of bond strength, which is proven to affect the stress level in the literature. Still, the cement joints are an addition to the skeleton of shells, and thus, the basic analytical model for shells only constitutes a good reference and a starting point for this development.

The shape of shell

Hereinbefore, only tube thickness was analysed. Other variations of shell geometry may lead to an optimisation of the shape in the context of compressibility and strength. Unfortunately, the true force scattering and the change of the shell stiffness was not tested experimentally. This part of the study was supported with FEM modelings of a 2D ring. On one side, it could be an interesting

way to continue the study in this direction and fill this experimental gap. On the other side, the fabrication process is conducted by an external company as a massive production, the change of shape needs some technical adjustment that may not be economically friendly just for the supplementary research.

Other loading conditions

The background experimental campaign included also a series of standard triaxial tests, and data for the assembly with and without coating wait to be compared with a numerical model. We have performed a primary modelling of a triaxial test on a cubic sample with rigid walls. However, the rigid boundary conditions highly influence the freedom of deformation and of shear band formation. This is one of the motives for further improvements of the DEM tool, discussed as follows.

Boundary conditions – the technical enhancement of model

An appealing candidate to be implemented in the numerical scheme is a concept of the periodic boundary conditions. Above all, the FEM$\times$DEM specifically requires its numerical implementation. As discussed, it will upgrade the reliability of more advanced deformation patterns. Periodic boundary conditions will also erase the effect of rigid boundary, and thus, it may lead to a further reduction of the number of shells – a lower computational time.

Experimental improvements

The experimental characterisation of material both for a single shell and a coated shell assembly has developed some difficulties. For example, an attempt to extract a shear force has not been satisfactory. As it was discussed, the analysis of the 3D image cannot be limited to classic image analysis tools. Perhaps starting with less complex case and supporting the results with X-ray tomography of the non-cemented assembly would help to develop/enhance more capable tools.

A Uniaxial radial compression

A.1 Shape of cluster

Shape	t (mm)	d (mm)	h (mm)	$N^{\star}_{radial}$	$N^{\star}_{axial}$	Front view	Side view
d18-S1	2.4	17.0	17.0	12	1	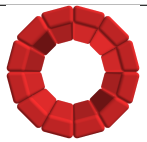	
d18-S2	2.4	17.0	17.0	12	2	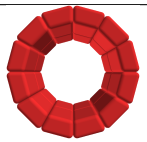	
d18-S3	2.4	17.0	17.0	16	1	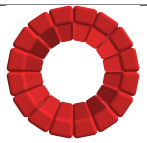	
d18-S4	3.6	17.0	17.0	12	1	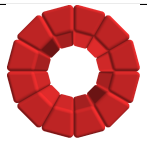	
d18-S5	4.8	17.0	17.0	12	1	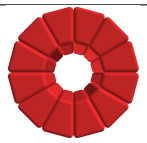	
d18-S6	2.4	17.0	17.0	24	1	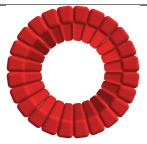	
d18-S7	2.4	17.0	17.0	8	1	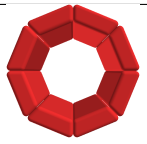	
d20-S1	2.8	18.6	18.5	12	1	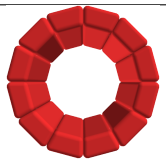	

Table A.1 : The characteristics of the cluster shape.

A.2 Adjustment of tensile strength – FEM modelling

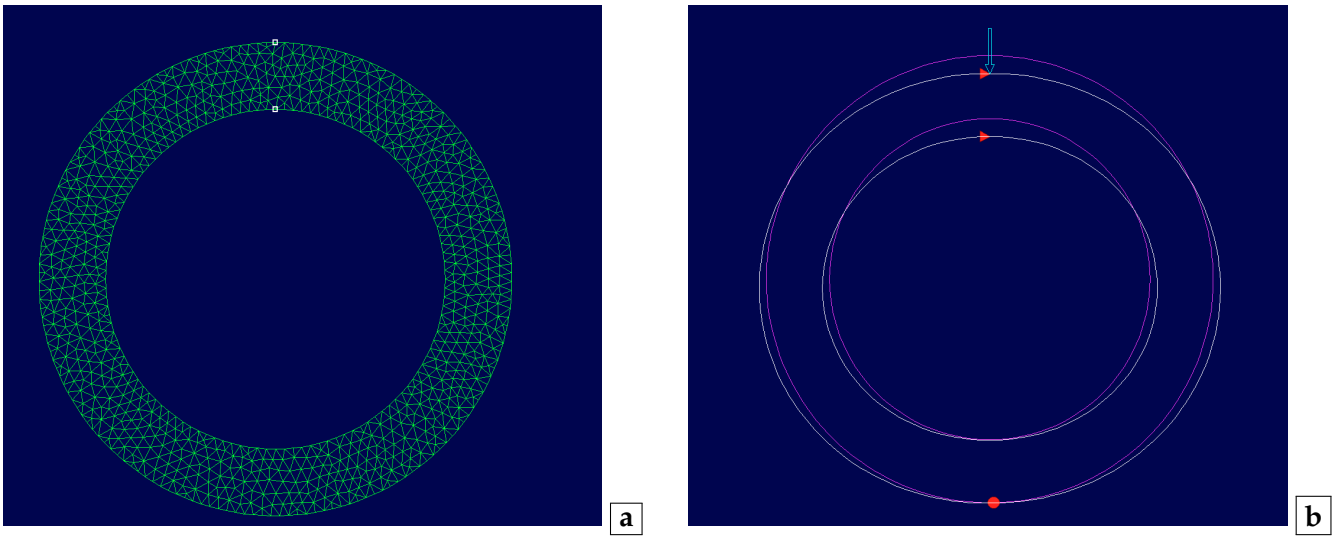

Figure A.1 : 2D FEM. A model in a plain stress condition: **a** – the irregular mesh with 2 500 elements **b** – the boundary conditions. The force $F_I = 120$ N acts in the vertical diameter. In the points marked by the bullet, neither a vertical nor a horizontal displacement is allowed. In the points marked by the triangle, only a vertical displacement is admitted. Tool: RDM.

Finite Element Method (FEM) is a numerical technique used to analyse various phenomena both in the engineering field and science. Since it can provide a full stress field, we have decided to perform 2D FEM modelling of the diametrically loaded shell. To this end, an open source finite element code called *RDM* was used (Institut Universitaire de Technologie du Mans, 2018).

FEM subdivides the domain into a finite number of smaller and simpler parts, called elements. **Figure A.1a** presents the mesh used to discretise the ring with diameters $d_{out} = 17.0$ mm and $d_{in} = 12.2$ mm (as for cluster *d18*-S1) into 2 500 elements. Then, a point load is applied in the vertical axis $F_I = 120$ N. In **Figure A.1b** the boundary conditions are presented assuming a plain stress state in the remaining dimension. The bottom of the ring is fixed such that no displacement can appear (red bullet). The point of loading can move only vertically (red triangle). Two elasticity parameters were used $E = 5$ GPa and $\nu = 0.3$ that are of the same order as the one found in the literature for COx clay-stone.

Figure A.2 presents the stress distribution within the shell cross-section. Because we deal with an orthogonal coordinate system, we show the horizontal stress σ_{xx} (**Figure A.2a**) and vertical ones σ_{yy} (**Figure A.2b**). This is sufficient to verify the tensile stresses (leading to mode I feature) in vertical and horizontal plane, respectively. The localisation of tensile stress stands in a good agreement with DEM modelling and theoretical solutions. The maximum tensile stress $\sigma_I = 16.93$ MPa is higher than analytical estimation with the average equal to 9.44 ± 1.47 MPa (**Figure 3.15**). Additionally, **Figure A.2a** distinguishes where the failure appears in DEM simulations of uniaxial radial compression, when the configuration of shells is rotated (the failure plane is inclined with respect to the vertical axis, **Figure 3.27b**).

Furthermore, this simple FEM modelling can supplement the DEM modelling. For example, it was employed in the scheme to determine $f_I^\star$, tensile strength of material, when modifying the shell thickness. DEM operates on the contact forces, which values depend on the amount of material per shell. Then, more material per cluster must lead to higher forces. Thus, $f_I^\star$ must be increased, but without experimental measurements it is not possible to calibrate our DEM model. In con-

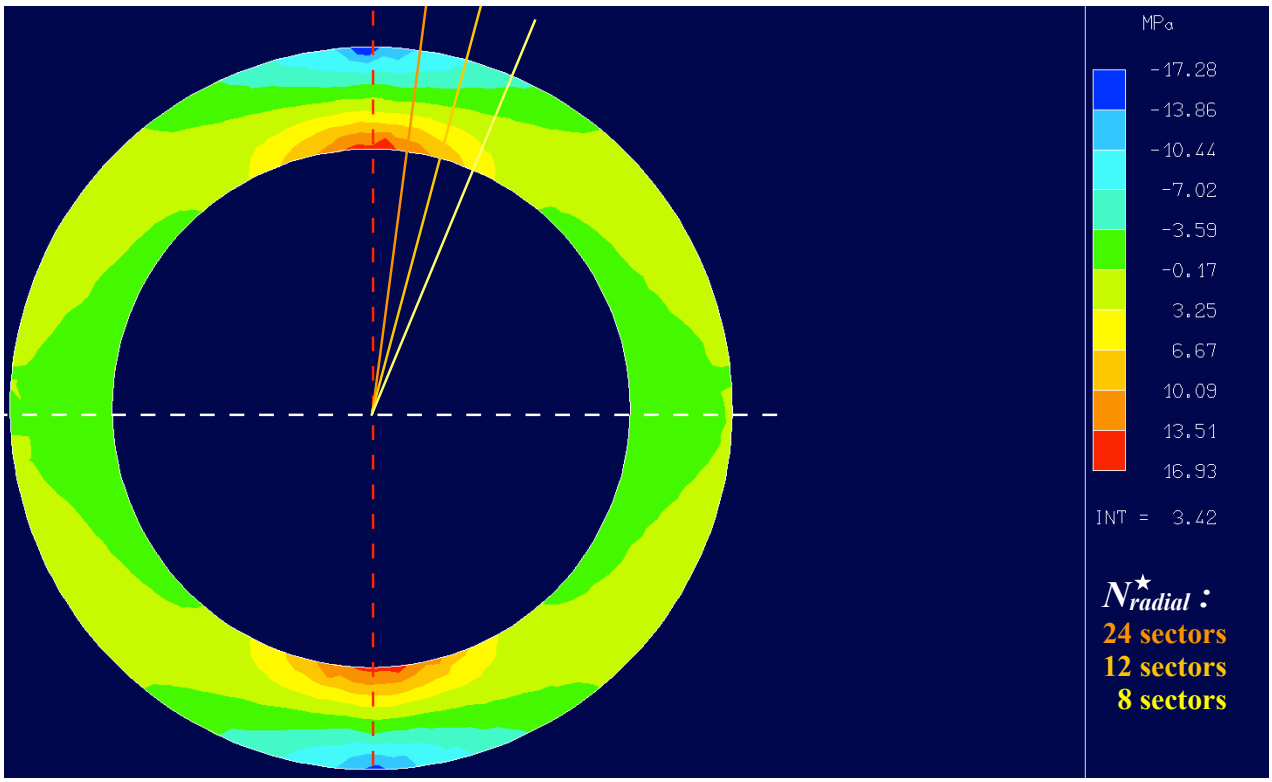

a

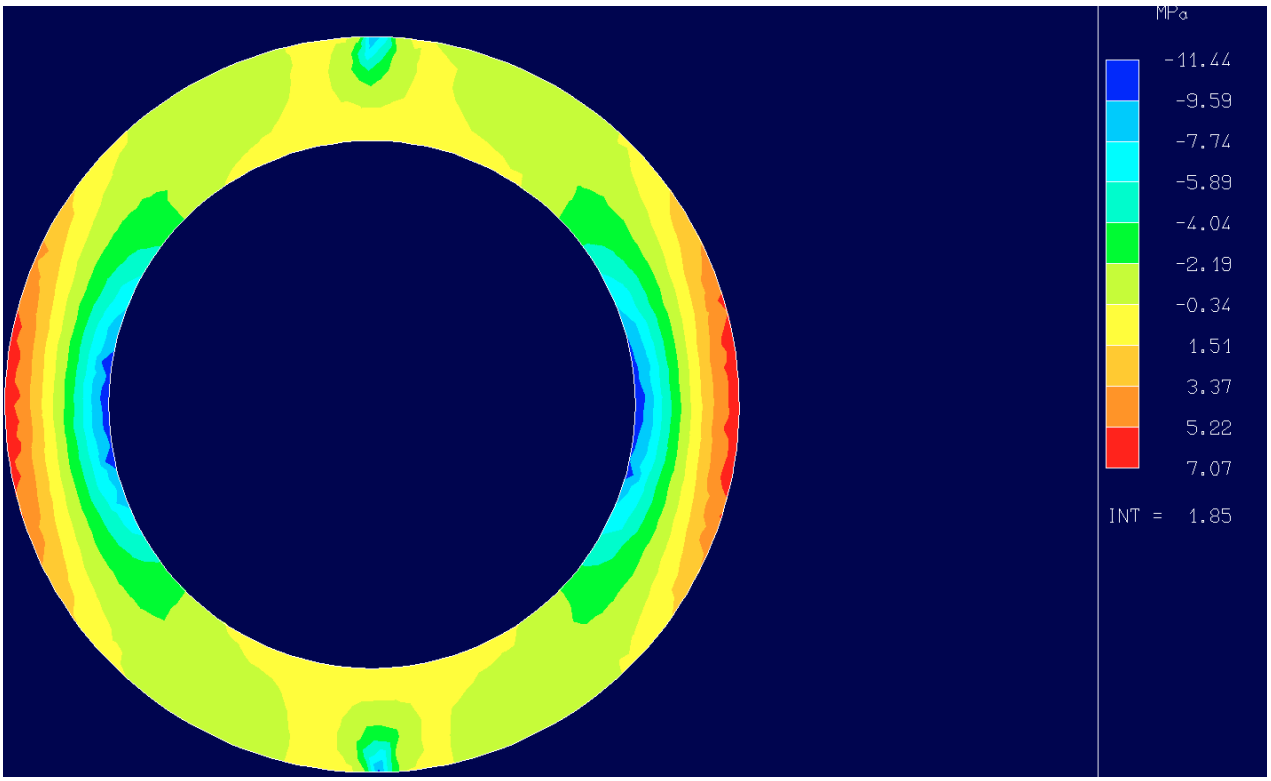

b

Figure A.2 : The results of 2D FEM modelling of shell. The internal stress distribution in the uniaxial radial compression loaded by the external force $F_I = 120$ N: **a** – the horizontal stress σ_{xx} and **b** – the vertical stress σ_{yy}.

trast, the tensile stress causing breakage is treated as a material constant. Even if the geometry of shell changes, σ_I should be constant. **Figure A.3** presents the scheme to determine $f_I^\star$ taking advantage of FEM model:

- ***step* 1**: In the case of shells *d18*, $f_I^\star$ was adjusted in DEM such that the cluster resists the load lower then the experimental average force F_I.
- ***step* 2**: Applying the load F_I, FEM model provides an equivalent tensile stress σ_I.
- ***step* 3**: A ring with new thicknesss is modelled with FEM. The process of trial and error leads to a determination of load F_I' triggering the same σ_I.
- ***step* 4**: Keeping F_I', the limit of tensile cohesion can be found in DEM modelling.

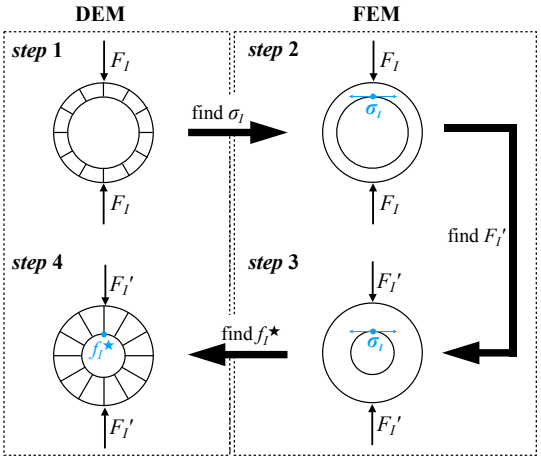

Figure A.3 : The numerical scheme to determine the tensile strength, if the geometry of the ring cross-section was modified. DEM and FEM supplement each other. Thanks to experimental campaign the tensile yield threshold $f_I^\star$ has been adjusted (***step* 1**). FEM modelling provided us with an equivalent tensile stress σ_I (***step* 2**). Once the geometry was modified, thanks to FEM, the updated critical load F_I' was selected to match the same critical σ_I (***step* 3**). Keeping F_I', the new $f_I^\star$ could have been found (***step* 4**).

This scheme has been used for shells with smaller internal void in the cases of shapes *d18*-S4 and *d18*-S5 used in chapter 5 in section 5.1.5 to study an affect of the high internal porosity. **Table A.2** sums up the results of the yield paramter determination as described above. One can see that the increase of $f_I^\star$ is not linearly proportional to F_I. The $F_I/f_I^\star$ ratio depends on thickness, indicating the importance of the relative radius (the void size) in the scattering of force.

Shape	*d18*-S1	*d18*-S4	*d18*-S5
			
t (mm)	2.4	3.6	4.8
$\bar{r}$	0.718	0.576	0.435
F_I (N)	121.3	286.0	517.7
$f_I^\star$ (N)	85	105	115
$F_I/f_I^\star$	1.4	2.7	4.5

Table A.2 : The results of normal yield threshold $f_I^\star$ adjustment of DEM parameters for the shells with smaller void see also **Table A.1**. The relative radius: $\bar{r} = r_{out}/r_{in}$.

B Initial state of samples

Sample	N	Cluster shape	H_0 (m)	n (m^{-3})	$e^\star$	e	Z_c	Z_n	N_{NHB}/N	N_{NRB}/N	N_{NB}/N
Sample D = 35 cm and $H_0 \approx$ 12 cm											
Various configuration											
C_35×12_d_01_A	1926	*d18*-S1	0.1220	164 139	0.579	2.423	9.62	6.23	0.66	0.79	0.52
C_35×12_d_02_A	1926	*d18*-S1	0.1225	163 468	0.585	2.437	9.76	6.17	0.67	0.79	0.53
C_35×12_d_03_A	1926	*d18*-S1	0.1223	163 674	0.583	2.433	9.83	6.28	0.67	0.79	0.53
C_35×12_d_04_A	1926	*d18*-S1	0.1231	162 566	0.594	2.456	9.79	6.30	0.68	0.79	0.54
C_35×12_d_05_A	1926	*d18*-S1	0.1216	164 640	0.574	2.413	9.79	6.28	0.67	0.80	0.53
C_35×12_d_06_A	1926	*d18*-S1	0.1228	163 004	0.590	2.447	9.96	6.22	0.67	0.79	0.53
Different shell geometry											
C_35×12_d_07_B	1926	*d18*-S2	0.1231	162 573	0.594	2.450	9.46	6.24	0.67	0.79	0.53
C_35×12_d_08_C	1926	*d18*-S5	0.1252	159 940	0.620	1.082	10.74	6.37	0.71	0.79	0.56
C_35×12_d_09_D	1926	*d18*-S4	0.1241	161 250	0.607	1.516	10.20	6.36	0.68	0.79	0.54
Sample D = 35 cm and $H_0 \approx$ 5 cm											
C_35×5_d_01_A	1579	*d18*-S1	0.0510	160 965	0.610	2.490	9.51	5.78	0.21	0.79	0.16
C_35×5_d_02_A	1579	*d18*-S1	0.0510	161 004	0.610	2.490	10.12	5.91	0.22	0.80	0.16
C_35×5_d_03_A	1579	*d18*-S1	0.0510	161 004	0.610	2.490	9.99	5.88	0.22	0.79	0.16
C_35×5_d_04_A	1579	*d18*-S1	0.0510	160 940	0.610	2.491	9.86	5.97	0.22	0.79	0.17
C_35×5_d_05_A	1579	*d18*-S1	0.0510	161 003	0.610	2.490	10.39	5.86	0.22	0.80	0.17
C_35×5_d_06_A	1579	*d18*-S1	0.0508	161 660	0.603	2.475	9.16	5.96	0.19	0.79	0.15
C_35×5_d_07_A	1579	*d18*-S1	0.0510	161 016	0.610	2.489	9.03	5.73	0.21	0.79	0.15
C_35×5_d_08_A	1579	*d18*-S1	0.0510	161 006	0.610	2.490	9.77	5.97	0.22	0.79	0.17
C_35×5_d_09_A	1579	*d18*-S1	0.0510	161 006	0.610	2.490	9.83	5.83	0.22	0.79	0.17
C_35×5_d_10_A	1579	*d18*-S1	0.0510	161 008	0.610	2.490	9.56	6.01	0.21	0.80	0.17
Sample D = 35 cm and $H_0 \approx$ 7 cm											
C_35×7_d_01_A	1105	*d18*-S1	0.0734	156 479	0.656	2.591	9.59	5.95	0.43	0.80	0.34
C_35×7_d_02_A	1105	*d18*-S1	0.0725	158 344	0.637	2.548	9.70	6.00	0.42	0.79	0.33
C_35×7_d_03_A	1105	*d18*-S1	0.0728	157 774	0.643	2.561	9.81	6.06	0.42	0.79	0.33
C_35×7_d_04_A	1105	*d18*-S1	0.0731	157 097	0.650	2.576	9.69	5.97	0.43	0.80	0.33
C_35×7_d_05_A	1105	*d18*-S1	0.0724	158 683	0.633	2.541	9.98	5.97	0.43	0.79	0.34
C_35×7_d_06_A	1105	*d18*-S1	0.0723	158 930	0.631	2.535	9.83	5.99	0.42	0.80	0.33
Sample D = 35 cm and $H_0 \approx$ 10 cm											
C_35×10_d_01_A	1579	*d18*-S1	0.1009	162 717	0.593	2.453	9.63	6.16	0.60	0.79	0.47
C_35×10_d_02_A	1579	*d18*-S1	0.1012	162 105	0.599	2.466	9.43	6.24	0.61	0.80	0.49

Continued on next page...

Sample	N	Cluster shape	H_0 (m)	n (m^{-3})	$e^\star$	e	Z_c	Z_n	N_{NHB}/N	N_{NRB}/N	N_{NB}/N
C_35×10_d_03_A	1579	*d18*-S1	0.1014	161 877	0.601	2.471	9.70	6.18	0.60	0.80	0.47
C_35×10_d_04_A	1579	*d18*-S1	0.1016	161 609	0.604	2.477	9.75	6.20	0.60	0.79	0.47
C_35×10_d_05_A	1579	*d18*-S1	0.1009	162 680	0.593	2.454	9.68	6.10	0.60	0.80	0.47
C_35×10_d_06_A	1579	*d18*-S1	0.1009	162 608	0.594	2.455	9.45	6.23	0.61	0.79	0.48
Sample D = 25 cm and $H_0 \approx$ 13 cm											
Various configuration											
C_25×13_d_01_A	1047	*d18*-S1	0.1308	163 068	0.589	2.445	9.68	6.15	0.70	0.72	0.50
C_25×13_d_02_A	1047	*d18*-S1	0.1324	161 084	0.609	2.488	9.97	6.17	0.70	0.72	0.50
C_25×13_d_03_A	1047	*d18*-S1	0.1304	163 567	0.584	2.435	9.92	6.20	0.69	0.72	0.49
C_25×13_d_04_A	1047	*d18*-S1	0.1318	161 833	0.601	2.472	9.57	6.15	0.70	0.72	0.50
C_25×13_d_05_A	1047	*d18*-S1	0.1323	161 264	0.607	2.484	9.56	6.22	0.69	0.72	0.49
C_25×13_d_06_A	1047	*d18*-S1	0.1309	162 980	0.590	2.447	9.62	6.23	0.70	0.72	0.50
C_25×13_d_07_A	1047	*d18*-S1	0.1303	163 699	0.583	2.432	9.67	6.19	0.69	0.72	0.49
Different shell geometry											
C_25×13_d_01_E	804	*d20*-S1	0.1325	123 582	0.610	2.296	9.85	6.10	0.67	0.69	0.47
Preferential orientation											
C_25×13_d_01_AV	1047	*d18*-S1	0.1329	160 452	0.615	2.502	10.08	6.07	0.74	0.71	0.53
C_25×13_d_02_AV	1047	*d18*-S1	0.1320	161 602	0.604	2.477	10.76	6.01	0.74	0.72	0.53
C_25×13_d_03_AV	1047	*d18*-S1	0.1363	156 488	0.656	2.590	9.21	5.40	0.80	0.70	0.56
C_25×13_d_01_AH	1047	*d18*-S1	0.1322	161 324	0.606	2.483	9.36	6.21	0.66	0.72	0.47
C_25×13_d_02_AH	1047	*d18*-S1	0.1336	159 707	0.623	2.518	9.15	6.19	0.66	0.72	0.47
Various density											
C_25×13_l_01_A	1047	*d18*-S1	0.1519	140 388	0.846	3.002	5.53	4.24	0.74	0.71	0.53
C_25×13_D_01_A	1047	*d18*-S1	0.1244	171 450	0.512	2.277	11.70	7.08	0.67	0.72	0.48
C_25×13_exp_01_A	1047	*d18*-S1	0.1384	154 076	0.510	2.647	6.19	4.54	0.72	0.71	0.51
Sample D = 11 cm and $H_0 \approx$ 13 cm											
C_11×13_d_01_A	203	*d18*-S1	0.1345	158 800	0.632	2.538	9.56	5.99	0.69	0.41	0.28
C_11×13_d_02_A	203	*d18*-S1	0.1364	156 606	0.655	2.588	9.15	5.86	0.72	0.41	0.30
C_11×13_d_03_A	203	*d18*-S1	0.1363	156 722	0.654	2.585	9.05	5.94	0.73	0.41	0.29
C_11×13_d_04_A	203	*d18*-S1	0.1348	158 502	0.635	2.545	9.20	5.61	0.72	0.42	0.30
C_11×13_d_05_A	203	*d18*-S1	0.1368	156 128	0.660	2.599	9.30	5.82	0.72	0.40	0.29
C_11×13_d_06_A	203	*d18*-S1	0.1388	153 933	0.684	2.650	9.09	5.99	0.73	0.40	0.30
C_11×13_d_07_A	203	*d18*-S1	0.1377	155 163	0.670	2.621	9.59	5.87	0.72	0.42	0.30

Continued on next page...

Sample	N	Cluster shape	H_0 (m)	n (m^{-3})	$e^\star$	e	Z_c	Z_n	N_{NHB}/N	N_{NRB}/N	N_{NB}/N
C_11×13_d_08_A	203	*d18*-S1	0.1354	157 790	0.642	2.561	9.85	6.05	0.70	0.41	0.28
C_11×13_d_09_A	203	*d18*-S1	0.1354	157 786	0.642	2.561	9.80	5.76	0.70	0.41	0.29
C_11×13_d_10_A	203	*d18*-S1	0.1363	156 727	0.654	2.585	9.47	5.75	0.73	0.42	0.32
C_11×13_d_11_A	203	*d18*-S1	0.1386	154 175	0.681	2.644	9.61	5.83	0.72	0.41	0.29
C_11×13_d_12_A	203	*d18*-S1	0.1363	156 701	0.654	2.585	9.34	5.81	0.71	0.41	0.28
C_11×13_d_13_A	203	*d18*-S1	0.1393	153 385	0.690	2.663	9.45	5.78	0.72	0.41	0.31
C_11×13_d_14_A	203	*d18*-S1	0.1374	155 458	0.667	2.614	9.41	5.70	0.73	0.41	0.31
C_11×13_d_15_A	203	*d18*-S1	0.1389	153 748	0.686	2.654	8.92	5.57	0.73	0.41	0.32
C_11×13_d_16_A	203	*d18*-S1	0.1373	155 556	0.666	2.612	9.39	6.15	0.71	0.42	0.30
C_11×13_d_17_A	203	*d18*-S1	0.1389	153 799	0.685	2.653	9.13	6.05	0.70	0.42	0.30
C_11×13_d_18_A	203	*d18*-S1	0.1407	151 872	0.706	2.699	9.54	5.90	0.75	0.41	0.31
C_11×13_d_19_A	203	*d18*-S1	0.1370	155 897	0.662	2.604	8.93	5.78	0.73	0.41	0.30
C_11×13_d_20_A	203	*d18*-S1	0.1382	154 622	0.676	2.634	9.69	6.01	0.73	0.42	0.32
C_11×13_d_21_F	203	*d18*-S2	0.1375	155 380	-	2.645	9.34	5.85			
Prism Sample $L_X = L_Z = 19$ cm and $L_Y = H_0 = 17$ cm											
P_19×17_d_01_A	203	*d18*-S1	0.1705	162 468	0.595	2.458	5.51	3.58			

Table B.1 : The state of sample after the deposit. Each sample is described by a following set of internal variables and descriptors: the number of shells N, a height of sample H_0, a number density n, an inter-cluster (modified) void ratio $e^\star$, a total void ratio e, the coordination numbers of the neighbours and the contacts Z_n and Z_c, respectively, the percentage of shells located at boundary zone next to: the horizontal boundaries N_{NHB}/N, the radial boundaries N_{NRB}/N and any boundary N_{NB}/N.
A Sample name is established as follows: *Geometry_Size_Aimed-Density_Configuration_Additional-Specification* with options as follows:
(*a*) Geometry: **C** – cylinder or **P** – prism,
(*b*) Size: $D \times H_0$ for C or $L_x \times L_z$ with $L_y = Lx$ for P,
(*c*) Aimed density: **l** – relatively loose, **d** – relatively dense and **D** – dense,
(*d*) Additional specification: **A** to **F** – a shape of cluster (as presented in the **Table A.1** in **Appendix A.1**) or a preferential shell orientation: **H** – horizontal or **V** – vertical.

C Simulation of uniaxial compression (oedometer tests)

		Links						Contacts			
Modeling	Initial state	$f_I^\star$ (N)	$f_{II}^\star$ (N)	$f_I^\star/f_{II}^\star$	k_I (N/m)	k_I/k_{II}	q	k_n (N/m)	k_n/k_t	μ_{shells}	μ_{wall}
Section **5.1.1** A primary comparison with the experiments											
Oedo_first	C_35×12_d_01_A	85	50	1.70	$5.5\ 10^6$	1.00	2	$5.5\ 10^6$	1.00	0.36	0.15
Section **5.1.1** Size dependency											
Oedo_H12	C_35×12_d_01_A	85	50	1.70	$5.5\ 10^6$	1.00	2	$5.5\ 10^6$	1.00	0.36	0.15
(Oedo_first)											
Oedo_H10	C_35×10_d_01_A	85	50	1.70	$5.5\ 10^6$	1.00	2	$5.5\ 10^6$	1.00	0.36	0.15
Oedo_H7	C_35×7_d_01_A	85	50	1.70	$5.5\ 10^6$	1.00	2	$5.5\ 10^6$	1.00	0.36	0.15
Oedo_H5	C_35×5_d_01_A	85	50	1.70	$5.5\ 10^6$	1.00	2	$5.5\ 10^6$	1.00	0.36	0.15
Oedo_D25	C_25×13_d_01_A	85	50	1.70	$5.5\ 10^6$	1.00	2	$5.5\ 10^6$	1.00	0.36	0.15
Oedo_D11	C_11×13_d_01_A	85	50	1.70	$5.5\ 10^6$	1.00	2	$5.5\ 10^6$	1.00	0.36	0.15
Section **5.1.3** Influence of the parameters controlling the force laws											
(*i*) On the shear strength of shells											
Oedo_$f_{II}^\star$-50	C_25×13_d_01_A	85	50	1.70	$5.5\ 10^6$	1.00	2	$5.5\ 10^6$	1.00	0.36	0.15
(Oedo_D25)											
Oedo_$f_{II}^\star$-250	C_25×13_d_01_A	85	250	0.34	$5.5\ 10^6$	1.00	2	$5.5\ 10^6$	1.00	0.36	0.15
Oedo_$f_{II}^\star$-85	C_25×13_d_01_A	85	85	1.00	$5.5\ 10^6$	1.00	2	$5.5\ 10^6$	1.00	0.36	0.15
(*ii*) On the shape of yield line											
Oedo_q-2	C_25×13_d_02_A	85	250	0.34	$5.5\ 10^6$	1.00	2	$1.0\ 10^7$	1.00	0.30	0.15
Oedo_q-3	C_25×13_d_02_A	85	250	0.34	$5.5\ 10^6$	1.00	3	$1.0\ 10^7$	1.00	0.30	0.15
Oedo_q-5	C_25×13_d_02_A	85	250	0.34	$5.5\ 10^6$	1.00	5	$1.0\ 10^7$	1.00	0.30	0.15
(*iii*) On the tensile strength of shells											
Oedo_$f_I^\star$-92_Wm-7	C_25×13_d_01_A	$m=7.2, x_0=92$	250	–	$3.0\ 10^6$	1.00	2	$1.0\ 10^7$	1.00	0.36	0.45
Oedo_$f_I^\star$-150_Wm-4	C_25×13_d_01_A	$m=4.0, x_0=150$	250	0.60	$3.0\ 10^6$	1.00	2	$1.0\ 10^7$	1.00	0.36	0.15
Oedo_$f_I^\star$-130_Wm-5	C_25×13_d_01_A	$m=5.0, x_0=130$	250	0.52	$3.0\ 10^6$	1.00	2	$1.0\ 10^7$	1.00	0.36	0.15
Oedo_$f_I^\star$-110_Wm-6	C_25×13_d_01_A	$m=6.0, x_0=110$	250	0.44	$3.0\ 10^6$	1.00	2	$1.0\ 10^7$	1.00	0.36	0.15
Oedo_$f_I^\star$-92_Wm-4	C_25×13_d_01_A	$m=4.0, x_0=92$	250	0.37	$3.0\ 10^6$	1.00	2	$1.0\ 10^7$	1.00	0.36	0.15
Oedo_$f_I^\star$-150_Wm-7	C_25×13_d_01_A	$m=7.2, x_0=150$	250	0.60	$3.0\ 10^6$	1.00	2	$1.0\ 10^7$	1.00	0.36	0.15
Oedo_$f_I^\star$-40	C_25×13_d_02_A	40	118	0.34	$5.5\ 10^6$	1.00	2	$1.0\ 10^7$	1.00	0.30	0.15
Oedo_$f_I^\star$-225	C_25×13_d_02_A	255	750	0.34	$5.5\ 10^6$	1.00	2	$1.0\ 10^7$	1.00	0.30	0.15
Oedo_$f_I^\star$-85	C_25×13_d_02_A	85	250	0.34	$5.5\ 10^6$	1.00	2	$1.0\ 10^7$	1.00	0.30	0.15
(*iv*) On the contacts stiffnesses k_I, k_{II} in bonded contacts											

Continued on next page...

		Links						Contacts			
Modeling	Initial state	$f_I^\star$ (N)	$f_{II}^\star$ (N)	$f_I^\star/f_{II}^\star$	k_I (N/m)	k_I/k_{II}	q	k_n (N/m)	k_n/k_t	μ_{shells}	μ_{wall}
Oedo_k_I-3e^6	C_25×13_d_01_A	$m=4.0, x_0=150$	250	0.60	$3.0\ 10^6$	1.00	2	$1.0\ 10^7$	1.00	0.36	0.15
Oedo_k_I-7e^6_Wm-6	C_25×13_d_01_A	$m=4.0, x_0=150$	250	0.60	$m=6.15, x_0=7.2\ 10^6$	1.00	2	$1.0\ 10^7$	1.00	0.36	0.15
Oedo_k_I-4e^6_Wm-6	C_25×13_d_01_A	$m=4.0, x_0=150$	250	0.60	$m=6.15, x_0=4.0\ 10^6$	1.00	2	$1.0\ 10^7$	1.00	0.36	0.15
(v)On the inter-granular friction											
Oedo_μ_0	C_25×13_d_01_A	$m=7.2, x_0=92$	250	–	$3.0\ 10^6$	1.00	2	$1.0\ 10^7$	1.00	0.36	0.45
Oedo_$\hat{\mu}_{shell}$	C_25×13_d_01_A	$m=7.2, x_0=92$	250	–	$3.0\ 10^6$	1.00	2	$1.0\ 10^7$	1.00	0.60	0.15
Oedo_$\hat{\mu}_{wall}$	C_25×13_d_01_A	$m=7.2, x_0=92$	250	–	$3.0\ 10^6$	1.00	2	$1.0\ 10^7$	1.00	0.36	0.15
Section 5.1.4 An influence of initial state of an assembly											
(i) On the number density n											
Oedo_d	C_25×13_d_02_A	$m=4.0, x_0=150$	250	0.60	$m=6.15\, x_0=4\ 10^6$	1.00	2	$1.0\ 10^7$	1.00	0.36	0.15
Oedo_l	C_25×13_l_01_A	$m=4.0, x_0=150$	250	0.60	$m=6.15\, x_0=4\ 10^6$	1.00	2	$1.0\ 10^7$	1.00	0.30	0.15
Oedo_D	C_25×13_D_01_A	$m=4.0, x_0=150$	250	0.60	$m=6.15\, x_0=4\ 10^6$	1.00	2	$1.0\ 10^7$	1.00	0.30	0.15
(ii) On the anisotropy of shells orientations											
Oedo_r	C_25×13_d_02_A	85	250	0.34	$5.5\ 10^6$	1.00	2	$1.0\ 10^7$	1.00	0.30	0.15
Oedo_h	C_25×13_d_01_AH	85	250	0.34	$5.5\ 10^6$	1.00	2	$1.0\ 10^7$	1.00	0.30	0.15
Oedo_H	C_25×13_d_02_AH	85	250	0.34	$5.5\ 10^6$	1.00	2	$1.0\ 10^7$	1.00	0.30	0.15
Oedo_v	C_25×13_d_01_AV	85	250	0.34	$5.5\ 10^6$	1.00	2	$1.0\ 10^7$	1.00	0.30	0.15
Oedo_V	C_25×13_d_03_AV	85	250	0.34	$5.5\ 10^6$	1.00	2	$1.0\ 10^7$	1.00	0.30	0.15
Section 5.1.5 Geometry of elementary particles – sectors											
(i) On the number of sectors per shell											
Oedo_$N_{circ}^\star$-12 (Oedo_first)	C_35×12_d_01_A	85	50	1.70	$5.5\ 10^6$	1.00	2	$5.5\ 10^6$	1.00	0.36	0.15
Oedo_$N_{circ}^\star$-16	C_35×12_d_07_B	85	50	1.70	$5.5\ 10^6$	1.00	2	$5.5\ 10^6$	1.00	0.36	0.15
Oedo_$N_{axial}^\star$-1	C_11×13_d_01_A	85	50	1.70	$5.5\ 10^6$	1.00	2	$5.5\ 10^6$	1.00	0.36	0.15
Oedo_$N_{axial}^\star$-2	C_11×13_d_21_F	85	50	1.70	$2.8\ 10^6$	1.00	2	$5.5\ 10^6$	1.00	0.36	0.15
(ii) On the thickness of shell t											
Oedo_t-2.4	C_35×12_d_01_A	85	250	0.34	$5.5\ 10^6$	1.00	2	$1.0\ 10^7$	1.00	0.30	0.15
Oedo_t-4.8	C_35×12_d_08_C	115	338	0.34	$5.5\ 10^6$	1.00	2	$1.0\ 10^7$	1.00	0.30	0.15
Oedo_t-3.6	C_35×12_d_09_D	105	309	0.34	$5.5\ 10^6$	1.00	2	$1.0\ 10^7$	1.00	0.30	0.15
Section 5.1.6 Comparison with experiments											
Oedo_Adjusted_Cyc	C_35×12_d_01_A	$m=5.0, x_0=190$	f($f_I^\star$)	0.34	$5.5\ 10^6$	1.00	5	$1.0\ 10^7$	1.00	0.40	0.40
Oedo_True_Cyc	C_25×13_exp_01_A	$m=5.0, x_0=190$	f($f_I^\star$)	0.34	$5.5\ 10^6$	1.00	5	$1.0\ 10^7$	1.00	0.40	0.40

Continued on next page...

		Links						Contacts			
Modeling	Initial state	$f_I^\star$ (N)	$f_{II}^\star$ (N)	$f_I^\star / f_{II}^\star$	k_I (N/m)	k_I / k_{II}	q	k_n (N/m)	k_n / k_t	μ_{shells}	μ_{wall}
Oedo_*d18*	C_25×13_d_02_A	85	250	0.34	5.5 10^6	1.00	2	1.0 10^7	1.00	0.30	0.15
Oedo_*d20*	C_25×13_d_01_E	100	295	0.34	4.0 10^6	1.00	2	1.0 10^7	1.00	0.30	0.15
Section **6.1** Study of mechanical behaviour as a consequence of grain breakage											
Oedo_Adjusted	C_25×13_l_01_A	$m = 5.0\, x_0 = 190$	f($f_I^\star$)	0.34	5.5 10^6	1.00	5	1.0 10^7	1.00	0.40	0.40
Oedo_True	C_25×13_d_02_A	85	250	0.34	5.5 10^6	1.00	2	1.0 10^7	1.00	0.30	0.15
Oedo_l_$f_I^\star$-85	C_25×13_l_01_A	85	250	0.34	$m = 6.15\, x_0 = 4$ 10^6	1.00	2	1.0 10^7	1.00	0.30	0.15
Oedo_l_$f_I^\star$-150	C_25×13_l_01_A	150	250	0.60	$m = 6.15\, x_0 = 4$ 10^6	1.00	2	1.0 10^7	1.00	0.30	0.15
Oedo_l_$f_I^\star$-225	C_25×13_l_01_A	255	750	0.34	$m = 6.15\, x_0 = 4$ 10^6	1.00	2	1.0 10^7	1.00	0.30	0.15
Section **6.3** Micro-mechanics and anisotropy of fragments orientation during progressive breakage											
Oedo_control-ε_a	C_25×13_d_02_A	85	250	0.34	5.5 10^6	1.00	2	1.0 10^7	1.00	0.30	0.15
Oedo_control-σ_a	P_19×17_d_01_A	85	250	0.34	5.5 10^6	1.00	2	5.5 10^6	1.00	0.36	0.15

Table C.1 : The numerical input parameters used in the DEM simulations.
The force laws for cohesive links as explained in the **Figure** **3.5** in section **3.2**, and for the contacts as in the **Figure** **3.2** in section **3.1**.
An additional notation:
Wm – Weibull's modulus,
x_0 – Weibull's scale parameter

Name	Initial state	e_n^2	β	δt (s)	t_{Verlet} (δt)	D_{Verlet} (m)	d_{Verlet} (m)	$\vec{g}$
Section **5.1.1** A primary comparison with the experiments								
Oedo_first	C_35×12_d_01_A	1.00	0.7	$2\,10^{-7}$	1 000	0.010	0.001	yes
Section **5.1.1** Size dependency								
Oedo_H12	C_35×12_d_01_A	1.00	0.7	$2\,10^{-7}$	1 000	0.010	0.001	yes
(Oedo_first)								
Oedo_H10	C_35×10_d_01_A	1.00	0.7	$2\,10^{-7}$	1 000	0.010	0.001	yes
Oedo_H7	C_35×7_d_01_A	1.00	0.7	$2\,10^{-7}$	1 000	0.010	0.001	yes
Oedo_H5	C_35×5_d_01_A	1.00	0.7	$2\,10^{-7}$	1 000	0.010	0.001	yes
Oedo_D25	C_25×13_d_01_A	1.00	0.7	$2\,10^{-7}$	1 000	0.010	0.001	yes
Oedo_D11	C_11×13_d_01_A	1.00	0.7	$2\,10^{-7}$	500	0.010	0.001	yes
Section **5.1.3** Influence of the parameters controlling the force laws								
(*i*) On the shear strength of shells								
Oedo_$f_{II}^\star$-50	C_25×13_d_01_A	1.00	0.7	$2\,10^{-7}$	1 000	0.010	0.001	yes
(Oedo_D25)								
Oedo_$f_{II}^\star$-250	C_25×13_d_01_A	1.00	0.7	$2\,10^{-7}$	1 000	0.010	0.001	yes
Oedo_$f_{II}^\star$-85	C_25×13_d_01_A	1.00	0.7	$2\,10^{-7}$	1 000	0.010	0.001	yes
(*ii*) On the shape of yield line								
Oedo_q-2	C_25×13_d_02_A	0.02	0.7	$2\,10^{-7}$	1 000	0.010	0.001	yes
Oedo_q-3	C_25×13_d_02_A	0.02	0.7	$2\,10^{-7}$	1 000	0.010	0.001	yes
Oedo_q-5	C_25×13_d_02_A	0.02	0.7	$2\,10^{-7}$	1 000	0.010	0.001	yes
(*iii*) On the tensile strength of shells								
Oedo_$f_I^\star$-92_Wm-7	C_25×13_d_01_A	0.02	0.7	$2\,10^{-7}$	1 000	0.010	0.001	yes
Oedo_$f_I^\star$-150_Wm-4	C_25×13_d_01_A	0.02	0.7	$2\,10^{-7}$	1 000	0.010	0.001	yes
Oedo_$f_I^\star$-130_Wm-5	C_25×13_d_01_A	0.02	0.7	$2\,10^{-7}$	1 000	0.010	0.001	yes
Oedo_$f_I^\star$-110_Wm-6	C_25×13_d_01_A	0.02	0.7	$2\,10^{-7}$	1 000	0.010	0.001	yes
Oedo_$f_I^\star$-92_Wm-4	C_25×13_d_01_A	0.02	0.7	$2\,10^{-7}$	1 000	0.010	0.001	yes
Oedo_$f_I^\star$-150_Wm-7	C_25×13_d_01_A	0.02	0.7	$2\,10^{-7}$	1 000	0.010	0.001	yes
Oedo_$f_I^\star$-40	C_25×13_d_02_A	0.02	0.7	$2\,10^{-7}$	1 000	0.010	0.001	yes
Oedo_$f_I^\star$-225	C_25×13_d_02_A	0.02	0.7	$2\,10^{-7}$	1 000	0.010	0.001	yes
Oedo_$f_I^\star$-85	C_25×13_d_02_A	0.02	0.7	$2\,10^{-7}$	1 000	0.010	0.001	yes
(*iv*) On the contacts stiffnesses k_I, k_{II} in bonded contacts								
Oedo_k_I-3e^6	C_25×13_d_01_A	0.02	0.7	$2\,10^{-7}$	1 000	0.010	0.001	yes
Oedo_k_I-7e^6_Wm-7	C_25×13_d_01_A	0.02	0.7	$2\,10^{-7}$	1 000	0.010	0.001	yes
Oedo_k_I-4e^6_Wm-6	C_25×13_d_01_A	0.02	0.7	$2\,10^{-7}$	1 000	0.010	0.001	yes
(*v*)On the inter-granular friction								
Oedo_μ_0	C_25×13_d_01_A	0.02	0.7	$2\,10^{-7}$	1 000	0.010	0.001	yes
Oedo_$\hat{\mu}_{shell}$	C_25×13_d_01_A	0.02	0.7	$2\,10^{-7}$	1 000	0.010	0.001	yes
Oedo_$\hat{\mu}_{wall}$	C_25×13_d_01_A	0.02	0.7	$2\,10^{-7}$	1 000	0.010	0.001	yes
Section **5.1.4** An influence of initial state of an assembly								
(*i*) On the number density n								
Oedo_d	C_25×13_d_02_A	0.02	0.7	$2\,10^{-7}$	1 000	0.010	0.001	yes
Oedo_l	C_25×13_l_01_A	0.02	0.7	$2\,10^{-7}$	1 000	0.010	0.001	yes
Oedo_D	C_25×13_D_01_A	0.02	0.7	$2\,10^{-7}$	1 000	0.010	0.001	yes
(*ii*) On the anisotropy of shells orientations								
Oedo_r	C_25×13_d_02_A	0.02	0.7	$2\,10^{-7}$	1 000	0.010	0.001	yes

Continued on next page...

Name	Initial state	e_n^2	β	δt (s)	t_{Verlet} (δt)	D_{Verlet} (m)	d_{Verlet} (m)	$\vec{g}$
Oedo_h	C_25×13_d_01_AH	0.02	0.7	$2\ 10^{-7}$	500	0.010	0.001	yes
Oedo_H	C_25×13_d_02_AH	0.02	0.7	$2\ 10^{-7}$	500	0.010	0.001	yes
Oedo_v	C_25×13_d_01_AV	0.02	0.7	$2\ 10^{-7}$	500	0.010	0.001	yes
Oedo_V	C_25×13_d_03_AV	0.02	0.7	$2\ 10^{-7}$	500	0.010	0.001	yes
Section **5.1.5** Geometry of elementary particles – sectors								
(*i*) On the number of sectors per shell								
Oedo_$N^\star_{circ}$-12 (Oedo_first)	C_35×12_d_01_A	1.00	0.7	$2\ 10^{-7}$	1 000	0.010	0.001	yes
Oedo_$N^\star_{circ}$-16	C_35×12_d_07_B	1.00	0.7	$2\ 10^{-7}$	1 000	0.010	0.001	yes
Oedo_$N^\star_{axial}$-1	C_11×13_d_01_A	1.00	0.7	$2\ 10^{-7}$	500	0.010	0.001	yes
Oedo_$N^\star_{axial}$-2	C_11×13_d_21_F	1.00	0.7	$2\ 10^{-7}$	500	0.010	0.001	yes
(*ii*) On the thickness of shell t								
Oedo_t-2.4	C_35×12_d_01_A	1.00	0.7	$2\ 10^{-7}$	1 000	0.010	0.001	yes
Oedo_t-4.8	C_35×12_d_08_C	0.02	0.7	$2\ 10^{-7}$	1 000	0.010	0.001	yes
Oedo_t-3.6	C_35×12_d_09_D	0.02	0.7	$2\ 10^{-7}$	1 000	0.010	0.001	yes
Section **5.1.6** Comparison with experiments								
Oedo_Adjusted_Cyc	C_35×12_d_01_A	0.02	0.7	$2\ 10^{-7}$	1 000	0.010	0.001	yes
Oedo_True_Cyc	C_25×13_exp_01_A	0.02	0.7	$2\ 10^{-7}$	1 000	0.010	0.001	no
Oedo_*d18*	C_25×13_d_02_A	0.02	0.7	$2\ 10^{-7}$	1 000	0.010	0.001	yes
Oedo_*d20*	C_25×13_d_01_E	0.02	0.7	$2\ 10^{-7}$	500	0.010	0.001	yes
Section **6.1** Study of mechanical behaviour as a consequence of grain breakage								
Oedo_Adjusted	C_25×13_l_01_A	0.02	0.7	$2\ 10^{-7}$	1 000	0.010	0.001	yes
Oedo_True	C_25×13_d_02_A	0.02	0.7	$2\ 10^{-7}$	1 000	0.010	0.001	yes
Oedo_l_$f_I^\star$-85	C_25×13_l_01_A	0.02	0.7	$2\ 10^{-7}$	1 000	0.010	0.001	yes
Oedo_l_$f_I^\star$-150	C_25×13_l_01_A	0.02	0.7	$2\ 10^{-7}$	1 000	0.010	0.001	yes
Oedo_l_$f_I^\star$-225	C_25×13_l_01_A	0.02	0.7	$2\ 10^{-7}$	1 000	0.010	0.001	yes
Section **6.3** Micro-mechanics and anisotropy of fragments orientation during progressive breakage								
Oedo_control-ε_a	C_25×13_d_02_A	0.02	0.7	$2\ 10^{-7}$	1 000	0.010	0.001	yes
Oedo_control-σ_a	P_19×17_d_01_A	$4\ 10^{-9}$	0.0	$2\ 10^{-7}$	1 000	0.010	0.001	no

Table C.2 : The numerical parameters (*vol.* 2) used in the DEM simulations. Two damping parameters for viscous damping e_n^2 and Cundall damping β, a times step δt, neighbourhood list parameters according Verlet algorithm (t_{Verlet}, D_{Verlet}, d_{Verlet}) and the gravity vector $\vec{g}$.

List of Figures

List of Tables

Bibliography

Abreu, C. R. A., Tavares, F. W., and Castier, M. (2003). Influence of particle shape on the packing and on the segregation of spherocylinders via monte carlo simulations. *Powder Technology*, 134:167–180.

Allen, M. P. and Tildesley, D. J. (1989). *Computer simulation of liquids*. Oxford University Press, USA.

Alonso, E. E., Pinyol, N. M., and Olivella, S. (2005). A review of beliche dam. *Géotechnique*, 55:267–285.

Andra (2005). Synthesis: Evaluation of the feasibility of a geological repository in an argillaceous formation. Technical Report RPFMFS170011, Meuse/Haute-Marne site.

Andra (2016). Rapport d'activité R&D. Technical report, Meuse/Haute-Marne site.

Andra (2016). Voussoir Monobloc Compressible. https://www.youtube.com/watch?v=H2r3T1cemuk.

Armand, G., Noiret, A., Zghondi, J., and Seyedi, D. (2013). Short- and long-term behaviors of drifts in the callovo-oxfordian claystone at the meuse/haute-marne underground research laboratory. *Joumal of Rock Mechanics and Geotechnical Engineering*, 5:221–230.

Atman, A. P. F., Claudin, P., and Combe, G. (2009). Departure from elasticity in granular players: Investigation of a crossover overload force. *Computer Physcis Communications*, 180:612–615.

Azéma, E., Estrada, N., and Radjaï, F. (2012). Nonlinear effects of particle shape angularity in sheared granular media. *Physical Review E*, 86:041301.

Azéma, E., Radjaï, F., and Dubois, F. (2013a). Packings of irregular polyhedral particles: Strength, structure, and effects of angularity. *Physical Review E*, 87:062203.

Azéma, E., Radjaï, F., Saint-Cyr, B., Delenne, J.-Y., and Sornay, P. (2013b). Rheology of three-dimensional packings of aggregates: Microstructure and effects of nonconvexity. *Physical Review E*, 87:052205.

Azéma, E., Radjaï, F., and Saussine, G. (2009). Quasistatic rheology, force transmission and fabric properties of a packing of irregular polyhedral particles. *Mechanics of Materials*, 41:729–741.

Bauer, E. (1996). Calibration of a Comprehensive Hypoplastic Model for Granular Materials. *Soils and foundations*, 36(1):12–26.

Bauer, E., Li, L., and Khosravi, M. (2017). Modelling grain damage under plane strain compression using a micro-polar continuum. In *Bifurcation and Degradation of Geomaterials with Engineering Applications: Proceedings of the 11th International Workshop on Bifurcation and Degradation in Geomaterials*, pages 539–546.

Bažant, Z. P., Tabbara, M. R., Kazemi, M. T., and Pijaudier-Cabot, G. (1990). Random particle model for fracture of aggregate or fiber composites. *Journal of Engineering Mechanics*, 116:1686.

Ben-Nun, O. and Einav, I. (2010). The role of self-organization during confined comminution of granular materials Oded Ben-Nun and Itai Einav Receive free email alerts when new articles cite this article - sign up. *Philosophical Transactions of The Royal Society A*, 368:231–247.

Blanc, N., Richefeu, V., Mayer, C., and Delenne, J.-Y. (2017). Deconvolution of grading curves during milling: example of wheat straw. In *EPJ Web Conf*, volume 140, page 13019.

Bolton, M. D. and McDowell, G. R. (1997). Clastic Mechanics. In Fleck, N. and Cocks, C. F., editors, *IUTAM Symposium on Mechanics of Granular and Porous Materials*, pages 35–46. Kluwer Academic Publisher.

Bolton, M. D., Nakata, Y., and Cheng, Y. P. (2008). Micro- and macro-mechanical behaviour of DEM crushable materials. *Géotechnique*, 58(6):471–480.

Bosgiraud, J.-M., Armand, G., and Simon, J. (2017). Compressible Arch Segments for the Cigéo Access Ramps, Drifts and Vaults-A Field Test. In *WM2017 Conference, March05-09,2017, Phoenix, Arizona, USA*, page 17011.

Brewer, R. (1964). *Fabric and mineral analysis of soils*. Wiley.

Calvetti, F., Combe, G., and Lanier, J. (1997). Experimental micromechanical analysis of a 2D granular material: relation between structure evolution and loading path. *Mechanics of Cohesive-frictional Materials*, 2:121–163.

Cantor, D. and Estrada, N. (2015). New approach to grain fragmentation for discrete element methods. In *Geomechanics from Micro to Macro*, pages 257–262. Taylor & Francis Group.

Cantor García, D. (2017). *Compaction des materiaux granulaires fragmentables en 3D*. PhD thesis, Université de Montpellier.

Casini, F., Viggiani, G. M., and Springman, S. M. (2013). Breakage of an artificial crushable material under loading. *Granular Matter*, 15:661–673.

CEGEO, Saint-Cyr, B., Szarf, K., Voivret, C., Azéma, E., Richefeu, V., Delenne, J.-Y., Combe, G., Nouguier-Lehon, C., Villard, P., Sornay, P., Chaze, M., and Radjai, F. (2012). Particle shape dependence in 2d granular media. *Europhysics Letters*, 98:44008.

Charalampidou, E.-M., Combe, G., Viggiani, G., Lanier, J., Nakagawa, M., and Luding, S. (2009). Mechanical behavior of mixtures of circular and rectangular 2d particles. In *AIP Conference Proceedings*. AIP.

Cheng, Y. P., Nakata, Y., and Bolton, M. D. (2003). Discrete element simulation of crushable soil. *Géotechnique*, 53(7):633–641.

Chevalier, B., Combe, G., and Villard, P. (2012). Experimental and discrete element modeling studies of the trapdoor problem: influence of the macro-mechanical frictional parameters. *Acta Geotechnica*, 7:15–39.

Chianese, R. B. and Erdlac, R. J. (1988). The general solution to the distribution of stresses in as circular ring compressed by two forces acting along a diameter. *The Quarterly Journal of Mechanics and Applied Mathematics*, 41:239–247.

Cho, G.-C. and Dodds, J.and Santamarina, J. C. (2006). Particle shape effects on packing density, stiffness, and strength: Natural and crushed sands. *Journal of Geotechnical and Geoenvironmental Engineering*, 132:591–602.

Ciantia, M. O., Arroyo, M., Calvetti, F., and Gens, A. (2015). An approach to enhance efficiency of dem modelling of soils with crushable grains. *Géotechnique*, 65:91–110.

Cil, M. B. and Alshibli, K. A. (2012). 3d assessment of fracture of sand particles using discrete element method. *Géotechnique Letters*, 2:161–166.

Colliat-Dangus, J.-L. (1986). *Comportement des matériaux granulaires sous fortes contraintes: influence de la nature minéralogique du matériau étudié*. PhD thesis, Université de Grenoble.

Combe, G. and Roux, J.-N. (2017). Good practice and sample preparation - construction of granular packings. *ALERT geomaterials Doctoral School 2017, Aussois, France*.

Coop, M. R. and Altuhafi, F. N. (2011). Changes to particle characteristics associated with the compression of sands. *Géotechnique*, 61:459–471.

Cruz, F., Emam, S., Prochnow, M., Roux, J.-N., and Chevoir, F. (2005). Rheophysics of dense granular materials: Discrete simulation of plane shear flows. *Physical Review E*, 72:(021309)1–17.

Cundall, P. A. and Strack, O. D. L. (1979). A discrete numerical model for granular assemblies. *Géotechnique*, 29(1):47–65.

de Bono, J. P. and McDowell, G. R. (2014). Discrete element modelling of one-dimensional compression of cemented sand. *Granular Matter*, 16:79–90.

de Bono, J. P. and Mcdowell, G. R. (2016a). Investigating the effects of particle shape on normal compression and overconsolidation using DEM. *Géotechnique*, pages 1–14.

de Bono, J. P. and Mcdowell, G. R. (2016b). Particle breakage criteria in discrete-element modelling. *Granular Matter*, 18:55.

de Bono, J. P. and Mcdowell, G. R. (2018). On the micro mechanics of yielding and hardening of crushable granular soils. *Computers and Geotechnics*, 97:167–188.

De-Lin, M. (1990). Elastic Stress Solution for a Ring Subjected to Point-loaded Compression. *International Journal of Pressure Vessels and Piping*, 42:185–191.

Delay, J., Bossart, P., Ling, L. X., Blechschmidt, I., Ohlsson, M., Vinsot, A., Nussbaum, C., and Maes, N. (2014). Three decades of underground research laboratories: what have we learned? *Geological Society London Special Publications*, 400:7–32.

Delenne, J.-Y. (2002). *Milieux granulaires à comportement solide. Modélisation, analyse expérimentale de la cohésion, validation et applications*. PhD thesis, Université Montpellier II.

Desrues, J., Argilaga, A., Caillerie, D., Combe, G., Nguyen, T. K., Richefeu, V., and Dal Pont, S. (2019). From discrete to continuum modelling of boundary value problems in geomechanics: An integrated fem-dem approach. *International Journal for Numerical and Analytical Methods in Geomechanics*.

Di Emidio, G., Verástegui Flores, R. D., and Van Impe, W. F. (2009). Crushability of granular materials at high stress levels. In *Proceedings of the 17th International Conference on Soil Mechanics and Geotechnical Engineering*.

Doreau-Malioche, J. (2018). *Grain-scale investigation of sand-pile interface under axial loading conditions using x-ray tomography*. PhD thesis, Université Grenoble Alpes.

Druckrey, A. M. and Alshibli, K. A. (2016). 3d finite element modeling of sand particle fracture based on in situ x-ray synchrotron imaging. *International Journal for Numerical and Analytical Methods in Geomechanics*, 40:105–116.

Duran, J. (2000). *Sands, Powders, and Grains: An Introduction to the Physics of Granular Materials*. Springer-Verlag New York, 1 edition.

Einav, I. (2007a). Breakage mechanics—Part I: Theory. *Journal of the Mechanics and Physics of Solids*, 55.

Einav, I. (2007b). Breakage mechanics—Part II: Modelling granular materials. *Journal of the Mechanics and Physics of Solids*, 55.

Elandalousi, R., Dupla, J.-C., and Canou, J. (2018). Caractérisation mécanique d'un matériau compressible du type "coques". Technical Report DRPFMFS180025, Laboratoire Navier, Paris.

Emam, S., Canou, J., Corfdir, A., Dupla, J.-C., and Roux, J.-N. (2006). Elaboration et comportement mécanique de matériaux granulaires solides modèeles : expériences et simulations numériques. In Cazacliu, B. and Roux, J.-N., editors, *Rhéologie des pâtes et des matériaux granulaires*, Sciences pour le génie civil SI 12, Etudes et Recherches des Laboratoires des Ponts et Chaussées, pages 105–146. Laboratoire Central des Ponts et Chaussées, Paris.

Esnault, V. P. B. and Roux, J.-N. (2013). 3D numerical simulation study of quasistatic grinding process on a model granular material. *Mechanics of Materials*, 66:80–109.

Ferellec, J.-F. and McDowell, G. R. (2008). A simple method to create complex particle shapes for dem. *Geomechanics and Geoengineering*, 3:211–216.

Fukumoto, T. (1992). Particle breakage characteristics of granular soils. *Soils and Foundations*, 32:26–40.

Griffith, A. A. (1921). The phenomena of rupture and flow in solids. *Philosophical Transactions of the Royal Society of London. Series A, Containing Papers of a Mathematical or Physical Character*, 221:163–198.

Guayacán-Carrillo, L. M. (2016). *Analysis of long-term closure in drifts excavated in Callovo-Oxfordian claystone: roles of anisotropy and hydromechanical couplings*. PhD thesis, Université Paris-Est.

Gudehus, G. (1996). A comprehensive constitutive equation for granular material. *Soils and Foundations*, 36(1):1–12.

Guida, G., Casini, F., Viggiani, G. M. B., Andò, E., and Viggiani, G. (2018). Breakage mechanisms of highly porous particles in 1D compression revealed by X-ray tomography. *Géotechnique Letters Engineering*, 8:155–160.

Hardin, B. (1985). Crushing of soil particles. *Journal of Geotechnical Engineering*, 111.

Hardin, B. O. (1987). 1- d strain in normally consolidated cohesionless soils. *Journal of Geotechnical Engineering*, 113:1449–1467.

Hencky, H. (1928). Uber die form des elastizitatsgesetzes bei ideal elastischen stoffen. *Zeit. Tech. Phys.*, 9:215–220.

Hobbs, D. (1964). The tensile strength of rocks. *International Journal of Rock Mechanics and Mining Sciences and Geomechanics Abstracts*, 1:385–396.

Hondros, G. (1959). The evaluation of poisson's ratio and the modulus of materials of a low tensile resistance by the brazilian test with particular reference to concrete. *Australian Journal Applied Science*, 10:243–264.

Hu, W., Yin, Z. Y., Dano, C., and Hicher, P.-Y. (2011). A constitutive model for granular materials considering grain breakage. *Science China Technological Sciences*, 54(8):2188–2196.

Hudson, J. A. (1969). Tensile strength and the ring test. *International Journal of Rock Mechanics and Mining Sciences and Geomechanics Abstracts*, 6:91–97.

Institut Universitaire de Technologie du Mans (2018). RDM. http://iut.univ-lemans.fr/ydlogi/presentation.html.

Issa, J. A. and Nelson, R. B. (1992). Numerical analysis of micromechanical behaviour of granular materials. *Engineering Computations*, 9:211–223.

Jacobson, L., Sandoval, D., and Rodella, D. (1998). Report on the testing of Raschig Rings. Technical Report LA-UR–98-3450, Los Alamos National Laboratory.

Jensen, R. P., Plesha, M. E., Edil, T. B., Bosscher, P. J., and K., N. B. (2001). Dem simulation of particle damage in granular media — structure interfaces. *International Journal of Geomechanics*, 1:21–39.

Karatza, Z. (2017). *A study of temporal and spatial evolution of deformation and breakage of dry granular materials using x-ray computed tomography and the discrete element method*. PhD thesis, The University of Edinburgh.

Khalili, M. H. (2016). *Tracking and modelling small motions at grain scale in granular materials under compression by x-Ray microtomography and discrete simulations*. PhD thesis, Université Paris-Est.

Lade, P. V., Y., J. A., and Bopp, P. A. (1996). Significance of particle crushing in granular materials. *Journal of Geotechnical Engineering*, 122:309–316.

Langston, P. A., Al-Awamleh, M. A., Fraige, F. Y., and Asmar, B. N. (2004). Distinct element modelling of non-spherical frictionless particle flow. *Chemical Engineering Science*, 59:425–435.

Laufer, I. (2015). Grain crushing and high-pressure oedometer tests simulated with the discrete element method. *Granular Matter*, pages 389–412.

Lobo-Guerrero, S. and Vallejo, L. E. (2005). Crushing a weak granular material: experimental numerical analyses. *Géotechnique*, 55:245–249.

Luding, S. (1997). Stress distribution in static two dimensional granular model media in the absence of friction. *Physical Review E*, 55(4):4720–4729.

Luding, S., Clément, E., Blumen, A., Rajchenbach, J., and Duran, J. (1994). Anomalous energy dissipation in molecular-dynamics simulations of grains: The "detachment" effect. *Physical Review E*, 50:4113–4122.

Luo, T., Ooi, E., Chan, A., and Fu, S. (2017). The combined scaled boundary finite-discrete element method: Grain breakage modelling in cohesion-less granular media. *Computers and Geotechnics*, 88:199–221.

Ly, B. Q. H. (2018). *Contribution à l'étude des soutènements compressibles puor les ouvrages souterrains. Validation du modèle rhéologique SC2D pour l'argilite du COx et construction d'un modèle rhéologique Coqcéram pour le matériau compressible"*. PhD thesis, INSA Rennes.

Ly, B. Q. H. and Robinet, J. C. (2017). Réalisation d'essais oedométriques sur des galettes fabriquées par l'entreprise STRADAL - Déliverable n°7. Technical Report CRP0EUG170004, Euro-Géomat-Consulting EGC.

Ma, G., Zhou, W., Chang, X.-L., and Chen, M.-X. (2016). A hybrid approach for modeling of breakable granular materials using combined finite-discrete element method. *Granular Matter*, 18:7.

Matsushima, T., Saomoto, H., Matsumoto, M., Toda, K., and Yamada, Y. (2003). Discrete element simulation of an assembly of irregularly –shaped grains: Quantitative comparison with experiments. In *16th ASCE Engineering Mechanics Conference*.

McDowell, G. and Amon, A. (2000). The application of weibull statistics to the fracture of soil particles. *Soils and Foundations*, 40:133–141.

McDowell, G., Bolton, M., and Robertson, D. (1996). The fractal crushing of granular materials. *Journal of the Mechanics and Physics of Solids*, 44(12):2079–2102.

McDowell, G. R. (2001). Statistics of soil particle strength. *Géotechnique*, 51(10):897–900.

McDowell, G. R. and Bolton, M. D. (1998). On the micromechanics of crushable aggregates. *Géotechnique*, 48:667–679.

McDowell, G. R. and De Bono, J. (2013). On the micro mechanics of one-dimensional normal compression. *Géotechniqe*, 63(11):895–908.

McDowell, G. R. and Harireche, O. (2002). Discrete element modelling of soil particle fracture. *Géotechnique*, 52(2):131–135.

Mellor, M. and Hawkes, I. (1971). Measurement of tensile strength by diametral compression of discs and annuli. *Engineering Geology*, 5:173–225.

Nader, F., Silvani, C., and Djeran-Maigre, I. (2017). Grain breakage under uniaxial compression, through 3D DEM modelling. *EPJ Web of Conferences*, 140:07005.

Nakata, Y., Kato, Y., Hyodo, M., Hyde, A. F., and Murata, H. (2001a). One-dimensional compression behaviour of uniformly graded sand related to single particle crushing strength. *Soils and Foundations*, 41(2):39–51.

Nakata, Y., Masayuki, H., and Hyde, A. F. L. (2001b). Microscopic particles crushing of sand subjected to high pressure one-dimensional compression. *Soils and Foundations*, 41(1):69–82.

Nguyen, D.-H., Azéma, E., Philippe, S., and Radjaï, F. (2015). Bonded-cell model for particle fracture. *Physical Review E*, 91(2):022203.

Nguyen, T. K., Combe, G., Caillerie, D., and Desrues, J. (2014). FEM × DEM Modelling of Cohesive Granular Materials : Numerical Homogenisation. *Acta Geophysica*, 62(5):1109–1126.

Oda, M. (1972). Initial fabrics and their realtions to mechanical properties of granular material. *Soils and Foundations*, 12(1):17–36.

Oquendo, W. F., Muñoz, J. D., and Lizcano, A. (2009). Oedometric test , Bauer's law and the micro-macro connection for a dry sand. *Computer Physics Communications*, 180(4):616–620.

Papazoglou, A. (2018). *An experimental study of localized compaction in high porosity rocks: the example of Tuffeau de Maastricht*. PhD thesis, Université Grenoble Alples.

Potyondy, D. O. and Cundall, P. A. (2004). A bonded-particle model for rock. *International Journal of Rock Mechanics and Mining Sciences*, 41:1329–1364.

Radjai, F., Delenne, J.-Y.and Azéma, E., and Roux, S. (2012). Fabric evolution and accessible geometrical states in granular materials. *Granular Matter*, 14:190–198.

Radjaï, F. and Dubois, F. (2011). *Discrete-Element Modeling of Granular Materials*. Wiley-Iste.

Radjai, F., Jean, M., Moreau, J.-J., and Roux, S. (1996). Force distributions in dense two-dimensional granular systems. *Physical Review Letters*, 77:274–277.

Richefeu, V. (2016). Rockable – documentation. https://richefeu.gitbooks.io/mbox-documentation/content/rockable/.

Roux, J.-N. and Chevoir, F. (2005). Discrete numerical simulation and the mechanical behaviour of granular materials. *Bulletin des Laboratoires des Ponts et Chaussées*, 254:109–138.

Salami, Y., Dano, C., and Hicher, P.-Y. (2017). An experimental study on the influence of the coordination number on grain crushing. *European Journal of Environmental and Civil engineering*, pages 1–17.

Salem, A. and Akbari Sene, R. (2012). Optimization of zeolite-based adsorbent composition for fabricating reliable raschig ring shaped by extrusion using weibull statistical theory. *Microporous and Mesoporous Materials*, 163:65–75.

Sukumaran, B., Einav, I., and Dyskin, A. V. (2006). Qualitative assessment of the influence of coordination number on crushing strength using DEM. In *Fifth World Congress on Particle Technology*, page 23–27.

Szarf, P., G. Combe, G., and Villard, P. (2011). Polygons vs. clumps of discs: A numerical study of the influence of grain shape on the mechanical behaviour of granular materials. *Powder Technology*, 208:279–288.

Tapias, M., Alonso, E. E., and Gili, J. (2015). A particle model for rockfill behaviour. *Géotechnique*, 65:975–994.

Thornton, C. and Yin, K. (1991). Impact of elastic spheres with and without adhesion. *Powder Technology*, 65:0–166.

Thornton, C., Yin, K. K., and Adams, M. J. (1996). Numerical simulation of the impact fracture and fragmentation of agglomerates. *Journal of Physics D Applied Physics*, 29:424–435.

Tsoungui, O., Vallet, D., and Charmet, J.-C. (1999). Numerical model of crushing of grains inside two-dimensional granular materials. *Powder Technology*, 105:190–198.

Turcotte, D. L. (1986). Fractals and fragmentation. *Journal of Geophysical Research*, 91:1921.

Ueda, T., Matsushima, T., and Yamada, Y. (2013). Dem simulation on the one-dimensional compression behavior of various shaped crushable granular materials. *Granular Matter*, 15:675–684.

Vallet, D. and Charmet, J. C. (1995). Mechanical behaviour of brittle cement grains. *Journal of Materials Science*, 30:2962–2967.

Wang, J. F. and Yan, H. B. (2011). 3d dem simulation of crushable granular soils under plane strain compression condition. *Procedia Engineering*, 14:1713–1720.

Weibull, W. (1951). A statistical distribution function of wide applicability. *Journal of applied mechanics*, 18:293–297.

Wiebicke, M., Andó, E., Viggiani, G., and Herle, I. (2015). Towards the measurement of fabric in granular materials with x-ray tomography. In Rinaldi, V. A., Zaballos, M. E., and Clariá, J. J., editors, *6th International Symposium on Deformation Characteristics of Geomaterials*, pages 423–430. IOS Press BV.

Wileveau, Y., Cornet, F. H., Desroches, J., and Blumling, P. (2007). Complete in situ stress determination in an argillite sedimentary formation. *Physics and Chemistry of the Earth*, 32:866–878.

Yang, Z. X., Jardine, R. J., Zhu, B. T., Foray, P., and Tsuha, C. H. C. (2010). Sand grain crushing and interface shearing during displacement pile installation in sand. *Géotechnique*, 60(6):469–482.

Zghondi, J., Armand, G., Bosgiraud, J. M., and Simon, J. (2018). Qualification, construction and analysis of precasted compressible Arch Segments drift test in the Andra Meuse/Haute-Marne Underground Research Laboratory (URL). In *ITA - Aites World Tunnel Congress*.

Zhang, X., Zhao, C., and Zhai, W. (2017). Dem analysis of ballast breakage under train loads and its effect on mechanical behaviour of railway track. In *7th International Conference on Discrete Element Methods*, volume 188, pages 1323–1333.

Zhou, W., Xu, K., Ma, G., and Chang, X. (2019). On the breakage function for constructing the fragment replacement modes. *Particuology*.

Zhu, F. and Zhao, J. (2019). Modeling continuous grain crushing in granular media: A hybrid peridynamics and physics engine approach. *Computer Methods in Applied Mechanics and Engineering*, 348:334–355.

Åström, J. and Herrmann, H. (1998). Fragmentation of grains in a two-dimensional packing. *The European Physical Journal B / Condensed Matter and Complex Systems*, 5:551–554.